Proteins at soft interfaces:
A self-assembly, structure, kinetics and function study

Universidad del País Vasco
Euskal Herriko Unibertsitatea

Aitziber Eleta Lopez

Leioa 2011

Proteins at soft interfaces:
A self-assembly, structure, kinetics and function study

Dissertation presented to the
Biochemistry and Molecular Biology department
UPV/EHU

for the degree of Doctor of Philosophy

presented by

AITZIBER ELETA LOPEZ

Thesis advisor: Prof. Dr. José Luis Toca-Herrera

Leioa 2011

This PhD thesis has been performed at,

Biosurfaces Unit
CICbiomaGUNE Institute
Donostia/San Sebastian

Institute for transfusion medicine
Charité Medicine University
Berlin

Center for Nanobiotechnology
University of Natural Resources and
Applied Life Sciences (BOKU)
Vienna

Colloids and interface of
Max Planck Institute
Golm-Potsdam

Familiari eskainia,

"Oiu bat aditua izan da
Euskaldunen mendien artetik"

2002-XI-12

Eskerrak/Acknowledgments

Tesia egiten hasi nintzenean nanoteknologia eta biomimetika bezalako gauzei buruz ezer gutxi ezagutzen nuen. Dena berria eta hein haundi batean ezezaguna zen niretzat, baina ilusio haundiz hartu nuen bizitzak eskaintzen zidan erronka berria. Lau urte pasa dira honez gero (azkar pasa ere) eta bai ezagutza aldetik bai pertsonalki urte hauek oso emankorrak izan dira. Tesiak alor ezberdinak (biologia, fisika eta kimika) konbinatuz, gai zehatz batean sakontzeko aukera eman dit baina orokorrean zientziaren ikuspegi zabalago bat izatea lortu dudala iruditzen zait.

Lan hau aurrera ateratzeko, dudarik gabe, urte hauetan zehar pertsona askorengandik jaso dudan laguntza ezinbestekoa izan da. Pertsona guzti hauek lan honen parte dira eta ez da erreza izango denei behar bezela eskertzea.

Primeramente me gustaría agradecer a mi director de tesis el Profesor José Luis Toca Herrera por abrirme las puertas a la investigación y darme la oportunidad de hacer la tesis en su grupo. Estoy muy agradecida por haber tenido todos los medios disponibles para aprender y trabajar tanto dentro como fuera del centro. Baita CICbiomaGUNEri eskerrak sostengu ekonomikoagatik.

Thanks also to all the tribunal members and to Dr. Seta Küpcü and Dr. Mihaela Delcea for being external evaluators of the thesis.

El apoyo de todos los compañeros tanto del centro como del laboratorio ha sido muy importante a lo largo de estos años, han hecho que todo sea más fácil. Quiero agradecer a Susana por introducirme en el mundo de las técnicas y darme las bases para poder trabajar con ellas. También le agradezco mucho por la ayuda prestada para escribir el primer artículo. I want to thank Kathryn because she was always available to help and to correct the science and the English. I appreciate a lot her constructive criticism and that she always encourages me with the work (I will miss your cakes and cookies). Especialmente quiero agradecer a Mihaela por el apoyo que me ha dado durante todos estos años, por animarme siempre y por sus buenos consejos (multu pupici!). A Verónica por todos los ánimos que me ha dado durante su estancia en Donostia (¡ha sido un placer conocerte!). Ezin ditut nire laguntzaileak izan diren Leticia eta Aitor ahaztu. Nirekin hilabete gutxi egon arren beraiekin lanean oso gustora egon naiz eta asko estimatzen dut bien laguntza. Por otro lado, quiero agradecer a Juan Etxebarria por su ayuda con la síntesis y el NMR. Ainhoa Lejardirekin AFMan pasatako orduak ere gogoan ditut. Majina bat bidai egin behar izan ditu Markinatik Donostiara.

También quiero agradecer a Alicia Alonso porque está siendo una pieza clave para poder realizar toda la burocracia para la defensa de la tesis.

Now I move abroad where I have to thank Dr. Hans Bäumler and Dr. Radostina Georgieva for give me the opportunity to work in Charité (Berlin) and provide all the facilities to progress with my project. Thanks also to all the colleagues from the lab in Charité and MPI (Golm). Also I want to thank Jacqueline Friedmann from Vienna for being so helpful with me.

Zentruan egindako lagun guztiak oso garrantzitsuak izan dira. Lehendabiziko bi urteetan bigarren pisuan geneukan giroa nabarmentzen dut batipat. Bestalde, otorduak atsegingarri bihurtu dituzten orori ere eskerrak eman nahi dizkiet. Proiektuari hainbeste lan ordu eskaini eta gure artean giro ona edukitzea funtsezkoa izan da aurrera egiteko. Bereziki Jagoba eta Irantzuri eman nahi dizkiet eskerrak (mis Küllegens!!!), elkarrizketa produktiboak izateaz gainera ikaragarri ongi pasa dudalako beraiekin eta batez ere tesiaren azkeneko etapan izugarri animatu nautelako.

Bukatzeko, nire bizitzan zutabe garrantzitsuak direnei eskerrak eman nahi dizkiet. Familiari, hasieratik animatu nautelako eta laguntza eta aholkuak behar ditudanean beti laguntzeko prest daudelako. Nire kuadrilari, asteburuetan beraiekin elkartzea oso pozgarria delako. Eta nola ez, Ikerri (Txoko) beti ondoan egoteagatik.

Index

Summary

This PhD thesis reports the adsorption and immobilization of two dissimilar proteins, bacterial SbpA and Human Serum Albumin, on soft surfaces. These proteins have been selected due to differences in structure and biological function.

The thesis shows different strategies for surface chemistry modification that permit to generate crystalline surface layers, maintaining constant the lattice parameters, the thickness, the adsorbed protein mass, but changing the protein crystalline domain size and the protein adsorption rate.

Through the combination of Atomic Force Microscopy (AFM) and Quartz Crystal Microbalance with Dissipation monitoring (QCM-D), the mechanism of S-layer formation has been clarified at nanoscale resolution for the first time. First, S-protein adsorbs on surface forming nucleation points; second, S-proteins start the self-assembly process that build the protein crystal layer; and third, the protein crystal domains reorganize themselves to minimize the amount of surface defects and therefore the surface energy.

Furthermore, the thermal stability of Human Serum Albumin (HSA) and the free energy and binding constant HSA-ibuprofen and HSA-bilirubin complexes have been determined. In addition, systematic immobilization studies permitted to find the best substrate for HSA adsorption at physiological pH. HSA immobilization and a new strategy to functionalize AFM tips allow to investigate the interaction between ibuprofen and HSA, obtaining a first description of the energetic landscape: the distance to the transition state and dissociation rate constant at zero force. These results might indicate that albumin loses functionality through surface immobilization.

Key words: S-layer, human serum albumin, atomic force microscopy, quartz crystal microbalance with dissipation, calorimetry, surface chemistry modification, protein adsorption, self-assembly, protein recrystallization and biomimetics.

Laburpena

Doktoradutza tesi honek bi proteina ezberdinen, bakteria-SbpA (S-proteina) eta giza albuminaren adsortzioa eta inmobilizazioa gainazal biguinetan biltzen du. Bi proteina hauek egitura eta funtzio biologiko ezberdina dutelako aukeratuak izan dira.

Lan honek gainazalen kimika modifikatzeko estrategia ezberdinak erakusten ditu zeintzuk gainazal geruza kristalinoen formazioa ahalbideratzen duten. Estrategia hauei esker geruza kristalinoen sare-unitateak, lodiera eta adsorbatutako masa konstante mantentzen dira, proteina kristalen domeinuen tamaina eta proteinaren adsortzio abiadura aldatzerakoan.

Indar atomikoko mikroskopioa (AFM) eta disipazio neurridunezko kuartzo kristalezko mikrobalantza (QCM-D) konbinatuz, S-geruzen formazio mekanismoa eskala nanometrikoan argitu da lehen aldiz; lehenik, S-proteina adsorbatu egiten da gainazalean nukleazio puntuak sortuz; bigarrenik, S-proteinak berez elkartzen hasiko dira gainazalean geruza kristalinoa erakikiz (S-geruza); eta hirugarrenik, domeinu kristalinoak berrantolatu egiten dira gainazaleko defektuak gutxituz, hau da, gainazal-energia minimizatuz.

Bestalde, giza albuminaren (HSA) egonkortasun termikoa eta HSA-bilirubina eta HSA-ibuprofeno konplexuen energi askea eta lotura konstanteak determinatu dira. Are gehiago, HSA inmobilizazio azterketa sistematikoek HSA pH fisiologikoan adsorbatzeko gainazalik egokiena aurkitu da. HSAren inmobilizazioak eta AFM tip-a funtzionalizatzeko estrategie berriek, HSA eta ibuprofenoaren arteko interakzioa eta egoera energetikoa ikertzea ahalbideratu dute non transizo egoerarako distantzia eta disoziazio abiadura konstantea kalkulatu diren indarra zero denean. Emaitzek inmobilizatutako albuminak bere funtzionalitatea galdu dezakeela adierazten dute.

Hitz gakoak: S-geruza, giza albumina, indar atomikoko mikroskopioa, disipazio neurridunezko kuartzo kristalezko mikrobalantza, kalorimetria, gainazal kimikaren modifikazioa, proteinen adsortzioa, berezko elkarketa, proteinen errekristalizazioa, biomimetika.

Abbreviations

η	Viscosity		Man	Mannose
2D	Two dimension		$ManC_5S$	5,5'-Dithio bis (penthyl-α-D-mannopyranoside)
3D	Three dimension			
A	Absorbance		MeOH	Methanol
a, b	Unit cell vectors		MeONa	Sodium methoxide
aa	Amino acid		M_w	Molecular weight
AFM	Atomic Force Microscopy		n (chapter 2)	Overtone number
Al_2O_3	Alminium Oxide		n (chapter 6)	Binding constant
APTS	3-aminopropyltriethoxysilane		Na_2HPO_4	Sodium phosphate dibasic anhydrous
B_0	External magnetic field			
BSA	Bovine Serum Albumin		Na_2SO_4	Sodium sulfate
c	Concentration		NaCl	Sodium chloride
C	Proportionality constant		NaH_2PO_4	Sodium dihydrogen phosphate anhydrous
$CaCl_2$	Calcium chloride			
CD	Circular Dichroism		NAID	Non-steroidal antiinflamarory drug
$CH_3C_{11}S$	1-dodecanethiol			
CH_3C_5S	1-hexanethiol		NaOH	Sodium Hydroxide
$COOHC_{10}S$	11-mercapto undecanoic acid		$NH_2(EG)_6C_{11}Ac$	$NH_2((CH_2)_2O)_6(CH_2)_{11}SCOCH$
D	Diffusion coefficient			
d	Distance		NHS	Dimethylaminopyridine
d(H)	Dynamic diameter		NMR	Nuclear Magnetic Resonance
DLS	Dynamic Light Scattering		$OH(EG)_3C_{11}SH$	$OH((CH_2)_2O)_6(CH_2)_{11}SH$
DMF	Dimethylformamide		$OHC_{11}S$	11-mercapto-1-undecanol
DNA	Deoxiribonucleic acid		OTS	n-octadecyltrichlorosilane
DSC	Differential Scanning Calorimetry		PBS	Phosphate buffered saline
			PDADMAC	Polydiallyl Dimethyl Ammonium Chloride
EDCI	N-(3-dimethylaminopropyl)-N'-ethylcarbodiimide hydrochloride			
			PDLLA	Poly(L,D-lactide)
			PEI	Poly(ethylenimine)
EM	Electron Microscopy		PEM	Polyelectrolyte multilayer
E_M	Mechanical energy		PLCL	Poly(lactide-co-caprolactone)
E_T	Thermal energy		PLGA	Poly(lactide-co-glycolide)
EtOH	Ethanol		PLLA	Poly(L-lactide)
F	Force		PMe_3	Trimethylphosphine
f(Ka)	Henrys function		PSS	Poly(sodium 4-Styrenesulfonate)
f_0	Resonance frequency			
G'	Storage modulus		QCM-D	Quartz Crystal Microbalance with Dissipation
G''	Loss modulus			
Hb	Haemoglobin		r_p	Parallel reflection component
HSA	Human Serum Albumin		rpm	Revolutions per minute
I	Spin quantum number		R_q	Roughness
IgG	Immunoglobulin		r_s	Perpendicular reflection component
IS	International System			
ITC	Isothermal Titration Calorimetry		SAM	Self Assembly Monolayer
			SbpA	S-layer protein
K	Association constant		SDS	Sodium Dodecyl Sulfate
k_b	Boltzmann constant		Si_3N_4	Silicon nitride
kDa	Kilo Dalton		SiO_2	Silicon dioxide
K_e	Spring constant		T	Temperature
K_{off}	Dissociation rate constant		T_g	Glass Transition Temperature
l	Path length		THF	Tetrahydrofuran
Lam A	Enzyme		T_m	Transition temperature
LBL	Layer by layer		U_E	Electrophoretic mobility

UV	Ultraviolet
v_Q	Shear wave speed
x	Cantilever deflection
z (chapter 2)	ζ-potential
z (chapter 7)	Oscillation amplitude
γ (chapter 2)	Interfacial tension
γ (chapter 3)	angle between unit cell vectors
Δ	(delta) phase shift
Δc_p	Heat capacity
ΔD	Dissipation change
ΔF	Frequency change
ΔG	Gibbs free energy
ΔH	Enthalpy change
Δm	Mass density change
ΔS	Entropy change
ε (chapter 2)	Dielectric constant
ε (chapter 6)	Extinction coefficient
θ	Contact angle
ρ	Reflectivity coefficient
ψ	(psi) amplitude

Thesis outline

Chapter 1

Introduction

Proteins are one of the most important groups of macromolecules in the living organisms. Proteins are found in all living systems, from bacteria and viruses through unicellular and simple eukaryotes to vertebrates and mammals where they are involved in different functions.

Proteins basic units are amino acids, which bind together to build first a polypeptide chain. By means of intermolecular interactions, the polypeptide chains are able to fold into more complex three-dimensional structures that carry out specific functions (see figure 1.1). The simple combination of twenty different amino acids opens the possibility to form a number of different proteins that vary in chemistry, size, structure and function [1].
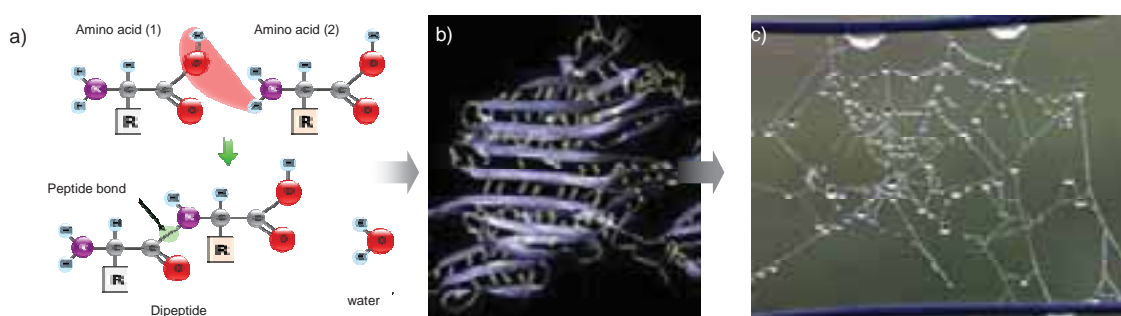
Figure 1.1. Proteins from the molecular view, to our eyes; a) The assembly of two amino acids by peptidic coupling to form a dipeptide (protein primary structure) [a] , b) Protein chains interact among themselves forming fibrous structures (quaternary structure) [b], c) Spider network made by proteins [c].

---

[a] Image adapted from *http://www.warpraptor.com*
[b] Image adapted from *http://www.hypography.com*
[c] Picture from Juan Antonio Garaikoetxea

Proteins perform different functions that are related to their conformation. There are transporter proteins, such as haemoglobin, the function of which is to transport the oxygen through the blood to the tissues [2]. Proteins (e.g. ferritin and casein) can also act as biological reserves to store ions and amino acids [3, 4]. Keratin is a structural protein found as hair, nails and in some animal shells [5]. The hormonal proteins coordinate certain body activities; for example, insulin regulates glucose metabolism [6]. Enzymes are proteins that catalyse chemical reactions. Examples of enzyme activity include the transcription of genetic information. Moreover, proteins (ie. antibodies) can bind to foreign biomolecules as past of the body's defense mechanism [7].

Some of the proteins mentioned above are found in solution but others are found at different interfaces. The behaviour of proteins at interfaces is relevant both natural and biotechnological processes [1, 8].

On one hand, protein adsorption at interfaces can lead to protein denaturation and loss of functionality [9-12]. This might be important for the build up of functional biomimetic supramolecular structures that could have potential application in biotechnology and biomedicine [13-15]. On the other hand, proteins inserted in natural membranes can interact with external molecules that affect their functionality. For example, malaria infected red blood cells synthesize proteins that are associated to membrane increasing the rigidity of the whole red blood cell [16].

The complete understanding of protein behaviour at interfaces is not a trivial task and requires the collaboration of interdisciplinary scientific areas: engineering, biology, chemistry and physics.

Protein adsorption at interfaces is a very complex process which is governed by different interaction forces such as hydrophobic, electrostatic, van der Waals interactions and hydrogen bonding. Moreover, the adsorption can be influenced by the protein properties itself, the substrate characteristics, the solvent, and the temperature [17-19]. The combination of these factors opens the possibility of many different scenarios for protein adsorption. Three possible scenarios are: 1) keeping the native structure after adsorption (maintenance of functionality), 2) denaturation after

20

adsorption (probable lost of functionality), 3) protein adsorption leading to new (supramolecular) structures (new functionality).

The two proteins studied in this thesis; the bacterial S-protein, SbpA (*Lysinibacillus sphaericus* CCM 2177) and Human Serum Albumin (HSA) have been chosen because of their different biological roles.

S-protein is a bacterial protein that naturally forms two-dimensional crystalline layers (so called S-layers) that cover the whole bacteria maintaining its shape and protecting from external agents. An especial property of these proteins is their intrinsic ability to create two dimensional nanostructures at different interfaces [20]. The second protein, human serum albumin is the most abundant protein found in plasma. Its main biological role is to transport different type of molecules [21].

1.1 Proteins

Bacterial SbpA and Human Serum Albumin (HSA) have different biological roles. This part of the introduction will give a general overview of the most important features of both proteins.

1.1.1   S-layers

S-layers are part of the outermost cell layer envelope of a broad variety of prokaryotic organism and archaea and represent the simplest biological membranes developed during evolution [22-24]. Most S-layers form monomolecular crystalline arrays composed of identical (glyco)protein subunits of molecular mass ranging from 30 to 220 kDa. In gram negative bacteria, S-layers are associated with the outer membrane, while in some archaea S-layers are the sole cell wall structure and are therefore only associated with the plasma membrane [23, 25].

The S-proteins amino acids include a high amount of charged and hydrophobic residues and a low content of sulfur-containing amino acids. Thus, S-proteins are characterized as being acidic proteins in which the isoelectric point may vary between pH 3 and 6 depending on the species. Due to the amino acid distribution, it is found that

S-proteins are highly anisotropic in their topography and physicochemical properties. Hence, the outer part (C terminal) is neutral, while the inner part (N terminal) is negatively charged due to the excess of acidic amino acids [26]. This contributes to the proper orientation during the lattice growth. Regarding secondary structure information obtained by circular dichroism, it is found that in most S-proteins, 40% is β-sheets and 10-20% is organized in α-helices [27].

S-proteins interact with each other by non-covalent forces, forming a crystalline cell envelope, the so called S-layer. The properties of the monomeric subunits are essential for the proper orientation and further self-assembly of S-protein. It has also been observed that calcium ions (or divalent ions) are indispensable for S-layer formation [28].

The S-layer lattices can have oblique (p1, p2), square (p4) or hexagonal (p3, p6) symmetry, with centre to centre spacing between 3 nm and 30 nm and thicknesses ranging from 5 to 25 nm. These crystalline structures exhibit uniform pore morphologies where the pore size varies between 2 nm and 8 nm (Figure 1.2) [29].
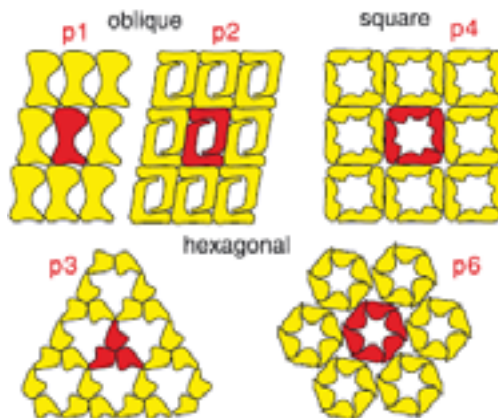

Figure 1.2. S-layer different lattice symmetries: oblique (p1, p2), square (p4) and hexagonal (p3 and p6) [30].

One of the most fascinating properties of isolated native and recombinant S-layer proteins is their inherent ability to reassemble into two dimensional arrays in solution (flat sheets, cylinders or spheres) on different solid supports, at air/water interfaces, on lipid films, and on liposomes (Figure 1.3), [20, 30-33].

In recent years, the physico-chemical properties of S-layers have been studied. So far, the stability of S-layers has been investigated in different solvents, and as a

function of the temperature. The interaction between two S-layers in solution has also been studied [34-37]. Preliminary kinetic studies about the adsorption mechanism of S-protein self-assembly process have been carried out [38, 39].
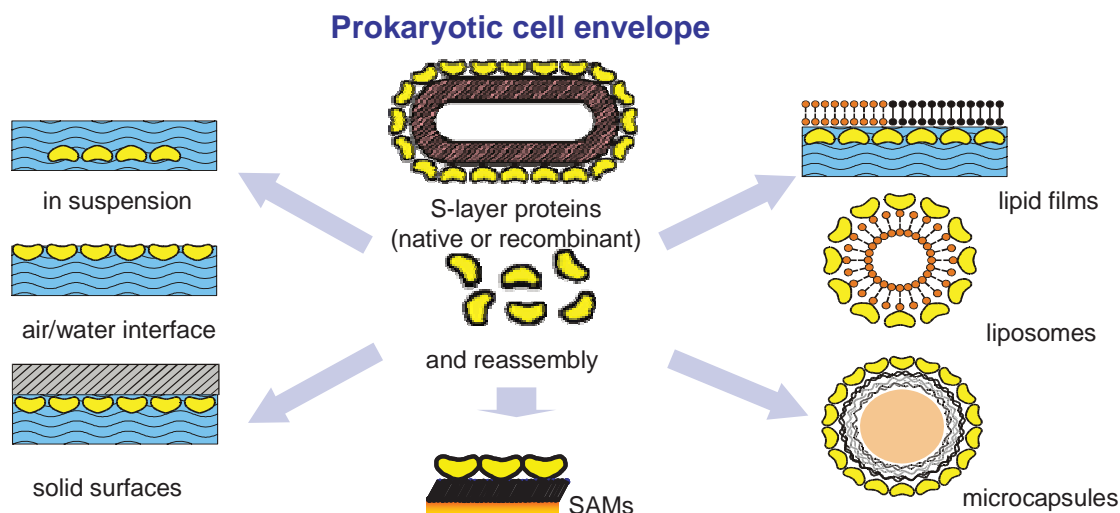

Figure 1.3. S-layers on native cells and the self-assembly at different interfaces [29, 40].

Recent studies have contributed with new experimental findings to the elucidation of the self-assembly mechanisms of S-proteins on lipid bilayers and self assembly monolayers suggesting that S-proteins, after adsorption, transform from amorphous to crystalline structure through several steps (see figure 1.4) [41, 42] .
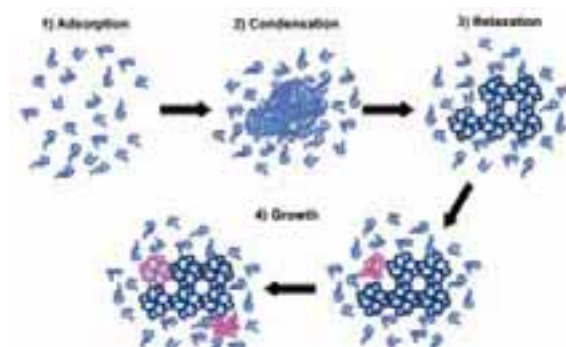
Figure 1.4. 2D mechanism scheme of S-protein recrystallization on lipid bilayers. S-protein subunits first are adsorbed (light blue) (1). Then, they condensed forming amorphous clusters (2). Afterwards, the S-protein rearranges and folds into crystalline arrays of tetramers subunits (relaxation) (dark blue) (3). Finally, the crystal growth continues by the incorporation of new tetramers (pink) at the edge of the crystalline clusters (4). Adapted from [41].

Bacterial proteins are also interesting from the technological point of view. S-layer technology has been exploited to build up 2D and 3D biomimetic supramolecular

structures. Thus, S-layers have been used as ultrafiltration membranes, as matrices for covalently binding biologically active molecules, for stabilizing matrices for functional lipid membranes and liposomes, and for formation of ordered arrays of metal clusters or nanoparticles [43-47].

The new challenge and paradigm around the S-layer technology is the bacterial fusion proteins. In the fusion protein, the S-protein molecule is used as scaffold and the incorporated additional molecule delivers the functionality. Examples of these fusion partners are GFP, streptavidin, and laminarinase LamA enzyme [28, 48-53]. An important part of the success of the bacterial fusion proteins is the control of the self-assembly properties of the S-protein scaffold.

The S-protein used in this work is SbpA from *Lysinibacillus sphaericus* CCM 2177 with a molecular weight of 120 kDa and an isoelectric point of 4.69. SbpA inner surface is negatively charged (hydrophilic) while the outer surface charge is neutral (more hydrophobic). The thickness of SbpA monolayer is about 9 nm and the lattice parameters correspond to square lattice symmetry (p4) with 13.1 nm lattice spacing [29].

1.1.2   Human Serum Albumin

Albumin is one of the most abundant blood proteins in mammals. In humans the serum albumin constitutes 60% of human plasma proteins [21]. A total of 9-12 g of albumin are synthesised daily by the hepatocytes [54].

Albumin controls the osmotic pressure of the blood vessels but its main function is the transport of endogenous or exogenous molecules which can be hydrophobic organic ions, long chain fatty acids, bilirubin and a wide range of insoluble drugs [55-60].

Human serum albumin has a molecular weight of 66.7 kDa and it is formed by 585 amino acids (aa). The primary structure contains a high amount of ionic aminoacids, which provide high solubility to albumin, and sulphur (cysteine) amino acids that are responsible for the folding of the albumin molecule. Regarding the secondary structure it is found that HSA contents just α-helix structure [61, 62]. HSA is formed of nine double loops that are grouped in three homologous domains called I, II

and III, starting from the amino terminal (see figure 1.5). Within each domain, two subdomains are found, termed A and B [63]. They are hydrophobic pockets where fatty acids and other water-insoluble molecules can bury their carbon-rich tails away from the aqueous environment and can be transported through the blood to their target organs. Fluorescence, circular dichroism, calorimetry and X-ray crystallography are some of the techniques that have been used to study the binding between albumin and the ligands [64-69].
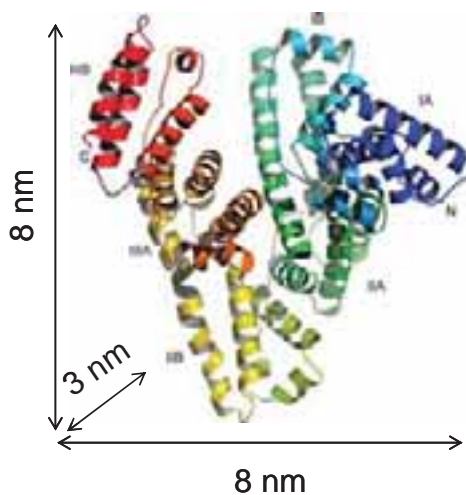

Figure 1.5. Human serum albumin (HSA) structure: subdomain IA: blue; subdomain IB: cyan; subdomain IIA: green; subdomain IIB: yellow-green; subdomain IIIA: yellow; subdomain IIIB: red. N terminal is located in the domain I while the C terminal is located in domain III.

HSA is a heart-shaped globular protein with the dimension 8 x 8 x 3 nm^3 as the work by *Carter and He* using X-ray diffraction demonstrated [70]. The albumin protein is a very flexible molecule which rapidly changes its structure in different environments or upon ligand binding. It presents different isomers depending on the pH; Extended (E) below pH 3, Fast (F) at pH 4, Normal (N) at physiological pH, basic (B) near pH 8 and aged (A) up to pH 10. At very extreme pHs the conformational changes of the protein will be irreversible, meaning that the albumin denatures. The isoelectric point of albumin is at pH 4.8, when the total net charge is zero. Nevertheless, the charge of albumin is not homogeneously distributed and shows a gradient along the molecule. The charge is greater at the amino terminal (domain I) than at the carbon terminal (domain III) [21, 71].

Since protein adsorption is a common event that occurs when a material is in contact with extracellular fluid (e.g. contact lenses, implanted material), albumin adsorption has been widely study on different biomedical materials for biocompatible purposes [72-75]. In addition, the ability of albumin to bind with a wide variety of molecules also is employed to develop albumin dialysis methods to remove toxic molecules from the circulatory system in a selective and biocompatible way [76-78].

In this work, two molecules have been used to study the binding properties of HSA: bilirubin and ibuprofen.

On one hand, bilirubin has a molecular weight of 585 g mol^{-1} and is a yellow-orange pigment produced from the break-down of hemoglobin and other hemoproteins in mammals. Unconjugated bilirubin is very insoluble in water, therefore it binds to albumin to be transported to the liver and excreted into the biliary system. Disorders in the metabolism of bilirubin may increase its concentration in the extracellular fluids (hyperbilirubinemia). This may cause jaundice, which is a yellow discoloration of the skin and tissues. High levels of bilirubin in plasma are dangerous, especially in prematurely born infants, where bilirubin may cross the blood-brain barrier causing brain damage, interfering in the normal neuronal development, and causing mental retardation or even death [79-81].

On the other hand, ibuprofen is not a physisological product but a commercial drug. It has a molecular weight of 208 g mol^{-1}, is a very common non-steroidal antiinflamatory and analgesic drug (NAID) [82-84].

1.2 Surface modification methods

Nature, through evolution, has developed simple and well-defined molecules (lipids, carbohydrates, DNA) that self-organize creating functional complex hierarchical architectures (e.g. cells) [85] . Nanobiotechnologists and material scientists have created new materials to try to understand how these basic molecules interact with each other, as well as their self-assembly pathways in order to mimic biology [86]. The main idea is the building of hierarchical structures using a bottom-up strategy controlling size, morphology and function, going from the nanometer to the micrometer scale. This process implies the generation of new surfaces and interfaces, where most of the

biological or chemical processes take place. Molecules located at surfaces normally show different properties and behaviour compared to when they are in the bulk solution [87]. Therefore, well defined surface chemistry is a crucial issue when working with molecules at interfaces. In the recent decades much effort has been made to design molecules and strategies to modified surfaces [88]. In this way, by changing the chemical and physical properties of a substrate, it is possible to immobilize molecules that retain their functionality [89-92].

In this work, silicon oxide and gold surfaces have been modified in a controlled way with different methods that will be explained in the following section.

1.2.1   Self assembled monolayers (SAMs)

Self assembly monolayers are flexible and simple systems to tailor interfacial properties of metal, oxides and semiconductors. SAMs are organic assemblies that are formed by the spontaneous adsorption of molecular components from solution or gas phase onto solid supports. The molecules that form SAMs comprise an *alkyl chain*, perpendicular to the surface, with a *head group* that shows affinity to the substrate and a *functional end group* (figure 1.6). The head group usually binds by covalent-like bonding and the neighbouring chains interact each other through lateral van der Waals interactions forming well-packed layers. SAM thickness can be range between 1- 3 nm [87].
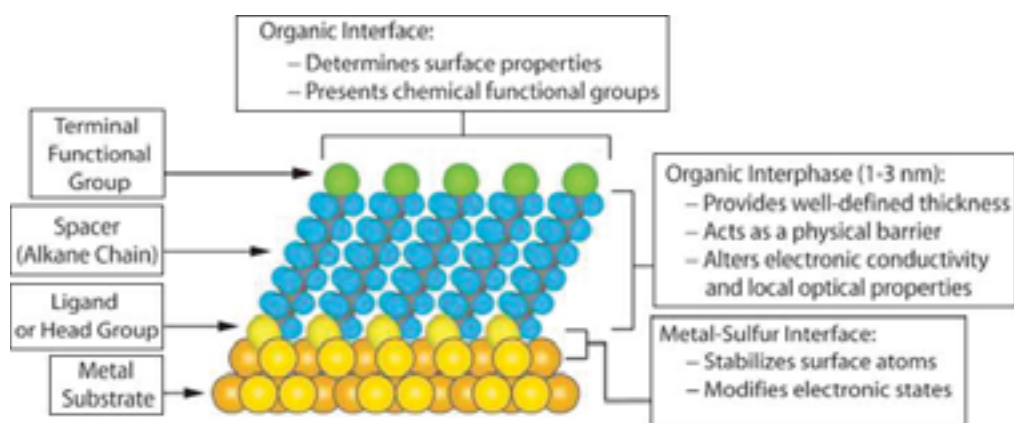

Figure 1.6. A cartoon showing a typical self assembly monolayer on metal although SAMs also can be formed on silica [87].

SAMs can be formed on a variety of surfaces. Organosilicon silanes form SAMs on silica and relate surfaces; alkanethiols form SAMs on gold silver and copper; alcohols and amines form SAMs on Platinum.

In the experiments presented in this thesis silane and thiols have been used. Silanes have an hydrolizable group that reacts with surface hydroxyl groups resulting in a Si-O-Si bond between the silane and the surface [93]. Alkanethiols, the most commonly used SAMs, have been proved to bind covalently to gold surfaces, providing high stability [87, 94, 95]. These SAMs permitted the control of the surface chemistry (hydrophobicity, hydrophilicity and charge) for protein adsorption, self-assembly and recrystallization.

1.2.2 Polymer coating

Polymers are macromolecules with repetitive units (monomer) that are connected by covalent bonds. Polymers are found in nature (proteins, complex carbohydrates, DNA) but also a variety of synthetic polymers have been developed with a wide range of physical and chemical properties that have industrial, environmental and medical applications [96, 97].

Thin film coating can be obtained ranging from nanometer to micrometer scale using several techniques including chemical deposition and spin coating.

Polylactic acid (or polylactide) has been selected for this work for its biocompatibility properties. Polylactide is often used in biomedical and pharmaceutical application as implanted material, in tissue engineering or new drug delivery systems [98, 99]. Polylactic acid has a chiral carbon atom that provides different optical activity and crystalline properties to the polymer [100, 101], a fact that has been used to study the formation of supramolecular structure based on bacterial proteins.

1.2.3 Layer by layer deposition technique (LBL)

The layer by layer method can be used to build up supramolecular structures in a controlled manner. The advantages of this technique are the versatility, simplicity and the high degree of control over the thickness at the nanoscale [102].

The most common method is to alternate oppositely charged macromolecules; however, there are many other interactions that have been used successfully for multilayer deposition including donor/acceptor interactions or hydrogen bonding. LBL build-up is carried out in different steps where positively or negatively charged surfaces are alternating dipped into the appropriate solutions. After each adsorption step the surfaces are rinsed with a solvent to remove the excess molecules (figure 1.7). The ionic strength, surface and the polyelectrolyte charge density are factors that influence the polyelectrolyte multilayer build up [102, 103].
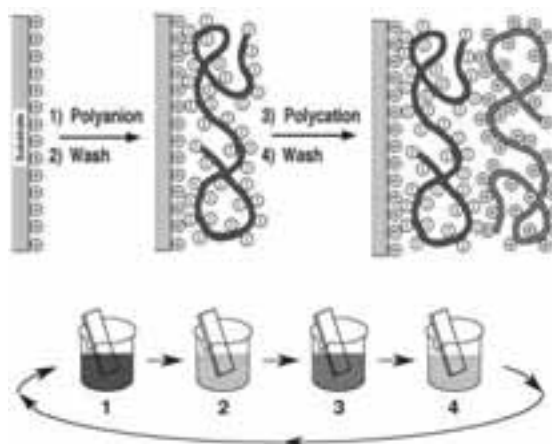

Figure 1.7. Polyelectrolyte Multilayer (PEM) building up alternating oppositely charged polyelectrolytes [102].

1.2.4 Covalent immobilization

Covalent immobilization is other way to attach molecules to the surface. The advantages of covalent immobilization respect to non-covalent immobilization are that molecules can bind in a specific way, the immobilized molecules are stable and they can keep its activity. The molecules used for covalent immobilization often have two reactive groups which lead the binding with the surface and the immobilized molecule. This method is widely employed in biology to immobilize biomolecules such as enzymes. Glutaraldehyde cross-linking agent has been chosen because is very common agent in biology for protein and enzyme immobilization [104, 105].

1.3 Objectives

For this PhD thesis, bacterial S-protein (SbpA) and human serum albumin (HSA) have been chosen, two different proteins with different structural properties. S-protein monomers have the ability to self-assemble and form two-dimensional crystalline layers on surfaces, similar to the native layers found in bacteria. On the contrary, HSA undergoes conformational changes when it adsorbs on surfaces.

The first objective of this thesis was to elucidate the S-layer formation mechanism, from adsorption to the final crystal formation. High resolution atomic force microscopy (AFM) and quartz crystal microbalance with dissipation (QCM-D) was used for that. Surface chemistry was modified to control the adsorption and recrystallization of bacterial S-proteins as well as S-layer properties, such as the thickness, lattice parameters and crystalline domains. Furthermore, the influence of the pH and protein concentration on S-protein adsorption and S-layer structure was determined.

The second objective was to demonstrate the functionality of adsorbed HSA layer. For that, bilirubin and ibuprofen were used, two molecules that bind to albumin. The thermal stability of HSA, HSA-ibuprofen and HSA-bilirubin complexes were determined, and a thermodynamic description of the binding of HSA with ibuprofen and bilirubin in bulk was obtained. Different strategies of HSA and ibuprofen immobilization on surfaces were investigated in order to carry out dynamic force spectroscopy experiments to study the interaction between HSA and ibuprofen.

1.4 References

[1]   D. Whitford, *Proteins: Structure and function*, John Wiley & Sons Ltd, Chichester, 2005.

[2]   M.F. Perutz, A.J. Wilkinson, M. Paoli, G. Dodson, *Annu. Rev. Bioph. Biom.* 27 (1998) 1-34.

[3]   P.M. Harrison, P. Arosio, *Biochim. Biophys. Acta.* 1275 (1996   ) 161-203.

[4]   J.E. Kinsella, *Crit. rev. food sci.* 21 (1984) 197-262.

[5]   R.M. Porter, E.B. Lane, *Trends Genet.* 19 (2003) 278-285.

[6]   G.M. Reaven, *Diabetes* 37 (1988) 1595-1607.

[7]   D.C. Wiley, J.J. Skehel, *Annu. Rev. Biochem.* 56 (1987) 365-394.

[8]   V. Renugopalakrishnan, R.V. Lewis, *Bionanotechnology: Proteins to Nanodevices*, Springer, Dordrecht, Netherlands, 2006.

[9]   J.J. Gray, *Current Opin. Struct. Biol.* 14 (2004) 110-115

[10]   A. Kondo, S. Oku, K. Higashitani, *J. Colloid Interf. Sci.* 143 (1991) 214-221.

[11]   W. Norde, A.C.I. Anusiem, *Colloid Surface* 66 (1992) 73-80

[12]   P. Sabatino, L. Casella, A. Granata, M. Iafisco, I.G. Lesci, E. Monzani, N. Roveri, *J. Colloid Interf. Sci.* 314 (2007) 389-397.

[13]   S.I. Jeon, J.H. Lee, J.D. Andrade, P.G.D. Gennes, *J. Colloid Interf. Sci.* 142 (1991   ) 149-158

[14]   N.W.S. Kam., H. Dai, *J. Am. Chem. Soc.* 127 (2005) 6021-6026

[15]   J. Yin, W. Wei, X. Liu, B. Kong, L. Wu, S. Gong, *Anal. Biochem.* 360 (2007) 99-104.

[16]   F.K. Glenister, R.L. Coppel, A.F. Cowman, N. Mohandas, B.M. Cooke, *Blood* 99 (2002) 1060-1063.

[17]   W. Norde, *Adv. Colloid Interfac.* 25 (1986) 267-340.

[18]   C.A. Haynes, W. Norde, *J. Colloid Interf. Sci.* 169 (1995) 313-328.

[19]   C.A. Haynes, W. Norde, *Colloid Surface B* 2 (1994) 517-566

[20]   U.B. Sleytr, C. Huber, N. Ilk, D. Pum, B. Schuster, E.M. Egelseer, *FEMS Microbiol. Lett.* 267 (2007) 131–144

[21]   T. Peters, *All about Albumin, biochemistry, genetics and medical applications.* , Academic Press, San Diego, 1996.

[22]   U.B. Sleytr, M. Sára, Z. Küpcü, P. Messner, *Arch. Microbiol.* 146 (1986) 19-24.

[23]   M.S. Sidhu, I. OIsen, *Microbiology* 143 (1997) 1039-1052

[24]   M. Sára, U.B. Sleytr, *J. Bacteriol.* 182 (2000) 859-868.

[25]   E.M. Egelseer, K. Leitner, M. Jarosch, C. Hotzy, S. Zayni, U.B. Sleytr, M. Sára, *J. Bacteriol.* 180 (1998) 1488-1495

[26]   D. Pum, U.B. Sleytr, *Colloid Surface A* 102 (1995) 99-104

[27]   A. Ciferri, *Supramolecular polymers*, Taylor & Francis 2005.

[28]   J.L. Toca-Herrera, R. Krastev, V. Bosio, S. Küpcü, D. Pum, A. Fery, M. Sára, U.B. Sleytr, *Small* 1 (2005) 339 -348

[29]   U.B. Sleytr, M. Sára, D. Pum, B. Schuster, *Prog. Surf. Sci.* 68 (2001) 231-278.

[30]   U.B. Sleytr, E.M. Egelseer, N. Ilk, D. Pum, B. Schuster, *FEBS Lett.* 274 (2007) 323-334.

[31]   D. Pum, U.B. Sleytr, *Supramol. Sci.* 2 (1995) 193-197

[32]   U.B. Sleytr, P. Messner, D. Pum, M. Sára, *Angew. Chem. Int. Edit.* 38 (1999) 1034-1054.

[33]   V. Saravia, S. Küpcü, M. Nolte, C. Huber, D. Pum, A. Fery, U.B. Sleytr, J.L. Toca-Herrera, *J. Biotechnol.* 130 (2007) 247-252.

[34]   J.L. Toca-Herrera, S.M.-. Flores, J. Friedmann, D. Pum, U.B. Sleytr, *Microsc. Res. Techniq.* 65 (2004) 226-234.

[35]   A. Martín-Molina, S. Moreno-Flores, E. Perez, D. Pum, U.B. Sleytr, J.L. Toca-Herrera, *Biophys. J.* 90 (2006) 1821-1829.

[36]   M. Delcea, R. Krastev, T. Gutberlet, D. Pum, U.B. Sleytr, J.L. Toca-Herrera, *Soft Matter* 4 (2008) 1414-1421

[37]   M. Delcea, R. Krastev, T. Gutleber, D. Pum, U.B. Sleytr, J.L. Toca-Herrera, *J. Nanosci. Nanotechno.* 7 (2007) 4260-4266.

[38]   S.A. Hemming, A. Bochkarev, S.A. Darst, R.D. Kornberg, P. Ala, D.S.C. Yang, A.M. Edwards, *J. Mol. Biol.* 246 (1995) 308-316

[39]   E.S. Györvary, O. Stein, D. Pum, U.B. Sleytr, *J. Microsc.* 212 (2003).

[40]   S. Moreno-Flores, A. Kasry, H.J. Butt, C. Vavilala, M. Schmittel, D. Pum, U.B. Sleytr, J.L. Toca-Herrera, *Angew. Chem. Int. Edit.* 47 (2008) 4707-1717.

[41]   S. Chung, S.-H. Shin, C.R. Bertozzi, J.J.D. Yoreo, *P. Natl. Acad. Sci.* 107 (2010) 16536-16541.

[42]   A. Eleta-Lopez, S. Moreno-Flores, D. Pum, U.B. Sleytr, J.L. Toca-Herrera, *Small* 6 (2010) 396-403.

[43]   U.B. Sleytr, H. Bayley, M. Sára, A. Breitwieser, S. Küpcü, C. Mader, S. Weigert, F.M. Unger, P. Messner, B. Jahn-Schmid, B. Schuster, D. Pum, K. Douglas, N.A. Clark, J.T. Moore, T.A. Winningham, S. Levy, I. Frithsen, J. Pankovc, P. Beale, H.P. Gillis, D.A. Choutov, K.P. Martin, *FEMS Microbiol. Rev.* 20 (1997) 151-175.

[44]   W. Shenton, D. Pum, U.B. Sleytr, S. Mann, *Nature* 389 (1997) 585-587.

[45]   U.B. Sleytr, B. Schuster, D. Pum, *IEEE ENG. Med. Biol.* (2003) 140-150.

[46]   S. Dieluweit, D. Pum, U.B. Sleytr, W. Kautek, *Mater. Sci. Eng.* 25 (2005) 727-732.

[47]   N. Ilk, E.M. Egelseer, J. Ferner-Ortner, S. Küpcü, D. Pum, B. Schuster, U.B. Sleytr, *Colloid Surface A* 321 (2008) 163–167.

[48]   J.L. Toca-Herrera, S. Küpcü, V. Diederichs, G. Moncayo, D. Pum, U.B. Sleytr, *Biomacromolecules* 7 (2006) 3298-3301.

[49] H. Tschiggerl, J.L. Casey, K. Parisi, M. Foley, U.B. Sleytr, *Bioconjugate Chem.* 19 (2008) 860-865

[50] H. Tschiggerl, A. Breitwieser, G.d. Roo, T. Verwoerd, C. Schäffer, U.B. Sleytr, *J. Biotechnol.* 133 (2008) 403-411.

[51] B. Schuster, U.B. Sleytr, *Soft Matter* 5 (2009) 334-341

[52] D. Moll, C. Huber, B. Schlegel, D. Pum, U.B. Sleytr, M. Sára, *P. Natl. Acad. Sci.* 99 (2002) 4646-14651.

[53] B. Kainz, K. Steiner, U.B. Sleytr, D. Pum, J.L. Toca-Herrera, *J. Struct. Biol.* 172 (2010) 276-283.

[54] N. Soni, M. Margarson, *Current Anaesth. Crit.Care* 15 (2004) 61-68.

[55] D.C. Carter, J.X. Ho, *Adv. Protein Chem.* 45 (1994) 153-203.

[56] N.A. Kratochwil, W. Huber, F. Müller, M. Kansy, P.R. Gerber, *Biochem. Pharmacol.* 64 (2002) 1355-1374.

[57] M.V. Fraile, M. Blanco-Melgar, R.M. Muñoz, G. López-Rodríguez, J.A. Gallego-Nicasio, P. Carmona, *J. Mol. Struct.* 651-653 (2003) 231-236.

[58] L. Trynda-Lemiesz, *Bioorgan. Med. Chem.* 12 (2004) 3269-3275

[59] B. Bojko, A. Sulkowskaa, M. Maciazek, J. Równicka, F. Njau, W.W. Sułkowski, *Int. J. Biol. Macromol.* 42 (2008) 314-323.

[60] F. Kratz, *J. Control Release* 132 (2008) 171-183.

[61] S.J. McClellan, E.I. Franses, *Colloid Surface A* 260 (2005) 265-275.

[62] W. Norde, C.E. Giacomelli, *J. Biotechnol.* 79 (2000) 259-268.

[63] P. Ascenzi, M. Fasano, *Biophys. Chem.* 148 (2010) 16-22.

[64] G. Sudlow, D.J. Birkett, D.N. Wade, *Mol. Pharmacol.* 11 (1975) 824-832.

[65] I. Petitpas, A.A. Bhattacharya, S. Twine, M. East, S. Curry, *J. Biol. Chem.* 276 (2001) 22804-22809

[66]   J. Ghuman, P.A. Zunszain, I. Petitpas, A.A. Bhattacharya, M. Otagiri, S. Curry, *J. Mol. Biol.* 353 (2005) 38-52

[67]   E.L. Gelamo, C.H.T.P. Silva, H. Imasato, M. Tabak, *BBA-Protein Struct. M* 1594 (2002) 84-99.

[68]   M. Pistolozzi, C. Bertucci, *Chirality* 20 (2008) 552-558.

[69]   M. Sánchez, F.J. Aranda, M.J. Espuny, A. Marqués, J.A. Teruel, Á. Manresa, A. Ortiz, *Langmuir* 24 (2008) 6487-6495

[70]   X.M. He, D.C. Carter, *Nature* 358 (1992) 209-215.

[71]   J.L. Oncley, *Biophys. Chem.* 100 (2003) 151-158.

[72]   P. Roach, D. Farrar, C.C. Perry, *J. Am. Chem. Soc.* 127 (2005) 8168-8173

[73]   D. Luensmann, L. Jones, *Contact Lens & Anterior Eye* 31 (2008) 179-187

[74]   M. Iwasashi, M. Sakane, H. Saito, T. Taguchi, T. Tateishi, N. Ochiai, *J. Biomed. Mat. Res. A* 90 (2009) 543-548.

[75]   L.-C. Xu, C.A. Siedlecki, *Biomaterials* 28 (2007) 3273-3283.

[76]   A.I. Ivanov, E.A. Korolenko, E.V. Korolik, S.P. Firsov, R.G. Zhbankov, M.K. Marchewka, H. Ratajczakc, *Arch. Biochem. Biophys.* 408 (2002) 69-77.

[77]   E. Magosso, M. Ursino, L. Colì, O. Baraldi, L. Bolondi, S. Stefoni, *Artif. Organs* 30 (2006) 285-300.

[78]   R.D. Hughes, *Int. J. Artif. Organs* 25 (2002) 911-917

[79]   M.A. Brito, R.F.M. Silva, D. Brites, *Clin. Chim. Acta* 374 (2006) 46-56.

[80]   R. Stocker, Y. Yamamoto, A.F. McDonagh, *Science* 235 (1987) 1043-1046

[81]   L. Chuniaud, M. Dessante, F. Chantoux, J.-P. Blondeau, J. Francon, F. Trivin, *Clin. Chim. Acta* 256 (1996) 103-114.

[82]   G. Fanali, P. Ascenzi, M. Fasano, *Biophys. Chem.* 129 (2007) 29-35.

[83]   H. Aki, M. Goto, M. Yamamoto, *Thermochim. Acta* 251 (1995) 379-388.

[84]   K.M. Stuhlmeier, H. Li, J.J. Kao, *Biochem. Pharmacol.* 57 (1999) 313-320.

[85]   S.R. Bolsover, J.S. Hyams, E.A. Shephard, H.A. White, C.G. Wiedemann, *Cell Biology*, John Wiley & Sons, Inc, Hoboken, New Jersey, 2004.

[86]   M.C. Roco, *Curr. Opin. Biotech.* 14 (2003) 337-346.

[87]   J.C. Love, L.A. Estroff, J.K. Kriebel, R.G. Nuzzo, G.M. Whitesides, *Chem. Rev.* 105 (2005) 1103-1169

[88]   K.L. Prime, G.M. Whitesides, *Science* 252 (1991) 1164.

[89]   P.J. Casey, *Science* 268 (1995) 221-225

[90]   F. Giess, M.G. Friedrich, J. Heberle, R.L. Naumann, W. Knoll, *Biophys. J.* 87 (2004) 3213-3220

[91]   U. Hersel, C. Dahmen, H. Kessler, *Biomaterials* 24 (2006) 4385-4415

[92]   R.O. Hynes, *Cell* 110 (2002) 673-687.

[93]   U. Ulman, *Chem. Rev.* 96 (1996) 1533.

[94]   C.D. Bain, J. Evall, G.M. Whitesides, *J. Am. Chem. Soc.* 111 (1989) 7155-7164.

[95]   E.B. Troughton, C.D.B. C.D., G.M. Whitesides, D.L. Allara, M.D. Porter, *Langmuir* 4 (1988) 365-385.

[96]   Y. Ikada, H. Tsuji, *Macromol. Rapid. Comm.* 21 (1999) 117-132.

[97]   S.S. Ray, M. Okamoto, *Prog. polym. Sci.* 28 (2003) 1539-1641.

[98]   P.A. Gunatillake, R. Adhikari, *Eur. Cells Mater.* 5 (2003) 1-16.

[99]   K. Nagahama, T. Ouchi, Y. Ohya, *Macromol. Biosci.* 8 (2008) 1044-1052.

[100] D. Maillard, R.E. Prud'homme, *Macromolecules* 39 (2006) 4272-4275.

[101] J.R. Sarasua, A.L. Arraiza, P. Balerdi, I. Maiza, *Polym. Eng. Sci.* (2005) 745-753.

[102]   G. Decher, J.B. Schlenoff, *Multilayer Thin Films*, Wiley-VCH, Weinheim, 2002.

[103]   G. Decher, *Science* 277 (1997) 1232-1237.

[104]   S.S. Caramori, F.N.D. Faria, M.P. Viana, K.F. Fernandes, L.B. Carvalho, *Mater. Sci. Eng.* 31 (2011) 252-257

[105]   D.R. Walt, V.I. Agayn, *Trend. Anal. Chem.* 13 (1994) 425-430.

Chapter 2

Experimental techniques

The results of this thesis have been obtained using different experimental techniques which can be divided in two groups; surface analytical techniques and bulk techniques.

Quartz Crystal Microbalance (QCM-D), Atomic Force Microscopy (AFM), contact angle and ellipsometry belong to the first group while Differential Scanning Calorimetry (DSC), and Isothemal Titration Calorimetry (ITC), ζ-potential, Dynamic Light Scattering (DLS), Circular Dichroism (CD) and Nuclear Magnetic Resonance (NMR) belong to the second group.

2.1 Quartz Crystal Microbalance with Dissipation monitoring (QCM-D).

QCM-D is a well established technique for simultaneous monitoring of mass load (in ng cm^{-2} range) and energy dissipation obtained from changes in the resonant frequency and the damping of a vibrating sensor.

Originally, QCM was used in vacuum and air environments but in the early eighties the device was improved to operate also in liquid systems opening the possibility to work with biological systems [1] such as protein adsorption, antibody-antigen binding and cell adhesion [2-5]. Furthermore, in the nineties it was developed a QCM with dissipation (QCM-D) which had the ability to quantify the adsorbed mass and characterize the viscoelastic properties of the adlayer [6].

The QCM-D set up consists of a thin AT-cut piezoelectric quartz crystal sandwiched between two electrodes that when applying a voltage oscillates in a shear mode at its resonant frequency, f_0 (figure 2.1). The resonance frequency depends on the thickness of the crystal *(d)* and the speed of shear waves in quartz *(v_Q)*: $f_o=v_Q/2d$.
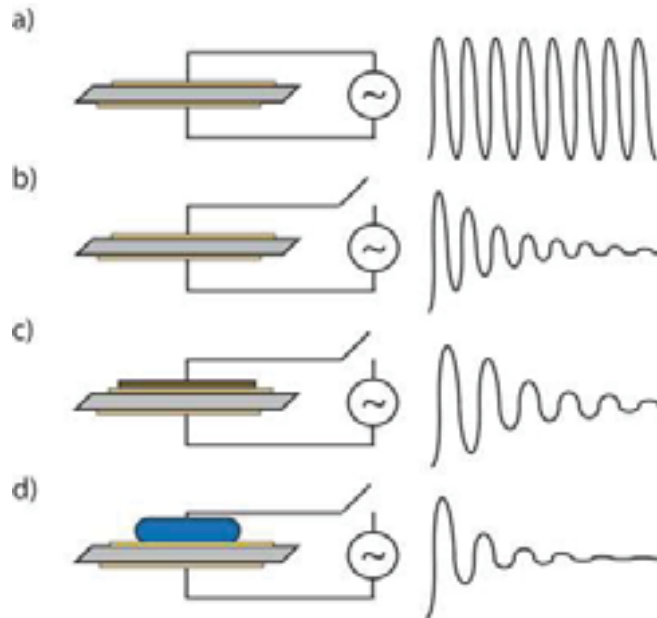

Figure 2.1. QCM-D operation principle; a) The quartz crystal by applying a voltage oscillates at its resonant frequency, b) when the voltage is switched off the oscillation decays due to energy dissipation, c) The resonant frequency decreases due to mass adsorption, d) the energy dissipation is higher in a more viscous system [d].

The oscillating frequency changes when an amount of mass is adsorbed on the crystal. In many cases, this frequency shift is proportional to the deposit mass as the Sauerbrey equation describes (see bellow and explanation when this equation can be applied) [7];

$$\Delta m = -C \cdot \frac{\Delta f}{n}$$

where *Δm* represents the mass surface density (ng cm^{-2}), *C* is a proportionality constant that depends only on the intrinsic properties of the sensor (-17.7 ng Hz^{-1}·cm^{-2} for 5 MHz crystals), *ΔF* is the frequency shift and *n* is the overtone number (1, 3, 5,…). The total mass oscillating with the crystal is the sum between the adsorbed molecules and coupled and trapped water.

---

[d] Image adapted from *http://www.chalmers.se/ap/EN/research/biophysics/research/sensing/qcm-d*

Furthermore, frictional energy losses originated from the contact of the crystal with the surrounding medium can be used to obtain viscoelastic information. Thus, exciting the crystal intermittently and measuring the decay of the oscillations as a function of time the energy losses can be calculated. This is represented in terms of the dissipation factor (D) and it is related with the viscoelastic properties, or rigidity of the adlayer (figure 2.1).

Nevertheless, the Sauerbrey equation is not valid for thick layers or high dissipative systems. It is a good approximation under the following assumptions: i) the adsorbed layer is homogeneously distributed over the surface, and ii) is rigid enough to avoid any oscillatory deformation. In addition, the overall dissipation-frequency shift ratio should be smaller than $0.2 \times 10^{-6} Hz^{-1}$ [8].

For dissipative, viscoelastic layers, more appropriated models have been developed for instance, Kelvin-Voigt model. The model assumes that the oscillatory quartz plate is covered by a viscoelastic film of uniform thickness and density that is in contact with a semi-infinite Newtonian liquid under no-slip conditions. The overall viscoelasticity of the layers is represented by the ratio *G''/G'* of the layer's loss and storage moduli (G_f);

$$G_f = G_f^{'} + iG_f^{"}$$

where the storage modulus (*G'*), is the same as film's shear elasticity modulus obtained by fitting the frequency and dissipation curves with the model. The loss modulus, (*G''*), is calculated as the product of the sensing frequency (*f*) and the film's viscosity (η_f) Thereby, the thickness, shear modulus and shear viscosity of the adlayer can be calculated [9, 10].

2.2 Atomic Force Microscopy (AFM).

Atomic Force Microscopy (AFM) was developed in the late eighties as a member of a family of scanning probe techniques [11, 12]. Since AFM has been used as a high resolution imaging (nanoscale range), on a wide variety of substrates and biomolecules [13] including metals, polymers, proteins or even cells [14, 15]. An advantage of AFM against other structural techniques such as electron microscopy is that AFM can work in different aqueous environments in wide range of temperatures.

The AFM consist on a sharp tip mounted on a soft cantilever of a specific spring constant that scans the surface in x-y direction. Depending on the topographical features of the surface the cantilever deflects in the z direction (due to the interaction forces between the tip and the sample). The detection system consists of a laser beam that is reflected at the back side of the cantilever and a photodiode that follows the cantilever deflection while scanning. The electrical differential signal of the photodiode is processed by a computer that generates a feedback signal for the piezoscanner to keep the force on the tip constant. The measured cantilever deflections allow a computer to generate a 2D map of surface topography (figure 2.2).
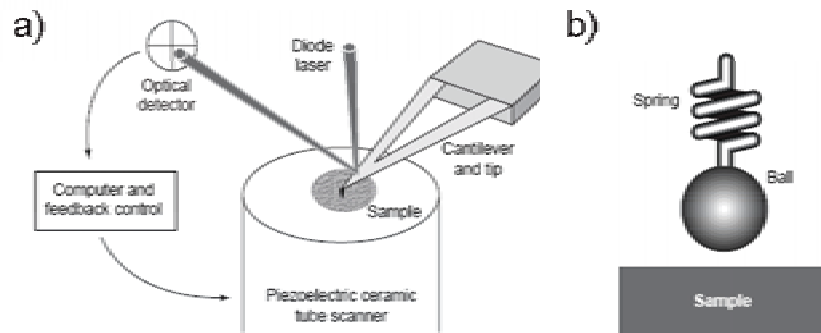
Figure 2.2. a) Different parts of the AFM set up: the cantilever and the tip constitute the sensor of the AFM, the optical detector and the laser are the detection systems and the nanometric position of the sample is controlled with a piezoelectric scanner. The computer has a feedback controls between the optical detector and piezo scanner, b) mechanical analogy: the cantilever and the tip can be represented by a spring and ball respectively [16].

Among the different ways to operate with AFM the results presented in this thesis have been measured in contact mode, tapping mode and force mode. Contact and tapping mode are used for high resolution imaging while force mode spectroscopy is applied to obtain quantitative information of the forces between tip and the sample as a function of the distance; so called force-distance curves (figure 2.3). The force mode surface is used to measure mechanical properties (elasticity, hardness, adhesion forces and surface charge densities) [17].

In contact mode the tip is physically in contact with the sample and the force between the tip and the sample is kept constant via an electronic feedback loop. The

surface topography is imaged from the cantilever deflection required to maintain a constant force over the surface. In tapping mode the tip oscillates close to the surface but is not physically in contact. The amplitude of the tip oscillation (in air 50-500 KHz and in liquid 10 kHz) decreases as the tip is close to the sample. In this way, the topographic features of the sample are detected. The average cantilever deflections are used as an input signal into the feedback loop to maintain a constant average applied force. The AFM image resolution depends specially on the quality, shape and geometry of the tip which in our case consist of microfabricated pyramidal Si_3N_4 with a radii that varies between 20-60 nm.

In the force mode the tip, initially at rest (zero force), is approached towards the surface at constant rate until get into contact with the surface (at that point different loads can be exerted on the sample).
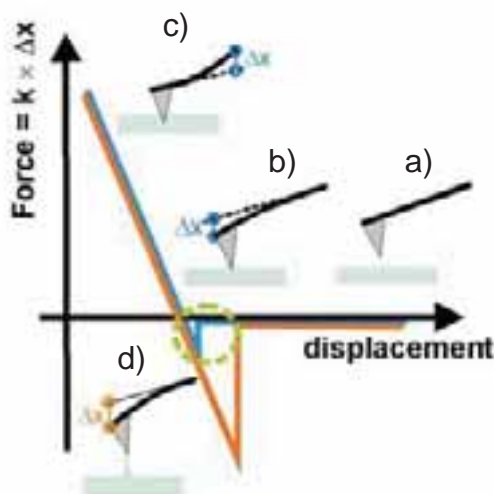

Figure 2.3. Schematic diagram of typical adhesion measurement. a) the cantilever is approaching to the surface but the deflection is zero, b) the tip get into contact with the surface, c) the point of maximum load, d) maximum adhesive force and the tip is separated from the surface to its original position [18].

Afterwards, the tip is separated away from the surface until the cantilever reaches its original position (zero force) (see figure 2.3). The force sensed by the cantilever is determined by Hook's law, $F=K_e\ x$, where F is the force, K_e the cantilever spring constant and x the cantilever deflection. This method allows to measure long and short range forces; from electrostatic interactions to steric interaction. Depending on the nature of interaction different force-distance can be obtained as it is shown in figure 2.4 [19].
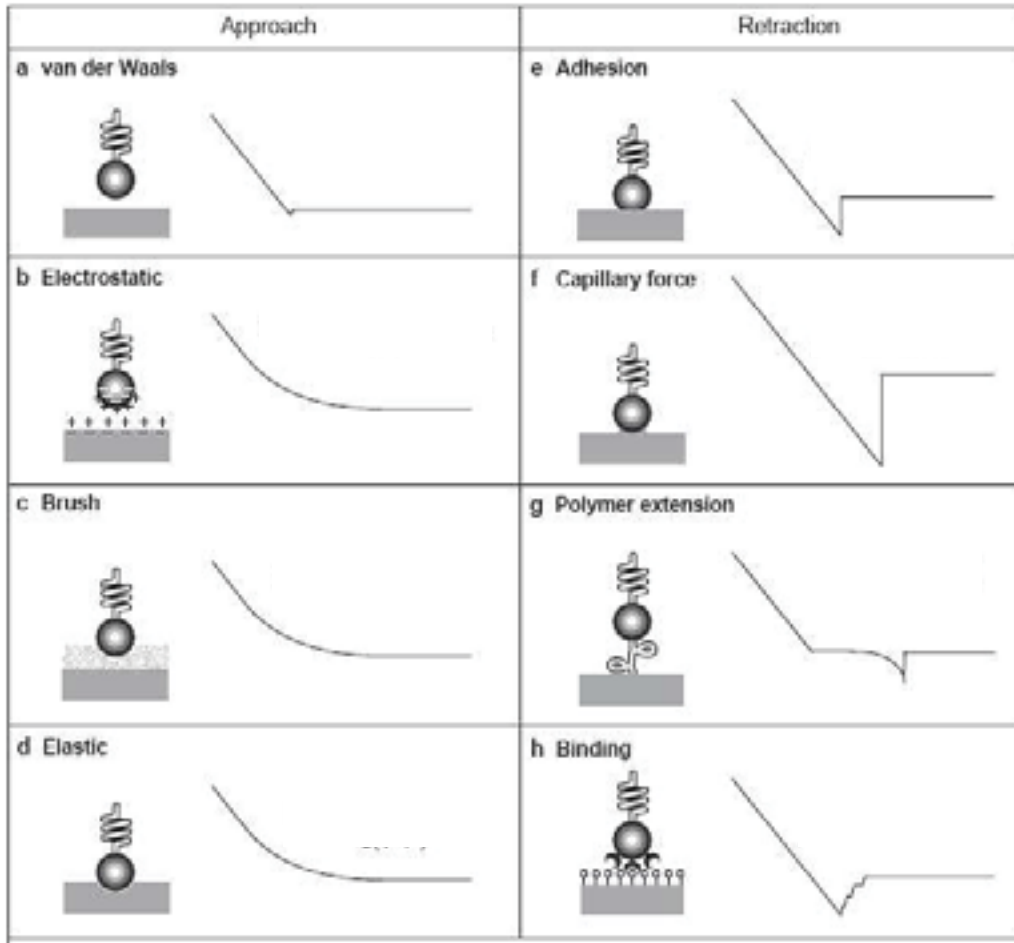
Figure 2.4. Force-distance curves are sensitive to the nature of the interaction between the tip and the sample and to the mechanical properties of the sample. For example by approaching van der Waals or electrostatic can be measure while for retracting polymer extension or binding between molecules [16].

2.3 Contact angle.

Contact angle measurements, studied since early 19th century, are widely used for different interfacial characterization phenomena such us, wetting of solid surfaces, capillarity penetration into porous media, coating, painting etc [20, 21].

The contact angle (θ) of a liquid drop on a solid surface is determined by the mechanical equilibrium of three interfacial tensions: liquid-vapor (γ_{LV}), solid-vapor (γ_{SV}), and solid-liquid (γ_{SL}) (figure 2.5). At mechanical equilibrium the relation between interfacial tensions is given by Young's equation which can be applied for

ideal systems (the surface is rigid, smooth, nonreactive, plane and homogeneous) [22, 23]:
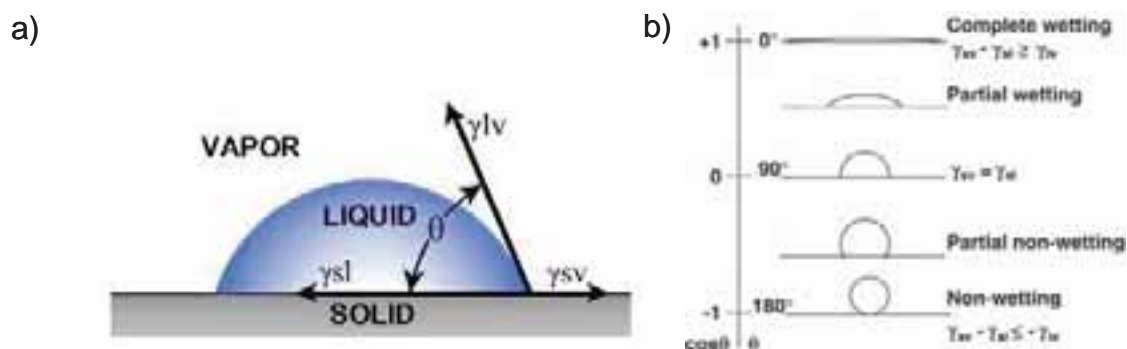
$$\gamma_{LV} \cos\theta = \gamma_{SV} - \gamma_{SL}$$

a)   b)

Figure 2.5. a) The picture shows a drop on a surface and the corresponding interfacial tensions: liquid-vapor (γ_{LV}), solid-vapor (γ_{SV}), and solid-liquid (γ_{SL}). The θ is the contact angle [e]. b) The degree surface wetability can be described by the interplay of the interfacial tensions (Young equation). Drop shape variation depending on the wettability (hydrophobic) properties of the solid support. Non wetting systems (hydrophobic systems) present high contact angle values while a wetting system (hydrophilic) presents low contact angle values [21].

The contact angle can be measured with a goniometer where a droplet is deposited over the surface with a syringe while a camera captures droplet images. The drop profiles are analyzed with an image software in order to calculate the contact angle. The contact angle is a direct estimation of the wettability of any surface. Thus, a large contact angle might indicate a hydrophobicity surface (non wetting) while low contact angle refers to hydrophilic surfaces (wetting surfaces) (Figure 2.5b).

2.4 Ellipsometry.

Ellipsometry is a non invasive, high sensitivity optical technique for the investigation of the thickness, refractive index and extinction coefficient of thin films and organic material deposited on a reflective substrate [24-26]

In this technique the change of the polarization of an incident monochromatic beam after the reflection on a surface is measured by the coefficient of reflectivity, ρ.

---

[e] Figure adapted from *www.face-kyowa.com*

The electric field of the light beam can be described by a parallel (r_p) and a perpendicular (r_s) component of the incident plane of reflection. At reflection the amplitude and the phase of every component change depends on the structure of the surface (figure 2.6).
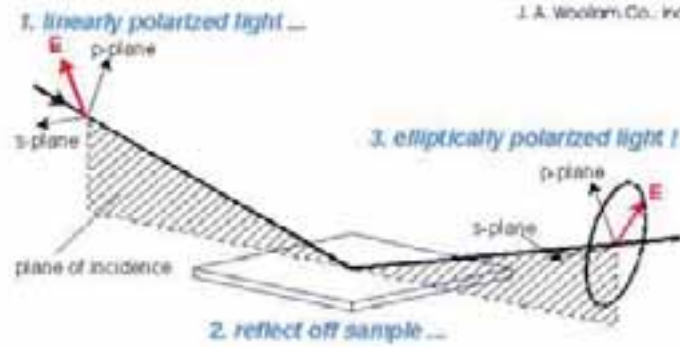

Figure 2.6. Schematic illustration of ellipsometric experiment where linearly polarized light is reflected from the sample surface and the polarization change is measured to determine the sample response [f].

The ellipsometric angles Ψ and Δ can be obtained from the amplitude and phase changes of r_p and r_s using the fundamental equation of ellipsometry [27, 28];

$$\rho = \frac{r_P}{r_S} = \tan(\psi)e^{i\Delta}$$

The relation between the ellipsometric angles gives information about the thickness and refractive index of the sample. A two term Cauchy model was used to determine the thickness and the optical properties of the material [24, 29], $n(\lambda) = A_n + \dfrac{B_n}{\lambda^2}$, where n is the refractive index, λ the wavelength, A is a parameter related with the average index of the material and B parameter provide the shape of the dispersion curve.

---

[f] Image adapted from *http://www.jawoollam.com*

Differential Scanning Calorimetry (DSC).

DSC is a thermoanalytical technique that monitors thermally induced transitions processes. The technique provides quantitative information of heat capacity as a function of temperature. Different information that can we obtain from DSC measurements are melting, purity, glass transition temperature, conformational changes of different type of materials that can vary from polymers to biomolecules [30].

The sample and the reference are simultaneously heated in a predetermined temperature range and rate. When the sample undergoes a transition event the control system senses the temperature difference between the sample and reference cell and supplies more or less heat (power) to the sample cell. Thus, reference and sample cells are kept at the same temperature. The recorded parameter in DSC measurements is thus the differential heat as a function of temperature. If the event is exothermic the curve is negative while when the transition is endothermic the curve is positive [31, 32].
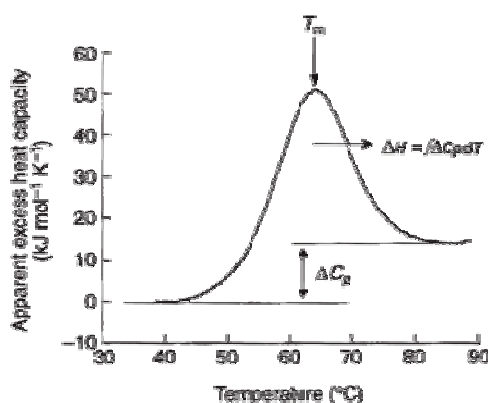

Figure 2.7. From DSC thermograms direct information about the transition process can be obtained such as the transition temperature (T_m) when the excess heat reached the maximum. The peak area under DSC trace determines the enthalpy of the transition (ΔH) and the difference between the initial and final sates indicates the heat capacity change. Since at the transition point the Gibss free energy is zero, thus the entropy can be calculated from $\Delta G = \Delta H - T \Delta S$ [g].

2.6 Isothermal Titration Calorimetry (ITC)

Isothermal titration calorimetry (ITC) is an experimental technique that measures the heat released or heat absorbed after a binding process between two molecules at constant temperature. These measurements allow to determine the binding

---

[g] Figure adapted from *http://www.microcal.com*

constant *(K)*, the reaction stoichiometry *(n)*, the enthalpy *(ΔH)*, the entropy *(ΔS)*, the heat capacity *(ΔCp)* and the Gibbs free energy *(ΔG)*, obtaining a complete thermodynamic profile of the molecular interaction. The relation between *K, ΔH, T , ΔS* is given by Gibbs equation *ΔG=-RlnK=ΔH-TΔS* [33].

The ITC set up consists of a syringe containing a ligand that is titrated in a sample cell. The injection is carried out adding small amounts of ligand that are directly related with the amount of binding. As the molecules interact the heat is released or absorbed and monitored as a function of time (see figure 2.8).

Each peak is related with the heat change associated with each injection. When the system reaches saturation, the signal is reduced and only the heat of the dilution is observed. After the integration of each peak, the obtained values are plotted against the ligand:binding-molecule ratio. The resulting binding curve is fitted with an appropriate model to determine the thermodynamic parameters [32, 34, 35].
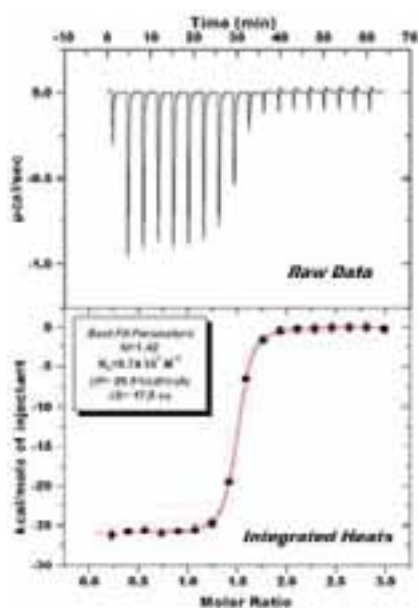

Figure 2.8. Above: raw data obtained in a typical ITC experiment, bellow: plot showing the values of the integration of the raw data vs. molar ratio. After applying an appropriate model the fit of the curve delivers main thermodynamic parameters: binding constant, association constant, enthalpy and entropy [h].

---

[h] Figure adapted from *http://www.microcal.com*

2.7 ζ-Potential

The ζ-potential is used to obtain the surface charge of suspended bodies as well as to elucidate their colloidal stability. In general, colloidal particles in solution are normally surrounded by an electrical double layer. In the inner region layer (Stern layer) the ions are strongly bound to the particle surface while in the outer layer the ions are not so strongly attached. The ions from the electrical double layer (counter ions) move together with the particle. The boundary between this layer and the solution is called hydrodynamic shear (slipping plane) and the potential measured in this boundary is the ζ-potential.

The ζ -potential is obtained by measuring the velocity of the particles (electrophoretic mobility). The ζ-potential (z) and the electrophoretic mobility (U_E) are related with the Henry's equation:

$$U_E = \frac{2\varepsilon z f(ka)}{3\eta}$$

it is dependant of dielectric constant (ε), viscosity (η) and Henry's function (f(ka)) where *a* is the particle radius and *1/k* the Debye length. If the particles are larger than 0.2 μm the Smoluchowski approximation is considered and f(ka) is about 1.5. For small particles, the Huckel approximation is taken into account and f(ka) is 1 [36].

2.8 Dynamic Light Scattering (DLS)

Dynamic light scattering can be used to determine the size distribution profile of particles in suspension. This is normally obtained by measuring the speed at which the particles are diffusing due to the Brownian motion, which is defined as the random movement of the particles in suspension. Thus, the larger the particle the slower is the Brownian motion.

The velocity of the Brownian motion is defined by the translational diffusion coefficient *(D)* which can be calculated by Stokes-Einstein equation:

$$d(H) = \frac{k_b T}{3\pi\eta D}$$

where *d(H)* is hydrodynamic diameter, *D* translational diffusion coefficient, k_b Boltzmann's constant, *T* absolute temperature and η the viscosity. The translational diffusion coefficient will depend not only on the size of the particle, but also on any surface structure, as well as the concentration and type of ions in the medium.

In DLS the speed of the particles is measured using an optical system. Thus, when a small particle is illuminated by a light source (laser monochromatic with coherent light), the particle scatters the light in all directions. The light intensity will fluctuate due to the Brownian motion of the particles and the rate at which the intensity of the scattered light fluctuation occurs is used to calculate the size of the particles. A correlation function is used for particle size calculation using different algorithms [37].

2.9 Circular Dichroism (CD).

Circular Dichroism (CD) is widely used to obtain the secondary structure of proteins. CD is defined as the difference between the absorption left circularly and right circularly polarized light. Therefore a sample has a circular dichroism spectrum if it absorbs left (I_L) and right (I_R) circularly polarized radiation with different intensities. The CD spectrum itself is a record of I_L- I_R against the frequency of the incident radiation [38].
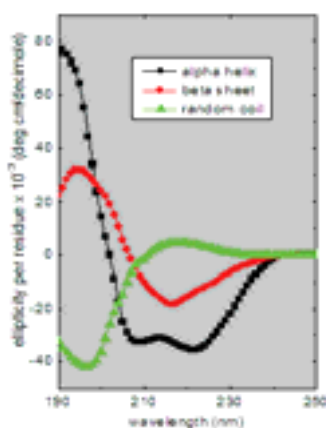

Figure 2.9. Circular Dichroism curves of protein secondary structure: α-helix, β-sheets and random coil [i].

The spectra of α proteins display a negative band between about 203 and 240 nm with minima at about 209-222. The positive band bellow 203 nm presents a maximum 192

---

[i] Figure adapted from *http://www.ap-lab.com/circular_dichroism.htm*

nm. The difference in band intensity reflects different α helical content. Regular β proteins present a minimum between 210-225 nm and a maximum 190 and 200. The CD spectra of alpha and beta proteins can be considered as mixtures in which the stronger α-helix band intensities dominate (see figure 2.9) [38].

2.10 Nuclear Magnetic Resonance spectroscopy (NMR).

Nuclear magnetic resonance is a powerful tool in organic chemistry to obtain information about chemical compounds structure. The technique is based on the quantum properties of the atomic nuclei and is applicable those nuclei which possess a spin quantum number (I) greater than zero. The most important nuclei are ^{1}H and ^{13}C, that have a spin quantum number of 1/2

In the absence of an external magnetic field (B_0) the nuclei are randomly oriented. However, when an external static magnetic field is applied the nuclei magnetic moments align themselves in a distinct number of orientations that depends on the quantum number (2I+1). In the case of 1/2 there are two possible states m=1/2 or m=-1/2 which have different energetic levels.

The relaxation of the excited nuclei back to lower energy level is accompanied by release of electromagnetic radiation. The latter is what we measure in a regular NMR experiment.

The difference between the energy levels of the spin orientation is influenced by the magnetic fields of the neighbouring nuclei. Thus, only nuclei which are in exactly the same magnetic environment will have exactly the same energy difference between spin orientations. In NMR spectroscopy these energy differences are detected to obtain information about the position of a certain nuclei in a molecule and thus find the molecular structure [39].

2.11   References

[1]   T. Nomura, M. Okuhara, *Anal. Chim. Acta* 142 (1982) 281-284.

[2]   Y. Lvov, K. Ariga, I. Ichinose, T. Kunitake, *J. Am. Chem. Soc.* 117 (1995) 6117-6123

[3]   C. Fredriksson, S. Kihlman, M. Rodahl, B. Kasemo, *Langmuir* 14 (1998) 248-251.

[4]   F. Höök, M. Rodahl, P. Brzezinski, B. Kasemo, *J. Colloid Interf. Sci.*   208 (1998) 63-67.

[5]   F. Höök, M. Rodahl, P. Brzezinski, B. Kasemo, *Langmuir* 14 (1998) 729-734.

[6]   M. Rodahl, F. Höök, C. Fredriksson, C.A. Keller, A. Krozer, P. Brzezinski, M. Voinova, B. Kasemoa, *Faraday discuss.* 107 (1997) 229-246.

[7]   G. Sauerbrey, *Z. Phys.* 155 (1959) 206-222.

[8]   K. Gläsmäster, C. Larsson, F. Höök, B. Kasemo, *J. Colloid Interf. Sci.* 246 (2002) 40-47.

[9]   T.J. Halthur, T. Arnebrant, L. Macakova, A. Feiler, *Langmuir* 26 (2010) 4901-4908.

[10]   M.V. Voinova, M. Rodahl, M. Jonson, B. Kasemo, *Phys. Scripta* 59 (1999) 391-.

[11]   G. Binning, C.F. Quate, C. Gerber, *Phys. Rev. Lett.* 56 (1986) 930-933.

[12]   V.L. Mironov, *Fundamentals of Scanning Probe Microscopy*, NT-MDT 2004.

[13]   Y.L. Lyubchenko, *Micron* 42 (2011) 196-206

[14]   A.L. Weisenhorn, P. Maivald, H.J. Butt, P.K. Hansma, *Phys. Rev. B* 45 (1992) 11226-11232.

[15]   H.J. Butt, E.K. Wolf, S.A.C. Gould, P.K. Hansma, *J. Struct. Biol.* 105 (1991) 54-61.

[16]   W.F. Heinz, J.H. Hoh, *Nanotechnology* 17 (1999) 143-150.

[17]   H.J. Butt, B. Cappella, M. Kappl, *Surf. Sci. Rep.* 59 (2005) 1-152

[18]   K.A. Melzak, S. Moreno-Flores, A. Eleta-Lopez, J.L. Toca-Herrera, *Soft Matter* 7 (2010) 332-342.

[19]   S. Lin, J.-L. Chen, L.-S. Huang, H.-W. Lin, *Current Proteom.* 2 (2005) 55-81.

[20]   D. Li, *Colloid Surface A* 116 (1996) 1-23.

[21]   G. Kumar, K.N. Prabhu, *Adv. Colloid Interf. Sci.* 133 (2007) 61–89.

[22]   A. Marmur, *Soft Matter* 2 (2006) 12-17.

[23]   T. Young, *Philos. T. R. Soc. Lond.* 95 (1805) 65.

[24]   J.P. Folkers, P.E. Laibinis, G.M. Whitesides, *Langmuir* 8 (1992) 1330-1341.

[25]   R. Winter, P.G. Nixon, G.L. Gard, D.J. Graham, D.G. Castner, N.R. Holcomb, D.W. Grainger, *Langmuir* 20 (2004) 5776-5781.

[26]   D.K. Goyal, A. Subramanian, *Thin Solid Films* 518 (2010) 2186-2193

[27]   R.M.A. Azzam, N.M. Bashara, *Ellipsometry and Polarized Light*, North-Holland, Amsterdam, 1997.

[28]   H. Arwin, *Sensor. Actuator.* 92 (2001) 43-51

[29]   K. Bierbaum, M. Grunze, A.A. Baski, L.F. Chi, W. Schrepp, H. Fuchs, *Langmuir* 11 (1995) 2143-2150.

[30]   H.F. Ferguson, D.J. Frurip, A.J. Pastor, L.M. Peerey, L.F. Whiting, *Thermochim. Acta* 363 (2000) 1-21.

[31]   R.N. Mcelhaney, *Chem. Phys. Lipids* 30 (1982) 229-259.

[32]   G.A. Holdgate, W.H.J. Ward, *Drug Discov. Today* 10 (2005) 1543-1550.

[33]   V. Ball, C. Maechling, *Int. J. Mol. Sci.* 10 (2009) 3283-3315.

[34]   A.A. Saboury, *J. Iranian Chem. Soc.* 3 (2006) 1-21.

[35]   E. Freire, *Drug Discov. Today* 1 (2004) 295-299.

[36]   R.J. Hunter, *Zeta potential in colloid science. Principles and applications*, Academic Press, London, 1981.

[37]   T. Allen, *Particle size measurement*, Chapman and Hall, London, 1975.

[38]   I.N. Serdyuk, N.R. Zaccai, J. Zaccai, *Methods in molecular biophysics, structure, dynamics and function.* , Cambridge University Press, Cambridge UK, 2007.

[39]   R.S. Macomber, *A complete Introduction to modern NMR spectroscopy*, John Wiley & Sons, Inc, New York, 1998.

Chapter 3

Surface dependence of S-protein nanocrystal formation

In this thesis first we will work with SbpA (S-protein) which has interesting biotechnological applications due to its capacity to fom crystalline nanostructures. In this chapter we will investigate the recrystallization mechanism of SbpA using substrates with different chemistry and hydrophobicity. The S-layer formation is characterized with Atomic Force Microscopy (AFM) and Quartz Crystal Microbalance with Dissipation (QCM-D).

3.1 Introduction

Proteins have a great importance in our world since they are the machinery of life [1]. Besides their role for all living organisms, proteins also play a main role in many technological processes such as food, pharmaceutical, cosmetic, biotechnology and nanotechnology industries [2, 3]. Proteins perform specific functions that are predetermined by their conformational structure. Hence, the knowledge of the three-dimensional (3-D) structure of proteins contributes towards understanding biological mechanisms at the molecular level. Protein crystallization is a first experimental step to solve the 3-D structure [4, 5]. The most common techniques to determine protein structure are X-ray crystallography [6], atomic force microscopy (AFM) [7, 8], electron microscopy (EM) [9] and nuclear magnetic resonance (NMR) [10]. However,

understanding two dimensional protein crystallization is not an easy task since several factors affect the protein crystal structure, such as surface chemistry, ionic strength, pH and protein concentration among others. Investigations carried out with streptavidin on biotinylated lipid monolayers show three distinct crystal structures depending on the crystallization pH [11], while for annexin it has been shown that the local membrane environment influences the final crystal structure [12, 13].

In this work we study the self-assembly kinetics of a bacterial protein that is able to form crystalline cell surface layers, commonly known as S-layers. S-layers are the most common outermost envelope component in prokaryotic organisms, playing an important role in the protection of the organism against environmental conditions. They are isoporous structures with repetitive properties on a nanometer scale and are composed of a single (glyco)protein. S-layers show oblique, square and hexagonal lattice symmetry with a pore size between 2-8 nm and a thickness of 5-25 nm [14-16]. The most important characteristic of S-proteins is their ability to self- assemble after they are isolated, thus recrystallizing on wide range of environments: in suspension, at the air-water interface, and at different solid-liquid interfaces (i.e. silicon dioxide, mica, polyelectrolytes, self assembled monolayers and lipid films) [16-21].

In recent years S-layer technology has been combined with polyelectrolyte multilayers to design robust biomimetic surfaces and membranes [22-24]. Moreover, the synthesis of S-layer fusion proteins has constituted a big step in nanobiotechnology due to the fact that the biofunctional molecules (ie. enhanced green fluorescent protein, laminarinase or antibodies) could be organized in 2-D regular arrays, showing the potential of the S-protein for biosensor development [25-27]. Some AFM preliminary S-protein recrystallization studies have been carried out on different surfaces, such as silicon [28], mica [29] and functionalized gold with disulfides [30]. However, there are some fundamental questions that still remain open.

In this work, we show that S-protein adsorption and nanocrystal growth are altered by functionalizing silicon dioxide substrates with silanes. Quartz Crystal Microbalance with Dissipation (QCM-D) monitoring is used to follow the kinetics of the process, the protein mass deposited per unit area and the steps that lead to the protein layer formation; these being adsorption, self-assembly and recrystallization, and crystal reorganization. The lattice parameters and domain size of the protein surface layers were calculated from atomic force microscopy measurements. Furthermore, in-

situ AFM experiments show in detail how single proteins incorporate into the nanocrystal as well as the growth of crystal domains as function of time.

3.2 Materials and methods

Materials

Silicon wafers with a native silicon dioxide layer (IMEC, Leuven, Belgium) and silicon dioxide coated quartz crystals (Q-sense, Gothenburg, Sweden) were used as substrates. Silane coupling agents, 3-aminopropyltriethoxysilane (APTS) and n-octadecyltrichlorosilane (OTS) were purchased from ABCR (Karlsruhe, Germany). The bacterial cell surface layer protein, SbpA (M_w=120 kDa), was isolated from *Lysinibacillus sphaericus CCM 2177* according to a reported procedure [31]. Protein recrystallization buffer was prepared with 0.5 mM Trizma (Sigma) base and 10 mM CaCl$_2$ (98%, Sigma) and adjusted to pH 9 by titration. Dimethyl sulfoxide (99%, ABCR), ethanol absolute (99%, Sharlau), NaOH (Sigma-Aldrich), toluene (99.9%, Riedel-de Haen), chloroform (99.9%, Sigma), methanol (99.9%, Riedel-de Haen), decalin Cis+Trans (98.0%, Fluka) were used as rinsing agents. 2% sodium dodecyl sulphate, SDS, (99%, Fluka), Hellmanex II (2%, Hellma) were used as cleaning solutions. Aqueous solutions of 100 mM NaCl (Sigma) were used as media in AFM experiments.

Silicon dioxide treatment. Silicon substrates with native silicon dioxide layers were cleaned in 2% sodium SDS for 30 minutes, rinsed with ultrapure water (Barnstead) and dried under a stream of nitrogen. Afterwards the substrates were treated with ultraviolet radiation (Bioforce Nanoscieces) for another 30 minutes before silane modification or protein self-assembling.

Silanization.

3-aminopropyltriethoxysilane, APTS. Silicon wafers were washed with dimethyl sulfoxide, ethanol and water. Afterwards the wafers were etched in aqueous 10% (w/w) NaOH for 1 hour. After being washed gently with water and ethanol, the substrates were immersed in the silane solution (10 ml APTS/200 ml EtOH) for 1 hour at room

temperature. The samples were then washed to remove unbound silanes, first with ethanol and then with water. Finally the surfaces were dried with nitrogen and heated for 20 minutes under vacuum at 110ºC to get a compact silane layer.

n-octadecyltrichlorosilane, OTS. The substrates were washed first in methanol, then in methanol:chloroform 1:1 mixture, and finally in chloroform. In every step the substrates were sonicated for 5 minutes. Afterwards silicon substrates were immersed in a decalin cis-trans /toluene/chloroform 7:2:1 mixture and 0.1% OTS was added. After 12 hours of incubation at room temperature, the substrates were removed from solution and rinsed first with chloroform, then with chloroform:methanol 1:1 mixture, and finally with methanol. This time the substrates were not sonicated. During the whole procedure it was very important to avoid water due to the tendency of OTS to hydrolyze.

The structure of APTS and OTS can be found in appendix 3.1. The contact angle of water on APTS and OTS functionalized substrates are 67º and 105º respectively. These values are higher than those encountered on bare silicon dioxide substrates (<5º) (see appendix 3.1) [32, 33]. The silane layer thickness was measured with ellipsometry; the values obtained were 2.65 nm for OTS and 0.95 nm for APTS (see appendix 3.2).

S-protein adsorption. The S-protein solution was isolated as explained in reference [39]. Due to the ability of S-proteins to self-assemble in solution, the protein extract solution (1 mg ml^{-1}) was centrifuged at 5000 rpm for 5 minutes to separate S-protein monomers from self-assembly products. Just before the experiments, the supernatant was diluted using the appropriate amount of recrystallizing buffer. On one hand, in-situ QCM-D and AFM experiments were carried out by protein solution injection into the experimental set up, once the substrates were stabilized in tris-buffer. On the other hand, ex-situ experiments were done using substrates where S-protein had been previously recrystallized. Small volume humidity chambers were used to prevent water evaporation. In both cases the protein was incubated for 12 hours at room temperature and afterwards the substrates were rinsed with recrystallizing buffer in order to remove excess protein.

Methods

Contact angle. Sessile-drop experiments were performed with a contact angle measuring system (KRUSS D100, Hamburg, Germany). Millipore water (specific resistance 18.2 MΩ cm^{-1}) was used as the liquid phase. Water drops were deposited on the substrates and the contact angles were obtained from the drop profiles.

Ellipsometry. A commercial spectroscopic ellipsometer (M2000V J. A. Woollam Co. Inc., USA) was used to measure the thickness of the silane coated samples in air. The changes in the ellipsometric angles, delta (Δ) and psi (Ψ), of elliptically polarized light upon reflection by a planar surface were obtained at different wavelengths and incident angles. Both the refractive index and film thickness could be calculated. Ellipsometric data, Δ and ψ, were acquired over a wavelength range from λ=380 to 1000 nm, at different incident angles varied between 65º-75º at room temperature. For thickness calculation the Cauchy dispersion equation was used assuming refractive index for the silane layer of 1.45 [34].

Quartz Crystal Microbalance with Dissipation monitoring, QCM-D. QCM-D (Q-sense E4, Gothenburg, Sweden) was used to carry out real time/in situ experiments. QCM-D is a well established technique for simultaneous monitoring of mass, and energy dissipation from changes in the resonant frequency and the damping of a vibrating sensor. This sensor consists of a thin AT-cut piezoelectric quartz crystal, sandwiched between two electrodes; one electrode is coated with silicon that has a silicon dioxide layer and this surface is used for experiments. The relation between the oscillating frequency change and the adsorbed mass is given by Sauerbrey equation [35];

$$\Delta m = -C \cdot \frac{\Delta f}{n}$$

where Δm represents the mass surface density (ng cm^{-2}), C is a proportionality constant that depends only on the intrinsic properties of the sensor (-17.7 ng Hz^{-1}·cm^{-2} for 5 MHz crystals), ΔF is the frequency shift and n is the overtone number (1, 3, 5,…).

Atomic Force Microscopy, AFM. Atomic Force microscopy was used to perform surface imaging. The images were recorded in tapping mode (at 1 Hz) in 100 mM NaCl aqueous solution at room temperature, using a Nanoscope V controller Multimode AFM

(Veeco, Santa Barbara, USA). Before use, the fluid cell, tubings and O-rings were washed overnight with 2% SDS, rinsed gently with ultrapure water and dried with nitrogen. Back side gold coated silicon nitride (Si_3N_4) cantilevers of 0.32 N m^{-1} with sharpened tips (DNP-S, Veeco) were used and cleaned in ethanol and acetone before use.

3.3 Results and discussion

3.3.1 Morphology of bacterial S-protein layers

The AFM images of figure 3.1 show that S-protein is arranged in an orderly manner within patches of varying size depending on whether the substrate was SiO_2, APTS or OTS. Fourier analysis on the AFM images shows that square lattice of S-protein is formed on each patch (domain), with lattice parameters values a and b (a=b) of 13.3 nm for SiO_2 and 14.0 nm and 14.1 nm for APTS and OTS, respectively, and γ close to 90º (see table 3.1), similar to the values found on bacteria [15]. The S-layer thickness was calculated by AFM scratching experiments (see appendix 3.3). The height profiles of the scratched area (500 x 250 nm^2) revealed that S-layer thickness is 15 nm for all substrates (see table 3.1). The estimation of the layer roughness (shown in table 3.1) indicates that the protein crystal is smoother on silicon dioxide (0.30 nm) than on APTS or OTS.

Substrate	Substrate covered with SbpA				
	SbpA Thickness (nm)	SbpA Roughness (nm)	a, b (nm)	γ (º)	Domains (μm^2)
SiO_2	15.2±0.3	0.30 ±0.01	a=b=13.3±0.2	γ=91.8º ±0.2	32.6±0. 5
APTS	15.1±0.4	0.46 ±0.04	a=b=14.0±0.6	γ=91.6º ±2.9	0.02±0.01
OTS	15.5±0.2	0.43±0.08	a=b=14.1±0.4	γ=87.5º ±1.8	0.05±0.01

Table 3.1. S-layer properties after 12 hours of incubation: thickness, roughness, protein domain size and lattice parameters. AFM scratching experiments shows that a 15 nm thick protein bilayer is formed in each case. The layer roughness is similar for the three substrates. The lattice parameters belong to p4 square symmetry. The major difference is observed in the created protein domains. Large patches are formed on silicon dioxide, while small protein domains are observed on silane modified substrates.

Figure 3.1 and table 3.1 also show that the S-layer monocrystalline domains formed on hydrophilic silicon dioxide are larger than those formed on hydrophobic silanes. The average size of the protein domains are 0.02 μm^2 and 0.05 μm^2 on APTS and OTS, respectively. Moreover, figure 3.1 shows that S-layer orientation in each domain varies on these substrates. In contrast, on silicon dioxide substrates crystalline domains larger than 32 μm^2 are typically encountered.

Silane coupling agents APTS and OTS, have been used to modify silicon substrates just to vary the protein-surface interaction with the goal of inducing possible new recrystallization pathways. The AFM results demonstrate that on hydrophobic surfaces smaller protein crystal domains are formed than on hydrophilic silicon dioxide. While on hydrophilic silicon dioxide unidirectional protein crystals are mainly observed, on hydrophobic silanes the orientation changes from domain to domain. Although the size and the domain orientation depend on the substrate, Fourier analysis shows that the lattice parameters (see table 3.1) are similar to those found on bacteria [15]. AFM scratching experiments revealed a thickness of ca. 15 nm for the protein layer on all substrates, which corresponds to a protein bilayer in all cases [22, 36]. Thus, bacterial protein recrystallization is influenced by the surface chemistry although the final thickness remains constant [30].
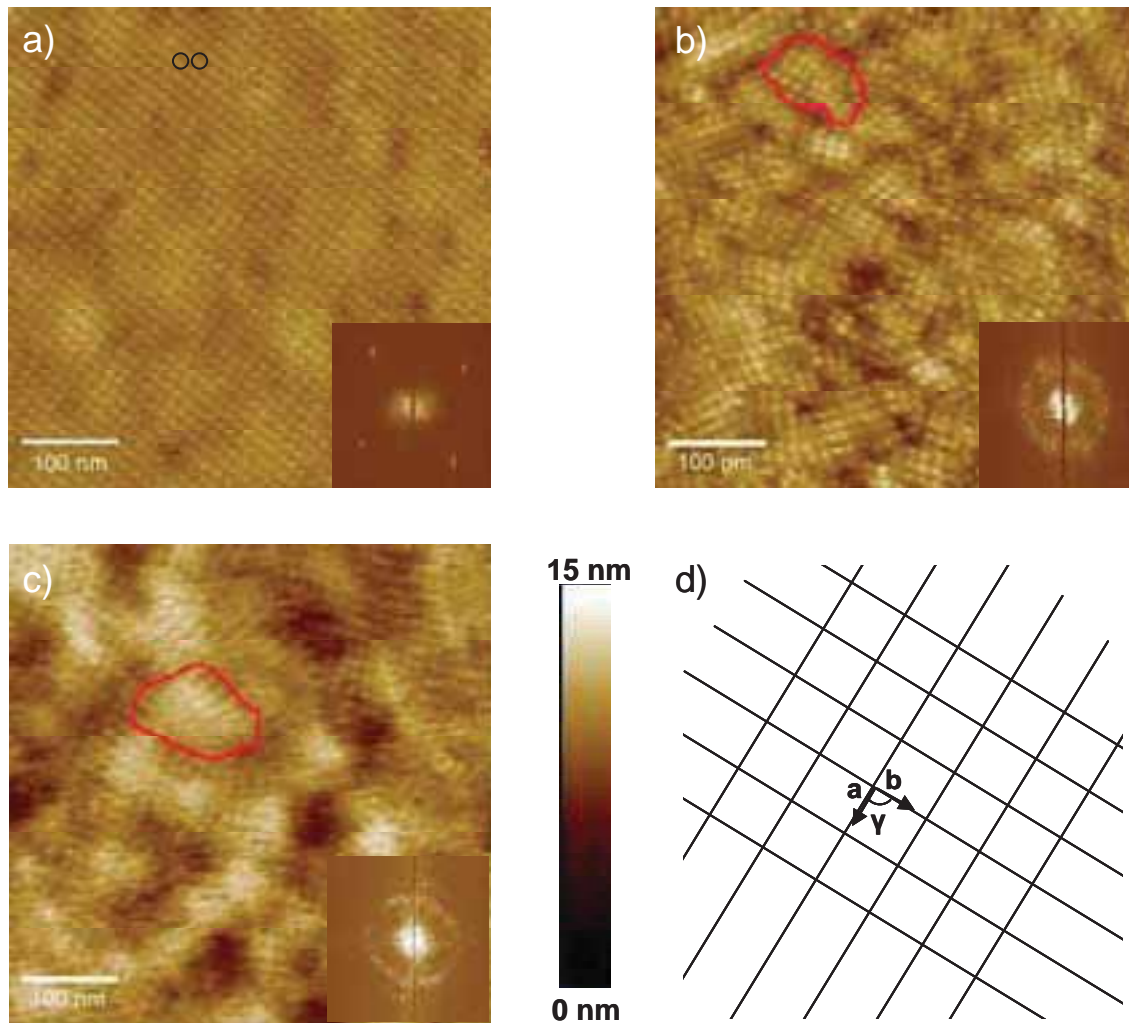
Figure 3.1. AFM images of recrystallized S-protein on a) silicon dioxide, b) APTS and c) OTS after 12 hours incubation. SbpA is recrystallized on both hydrophilic silicon dioxide and hydrophobic silanes. The black circles of a) indicate single protein while the red shapes of b) and c) delimit the protein domains. The bottom right-hand side insets are the corresponding 2D Fourier transform images. They reveal S-protein periodicity on both silicon dioxide (points) and on APTS and OTS (annular rings). The circular halo on APTS and OTS reveal the different orientation of S-protein patches. d) Square lattice diagram (p4) where a, b are the unit cell vectors and γ the angle between them.

The AFM images of the protein layers formed on the different substrates imply that the adsorption might be led by different mechanisms, as the surface hydrophobicity changes. We focused the investigation on understanding this process from the initial step (when the proteins start self organizing), to the final one (the end of S-layer formation).

3.3.2 Bacterial S-protein adsorption and recrystallization in real time

The process of SbpA recrystallization was monitored in real time by doing perfusion AFM experiments. Figure 3.2, from a) to d), illustrates the protein adsorption on silicon dioxide where it is possible to observe S-layer formation at the microscale over a 12 hour period. After the formation of the first nucleation points, the protein crystals grow as radially advancing fronts towards uncovered areas until the entire surface is covered. Table 3.2a shows that after 15 minutes, 33% of the silicon dioxide area is covered with S-protein (SbpA). It can be observed that at the beginning, the area occupied by the protein layer increases with time due to the incorporation of proteins in the growing front. However, after an hour, the 80% of the sample area is already covered with recrystallized S-layer and during the next time only 5% is recrystallized (see table 3.2a). Finally, after 12 hours of incubation, the surface coverage reaches 98%, with homogeneous protein layer domains of size larger than 32 μm^2. On APTS and OTS the adsorption occurs differently. Figure 3.2, from e) to h), shows the recrystallization process at the molecular scale on OTS. Both figures show how the protein subunits rearrange to build the lattice. In both cases, the surface is totally covered within 30 minutes; a general conclusion is that the recrystallization process occurs faster on the silane-coated substrates. More details are shown in figure 3.3 where we can even differentiate a three-step process; from 0 to 4 minutes the first nucleation points are formed (see figure 3.3a). In the next few minutes, (figure 3.3b), the S-protein subunits arrange forming the first crystalline self-assemblies. During this time, small domains consisting of 5-10 proteins are typically found. From 7-14 minutes the number of proteins increases, this can be observed in domain 1 and domain 2 (see figure 3.3c).
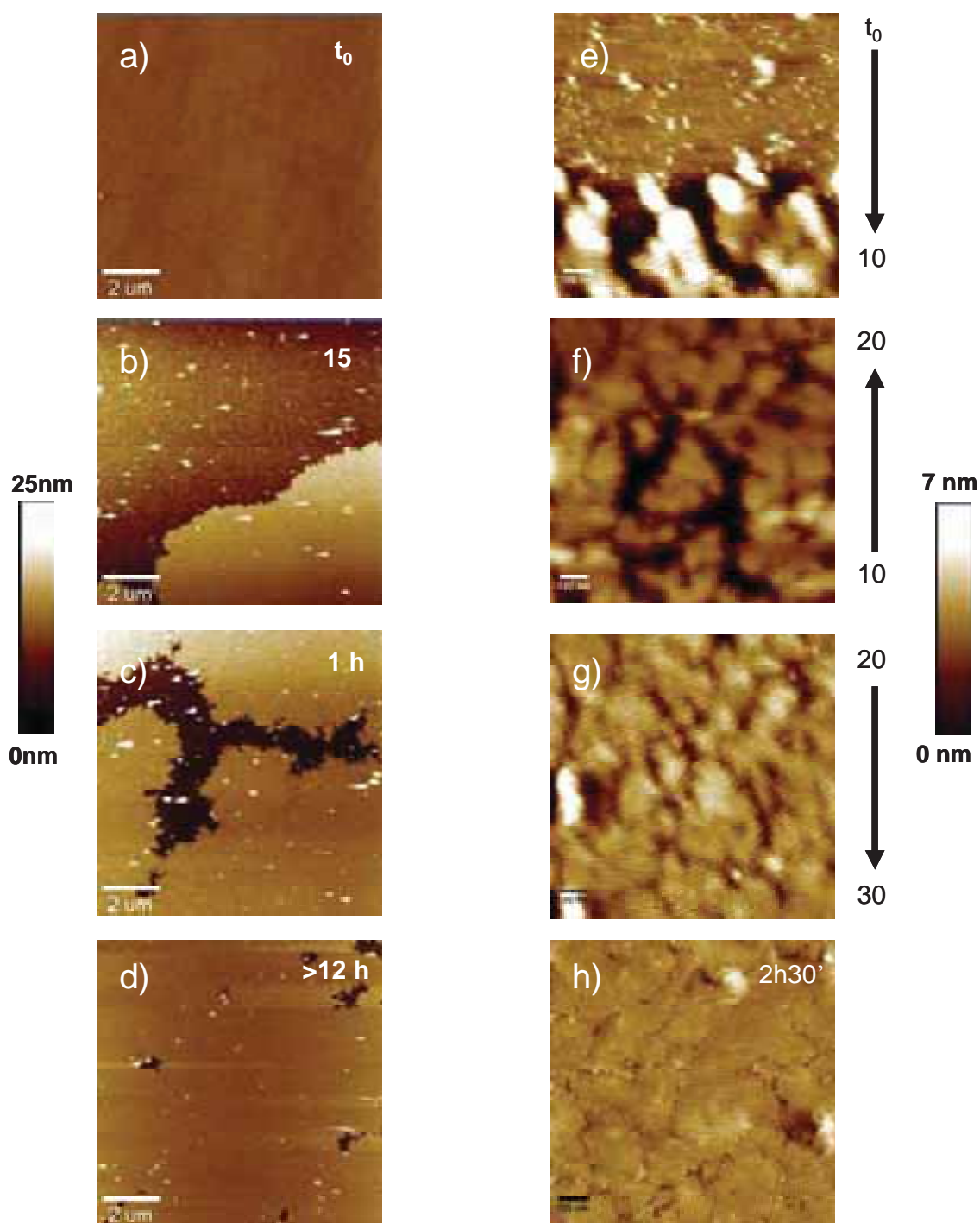
Figure 3.2. From a) to d) An overview of in-Situ SbpA recrystallization process on SiO_2 followed by AFM (height images). At t_0 the silicon surface is scanned in tris-buffer solution (pH 9). Afterwards, SbpA is injected which is adsorbed and recrystallized on the surface immediately after the injection. The surface coverage increases until it reaches 98% after 12 hours. **From e) to h)** In-Situ SbpA recrystallization process on OTS surface, by AFM (height images). At t_0=0min SbpA is injected, and the progressive recrystallization of the protein is followed at different times. 30 minutes is enough to have a complete S-layer. Note that the SbpA/buffer ratio is 0.1:0.9 and the pH of the buffer is 9. The numbers indicate the time in minutes or hours.

Finally from 14-28 minutes some neighboring domains with similar orientations even coalescence and reorganize forming larger crystalline domains (see figure 3.3d and figure 3.3e). These protein domains grow by incorporating at their boundaries new proteins from solution, until the entire surface is covered (see figure 3.3e and 3.3f).
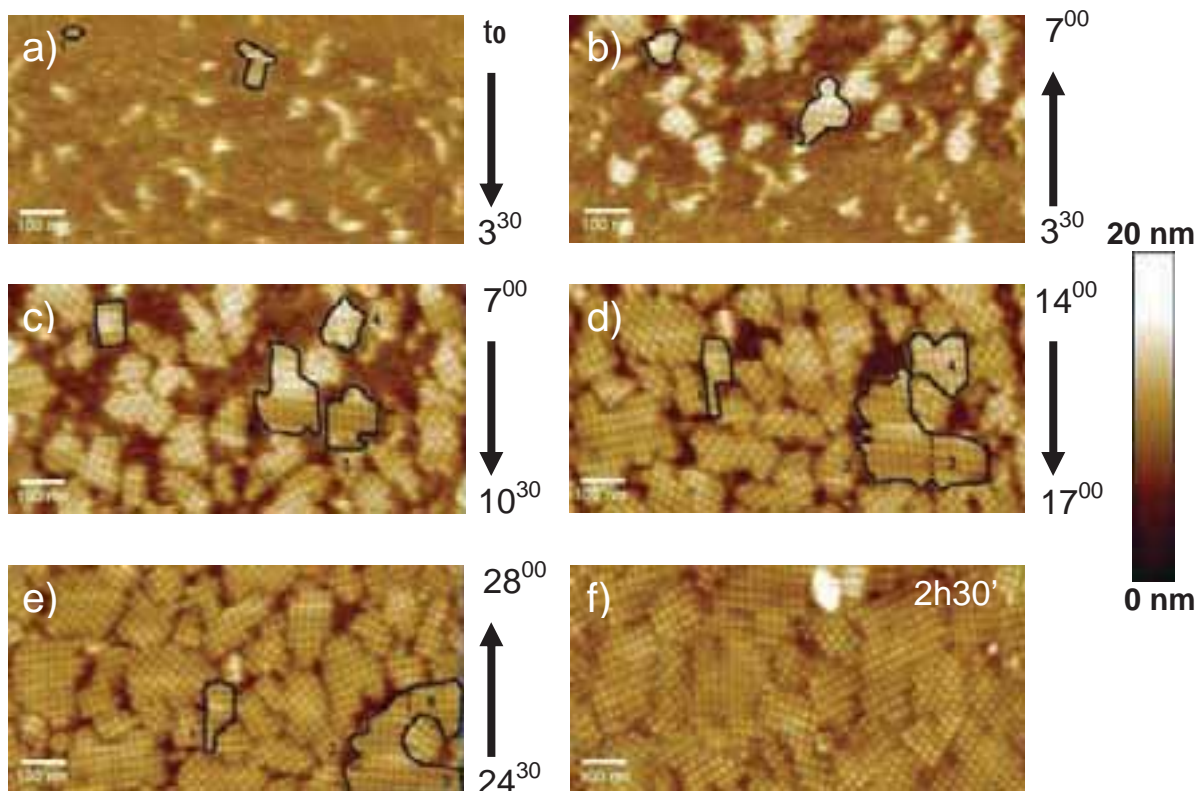

Figure 3.3. In-Situ SbpA recrystallization process on APTS surface, followed by AFM (height images). It is observed how the nucleation sites are formed, after protein injection (at t_0=0min) and the growth of protein patches until they meet the neighbouring domains. 1 and 2 indicate the time evolution of two crystal domains from their nucleation points until their final size or domain coalescence (domain 2 with domains 3 and 4).

SbpA recrystallization monitored in real time with perfusion AFM experiments illustrates how the microscopic protein layer grows, advancing until the SiO_2 surface is completely covered after 12 hours (figure 3.2). On APTS and OTS, protein adsorption occurs differently, finishing after 30 minutes. The quantitative values for surface coverage are reported in table 3.2 in detail. Thus, S-layer recrystallization occurs faster on silane coated substrates, that is, on hydrophobic substrates. Interestingly, in all cases the protein crystal formation is achieved by incorporating protein monomers from

solution to the growing front, as the profile analysis shows[j] (see appendix 3.4). More important, these figures show that the protein nanocrystal formation is driven in three steps: nucleation point formation, protein self-assembly and recrystallization, and crystal domain reorganization.

Quartz Crystal Microbalance with dissipation monitoring (QCM-D) provides in-situ additional information about the adsorbed mass and the layer rigidity. Figure 3.4 shows the variation of the frequency and dissipation as a function of time, measured with the QCM-D, for the three systems mentioned above. Once the protein solution is injected on the system, the frequency decreases due to the change of adsorbed mass associated with protein deposition. Simultaneously, the dissipation increases, indicating the formation of a layer that is not perfectly elastic. The process starts with a fast and abrupt change, followed by a gradual variation. After completion, when no further changes in frequency and dissipation are observed, the system is rinsed with fresh buffer to remove the excess of protein. Rinsing does not alter frequency and dissipation, which means that the S-layer does not desorb. It can be observed that the protein adsorption process is slower on silicon dioxide than on APTS and on OTS, which reinforce the AFM results, although the kinetics could not be identical due to the geometry of the AFM tip. Fifteen minutes after protein injection, AFM measurements showed that the adsorption reached 58% on SiO_2, while on APTS and OTS the value was 94% (table 3.2b). The overall dissipation changes are 5.45×10^{-6}, 4.54×10^{-6}, 2.47×10^{-6} for silicon dioxide, APTS and OTS, respectively as figure 3.4 shows, indicating that the protein layers formed on hydrophobic silanes are more rigid than those formed on silicon dioxide.

According to the Sauerbrey equation the mass per unit area calculated from overall frequency changes of the 5th overtone (ΔF), is 1628 ng cm^{-2} for SiO_2, 1735 ng cm^{-2} for APTS and 1770 ng cm^{-2} for OTS. Similar values were obtained in a previous work when SbpA was adsorbed on negatively charge polyelectrolyte PSS (poly(sodium 4-styrenesulfonate)) [22].

---

[j]Atomic force microscopy profile analysis of the protein front, on the three substrates, shows that the thickness is lower than 14 nm, approximately, the thickness of the protein dimer.
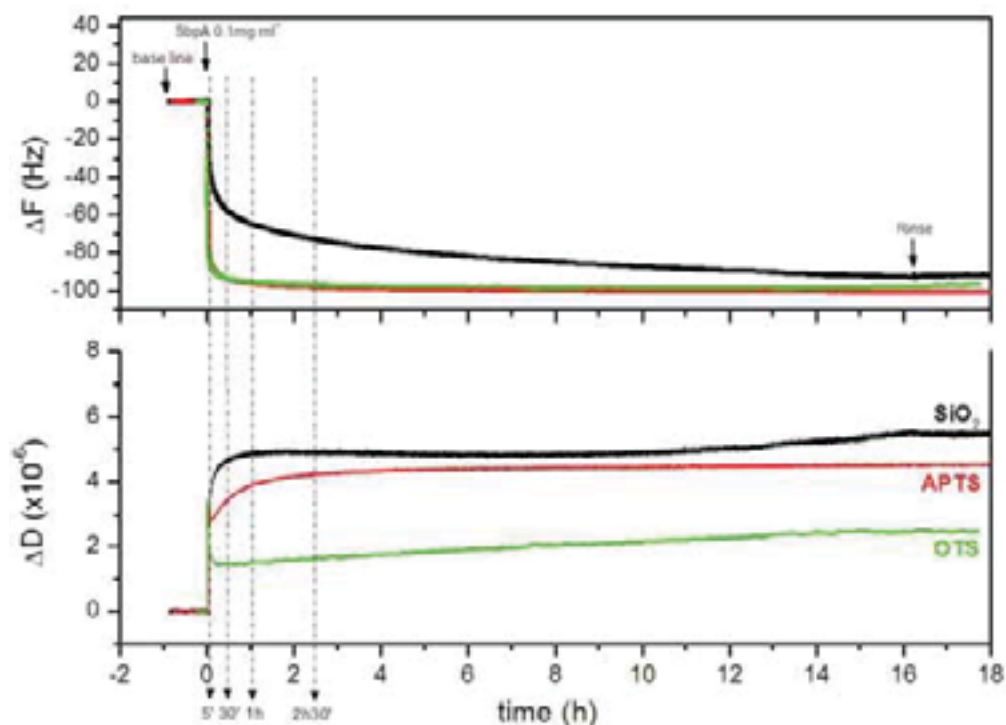
Figure 3.4. QCM-D Frequency (ΔF) and dissipation shifts (ΔD) as a function of time for SiO_2, APTS and OTS. Bacterial protein is added at a concentration of 0.1mg ml^{-1}. Even though the overall frequency shift is similar on all substrates the process is slower on silicon dioxide than on hydrophobic silanes. The overall dissipation shifts differ between substrates, with the most rigid layer being the one obtained on OTS.

time	SiO_2(%)	OTS(%)	APTS(%)
a)			
5min	X	31	21
15min	33	77	68
30min	62	96	83
1h	80	99	85
2h30min	85	99	95
>12h	98	100	100
b)			
5min	41	91	90
15min	58	94	94
30min	64	97	96
1h	71	98	98
2h30min	80	99	99
>12h	100	100	100

Table 3.2. a) S-layer coverage percentage on SiO_2, OTS and APTS. Values calculated from AFM images. b) Extent of S-protein adsorption (in units/area) on SiO_2, OTS and APTS. Values calculated from QCM-D experiments

The effect of the concentration on the protein adsorption kinetics is illustrated in figures 3.5. Figure 3.5a summarizes all frequency/concentration experiments where the overall frequency shift, ΔF, is plotted vs. protein concentration. It can be observed that ΔF increases with the concentration until it reaches a plateau. For silane-coated substrates, this plateau is detected at concentrations lower than 0.05 mg ml^{-1}, where the amount of deposited protein covers more than 90% of the available area. In contrast, the plateau for silicon dioxide is shifted to higher concentration (0.07 mg ml^{-1}), which indicates that the affinity of the protein for bare silicon dioxide is lower than for silane-coatings. This is clearly shown in figure 3.5b where the initial adsorption rate is plotted as a function of concentration for all systems. The linear dependence suggests a diffusion-controlled process, with a 5-fold change in slope between silicon dioxide and hydrophobic silanes. Initial adsorption rates at constant SbpA concentration (0.1 mg ml^{-1}) change from 2847 ng cm^{-2} min^{-1} for silicon dioxide to 13912 ng cm^{-2} min^{-1} and 13995 ng cm^{-2} min^{-1} for APTS and OTS respectively. These values agree with the AFM results; silane hydrophobic substrates accelerate S-protein adsorption rate.

The results obtained with QCM-D also indicate that S-protein adsorbs faster on silane coated substrates than on silicon dioxide, and that the mechanical properties of the protein layer depend on the substrate. The protein layer recrystallized on the most hydrophobic surface (OTS) dissipates the least energy, while the layer recrystallized on hydrophilic silicon dioxide dissipates the most, indicating that it is the most complaint. In addition, the effect of the protein concentration on the adsorption kinetics shows that more protein is necessary to reach a constant ΔF value on silicon dioxide, indicating that S-layer affinity for silicon dioxide substrates is lower than for silane coatings. The quantification of the initial adsorption rate gives evidence of a diffusion-controlled process. Note that the five-fold change in slope between silicon dioxide and hydrophobic silanes is associated with a dramatic effect on the nucleation process due to the surface chemistry.
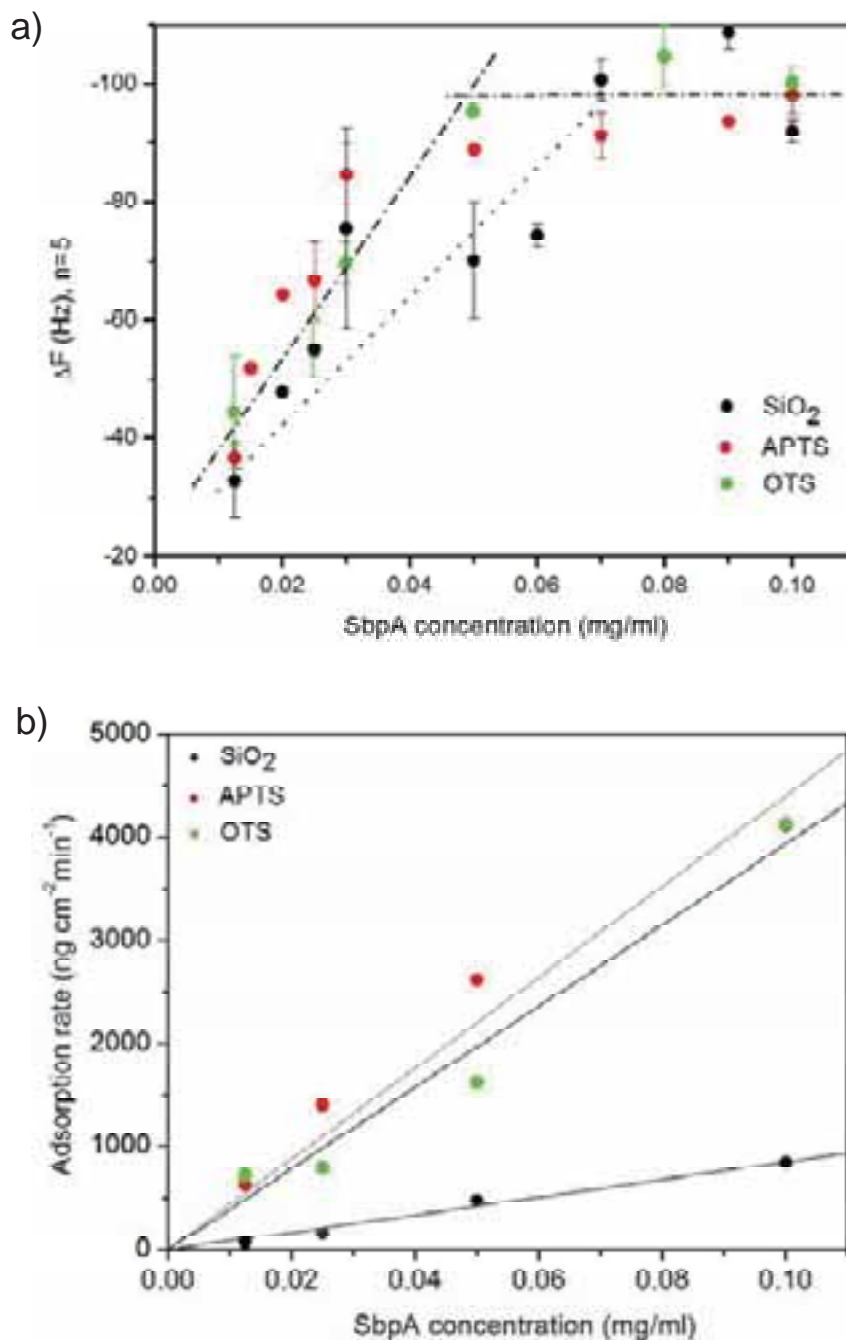
Figure 3.5. a) Overall frequency shift at different SbpA concentrations on SiO_2, APTS and OTS. ΔF increases with the concentration until a plateau is reached, where no further increase occurs with increase of concentration. On silanes the plateau is reached at 0.05 mg ml^{-1}, (dash-dot line). On SiO_2 this occurs at higher concentration, 0.07 mg ml^{-1} (dot-dot line). b) Initial adsorption rate calculated from the derivative of frequency-time curves from 0 to 5 minutes and at different concentrations for silicon oxide, APTS and OTS. A linear relation is found which suggest diffusion controlled. Comparing the three slopes it is observed that the adsorption rate is faster on hydrophobic substrates than on hydrophilic silicon dioxide.

In general terms any recrystallization process has two stages, nucleation and growth [7]. In the case of the bacterial protein SbpA we have distinguished an additional stage, the reorganization, which consists in the coalescence of small crystal domains to form a larger one. It was observed that the increase of surface hydrophobicity strongly affects the S-layer formation. The substrate-protein interaction is crucial for the formation of the nucleation points. On silane-coated substrates the number of nucleation points per unit area is approximately thousand times higher than on SiO_2 substrates[k], suggesting a stronger S-protein/surface interaction in the first case. This also affects the subsequent incorporation of proteins, which occurs at the domain boundaries. The number of adjacent sites, where the protein can self-assemble, is higher around the multiple small domains than around the smaller number of large domains.

This involves simultaneous growth of many independent protein domains which lead to a fast S-layer formation. Hence, the most characteristic feature of the fast protein adsorption is the small protein domains formation. The independent recrystallization points may have freedom to grow in different directions, which is what we found on silane-coated substrates (figure 3.2 and figure 3.3). On the contrary, on silicon dioxide where crystal growth occurs gradually, the proteins form large crystals, from few nucleation points with unique protein orientation (figure 3.1 and figure 3.2). As has been mentioned, the recrystallization is not finished once complete surface coverage is attained. A last step involving the rearrangement of neighbouring protein domains fusing into a bigger one has been observed.

The frequency-dissipation curves (figure 3.6) illustrate in a qualitative way the linkage between the stages of recrystallization and the mechanical properties of the layer. It has been mentioned that S-layer recrystallization on silicon dioxide is different from the silanes. In this case, a gradual increase of mass with dissipation was observed. Once the system had almost reached the maximal coverage, the big protein domains merged, which was accompanied by an increase of dissipation before completion. On the hydrophobic substrates, dissipation reaches a maximum (points 1 and 3 in figure 3.6a), which delimits the end of adsorption and the beginning of protein self assembly. The latter is accompanied by a decrease of the system dissipation (points 2 and 4 in figure 3.6a) due to the formation of a solid-like layer. As AFM images show (see figure

---

[k] The nucleation points have been calculated from figures 3.2 and figure 3.3.

3.3) this can be related with the crystalline domain reorganization (domain coalescence) where the S-layer minimizes the energy by reducing the layer defects. The final increase in dissipation in which the frequency values are constant (no mass adsorption) might correspond to local variation in viscosities near S-layer interface due to S-protein self assembly formation in solution. At this point, it has to be pointed out that the calculated S-layer mass is similar on the three substrates. Scratching AFM experiments also show that the protein layer thickness (ca. 14 nm) is the same on the three substrates (see appendix 3.3). Considering that the protein bilayer contains a similar amount of water, the changes in dissipation may be induced by the protein/substrate interaction, which increases with the degree of hydrophobicity.
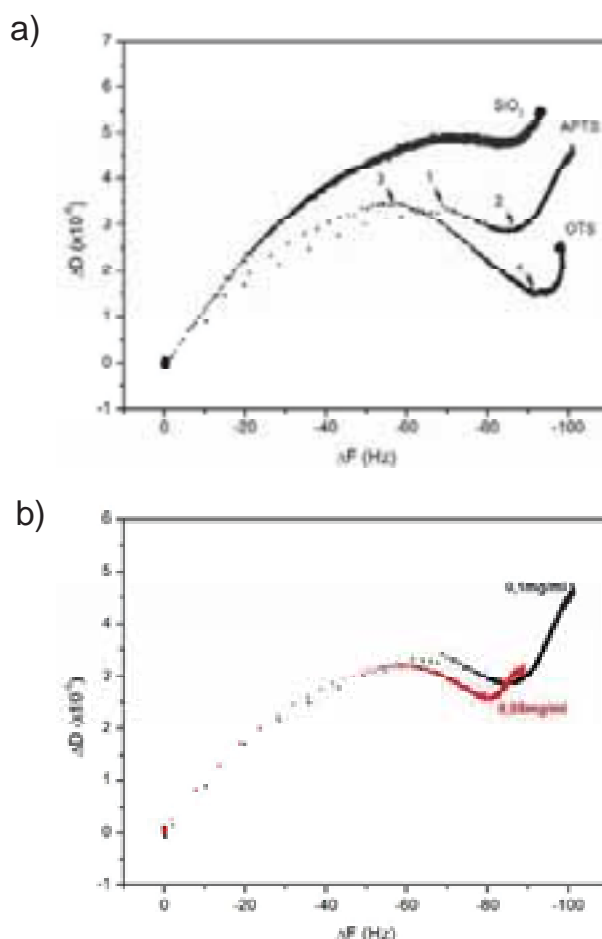
Figure 3.6. a) Frequency-dissipation curves at 0.1 mg ml^{-1} protein concentration for silicon dioxide, APTS and OTS. 1, 2, 3, 4 indicate S-layer transition points based on dissipation shift. b) Frequency–dissipation curves for 0.05 mg ml^{-1} and 0.1mg ml^{-1} protein concentration for APTS. The adsorption kinetics is affected by concentration variation as well as by substrate hydrophobicity.

The decrease of protein concentration on hydrophobic substrates might reduce the number of nucleation points, enhancing the growth of large crystals and hence limiting domain coalescence. In this regard dissipation-frequency curves should ressemble the curve obtained on the SiO_2 substrate. This is exactly what figure 3.6b shows for APTS-coated substrates and protein concentration between 0.1 mg ml^{-1} and 0.05 mg ml^{-1}. The dissipation-frequency curves gradually change with decreasing concentration. In this case, either modifying the surface chemistry (at constant protein concentration) or the protein concentration (at equal surface chemistry) has analogous effects on protein recrystallization kinetics. In the range between 0.05 mg ml^{-1} and 0.0125 mg ml^{-1}, the adsorption process may be truncated forming an uncompleted S-layer due to the lack of protein in solution.

At this point it is necessary to stress that the methodology presented in this study is also applicable to other proteins. Previous work has shown the use of atomic force microscopy to study the growth of inorganic calcite [37], lysozyme crystals [38] and annexin [12,13]. In general, two dimensional nucleation is significant for the growth of protein crystals [39]. In our case, the combination of high resolution atomic force microscopy and quartz crystal microbalance with dissipation permitted the elucidation of the recrystallization route of the S-protein SbpA, the mass per unit area[l] and the compliant properties of the protein crystal. The combination of both experimental techniques can be extended to other proteins or macromolecules.

In the last decades, 2D crystallization has been a way to determine the structure of proteins that do not crystallize easily in three dimensions [40]. A classical approach that facilitates 2D crystal growth is the use of the specific binding of proteins to ligand-bearing lipids. In this regard the S-proteins can also play a relevant role when used as scaffold or template to organize biomolecules [41] or nanoparticles in 2-D [42].

---

[l]This "mass per unit area" is composed of the mass of SbpA and the mass of the trapped water in the protein layer. Thus, the method can also be used to investigate hydration effects in macromolecular structures.

3.4. Conclusions

The study of S-protein adsorption kinetics has been carried out by Atomic Force Microscopy and Quartz Crystal Microbalance. Substrate hydrophobicity does not influence thickness, crystal lattice parameters or the final adsorbed mass density. However, there are clear differences between the S-layers formed on silane coated substrates and on silicon dioxide. The affinity between the protein and the substrate is fundamental with regards to this event. It is observed that hydrophobic forces (APTS and OTS) lead to a faster protein adsorption. Thus, in 5 minutes more nucleation points are formed on silane-coated substrates than on silicon dioxide. We have imaged the monomolecular protein self-assembly during the protein domains formation. On silane-coated substrates, differently oriented small protein domains of 0.02-0.05 μm^2 are formed, while on silicon dioxide unidirectional large crystals of at least 32 μm^2 are obtained. Independently of protein domain size, the domain growth occurs as radially advancing fronts, always towards uncovered areas. Finally, S-protein neighbouring domains coalesce to form the final S-layer. This reorganization effect is detected as a decrease in dissipation which is more significant for silane-coated systems due to the high number of small domains. Combining AFM and QCM-D we could demonstrate that the S-protein crystal formation occurs in three steps, nucleation, growth (self-assembly) and reorganization.

Experiments at different concentrations show that protein adsorption is governed by diffusion until reaching a threshold concentration, 0.7 mg ml^{-1} for silicon dioxide and 0.5 mg ml^{-1} for silane coated substrates. High resolution AFM images and QCM-D measurements are valuable tools to develop theoretical models not only to investigate S-layer recrystallization but also protein self-assembly in general at the nanoscale.

3.5 References

[1]   B. Alberts, D. Bray, A. Johnson, J. Lewis, M. Raff, K. Roberts, P. Walte, *Essential Cell Biology: an introduction to the Molecular Biology to the Cell*, Garland Publishing Inc. , New York & London, 1998.

[2]   G.Yampolskaya, D. Platikanov, *Adv. Colloid Interfac.* 128-130 (2006) 159-183.

[3]   A. McPherson, *J. Struct. Biol.* 142 (2003) 1-2

[4]   A.A. Chernov, *J. Struct. Biol.* 142 (2003) 3-21

[5]   C.-J. Tsai, C.S. Ejsing, A. Shevchenko, C. Ziegler, *J. Struct. Biol.* 160 (2007) 275-286.

[6]   M.L. Pusey, Z.-J. Liu, W. Tempel, J. Praissman, D. Lin, B.-C. Wang, J.A. Gavira, J.D. Ng, *Prog. Biophys. Mol. Bio.* 88 (2005) 359-386.

[7]   A. McPherson, Y.G. Kuznetsov, A. Malkin, M. Plomp, *J. Struct. Biol.* 142 (2003) 32-46

[8]   X. He, W. Li, S. Habelitz, *J. Struct. Biol.* 164 (2008) 314-321

[9]   S. Jonic, C. Vénien-Bryan, *Curr. Opin. Pharmacol.* 9 (2009) 636-642.

[10]   M. Billeter, G. Wagner, K. Wuthrich, *J. Biomol. NMR* 43 (2008) 155-158.

[11]   P. Ratanabanangkoon, A.P. Gast, *Langmuir* 19 (2003) 1794-1801

[12]   R.P. Richter, J.L.K. Him, B. Tessier, C. Tessier, A.R. Brisson, *Biophys. J.* 89 (2005) 3372-3385

[13]   S. Faiß, K. Kastl, A. Janshoff, C. Steinem, *Biochim. Biophys. Acta* 1778 (2008) 1601-1610.

[14]   M.S. Sidhu, I. Olsen, *Microbiology* 143 (1997) 1039-1052.

[15]   U.B. Sleytr, P. Messner, D. Pum, M. Sára, *Angew. Chem. Int. Edit.* 38 (1999) 1034-1054.

[16]   A. Ciferri, *Supramolcular Polymers*, CRC Press, Taylor & Francis Group, Boca Raton, FL 2005.

[17]   U.B. Sleytr, E.M. Egelseer, N. Ilk, D. Pum, B. Schuster, *FEBS Lett.* 274 (2007) 323-334.

[18]   U.B. Sleytr, M. Sára, D. Pum, B. Schuster, *Prog. Surf. Sci.* 68 (2001) 231-278.

[19]   U.B. Sleytr, E. Györvary, D. Pum, *Prog. Org. Coat.* 47 (2003) 279-287.

[20]   U.B. Sleytr, H. Bayley, M. Sára, A. Breitwieser, S. Kúpcú, C.M.S. Weigert, F.M. Unger, P. Messner, B. Jahn-Schmid, B. Schuster, D. Pum, K. Douglas, N.A. Clark, J.T. Moore, T.A. Winningham, S. Levy, I. Frithsen, J. Pankovc, P. Beale, H.P. Gillis, D.A. Choutov, K.P. Martin, *FEMS Microbiol. Rev.* 20 (1997) 151-175.

[21]   D. Pum, U.B. Sleytr, *Supramol. Sci.* 2 (1995) 193-197.

[22]   M. Delcea, R. Krastev, T. Gutberlet, D. Pum, U.B. Sleytr, J.L. Toca-Herrera, *Soft Matter* 4 (2008) 1414-1421.

[23]   M. Delcea, R. Krastev, T. Gutleber, D. Pum, U.B. Sleytr, J.L. Toca-Herrera, *J. Nanosci. Nanotechno.* 7 (2007) 4260-4266.

[24]   J.L. Toca-Herrera, S. Moreno-Flores, J. Friedmann, D. Pum, U.B. Sleytr, *Microsc. Res. Techniq.* 65 (2004) 226-234.

[25]   H. Tschiggerl, J.L. Casey, K. Parisi, M. Foley, U.B. Sleytr, *Bioconjugate Chem.* 19 (2008) 860-865.

[26]   H. Tschiggerl, A. Breitwieser, G.d. Roo, T. Verwoerd, C. Schäffer, U.B. Sleytr, *J. Biotechnol.* 133 (2008) 403-411.

[27]   U.B. Sleytr, C. Huber, N. Ilk, D. Pum, B. Schuster, E.M. Egelseer, *FEMS Microbiol. Lett.* 267 (2007) 131-144.

[28]   E.S. Györvary, O. Stein, D. Pum, U.B. Sleytr, *J. Microsc.* 212 (2003) 300-306.

[29]   A. Martín-Molina, S. Moreno-Flores, E. Perez, D. Pum, U.B. sleytr, J.L. Toca-Herrera, *Biophys. J.* 90 (2006) 1821-1829.

[30]   S. Moreno-Flores, A. Kasry, H.J. Butt, C. Vavilala, M. Schmittel, D. Pum, U.B. Sleytr, J.L. Toca-Herrera, *Angew. Chem. Int. Edit.* 47 (2008) 4707-1717.

[31]   U.B. Sleytr, M. Sára, S. Küpcü, P. Messner, *Arch. Microbiol.* 146 (1986) 19-24.

[32]   A.N. Parikh, D.L. Allara, I.B. Azouz, F. Rondelez, *J. Phys. Chem.* 98 (1994) 7577–7590

[33]   C. Krueger, *PhD thesis*, Mainz University (Germany), 2001.

[34] K. Bierbaum, M. Grunze, A.A. Baski, L.F. Chi, W. Schrepp, H. Fuchs, *Langmuir* 11 (1995) 2143-2150.

[35] G. Sauerbrey, *Z. Phys.* 155 (1959) 206-222.

[36] J.L. Toca-Herrera, R. Krastev, V. Bosio, S. Küpcü, D. Pum, A. Fery, M. Sára, U.B. Sleytr, *Small* 1 (2005) 339-348.

[37] A.J. Gratz, S. Manne, P.K. Hansma, *Geochim. Cosmochim. Ac.* 57 (1993) 1343-1346.

[38] Y.G. Kutnezsov, A.J. Mllakin, A. Greenwood, A. McPherson, *J. Struct. Biol.* 114 (1995) 184-196.

[39] A.J. Malkin, Y.G. Kutnezsov, T.A. Land, J.J. DeYoreo, A. McPherson, *Nature* 2 (1995) 956-959

[40] J. Dietrich, C. Venien-Bryan, *Strategies for Two-Dimensional Crystallization of Proteins using Lipid Monolayers*, College Press, London, 2005.

[41] D. Moll, C. Huber, B. Schlegel, D. Pum, U.B. Sleytr, M. Sára, *P. Natl. Acad. Sci.* 99 (2002) 4646-14651

[42] S. Dieluweit, D. Pum, U.B. Sleytr, W. Kautek, *Mat. Sci. Eng.* 25 (2005) 727-732.

Chapter 4

Influence of surface chemistry and protein concentration on adsorption rate and S-layer crystal formation

In this chapter we extend the investigation of SbpA adsorption and recrystallization to alkenothiol functionalized self assembly monolayers which differ in hydrophobicity and surface charge. Furthermore, the influence of the S-protein concentration in the protein adsorption kinetics is also studied in detail. In addition, to gain quantitative information of the mechanical properties of the S-layer, frequency and dissipation curves will be analyze with the Kelvin-Voigt model.

4.1 Introduction

The adsorption of proteins on surfaces has been widely studied due to the importance of protein-surface interactions in biological processes and bioengineering [1-3]. Adsorption of proteins on surfaces is a complex process that is generally associated with protein monomer conformational changes [4]. The control of the protein adsorption kinetics is crucial for protein function [5-7]. The final protein adlayer often depends on the adsorption rate that is influenced by different factors such as the protein concentration, salts, pH and the surface properties.

Self-assembled monolayers (SAMs) of alkanethiols are excellent model surfaces to study the interactions of proteins with organic surfaces because they form stable and

well defined organic layers on gold films [8]. In addition, they can be produced with a range of properties; the surface charge and hydrophilicity can be controlled by selecting appropriate thiols. The well-defined chemistry of the SAM layer makes it possible to obtain specific information about the forces that contribute to adsorption of a particular protein [9]. Surfaces can be tailored to promote specific interactions [10-13] or to promote resistance to proteins [14-16].

Crystalline bacterial cell surface layers, or S-layers, are the outermost envelope of prokaryotic organisms being the simplest biological membranes developed during evolution. They are composed of a single sort of protein or glycoprotein and show different lattice symmetries [17]. Isolated S-protein subunits have the intrinsic ability to reassemble on a wide variety of substrates [18-21]. Much work has been carried out showing the potential of S-proteins in biotechnology: one area of interest is the production of fusion proteins that will have both the S-layer ability to reassemble, and the properties of the fusion partner [22, 23].

In this work we have used the S-protein commonly called SbpA (*Lysinibacillus sphaericus CCM 2177*); monomers are nonglycosylated, have a molecular weight of 120 kDa and the protein crystal exhibits a square (p4) lattice symmetry with a spacing of about 13.1 nm between morphological units. The protein subunits are anisotropic where the outer part of the protein is neutral and smooth while the inner part is negatively charged and is more corrugated. The protein monolayer is 9 nm thick while the protein bilayer has a thickness of 15 nm [9].

Some studies have tackled the problem of the recrystallization kinetics at solid and soft interfaces at molecular level; however there are still some open questions concerning the recrystallization kinetics of S-proteins on functional thiols [9, 21, 24, 25]. Therefore we report how surface modification influences the protein adsorption rate and the formation of S-layer protein crystals. Gold substrates were functionalized with various alkanothiols of different hydrophobic properties and surface charge. Five kind of SAMs carrying methyl (CH_3), hydroxyl (OH), carboxylic acid (COOH) and mannose ($C_6H_{12}O_6$) terminal functional groups were used. Protein adsorption and S-layer formation were characterized by atomic force microscopy (AFM) while the adsorption kinetics study was carried out by quartz crystal microbalance with dissipation monitoring (QCM-D). The variation of the frequency and dissipation as a function of time obtained by QCM-D, were used to evaluate the adsorption rate and the viscoelastic properties of the adsorbed protein layer.

4.2 Materials and Methods

Materials

QCM-D gold substrates (Q-sense, Gothenburg, Sweden) were used as substrates. 1-dodecanethiol ($CH_3C_{11}S$, M_w. 202.4 g mol^{-1}), 1-hexanethiol (CH_3C_5S, M_w. 118.2 g mol^{-1}), 11-mercapto undecanoic acid ($COOHC_{10}S$, Mw. 218.4 g mol^{-1}), 11-mercapto-1-undecanol ($OHC_{11}S$, M_w. 204.4 g mol^{-1}) were purchase from Sigma-Aldrich. The mannose glycoconjugate, 5,5'-Dithio bis (penthyl-α-D-mannopyranoside) mixture with the corresponding thiol ($ManC_5S$, M_w. 282.4 g mol^{-1}), was prepared by a synthetic approach based on Fisher glycosylation [26, 27] (see appendix 4.1). Ethanol absolute (99%, Sharlau) and methanol (99.9%, Riedel-de Haen) were used to prepare thiol solutions. 2% sodium dodecyl sulphate (SDS) (99%, Fluka) was used as a cleaning solution.

The bacterial cell-surface layer protein, SbpA (molecular weight, 120 kDa), was isolated from *L. sphaericus CCM 2177* according to a reported procedure [28]. Protein recrystallization buffer was prepared with 0.5 mM Trizma base (Sigma) and 10 mM $CaCl_2$ (98%, Sigma) and adjusted to pH 9 by titration. Some experiments were carried out at pH 5 with and without calcium ions in solution. An aqueous solution of 100 mM NaCl (Sigma) was used as medium in AFM experiments.

Self assembly monolayer (SAM) preparation. Gold surfaces were cleaned in 2% SDS for 30 min, rinsed with ultrapure water (Barnstead), and dried under a stream of nitrogen. Afterwards, the substrates were cleaned with a UV/ozone cleaner (Bioforce Nanosciences) for another 30 min before the functionalization. All thiol solutions (1 mM) were prepared in ethanol absolute except the 1 mM mannose glycoconjugate which was prepared in methanol. The gold substrates were then immersed in the solutions and left overnight at room temperature.

S-protein preparation. The S-protein solution was isolated as explained elsewhere [28]. Due to the ability of S-proteins to self-assemble in solution, the protein solution (1 mg ml^{-1}) was centrifuged at 5000 rpm for 5 minutes to separate the S-protein monomers

from self-assembly products. Just before the experiments, the supernatant was diluted using the appropriate amount of recrystallizing buffer.

In QCM-D experiments S-protein adsorption was done in-situ. Once SAM substrates were placed inside flow chambers (Q-sense), and left to equilibrate with tris-buffer, SbpA was injected at maximum flow for 40 seconds and left to incubate overnight at 23ºC. Finally, the substrates were rinsed with recrystallizing buffer in order to remove any excess of protein. In the experiments, four different SbpA concentrations were used: 0.1 mg ml^{-1}, 0.05 mg ml^{-1}, 0.025 mg ml^{-1} and 0.0125 mg ml^{-1}.

In parallel, S-protein adsorption experiments were carried out ex-situ for AFM. 300 μl of protein solution was deposited on SAMs in small-volume humidity chambers, and incubated overnight and at room temperature. Afterwards, the substrates were rinsed with recrystallizing buffer in order to remove excess of protein.

Methods.

Contact Angle. In order to determine the wettability of the functionalized substrates, sessile-drop experiments were performed with a contact-angle measurement device (KRUSS D100, Hamburg, Germany). Millipore water (specific resistance 18.2 MΩ cm) was used as liquid phase. Three drops of water (2 μl) were deposited on each substrate. Table 4.1 summarizes the mean value of the contact angle for the five investigated substrates (see appendix 4.2) [29].

$CH_3C_{11}S$	$105^0\pm1$
CH_3C_5S	$100^0\pm2$
$COOHC_{10}S$	$44^0\pm1$
$OHC_{11}S$	$10^0\pm1$
$ManC_5S$	$<5^0$

(left axis label: Hydrophobic behaviour ↑)

Table 4.1. Contact angle values of $CH_3C_{11}S$, CH_3C_5S, $COOHC_{10}S$, $OHC_{11}S$, $ManC_5S$ functionalized gold substrates. The five substrates show different hydrophobic behaviour; $CH_3C_{11}S$ is the most hydrophobic substrate and $ManC_5S$ the most hydrophilic. The $COOHC_{10}S$ initial contact angle value is 20º, which increases to 44º once is exposed to air.

Quartz Crystal Microbalance with Dissipation monitoring (QCM-D). QCM-D (Q-sense E4, Gothenburg, Sweden) was used to carry out real-time/in situ experiments. QCM-D is a technique for simultaneous monitoring of the adsorbed mass per unit area

(by changes in resonant frequency) and layer viscoelasticity (by energy dissipation)[30]. The relation between the oscillating frequency change and the adsorbed mass is given by Sauerbrey equation (see chapter 2) which is valid under several assumptions given in [31].

A widely used model to evaluate the viscoelastic properties of adsorbed layers is the Kelvin-Voigt model. It relates the frequency shift (ΔF) and dissipation changes (ΔD) to the thickness, shear modulus and shear viscosity of the forming layer. The model assumes that the oscillatory quartz plate is covered by a viscoelastic film of uniform thickness and density that is in contact with a semi-infinite Newtonian liquid under no-slip conditions. QCM-D curves were analyzed with a commercial Q-tools program (Q-sense AB, Sweden) where the adsorbed film was modeled as a unique and uniform layer.

The overall viscoelasticity of the layers is represented by the ratio *G''/G'* of the layer's loss and storage moduli G_f.

$$G_f = G_f^{'} + iG_f^{''}$$

where the storage modulus, *G'*, is the same as film's shear elasticity modulus obtained by fitting the curves with the model. The loss modulus, *G''*, is calculated as the product of the sensing frequency (*f*) and the film's viscosity (η_f) which is obtained by modeling the film as the Kelvin-Voigt viscoelastic element and corresponds to the film's viscosity at the basic resonance frequency of 5 MHz [32, 33].

For the fitting of frequency and dissipation curves the protein layer thickness and density were kept constant. The thickness of 15 nm was attributed to a protein bilayer of a density value of (1.48 g cm^{-3}) [34]. In this way, the shear modulus and the shear viscosity of the protein layer were obtained.

Atomic Force Microscopy (AFM). Atomic force microscopy was performed using a Nanoscope V controller multimode AFM (Veeco, Santa Barbara, USA). The images were recorded in tapping mode, at 1 Hz in 100 mM NaCl aqueous solution at room temperature. Before use, the fluid cell was washed overnight with 2% SDS, rinsed thoroughly with ultrapure water, and dried with nitrogen. Silicon nitride (Si_3N_4) cantilevers of 0.1 N m^{-1} with sharpened tips (DNPS, Veeco) and gold-coated back sides were cleaned in ethanol and acetone before use. The image processing was performed with the Nanoscope v720 (Veeco) program and Image J (Java).

4.3 Results and discussion

4.3.1 Influence of surface chemistry in SbpA adsorption and S-layer formation

Figure 4.1 presents QCM-D results for SbpA adsorption kinetics on SAM-modified gold surfaces where frequency and dissipation are plotted as a function of time. The graph shows the change of frequency and dissipation on exposure of hydrophobic ($\theta=105°$) $CH_3C_{11}S$ and hydrophilic ($\theta=10°$) $OHC_{11}S$ SAM layers to protein solution (0.1 mg ml^{-1}) and subsequent rinsing steps.
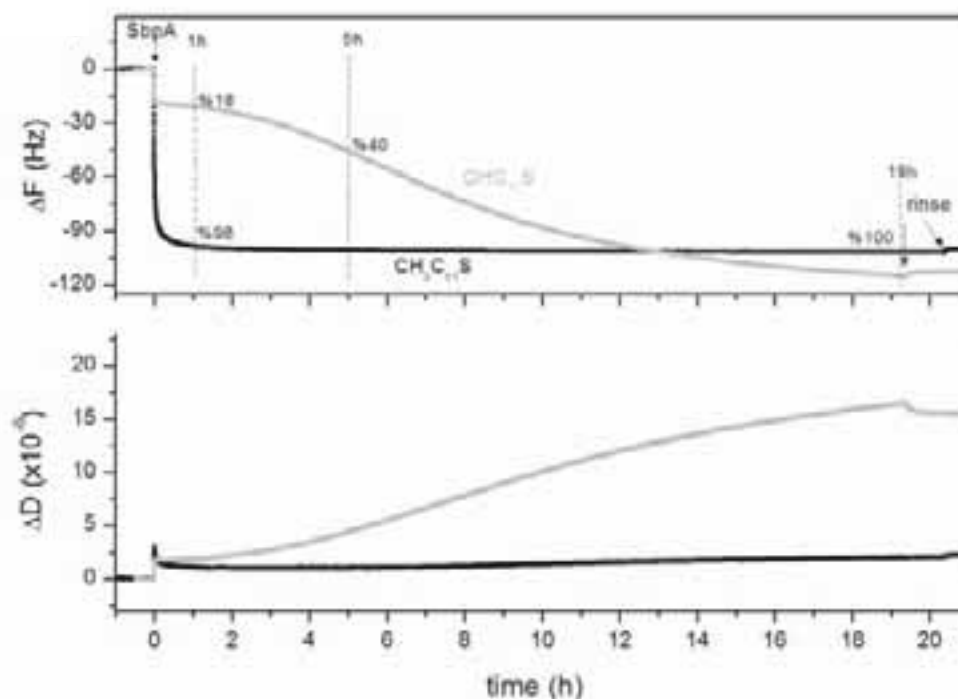
Figure 4.1. SbpA adsorption frequency and dissipation responses as a function of time on hydrophobic $CH_3C_{11}S$ and hydrophilic $OHC_{11}S$. At t=0 SbpA 0.1 mg ml^{-1} is injected and left overnight until is rinsed with tris-buffer solution. The values noted at 1 hour and 5 hours after the injection indicate adsorbed protein percentage with respect to the total adsorbed amount. Thus, after one hour of protein adsorption it is observed that on $CH_3C_{11}S$ 98% is adsorbed while on $OHC_{11}S$ just the 18%. Regarding the dissipation, it is observed that the protein layer on $OHC_{11}S$ is softer than on $CH_3C_{11}S$.

Since the SAMs are uncharged, the variation in protein adsorption (related to the variation in frequency) is only influenced by surface hydrophobicity. For instance, SbpA adsorption on hydrophobic $CH_3C_{11}S$ (black curve) reaches its steady state after 1 hour. The variation in frequency indicates that 98% of the maximum amount of mass

per unit area is adsorbed by this point (see figure 4.1). In addition, the increase in dissipation indicates the formation of a softer protein layer on hydrophobic thiol.

On the other hand, protein adsorption on hydrophilic $OHC_{11}S$ (grey curve) is a slower process although the final mass uptake per unit area is comparable to that observed on the hydrophobic substrate. It can be seen that after protein injection, a small change in frequency (-20 Hz) occurs. In the first hour only the 18% of the total mass uptake is seen. This percentage increased to 40% in the following five hours, indicating little protein affinity for the hydrophilic $OHC_{11}S$ substrate. Simultaneously, the dissipation increases to larger values (15×10^{-6}) than the ones obtained on other hydrophilic substrates, such as silicon oxide [21]. The changes in frequency and dissipation suggest that although there is protein adsorption, no crystal (S-layer) is formed.

Since QCM-D does not provide topographical information about the adsorbed protein layer, AFM was used to confirm the S-layer formation. Figure 4.2a and figure 4.2b refers to the protein layer adsorbed on $CH_3C_{11}S$ and $OHC_{11}S$ substrates, respectively. The 10×10 μm^2 images show that the protein layer on hydrophobic $CH_3C_{11}S$ substrate is more homogenous than on $OHC_{11}S$ substrate. This can be seen from the surface profile (white curve) and the vertical scale. However, these large images do not give valuable details about the nanostructure of the protein layer. A zoom of 1×1 μm^2 is therefore included on both images (located at the bottom right corner). Small protein crystal domains are only observed on hydrophobic $CH_3C_{11}S$ (figure 4.2a), while only random protein adsorption can be observed on hydrophilic $OHC_{11}S$ (figure 4.2b). This result is in agreement with QCM-D measurements: no protein crystal is formed on $OHC_{11}S$ substrate.
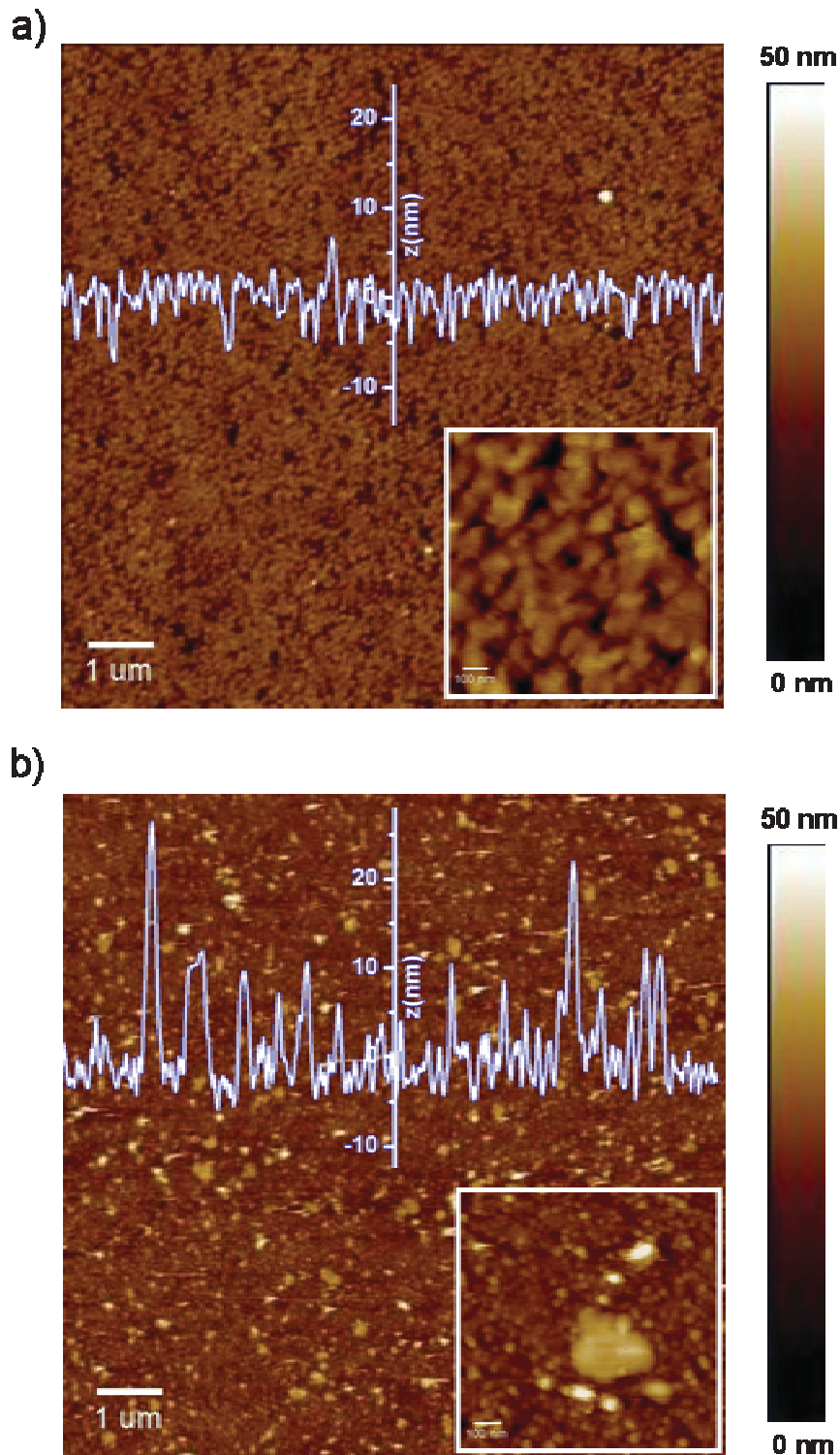
Figure 4.2. a) AFM height image of S-layer on $CH_3C_{11}S$ substrate, b) AFM height image of S-layer on $OHC_{11}S$ substrate. 10 x 10 μm^2 images illustrate the general overview of the S-layer while the bottom right insets (1 x 1 μm^2) show more detailed features of protein recrystallization. The z axis indicates the profile of the S-layer.

With numbers: the crystalline area of the S-layer recrystallized on $CH_3C_{11}S$ is 85%, being reduced to 4% on $OHC_{11}S$ for a protein sample concentration 0.1 mg ml^{-1}. Table 4.2 shows in detail the crystalline area, protein domain size, adsorbed mass density per unit area and roughness of the built S-layer on the five different substrates reported in this work.

A shorter hydrophobic thiol, CH_3C_5S, was used to study the influence of the chain length on S-protein recrystallization. In table 4.2 it can be seen that the crystalline area, protein domain, adsorbed mass density per unit area and surface roughness values are similar to the ones obtained when the longer hydrophobic thiol is the support for S-protein recrystallization (see appendix 4.3).

Additional experiments were carried out with a carboxyl-terminated thiol, $COOHC_{10}S$, to study the effect of the surface charge on S-protein adsorption at different pH values. While changing the pH, both substrate and protein will change their net charge; the isoelectric point of SbpA is about 4.69 [35].
The surface structure of the protein layer at pH 9 and pH 5 was studied with AFM and it is shown in figure 4.3a and figure 4.3b (1 x 1 μm^2). The figures show that in both cases the S-layer is formed of small protein domains that cover the majority of the surface (values in table 4.2).

Figure 4.3c and 4.3d shows the variation in frequency and dissipation for SbpA adsorption on $COOHC_{10}S$ at pH 9 and pH 5. In both cases, the frequency curve (black curve) indicates fast protein adsorption in a similar fashion as on $CH_3C_{11}S$ (the values for mass per unit area listed in table 4.2). However, at pH 5 the adsorption rate is two times slower than at pH 9. In fact, it is also observed that initial adsorption rate of SbpA on $COOHC_{10}S$ at pH 9 is two times faster than on $CH_3C_{11}S$ (see appendix 4.4).

The differences in dissipation curves support the idea that the pH affects the S-layer formation. It can be observed that the initial dissipation peak disappears when SbpA is adsorbed at pH 5. This effect (that also vanishes at lower concentration, see appendix 4.5) does not affect significantly S-layer formation. AFM images (figure 4.2a and 4.2b) demonstrate that the S-protein recrystallizes, implying that the recrystallization process might follow different pathways which are pH dependant.
Although the dissipation remains constant during the whole experiment at pH 5, significant variations were observed at pH 9. One hour after the injection at pH 9, the

dissipation reaches its steady state. At this point the dissipation is greater at pH 5 than at pH 9, which means that the S-layer formed at pH 5 is softer than the one at pH 9. Nevertheless, at pH 9, five hours after the injection, the dissipation increases considerably until the system is rinsed with buffer.

The increase in dissipation at pH 9 can be understood as a local variation of viscosity in the vicinity of the S-protein layer interface. This variation of viscosity would be caused by the self-assemblies formed from the excess of protein in solution. A similar effect was observed also on when SbpA (0.1 mg ml^{-1}) adsorbed on $CH_3C_{11}S$ and CH_3C_5S substrates, indicating that this bulk effect might primarily depend stronger on protein concentration than on substrate properties.

Experiments were carried out at pH 5 removing the calcium from the buffer. The results show that the protein is adsorbed and corroborate previous evidence that divalent ions are essential for protein recrystallization (see appendix 4.6).
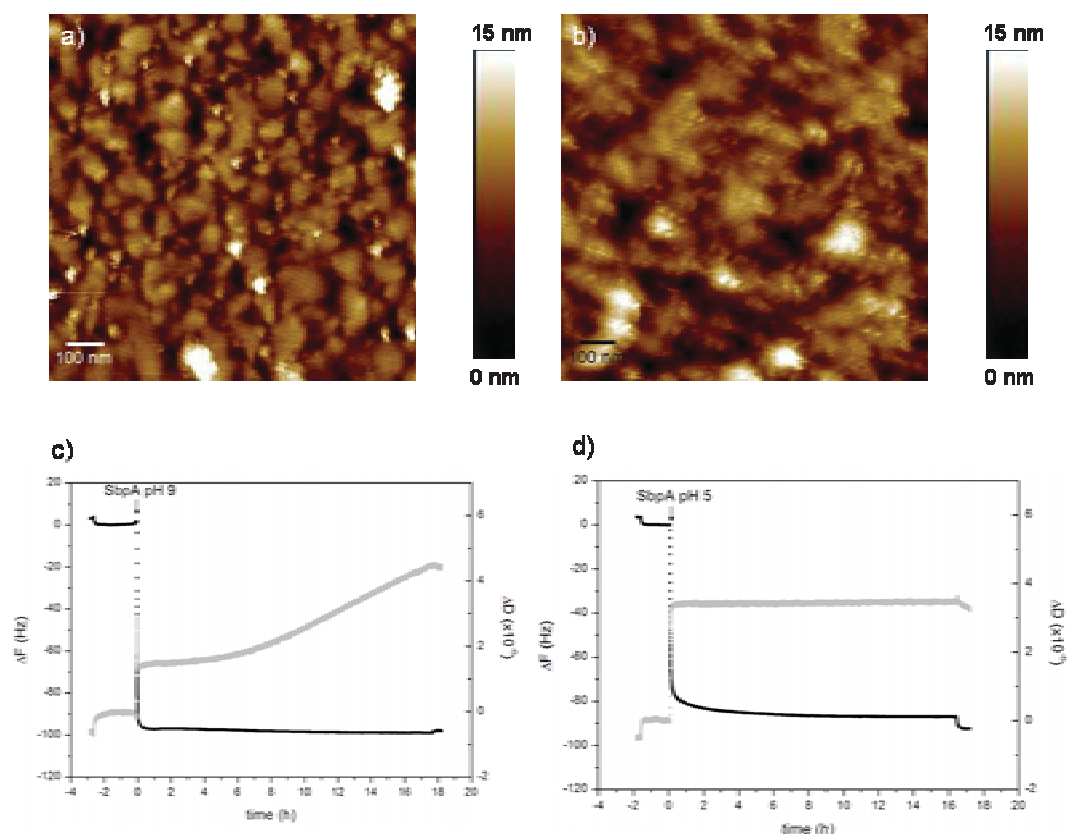
Figure 4.3. AFM height images of recrystallized SbpA on $COOHC_{10}S$ at a) pH 9 and b) pH 5 (1 x 1 µm^2). Frequency and dissipation curves as a function of time of SbpA adsorption on $COOHC_{10}S$ at c) pH 9 and d) pH 5.

The last of this group of experiments was carried out with a mannose-terminated thiol, since the natural support for SbpA is the secondary cell wall polymer (SCWP), composed by 2,3-dideoxydiacetamido mannosamine uronic acid [36, 37]. Contact angle measurements indicated that the surface functionalized with mannose is fairly hydrophilic (θ <5º). The adsorption kinetics of SbpA on $ManC_5S$ is faster than on $OHC_{11}S$ substrates. In this case the mass uptake per unit area is larger than the values obtained for $CH_3C_{11}S$, CH_3C_5S and $COOHC_{10}S$ (see table 4.2), which can be related to the formation of a protein bilayer (see appendix 4.7). Thus, although $OHC_{11}S$ and $ManC_5S$ are hydrophilic substrates, SbpA seems to interact stronger with the latter. Furthermore, the dissipation values obtained for SbpA adsorption on mannose are between the values obtained for hydrophobic (1×10^{-6}) and hydrophilic OH terminated substrates (15×10^{-6}) shown in figure 1a. Complementary AFM experiments show large crystalline protein domains on $ManC_5S$ substrates, which complied the 18% of the recrystallized area (see appendix 4.7). These measurements also show that the protein domains on $ManC_5S$ are significantly larger than the domains found on $OHC_{11}S$ substrates.

We can conclude that a mixture composed of amorphous protein and crystalline S-layers is found on $ManC_5S$ substrates. The outcome indicates that there is not specific interaction between SbpA and $ManC_5S$ like the one existing between SbpA and SCWP in bacteria; in fact, as AFM results showed, the majority of the adsorbed proteins could not formed crystalline layers.

Both substrates, $OHC_{11}S$ and $ManC_5S$, have OH groups distributed differently, which might be one of the reasons for dissimilar adsorption kinetics and protein crystal formation. Hence, $OHC_{11}S$ forms well packed SAMs assuring a homogenous distribution of hydroxyl groups. This homogeneity cannot be obtained in the case of $ManC_5S$ since mannose is a large molecule that may prevent the formation of a close-packed SAM.

4.3.2 SbpA concentration effect on the S-layer formation

Figure 4.4a and figure 4.4b depict the dissipation and frequency dependence for four protein concentrations on $CH_3C_{11}S$, CH_3C_5S, $COOHC_{10}S$, $OHC_{11}S$ and $ManC_5S$

substrates. In general, the higher the concentration the larger the adsorbed mass. However, there is a threshold concentration, 0.05 mg ml^{-1}, for maximum protein adsorption on $CH_3C_{11}S$, CH_3C_5S, $COOHC_{10}S$ substrates. In the cases of $OHC_{11}S$ and $ManC_5S$ substrates, the adsorbed mass density increases with the concentration showing a quasi linear behavior of protein adsorption, being very low at 0.0125 mg ml^{-1} (figure 4.4a).
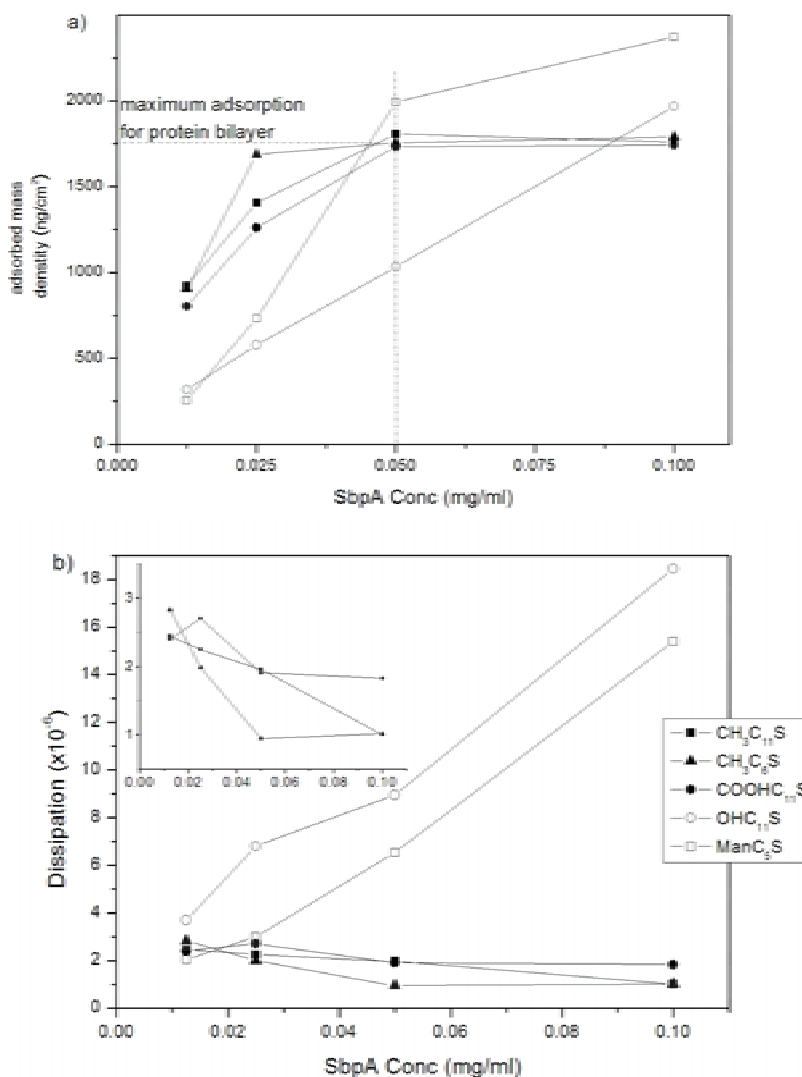

Figure 4.4. a) SbpA adsorbed mass density and b) dissipation as a function of SbpA concentration for $CH_3C_{11}S$, CH_3C_5S, $COOHC_{10}S$, $OHC_{11}S$ and $ManC_5S$ measured by QCM-D. The black spots indicate the SAMs where SbpA is recrystallized while the white spots indicate the surface where SbpA follows different adsorption pathways. a) 0.05 mg ml^{-1} is the minimum protein concentration for obtaining the maximum adsorption on $CH_3C_{11}S$, CH_3C_5S, $COOHC_{10}S$. b) The inset is a zoom of the dissipation values of $CH_3C_{11}S$, CH_3C_5S, $COOHC_{10}S$. The dissipation values correspond to the first five hours of adsorption.

Figure 4.4b shows the dissipation as a function of protein concentration. On $OHC_{11}S$ and $ManC_5S$ substrates, the dissipation varies linearly with the concentration. Although there is protein adsorption no crystal formation is achieved. It can be observed that on $CH_3C_{11}S$, CH_3C_5S and $COOHC_{10}S$ substrates the protein layer dissipates more energy at concentrations lower than 0.05 mg ml^{-1}, due probably to incomplete layer formation. Above this concentration the dissipation drops, corresponding to the maximum protein adsorption and the formation of a more rigid layer.

Figure 4.5 reports AFM height images of the S-layer structure at four different protein concentrations on $CH_3C_{11}S$ substrates. At the highest concentration (0.1 mg ml^{-1}), 90% of the surface is covered by a crystalline layer. As the concentration drops, more holes are found between the different protein domains, increasing the surface roughness (see table 4.2). This is also corroborated with the profile analysis (white line) which shows the presence of various adlayers at 0.025 mg ml^{-1} and 0.0125 mg ml^{-1}. In this way it was possible to distinguish between the thickness of a protein monolayer (about 8 nm) and a protein bilayer (15 nm). This indicates that SbpA is adsorbed as a monomer from solution, and not as a dimer.

In addition, the histograms show the decrease in protein domain size as the protein concentration is diminished, with 0.007 μm^2 and 0.003 μm^2 being the maximum and the minimum values respectively[m]. In the case of $COOHC_{10}S$ substrate it is observed that the coverage decreases with the concentration remaining the protein domain size constant (see appendix 4.8).

S-layer formation starts through initial nucleation points, at that moment the substrate protein interaction is crucial. However, for protein domain growth, protein-protein interactions should be also taken into account. The size of the protein domains will depend partly on the interplay between these two driving forces [21]. This would be the case for $COOHC_{10}S$ substrate: once enough nucleation points are formed, the protein-protein interaction seems to dominate over the protein-surface interaction.

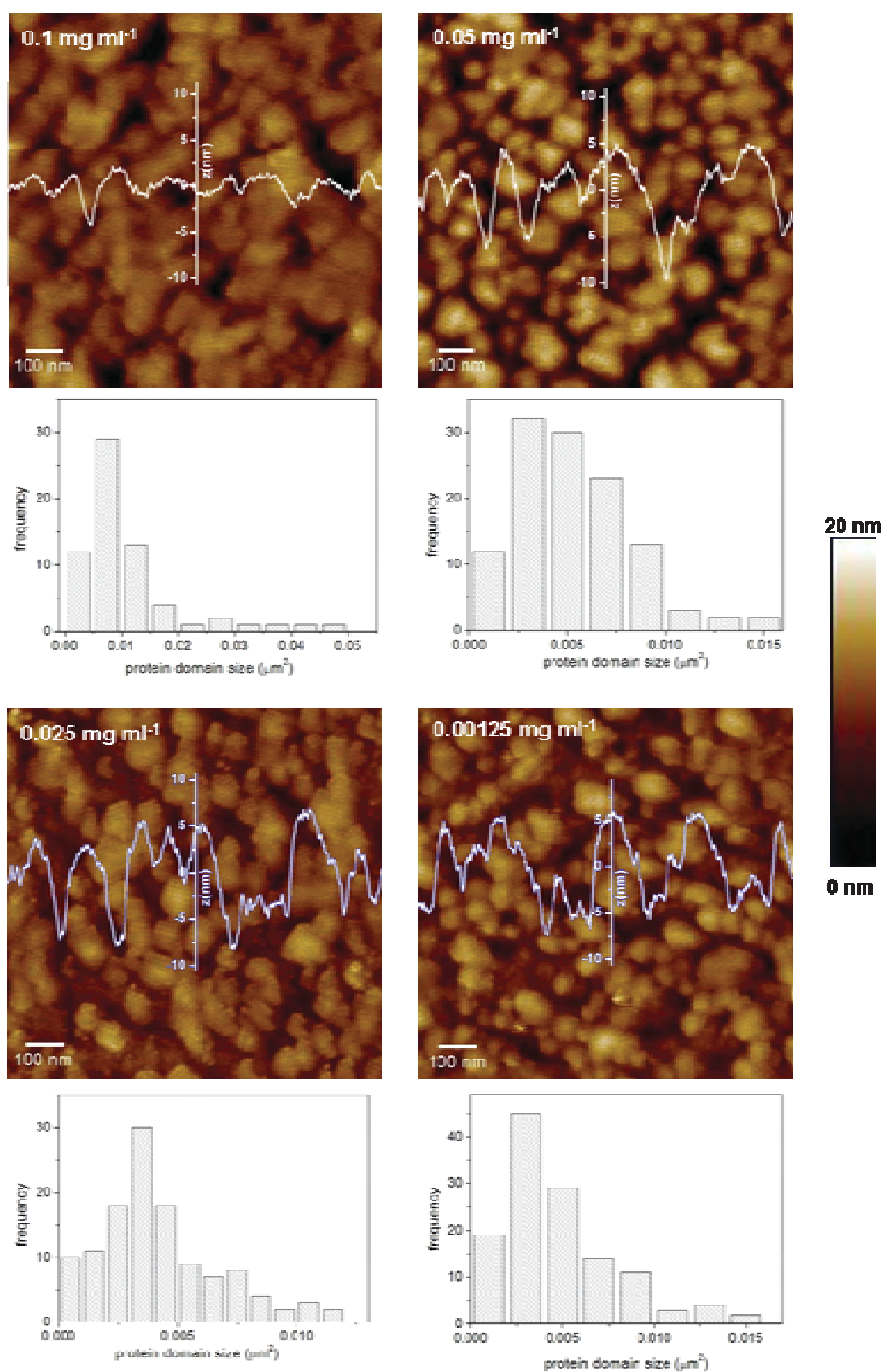[m] These values refer to the most repeated values in the histogram.

Figure 4.5. AFM height images of the S-layer on $CH_3C_{11}S$ at different concentrations: 0.1 mg ml^{-1}, 0.05 mg ml^{-1}, 0.0125 mg ml^{-1} and 0.0125 mg ml^{-1} with their respective profile. At the bottom of each AFM image are the histograms of protein domain size distribution.

SAM	[SbpA] (mg/ml)	crystalline area (%)	protein domain (μm^2)	Mass density (ng cm^{-2})	roughness (nm)
CH$_3$C$_{11}$S	0.1	85	0.010	1760	1.9
	0.05	69	0.005	1805	3.2
	0.025	56	0.004	1406	3.4
	0.0125	61	0.004	1045	3.1
CH$_3$C$_5$S	0.1	73	0.008	1789	2.3
	0.05	63	0.006	1755	3.7
	0.025	64	0.004	1687	3.6
	0.0125	64	0.002	977	2.8
COOHC$_{10}$S pH 9	0.1	90	0.009	1741	1.8
	0.05	75	0.007	1734	1.8
	0.025	61	0.008	1261	2.7
	0.0125	62	0.007	804	2.8
pH 5	0.1	65	0.006	1504	1.9
OHC$_{11}$S	0.1	4	0.010	1982	3.8
	0.0125	no crystals	no domains	248	2.7
ManC$_5$S	0.1	18	0.390	2036	6.2
	0.0125	no crystals	no domains	230	2.4

Table 4.2. S-layer crystalline area, protein domain size and roughness measured from AFM images for layers formed on CH$_3$C$_{11}$S, CH$_3$C$_5$S, COOHC$_{10}$S, OHC$_{11}$S, ManC$_5$S at four different concentrations. The mass density was obtained from QMC-D measurements.

4.3.3 *S-layer mechanical properties*

This section is devoted to elucidate the mechanical properties of the adsorbed protein layer. Figure 4.6 shows the relationship between the adsorbed mass per unit area (change in frequency) and the viscoelastic properties of the protein layer (change in dissipation). In figure 4.6 the frequency/dissipation (F/D) curves for protein adsorption on CH$_3$C$_{11}$S and OHC$_{11}$S substrates show clear differences in the viscoelastic properties. On one hand, it can be observed that for SbpA adsorbed on OHC$_{11}$S substrate the dissipation increases continuously with frequency, which means that a soft layer is formed while the protein is adsorbing on the surface. In fact, AFM images demonstrate that small crystals are formed but just cover 4% of the surface. This shows that in the mechanical behavior is related to the protein layer structure.

On the other hand, on $CH_3C_{11}S$ substrates the F/D curve presents another trend. In the first part of the curve the dissipation increases with frequency, reaching a maximum value (around -60 Hz), followed by a decrease in dissipation with further protein adsorption. The first part may be related to purely protein adsorption while the second part might be associated with the formation of the protein layer crystal, which should dissipate less energy than the single adsorbed proteins.
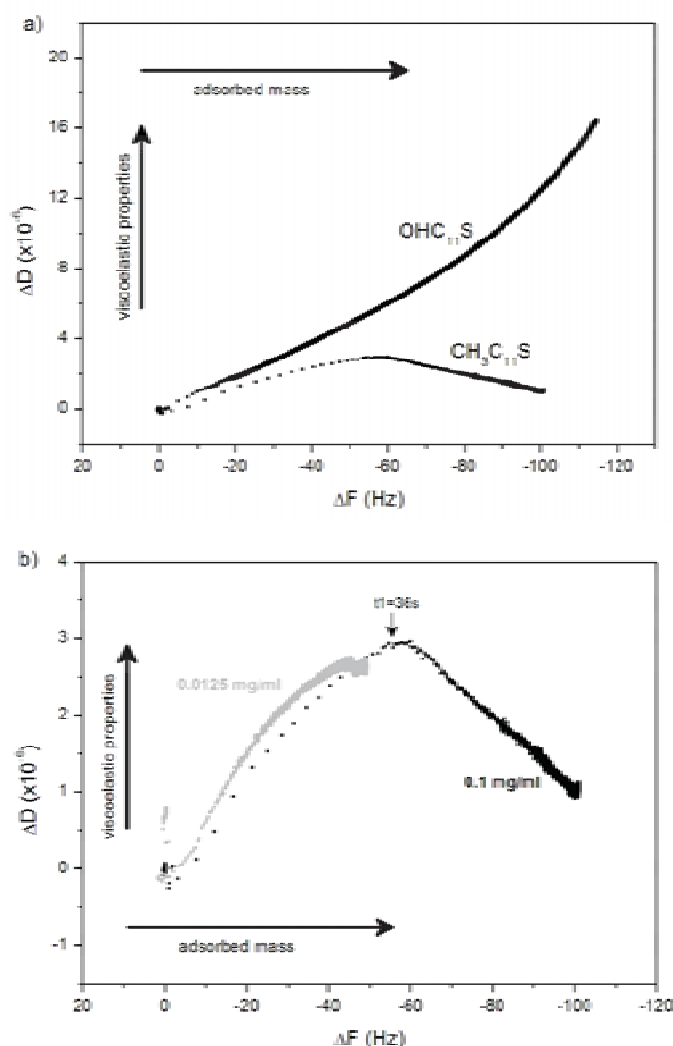

Figure 4.6. a) Frequency-Dissipation curves of hydrophobic $CH_3C_{11}S$ and hydrophilic $OHC_{11}S$ at constant protein concentrations, b) frequency-Dissipation curves of hydrophobic $CH_3C_{11}S$ for 0.1 mg ml^{-1} (black), and 0.0125 mg ml^{-1} (grey). The time, t_1, indicates the maximum dissipation point that is related with the start of the self assembly process of SbpA for 0.1 mg ml^{-1}. The F/D shown for $CH_3C_{11}S$ corresponds to the first five hours of the adsorption process while for $OHC_{11}S$ the complete time range is shown.

Figure 4.6b shows the effect of the concentration for protein adsorption on $CH_3C_{11}S$ substrate. The black line corresponds to a protein concentration of 0.1 mg ml^{-}

[1] and has been described in this paper and the grey line refers to a protein concentration of 0.00125 mg ml^{-1}. In this case, the maximum in dissipation indicates a greater change (-50 Hz). Immediately after the maximum, the protein layer is formed since there is no subsequent frequency variation (and therefore no additional protein adsorption). As table 4.2 shows, the adsorbed protein mass per unit area is 60% less than for the highest protein concentration. This leads to incomplete surface layer coverage and therefore to an increase of the final dissipation value (see appendix 4.9).

To gain quantitative information about the mechanical properties of the protein layer formed on the COOHC$_{10}$S substrate, the frequency and dissipation curves were analyzed with the Voigt model [33]. In this model, the adsorbed protein is modeled as a uniform layer. The fitting procedure was only carried out for the highest concentration (0.1 mg ml^{-1}) and in the case of pH 9 (only the first five hours of protein adsorption were considered, once the frequency variation was constant with time). Fixed values of protein layer density (1.4 g cm^{-3}) and thickness (15 nm) were introduced in the algorithm to obtain the best fit for viscosity and the shear modulus (see appendix 4.10) [34] .

COOHC$_{10}$S	Density (ng cm^{-3})	Thickness (nm)	Viscosity (Kg m^{-1} s^{-1})	Shear modulus (Pa)	Overall viscoelasicity
pH 9	1400	15	0.0057 ± 0.0001	1.50 x 10^5 ± 6x10^3	0.19
pH 5	1400	15	0.0033 ± 0.0001	1.14 x 10^5 ± 9x10^3	0.15

Table 4.3. Adsorbed protein layer density, thickness, viscosity, shear modulus, overall viscoelasticity (G''/G') and the fitting error calculated with Kelvin-Voigt model for COOHC$_{10}$S at pH 9 and pH 5.

According to table 4.3, the viscosity of the adsorbed layer decreases with the pH, whereas it varies from (5.7 x 10^{-3}) Kg m^{-1}s^{-1} for pH 9 to (3.3 x 10^{-3}) Kg m^{-1}s^{-1} for pH 5. The drop-off in viscosity at pH 5 might be caused due to the reduction in the adsorbed mass which also affects the crystalline protein domain size. However, a negligible change is observed for shear modulus and overall viscoelasticity (G''/G') meaning that the layers have similar mechanical properties. Viscosity, shear modulus and the overall viscoelasticity results are comparable with the ones reported for other proteins such as lysozyme or mucin [38].

4.4 Conclusions

Protein adsorption is faster on uncharged hydrophobic substrates ($CH_3C_{11}S$ and CH_3C_5S) than on hydrophilic $OHC_{11}S$ ones. Small S-layer domains were observed on hydrophobic ($CH_3C_{11}S$ and CH_3C_5S), while on $OHC_{11}S$ substrates the protein adsorbs without formation of crystalline layers. The interaction of SbpA with another hydrophilic surface made out of $ManC_5S$ led to partial S-layer recrystallization, but no specific carbohydrate/protein interaction was observed. However, the adsorption rate could be tuned by electrostatic interactions between the SbpA and $COOHC_{10}S$ substrate by decreasing the pH from 9 to 5, inducing different S-layer recrystallization pathways. The protein crystal domain size depends on concentration and surface chemistry.

For hydrophobic substrates ($CH_3C_{11}S$ and CH_3C_5S) crystalline domain area increases with concentration, while for $COOHC_{10}S$ substrates the domain size does not vary with protein concentration. Thus, protein-surface interactions dominate on hydrophobic surfaces at low concentrations, while for $COOHC_{10}S$ substrates, after the formation of the nucleation points, protein-protein interactions are predominant. These experiments also showed that the threshold concentration for maximum SbpA adsorption on $CH_3C_{11}S$, CH_3C_5S and $COOHC_{10}S$ substrates was 0.05 mg ml^{-1}. The shear modulus and the viscosity of the recrystallized S-layer on $COOHC_{10}S$ substrate were obtained and did not vary significantly with pH.

4.5 References

[1]   B. Kasemo, *Biol. Surf. Sci.* 500 (2002) 656-677.

[2]   N.K. Chaki, K. Vijayamchanan, *Biosens. Bioelectron.* 17 (2002) 1-12.

[3]   Y. Arima, H. Iwata, *Biomaterials* 28 (2007) 3074-3082.

[4]   D.E. Otzen, M. Oliveberg, F. Höök, *Colloid Surface B* 29 (2003) 67-73.

[5]   G.V. Lubarsky, M.M. Browne, S.A. Mitchell, M.R. Davidson, R.H. Bradley, *Colloid Surface B* 44 (2005) 56-63.

[6]   J.W. Yi Lin, L.-J. Wan, X.-H. Fang, *Ultramicroscopy* 105 (2005) 129-136.

[7]   J.H. Teichroeb, J.A. Forrest, L.W. Jones, J. Chan, K. Dalton, *J. Colloid Interf. Sci.* 325 (2008) 157-164.

[8]   K.L. Prime, G.M. Whitesides, *Science* 252 (1991) 1164-1167.

[9]   S. Moreno-Flores, A. Kasry, H.-J. Butt, C. Vavilala, M. Schmittel, D. Pum, U.B. Sleytr, J.L. Toca-Herrera, *Angew. Chem. Int. Edit*. 47 (2008) 4707-4717.

[10]   A.J. Pertsin, M. Grunze, *Langmuir* 16 (2000) 8829-8841.

[11]   Y.-Y. Luk, M. Kato, M. Mrksich, *Langmuir* 16 (2000) 9604-9608.

[12]   S.N. Rodrigues, I.C. Gonçalves, M.C.L. Martins, M.A. Barbosa, B.D. Ratner, *Biomaterials* 27 (2006) 5357-5367.

[13]   C. Hoffmann, G.E.M. Tovar, *J. Colloid Interf. Sci.* 295 (2006) 427-435.

[14]   R.G. Chapman, E. Ostuni, S. Takayama, R.E. Holmlin, L. Yan, G.M. Whitesides, *J. Am. Chem. Soc.* 122 (2000) 8303-8304.

[15]   V. Silin, H. Weetall, D.J. Vanderah, *J. Colloid Interf. Sci.* 185 (1997) 94-103.

[16]   M. Mrksich, G.B. Sigal, G.M. Whitesides, *Langmuir* 11 (1995) 4383-4385.

[17]   U.B. Sleytr, P. Messner, D. Pum, M. Sára, *Angew. Chem. Int. Edit.* 38 (1999) 1034-1054.

[18]   J.L. Toca-Herrera, R. Krastev, V. Bosio, S. Küpcü, D. Pum, A. Fery, M. Sára, U.B. Sleytr, *Small* 1 (2005) 339-348.

[19]   A. Martín-Molina, S. Moreno-Flores, E. Perez, D. Pum, U.B. Sleytr, J.L. Toca-Herrera, *Biophys. J.* 90 (2006) 1821-1829.

[20]   M. Delcea, R. Krastev, T. Gutlebert, D. Pum, U.B. Sleytr, J.L. Toca-Herrera, *J. Nanosci. Nanotechno.* 7 (2007) 4260-4266.

[21]   A. Eleta-Lopez, S. Moreno-Flores, D. Pum, U.B. Sleytr, J.L. Toca-Herrera, *Small* 6 (2010) 396-403.

[22]   U.B. Sleytr, C. Huber, N. Ilk, D. Pum, B. Schuster, E.M. Egelseer, *FEMS Microbiol. Lett.* 267 (2007) 131-144.

[23]   U.B. Sleytr, E.M. Egelseer, N. Ilk, D. Pum, B. Schuster, *FEBS Lett.* 274 (2007) 323-334.

[24]   E.S. Györvary, O. Stein, D. Pum, U.B. Sleytr, *J. Microsc.* 212 (2003) 300-306.

[25]   S. Chung, S.-H. Shin, C.R. Bertozzi, J.J.D. Yoreo, *P. Natl. Acad. Sci.* 107 (2010) 16536-16541.

[26]   B. Fraser-Reid, U.E. Udodong, H.O. Z. Wu, J.R. Merritt, C.S. Rao, C. Roberts, R. Madsen, *Synlett.* (1992) 927-929.

[27]   C.-C. Lin, Y.-C. Yeh, C.-Y. Yang, C.-L. Chen, G.-F. Chen, C.-C. Chen, Y.-C. Wu, *J. Am. Chem. Soc.* 124 (2002) 3508-3509.

[28]   U.B. Sleytr, M. Sára, Z. Küpcü, P. Messner, *Arch. Microbiol.* 146 (1986) 19-24.

[29]   C.D. Bain, J. Evall, G.M. Whitesides, *J. Am. Chem. Soc.* 111 (1989) 7155-7164.

[30]   M. Rodahl, F. Höök, A. Krozer, P. Brzezinski, B. Kasemo, *Rev. Sci. Instrum.* 66 (1995) 3924-3930

[31]   K. Gläsmäster, C. Larsson, F. Höök, B. Kasemo, *J. Colloid Interf. Sci.* 246 (2002) 40-47.

[32]   M.V. Voinova, M. Rodahl, M. Jonson, B. Kasemo, *Phys. Scripta* 59 (1999) 391-394.

[33]   T.J. Halthur, T. Arnebrant, L. Macakova, A. Feiler, *Langmuir* 26 (2010) 4901-4908.

[34]   E.M. Egelseer, K. Leitner, M. Jarosch, C. Hotzy, S. Zayni, U.B. Sleytr, M. Sára, *J. Bacteriol.* 180 (1998) 1488-1495.

[35]   M. Delcea, R. Krastev, T. Gutlebert, D. Pum, U.B. Sleytr, J.L. Toca-Herrera, *Soft Matter* 4 (2008) 1414-1421.

[36]   N. Ilk, C. Cöllenkle, E.M. Egelseer, A. breitwieser, U.B. Sleytr, M. Sára, *Appl. Environ. Microb.* 68 (2002) 3251-3260.

[37]   J.L. Toca-Herrera, S. Moreno-Flores, J. Friedmand, D. Pum, U.B. Sleytr, *Microsc. Res. Techniq.* 65 (2004) 226-234.

[38]   S. Paul, D. Paul, T. Basova, A.K. Ray, *J. Phys. Chem.* 112 (2008) 11822-11830.

Chapter 5

Bacterial S-layer recrystallization on biocompatible polylactide derivative films

In chapters 3rd and 4th we studied the recrystallization of SbpA on SAMs of well defined chemistry. In this chapter we report the recrystallization behaviour of SbpA on biocompatible polymer films that consist of polylactide derivatives. In this case, the physical properties (crystalline state and glass transition temperature (T_g)) will determine the adsorption rate kinetics as well as the final structure of the S-layer.

5.1 Introduction

In recent years, essential work has been carried out on the study of the interaction between proteins and biodegradable synthetic polymers which have great importance in biomedical and pharmaceutical applications. Examples of such applications include implant materials development as a scaffold in tissue engineering and new controlled drug delivery systems [1].

Protein adsorption and self-assembly mechanisms are an important issue in bionanotechnology laboratories. Both processes play a leading roll in protein conformation, orientation and functionality. Furthermore, the understanding and control of self-assembly mechanisms are crucial to create functional supramolecular structures [2, 3]. For example, it has been demonstrated that protein conformation affects the

immune response and inflammatory cell recruitment [4]. This fact is strongly related to the mechanical properties of the substrate that host the proteins, such us biocompatible polymers [5].

In our case we have chosen polylactic acid derivatives as support for the recrystallization of bacterial proteins due to their biocompatible properties and biomedical use. In particular we have worked with the following polymers: Poly(L-lactide) (PLLA), Poly(L,D-lactide) (PDLLA), Poly(lactide-co-glycolide) (PLGA) and Poly(lactide-co-caprolactone) (PLCL). The composition of repeat units and its arrangement in polylactide copolymers determines not only the physico-chemical properties but also the biodegradability and mechanical behaviour of the different studied systems. The monomer of such polymers, the lactic acid (2-Hydroxypropionic acid), presents a chiral carbon atom, which provides different possibilities of optical activity and crystallinity [6-8]. In particular PLLA is a semicrystalline polymer while the three other polymers are amorphous. These three polymers were chosen to evaluate the influence of temperature glass transition (T_g) and phase behaviour on protein recrystallization [9, 10].

As we have shown in the previous chapters the bacterial protein SbpA from *Lysinibacillus sphaericus* CCM 2177 is a good candidate to build biomimetic supramolecular structures due to its intrinsic self-assembly properties. In fact, SbpA forms crystalline and symmetric molecular layers of square symmetry lattice with a center-to-center spacing between tetrameric units of 13.1 nm [11-16]. These protein layers are commonly called S-layers, which in nature constitute the outermost envelope component in prokaryotic organisms, playing an important role in the protection of the organisms against extreme environmental conditions [17-20].

Moreover, in the last ten years bacterial proteins have been used as building blocks for the so called S-layer fusion proteins that have constituted a big step in nanobiotechnology [21-25]. Therefore, it is crucial to understand and control protein-surface interaction as well as the protein self-assembly that leads to protein crystal formation.

In more detail, we have investigated the interaction and protein crystal formation between some of the varieties of lactic acid based polymers with bacterial SbpA (S-protein).

Two main experimental techniques have been used to characterize the SbpA adsorption on polylactide supports and the nanostructure of the final biomimetic supramolecular structure. On one hand, Quartz Crystal Microbalance with Dissipation monitoring (QCM-D) was used to determine the protein kinetics, mass uptake, and viscoelastic layer properties. On the other hand, Atomic Force Microscopy (AFM) was utilized to obtain the lattice parameters and the protein domain size.

5.2 Materials and methods

Materials

Poly(L-lactide) (PLLA), Poly(L,D-lactide) (PDLLA), Poly(lactide-co-glycolide) (PLGA) and Poly (lactide-co-caprolactone) (PLCL) were supplied by Purac Biochem (The Netherlands)[n]. The polymers were used without further modification. See figure 5.1 to envisage their chemical structure.

The bacterial cell-surface layer protein, SbpA (molecular weight, 120 kDa), was isolated from *Lysinibacillus sphaericus* CCM 2177 according to a reported procedure [26]. Protein recrystallization buffer was prepared with 5 mM Trizma base (Sigma) and 10 mM $CaCl_2$ (98%, Sigma) and adjusted to pH 9. Sodium dodecyl sulphate 2% (SDS) (99%, Fluka), was used as a cleaning solution for that. Aqueous solution of 100 mM NaCl (Sigma) was used as media in AFM experiments.

AFM sample mounting disks and gold coated quartz crystals (Q-sense, Gothenburg, Sweden) were used as polymer/protein supports for AFM and QCM-D experiments, respectively. Chloroform (99.9%, Sigma) was used to prepare the polymer solutions.

---

[n] *http://www.purac.com/Purac-Biomaterials/Products/Polymers-for-medical-devices.aspx*
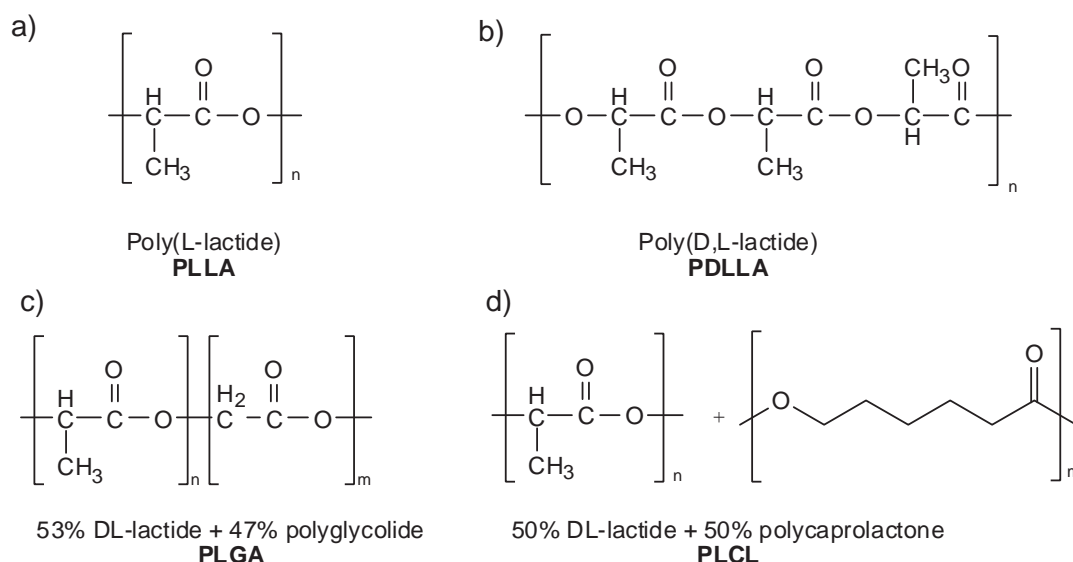
Figure 5.1. Chemical structures of: a) PLLA, b) PDLLA, c) PLGA and d) PLCL.

Polymer film preparation. Two methods were used to prepare polymer films. In the casting method all polymers were dissolved in chloroform at a polymer concentration 2.5 wt %. Then, the solutions were poured into steel dishes and dried at room temperature. These films were used as substrates for protein crystallization analysis by AFM. On the other hand, spin coating was used to prepare thin polymer films for protein adsorption studies by QCM-D. Gold QCM-D sensors were cleaned for 30 minutes with SDS 2%, and after rinsing with water and drying under a nitrogen stream they were exposed for 30 minutes to UV-ozone. Afterwards, the clean gold substrates were spin-coated with 40 µl of 5 mg ml^{-1} polymer solution (in chloroform). The sensors were spin coated for 20 seconds at 4000 rpm and used immediately for experiments.

S-protein self-assembly. The S-protein solution was isolated as explained in reference [26]. Due to the ability of S-proteins to self-assemble in solution, the protein-extract solution (1 mg ml^{-1}) was centrifuged at 5000 rpm for 5 minutes to separate the S-protein monomers from self-assembly products. Just before the experiments, the supernatant was diluted using the appropriate amount of recrystallizing buffer.

The S-protein assembly for AFM experiments was done ex-situ. 300 µl of protein solution at 0.1 mg ml^{-1} was deposited on polymer-coated supports for 12 hours, at room temperature into small-volume humidity chambers, which were used to prevent water evaporation. Afterwards, the substrates were rinsed with water in order to remove excess of protein.

In QCM-D experiments the S-protein assembly was done in-situ. The sensor/polymer systems were placed inside flow chambers (Q-sense). Tris-buffer was then injected and the system was left to equilibrate. Later, SbpA 0.1 mg ml^{-1} was injected into the chamber, at maximum flow for 40 seconds and let incubate for 12 hour at 23ºC. Finally, the substrates were rinsed with recrystallizing buffer in order to remove excess of protein.

Methods

Contact angle. Sessile drop experiments were performed with a contact angle measurements device (KRUSS D100, Hamburg, Germany). Millipore water (specific resistance 18.2 MΩ cm^{-1}) was used as the liquid phase. A drop of 2 µl of water was deposited on the polymer supports and the contact angles were obtained from the drop profiles.

Atomic Force Microscopy (AFM) was performed using Nanoscope V controller multimode AFM (Veeco, Santa Barbara, USA). The images were recorded in tapping mode at 1 Hz in 100 mM NaCl aqueous solution at room temperature. Before use, the fluid cell was washed overnight with 2% SDS, rinsed thoroughly with ultrapure water, and dried with nitrogen. Silicon nitride (Si_3N_4) cantilevers of 0.32 N m^{-1} with sharpened tips (DNPS, Veeco) and gold- coated back sides were cleaned in ethanol and acetone before use. The image processing was performed with the v720 (Veeco) and ImageJ (Java) programs.

Quartz Crystal Microbalance with Dissipation monitoring (QCM-D). QCM-D (Q-sense, Gothenburg, Sweden) was used to carry out real time experiments. QCM-D is a well established technique for simultaneous monitoring of mass adsorption and energy dissipation from changes in the resonant frequency and the damping of a vibrating sensor. This sensor consists of thin AT-cut piezoelectric quartz crystals sandwiched between two electrodes. The fundamental frequency (f_0) of the crystal is 5 MHz. The Sauerbrey equation was used to calculate the adsorbed mass per unit area [27, 28].

5.3 Results and discussion

Figure 5.2 shows AFM height images of the surface topography of polylactide derivatives films. The images size is 500 x 500 nm^2 and the vertical scale ranges from 10 nm to 15 nm. After imaging analysis we calculate the surface roughness[o] (see table 5.1). The results show that PDLLA films have the highest roughness value (1.95 nm) while the lowest values is obtained for PLCL (0.45 nm). The hydrophobicity of the polymer films have also been characterized by contact angle measurements (see table 5.1). The contact angle is similar for all the polymer surfaces and does not depend on the surface roughness. In the former chapters we have shown that the protein adsorption kinetics was faster on hydrophobic surfaces than on hydrophilic ones. In this case, the main parameter which will affect the protein adsorption and protein crystal formation might be the crystalline state of the polymers and the glass transition temperature (T_g). Concerning the polymers crystalline state, PLLA is semicrystalline while the copolymers are amorphous. The T_g of PLCL is about 15ºC smaller than experimental temperature (23ºC). This might imply that the protein adsorption could be influenced by the polymer change conformation due to molecular motion. The T_g of the polymers are shown in table 5.1 (paper in preparation).

Polymer support	T_g (ºC)	θ(º)	R_q (nm)
PLLA	63	82	1.20±0.18
PDLLA	53	83	1.95±0.29
PLGA	49	80	1.16±0.04
PLCL	15	81	0.45±0.05

Table 5.1. PLLA, PDLLA, PLGA and PLCL films properties; glass transition temperature (T_g), contact angle (θ) and roughness (R_q). The roughness was calculated from AFM height images.

---

[o] $Rq=[\sum(Xi-Xmean)^2 N^{-1}]^{1/2}$, i=1….N
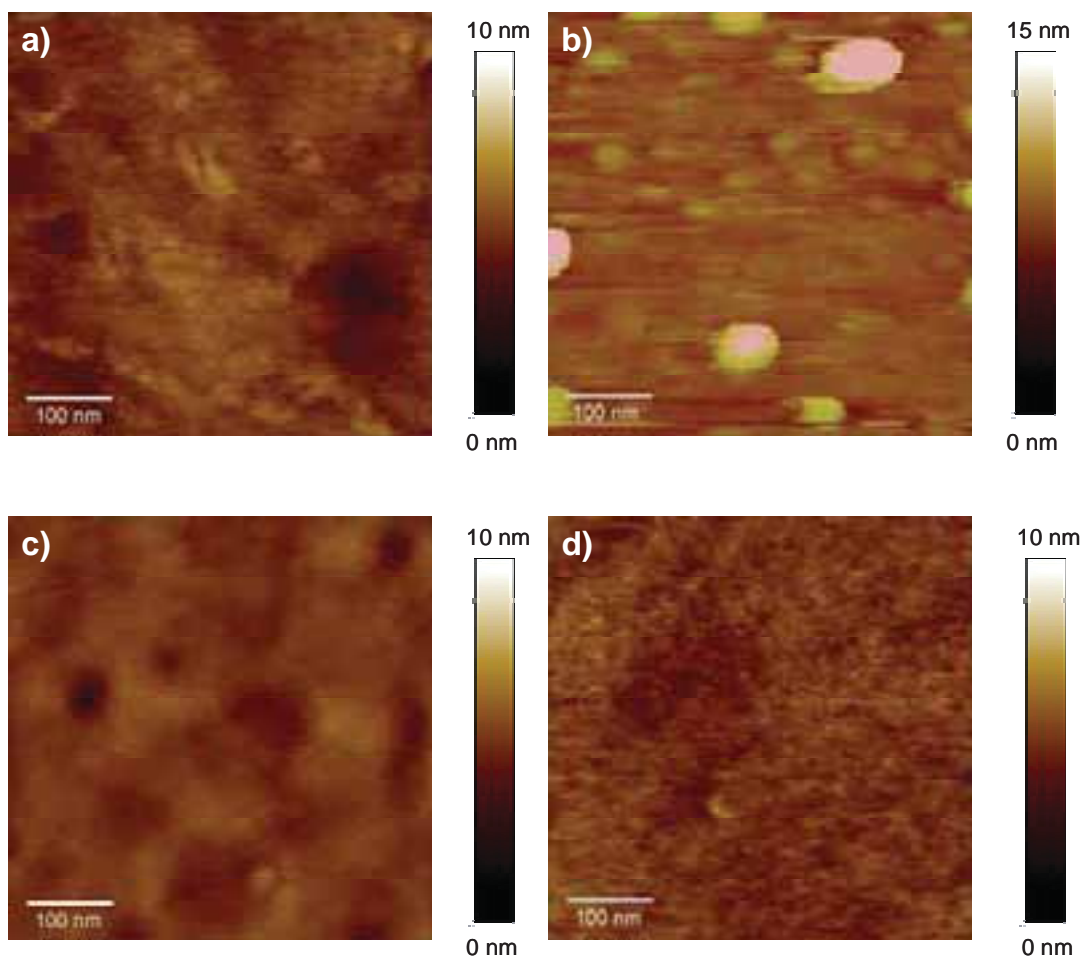
Figure 5.2. AFM topographical images of a) PLLA, b) PDLLA, c) PLGA and d) PLCL films in 100 mM NaCl aqueous solution.

After the characterization of the polymer supports we proceeded with the protein adsorption experiments (at concentration 0.1 mg ml^{-1}). Figure 5.3 shows the change in frequency (ΔF) (protein mass uptake) and dissipation (ΔD) (viscoelastic properties) on polymer-coated gold QCM-D crystals. A first look show that the frequency decreases rapidly with time achieving a constant value after an hour. On the contrary, although at the beginning the variation in dissipation rises in a fast way, its behaviour as a function of time is more complex. The arrows of the figures indicate the different steps of the experiment. Firstly, we introduce millipore water in the QCM-D chamber and after that tris-buffer. After the system equilibrates SbpA protein is pumped into the chamber at 0.5 ml s^{-1} for 40 seconds. Then, the protein is left in the measuring chamber incubating overnight and finally the system was rinsed with tris-buffer and millipore water. The final change in frequency for protein adsorption after rinsing with water is similar for all the polymer substrates ranging from 1700-1900 ng cm^{-2}, which implies approximately a

mass per unit area of protein bilayer [29]. From the frequency time curve it is also possible to obtain information about initial adsorption rate by taking the first derivative. The initial adsorption rate varies between 4700-3900 ng cm^{-2}min^{-1} (see table 5.3). The lowest value corresponds to PLCL substrates.
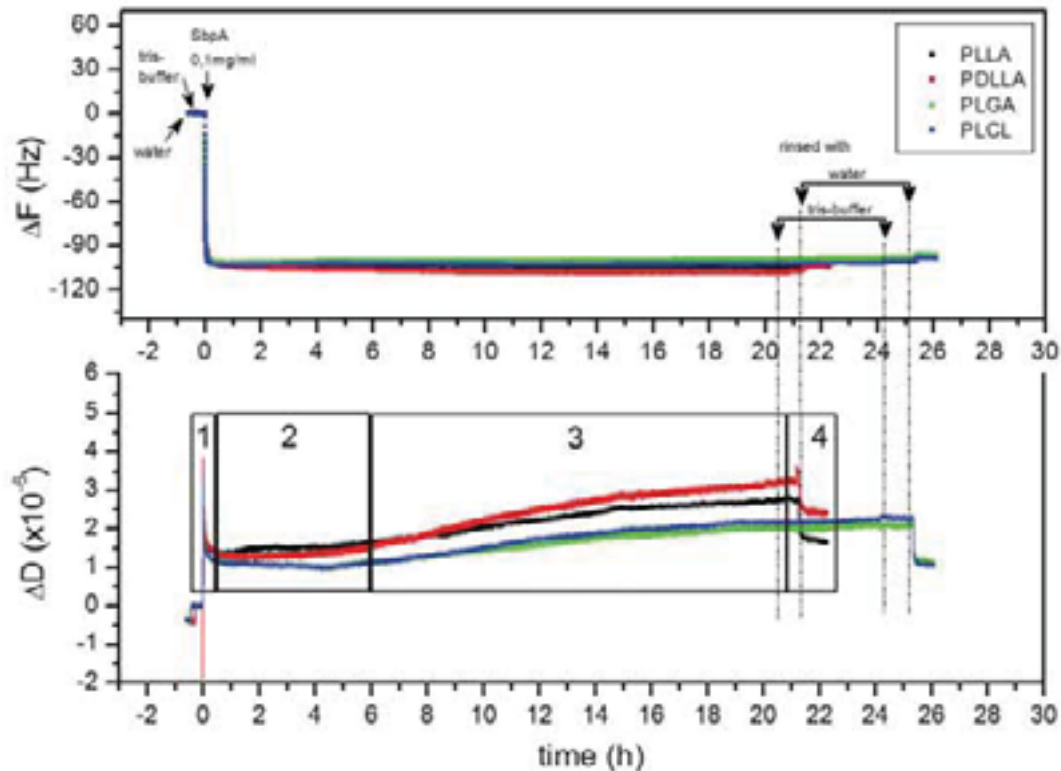
Figure 5.3. Frequency (ΔF) and dissipation (ΔD) response of SbpA adsorption on PLLA (black), PDLLA (red), PLGA (green) and PLCL (blue) at 23ºC. The numbered windows (1-4) refer to the different effects observed in dissipation during S-layer formation.

The variation of the dissipation with time presents four main effects. The first one (1) occurs immediately after protein injection and it is characterized by a narrow peak. The second one (2) corresponds to a plateau in the dissipation (the S-layer is already formed). The third effect (3) occurs after 6 hours: the dissipation increases gradually with time, which is due to the formation of S-layer assemblies in solution. The forth effect (4) occurs after rinsing with water, the final values are shown in table 5.2.

Polymer support	ΔF(Hz)	Δm (ng cm^{-2})	ΔD(x10^{-6})	Initial adsorption rate (ng cm^{-2}min^{-1})
PLLA	-106±4	1876	2.1±0.1	4516±486
PDLLA	-108±7	1912	2.4±0.5	4374±32
PLGA	-95±1	1682	1.4±0.1	4706±257
PLCL	-103±3	1823	1.2±0.1	3997±104

Table 5.2. Frequency change (ΔF), mass uptake (Δm) (calculated from Sauerbrey equation), dissipation (ΔD) and initial adsorption rate of SbpA adsorption on PLLA, PDLLA, PLGA and PLCL obtained from QCM-D experiments.

Once the protein rate adsorption and protein formation were monitored with the QCM-D, the next experimental step consisted in the study of the surface topography of the S-layer with atomic force microscopy (AFM). The AFM measurements were performed in 100 mM NaCl solution in tapping mode. The figure 5.4 shows the recrystallized S-layer on a) PLLA, b) PDLLA, c) PLGA and d) PLCL. The images size is 500 x500 nm^2 and the vertical scale ranges from 5-15 nm. The lattice parameters have been calculated with Fourier analysis; the Fast Fourier Transform is shown at the bottom right corner of each figure. The lattice parameters are similar for all the cases (see table 5.3) and coincides to the ones observed on native S-layers [17], and to recrystallize S-proteins on many different kind of substrates (silicon oxide, PEM, silanes and thiols) [13, 14, 16]. Although the lattice parameters are similar the protein crystal domain varies for each polymer substrate. A typical crystalline domain is encircled in white. The largest (0.09 μm^2) domains are obtained for PLCL substrates and the smallest (0.011 μm^2) for PLLA. The roughness of the S-layer crystals has been evaluated and ranged from 0.73-1.6 nm. These three parameters are listed in detail in table 5.3.
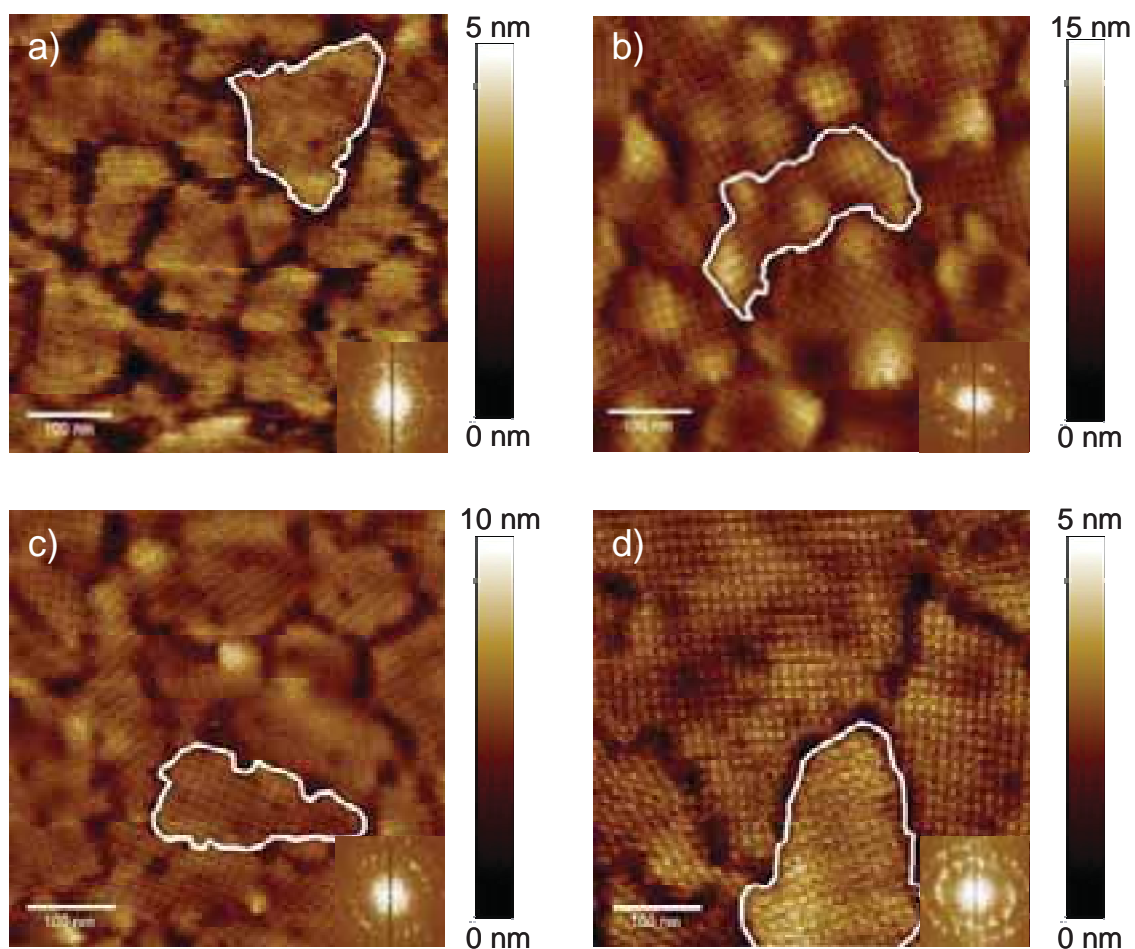
Figure 5.4. AFM height images of recrystallized SbpA forming a homogeneous and flat crystalline layer on polylactide derived biopolymers, a) PLLA, b) PDLLA, c) PLGA and d) PLCL

Polymer support	Domain size (μm^2)	Rq (nm)	a=b (nm)	γ (⁰)
PLLA	0.011±0.002	0.73±0.07	13.3±0.3	91±1
PDLLA	0.034±0.007	1.63±0.05	13.5±0.2	91±1
PLGA	0.039±0.006	0.93±0.07	13.2±0.2	90±1
PLCL	0.090±0.004	0.85±0.15	13.6±0.5	89±2

Table 5.3. S-layer crystalline domains size, roughness (R_q) and lattice parameters (a, b and γ) formed on PLLA, PDLLA, PLGA and PLCL calculated from AFM height images.

Now we are in the position to combine the information obtained by QCM-D and AFM to elucidate the S-layer formation mechanism. The first correlation to be made is between the crystal domain size and the protein adsorption rate. The largest crystal domains are observed for amorphous PLCL substrates which show the lowest protein adsorption rate and correspond to the polymer with the lowest T_g and smallest value in dissipation (which indicates the strongest protein crystal-polymer interaction). This variation might be also influenced by the polycaprolactone molecule of the PLCL (see figure 5.1). For amorphous PDLLA and PLGA the protein adsorption rate, the final mass uptake and protein domains size are similar but the final dissipation is higher for PDLLA than of PLGA. This indicates that the interaction between S-layer and the polymer is stronger in the case of PLGA.

In previous chapters, the influence of the hydrophobicity on the recrystallization process of SbpA has been reported. Since the hydrophobic properties of the polylactide derivative polymers are similar, the difference in protein domain size observed for PLLA might be due to its semicrystalline structure.

Another way to analyze the protein adsorption and crystal formation and the viscoelastic properties is to plot variation of dissipation as a function of frequency (in this case time is an implicit parameter) as shown in figure 5.5. Three different processes can be observed: The first process (1) corresponds to decrease in frequency (mass uptake) until the dissipation reaches a maximum which occurs approximately after 30 seconds (t_1). The second one (2) starts after the maximum and consists of an increase in mass while the dissipation is decreasing with time meaning that the protein crystal formation starts ending at a minimum (t_2=1 hour), where the crystalline domains reorganize [16]. The final process (3) in which the frequency values is constant (no mass adsorption) but the dissipation is increasing, might correspond to local variation in viscosities near S-layer interface due to S-protein self assembly formation in solution.
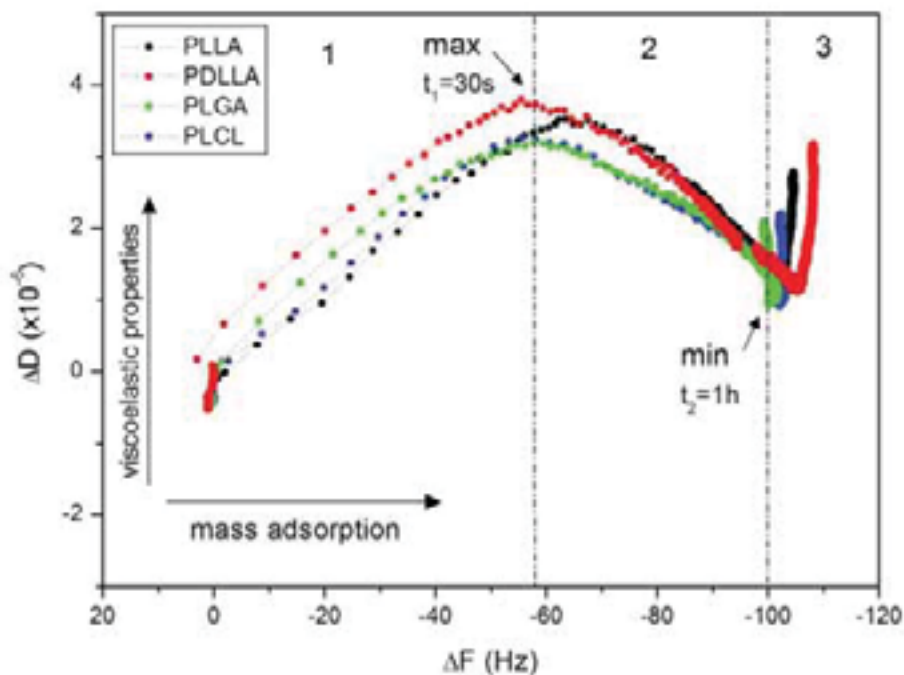
Figure 5.5 Dissipation vs. frequency curves for S-layer recrystallization on PLLA (black), PDLLA (red), PLGA (green) and PLCL (blue). The numbers indicate the three different processes observed in S-layer formation. The maximum in dissipation reaches within 30 seconds (t_1) while the minimum occurs 1 hour (t_2) after SbpA injection.

5.4 Conclusions

In this chapter we report on the fabrication of biomimetic supramolecular structures on amorphous and semicrystalline polylactide derivatives using bacterial S-proteins.

It has been found that, the crystalline state of the polymer supports does not hinder S-layer formation. QCM-D experiments show that the adsorbed mass per unit area is similar for all the polymer supports corresponding to a protein crystal bilayer. AFM results confirm that the polymer supports do not change the final lattice parameters of S-layer crystal.

Some differences have been observed in S-layer formation process. The slowest protein adsorption occurs for amorphous PLCL which has the lowest T_g and implies larger protein domain formation. Moreover, the lowest dissipation values are obtained also for recrystallize S-layers on PLCL, meaning that the interaction between the protein crystal and the polymer surface is stronger than on the other polymer supports.

On the other hand, the protein adsorption rate and the protein crystalline domains size are similar for amorphous PDLLA and PLGA supports; however, the variation in dissipation is higher for PDLLA than for PLGA, implying that the interaction between the S-layer crystal and PDLLA is weaker. The protein domain size is affected by the crystallinity of the polymer: The crystalline domains are the smallest ones on PLLA.

Finally, QCM-D frequency-dissipation measurements showed that S-layer formation process occurs in three main steps; protein adsorption, protein self-assembly (crystal formation) and crystal reorganization. In addition, QCM-D measurements monitored S-layer self-assembly formation in solution.

5.5 References

[1]   M. Chasin, *Biodegradable polymers as Drug delivery systems*, R.L. Dekker, New York, 1990.

[2]   W. Norde, *Adv. Colloid Interfac.* 25 (1986) 267-340.

[3]   M. Mrksich, G.M. Whitesides, *Annu. Rev. Bioph. Biom.* 25 (1996) 55-78.

[4]   D. Rossi, A. Zlotnik, *Annu. Rev. Immunol.* 18 (2000) 217-243

[5]   M. Berglin, E. Pinori, A. Selborn, M. Anderson, M. Hulander, H. Elwing, *Langmuir* 25 (2009) 5602-5608.

[6]   J.R. Sarasua, A. Lopez-Arraiza, P. Balerdi, Maiza, *Polym. Eng. Sci.* 45 (2005) 745-753.

[7]   H. Tsuji, *Biomaterials* 24 (2003) 537-547.

[8]   S. Lannace, A. Maffezzoli, G. Leo, L. Nicolais, *Polymer* 42 (2001) 3799-3807.

[9]   A. Södegard, M. Stolt, *Prog. Polym. Sci.* 27 (2002) 1123-1163.

[10]   J.R. Sarasua, R.E. Prud'homme, M. Wisniewki, A.L. Borgne, N. Spasski, *Macromolecules* 31 (1998) 3895-3995.

[11]   U.B. Sleytr, E. Györvary, D. Pum, *Prog. Org. Coat.* 47 (2003) 279-287.

[12] V. Saravia, S. Küpcü, M. Nolte, C. Huber, D. Pum, A. Fery, U.B. Sleytr, J.L. Toca-Herrera, *J. Biotechnol.* 130 (2007) 247-252.

[13] S. Moreno-Flores, A. Kasry, H.-J. Butt, C. Vavilala, M. Schmittel, D. Pum, U.B. Sleytr, J.L. Toca-Herrera, *Angew. Chem. Int. Edit*. 47 (2008) 4707-4717.

[14] M. Delcea, R. Krastev, T. Gutlebert, D. Pum, U.B. Sleytr, J.L. Toca-Herrera, *J. Nanosci. Nanotechno.* 7 (2007) 4260-4266.

[15] C. Kepplinger, N. Ilk, U.B. Sleytr, B. Schuster, *Soft Matter* 5 (2009) 325-333.

[16] A. Eleta-Lopez, S. Moreno-Flores, D. Pum, U.B. Sleytr, J.L. Toca-Herrera, *Small* 6 (2010) 396-403.

[17] U.B. Sleytr, P. Messner, D. Pum, M. Sára, *Angew. Chem. Int. Edit.* (1999) 1034-1054.

[18] U.B. Sleytr, M. Sára, D. Pum, B. Schuster, *Prog. Surf. Sci.* 68 (2001) 231-278.

[19] U. Sleytr, B. Schuster, D. Pum, *IEEE ENG. Med. Biol.* (2003) 140-150.

[20] M.S. Sidhu, I. Olsen, *Microbiology* 143 (1997) 1039-1052.

[21] U.B. Sleytr, C. Huber, N. Ilk, D. Pum, B. Schuster, E.M. Egelseer, *FEMS Microbiol. Lett.* 267 (2007) 131-144.

[22] N. Ilk, E.M. Egelseer, J. Ferner-Ortner, S. Küpcü, D. Pum, B. Schuster, U.B. Sleytr, *Colloid Surface A* 321 (2008) 163-167.

[23] J.L. Toca-Herrera, R. Krastev, V. Bosio, S. Küpcü, D. Pum, A. Fery, M. Sára, U.B. Sleytr, *Small* 1 (2005) 339-348.

[24] D. Moll, C. Huber, B. Schlegel, D. Pum, U.B. Sleytr, M. Sára, *P. Natl. Acad. Sci.* 99 (2002) 14646-14651.

[25] H. Tschiggerl, A. Breitwieser, G.d. Roo, T. Verwoerd, C. Schäffer, U.B. Sleytr, *J. Biotechnol.* 133 (2008) 403-411.

[26] U.B. Sleytr, M. Sára, Z. Küpcü, P. Messner, *Arch. Microbiol.* 146 (1986) 19-24.

[27] G. Sauerbrey, *Z. Physik* 155 (1959) 206-222.

[28] K. Gläsmäster, C. Larsson, F. Höök, B. Kasemo, *J. Colloid Interf. Sci.* 246 (2002) 40-47.

[29]   M. Delcea, R. Krastev, T. Gutlebert, D. Pum, U.B. Sleytr, J.L. Toca-Herrera, *Soft Matter* 4 (2008) 1414-1421.

Chapter 6

Albumin-bilirubin and albumin-ibuprofen complexes adsorption, thermal stability and ζ-potential

Until now we have presented the adsorption, self-assembly and protein crystal formation of bacterial proteins on a variety of solid supports of well defined chemistry and different physical properties. At that point we will like to extend our work studying a protein, Human Serum Albumin (HSA), which is important for physiological processes. On the contrary to the bacterial protein, HSA does not form nanocrystal structures but it has the ability to interact with many other molecules in order to fulfil its biological role. In this chapter we will present immobilization studies of HSA on two different substrates and we will study the interaction of albumin with bilirubin and ibuprofen.

6.1 Introduction

Human Serum Albumin (HSA) (M_w. 66.7 kDa) is a globular non-glycosylated protein with heart-shaped conformation of dimensions 8 x 8 x 3 nm^3 [1]. HSA is the most abundant protein in blood plasma being a key element in controlling the colloid-osmotic pressure in blood vessels. Furthermore, its main function is to transport a wide

variety of endogenous or exogenous compounds in the human body such as fatty acids, bile pigments (as bilirubin), drugs, ionic ligands etc.[2-6]. In order to perform its function the albumin needs to adopt different conformation depending on the environment. Albumin is formed by three domains (I, II, III) separated in subdomains A and B (see figure 6.1). In general the main interactions between albumin and the ligands occur via van der Waals, electrostatic, hydrogen bonds, hydrophobic, and disulfide bridges. The main albumin binding sites are located in the hydrophobic subdomains IIA and IIIA [7-10].

The albumin ability to bind such different molecules is exploited in biotechnology and medicine. For example albumin is currently used in dialysis to remove accumulated toxins from the circulating system or for elimination of protein-bound uremic toxins in chronic renal failure [11].

The interaction of any kind of ligands with HSA to form a complex leading to complex formation might affect the albumin physico-chemical properties [5, 12]. Thus, the knowledge of the interactions governing protein-ligand binding and the consequences regarding the native protein conformation would certainly improve the understanding of its biological activity. Therefore in this chapter, ibuprofen and bilirubin molecules were chosen to study their albumin complexes with albumin. Ibuprofen is a well known drug, widely used due to its antipyretic, analgesic, and antibacterial activity while bilirubin is a natural yellow-orange pigment produced from the break-down of haemoglobin and other hemoproteins in mammals [7, 13], which might be toxic if it is not properly excreted through the bile [14-16].

In this chapter, the thermodynamics of the binding HSA-ibuprofen and HSA-bilirubin has been investigated by DSC (Differential Scanning Calorimetry) and ITC (Isothermal Titration Calorimetry). The size, ζ-potential and secondary structure information was obtained by electrophoretic mobility and circular dichroism experiments. Furthermore, we proceed to study the adsorption behaviour of HSA and HSA complexes. We functionalized silicon oxide and gold surfaces with PEMs and glutaraldehyde respectively, to optimize HSA immobilization. The protein and complex immobilization was monitored with QCM-D, which provided information at real time

of the adsorbed mass per unit area and the viscoelastic properties of the new layer at nanogram scale.

6.2 Materials and methods

Materials

Silicon dioxide and gold coated quartz crystals (Q-sense, Gothenburg, Sweden) were used as substrates. Poly(ethylenimine) (PEI) (M_w.750kDa), Polydiallyl Dimethyl Ammonium Chloride (PDADMAC) (20% in water M_w. 2-3.5 x 10^5 kDa), poly(sodium 4-styrenesulfonate) (PSS) (M_w. 70 kDa) were purchased from Aldrich (see figure 6.1). Cysteamine hydrochloride (Sigma), 1% glutaraldehyde (25%, Sigma) (see figure 6.1). Human Serum Albumin (HSA) (M_w=66.7 kDa) [17] and Bovine Serum Albumin (BSA) (M_w=66.4 kDa) [18], were purchased form Sigma. Bilirubin mixed isomers (Sigma) (M_w. 585 g mol^{-1}) and ibuprofen sodium salt (Sigma) (M_w. 228 g mol^{-1}) were used as a ligand (see figure 6.1). Sodium dihydrogen phosphate anhydrous (NaH_2PO_4) and sodium phosphate dibasic anhydrous (Na_2HPO_4) and sodium citrate were purchased from Fluka and commercial phosphate buffered solution (PBS) and Trizma base from Sigma. 2% sodium dodecyl sulphate, SDS, (99%, Fluka), Hellmanex II (2%, Hellma) and COBAS formed by 1% SDS (99%, Fluka) and 2.5% HCl (37% hydrochloride acid, Fluka) were used as cleaning solutions. All the solutions were made with Millipore water (18.2 MΩ cm^{-1}) and all the chemicals were used without further purification.

UV-ozone treatment. Silicon gold substrates were cleaned in 2% sodium SDS for 30 minutes, rinsed with ultrapure water (Barnstead) and dried under a stream of nitrogen. Then, the substrates were treated with ultraviolet radiation (Bioforce Nanoscieces) for another 30 minutes just before substrate modification.

Polyelectrolyte Multilayer build-up. Hydrophilic QCM-D silicon sensors were coated with polyelectrolyte multilayer (PEM) using Layer-by-Layer technique [19]. The 1 mg ml^{-1} polyelectrolyte solutions were prepared in NaCl 0.5 M.
The multilayer formation was monitored at real time by QCM-D. First, polycationic PEI was injected as a precursor followed by negatively charged PSS and positively charged PDADMAC, forming a five layer system. At each polyelectrolyte injection the

frequency and dissipation responses were left stabilizing for approximately 10 minutes. Between each polymer deposition step the substrates were rinsed with NaCl 0.5 M in order to remove the excess of polymer. The last layer was positively charged PDADMAC (see appendix 6.1a).
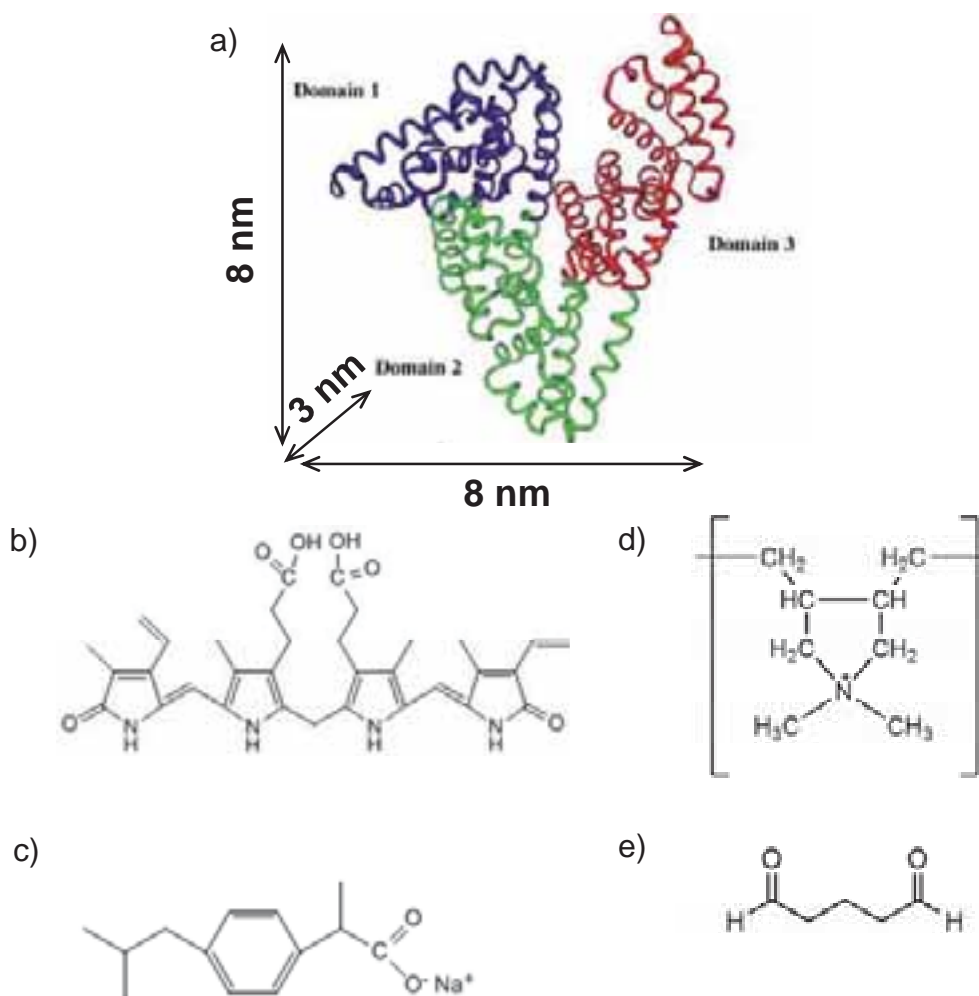
Figure 6.1. Structure of main molecules used in this chapter. a) HSA with its respective domains; domain 1, 2 and 3 are shown in blue, green and red, respectively [20], b) bilirubin, c) ibuprofen sodium salt , c) PDADMAC and e) glutaraldehyde.

Gold functionalization with glutaraldehyde. Clean QCM-D gold sensors were immersed in cysteamine hydrochloride 20 mM aqueous solution overnight at room temperature. The petri-dishes were covered with aluminium foil to kept them in the dark. Afterwards, the functionalized sensors were immersed in glutaraldehyde 1% aqueous solution and left for 1 hour shaking at room temperature. After each step, the

gold surfaces were rinsed with large amount of water. The thickness of the layer formed by cysteamine and glutaraldehyde in air was measured with ellipsometry being 1.1 ± 0.1 nm (see appendix 6.1b). The sensors were used for albumin immobilization immediately after surface modification [21, 22].

Human Serum Albumin (HSA) and Bovine Serum Albumin (BSA). Depending on the experiment albumin was diluted with different buffers (PBS (10 mM phosphate, 140 mM NaCl), Na_2HPO_4/NaH_2PO_4 [23], tris-buffer or Sodium Citrate/Na_2HPO_4) and left stabilizing for two hours before use. Then, the albumin was filtrated with 100 kDa centrifugal filters (Ultracel YM-100, Millipore) at 7000 rpm, 4ºC for 10 minutes.

Albumin complex preparation.

Albumin-bilirubin. 2 mg ml^{-1} of albumin was mixed with 0.2 mg ml^{-1} of bilirubin in NaOH pH 11 with 1:1 ratio. The mixture, covered with aluminium foil, was stirred for 30 minutes at room temperature. Afterwards, the pH was adjusted to 7.4, 4.9 or 3.7 and the formed precipitates due to excess of bilirubin were removed by centrifugation (7000 rpm, 4ºC, 20 minutes).

Albumin-ibuprofen. 2 mg ml^{-1} of albumin were mixed with 2 mg ml^{-1} of ibuprofen and stirred for 30 minutes. Afterwards, the mixture was dialyzed to remove the excess of ibuprofen. The sample was dialyzed three times, 2 hours for each case. The dialysis membrane had a cut off of 12-14 kDa (Medicell International Ltd).

Bilirubin solution preparation for ITC experiments. 0.5 mg of bilirubin was dissolve in 125 μl of NaOH 0.1 M. Then it was diluted with 5 ml of millipore water and titrated to pH 9. Brown eppendorf or aluminium foil covered vials were used to avoid bilirubin (yellow-red) oxidation to biliverdin (green) and the solutions were used immediately after preparation (within an hour) [24].

Methods

UV-visible spectroscopy. The concentrations of albumin, bilirubin and ibuprofen solutions were determined using an UV-vis spectroscopy (Nano Drop ND-1000 spectrophotometer). The absorbance of albumin, bilirubin and ibuprofen were measured

at 280 nm, 450 nm and 264 nm respectively [7]. The Beer-Lambert law, $A = \varepsilon \cdot l \cdot c$, was used to calculate the concentration, where A is the absorbance, ε is the extinction coefficient, l is the path length and c is the concentration.

Ellipsometry. The thickness of cysteamine/glutaraldehyde layer was measured with a commercial spectroscopic ellipsometer (M2000V J. A. Woollam Co. Inc., USA) in air. Ellipsometric data, Δ and ψ, were acquired over a wavelength range from λ=380 to 1000 nm, at different incident angles varied between 45-80º at room temperature. Cauchy dispersion equation was used to calculate the thickness, assuming a refractive index of 1.45 for the organic layer [25].

Differential Scanning Calorimetry (DSC). The thermal denaturation of albumin and albumin complexes was followed by DSC using VP-DSC high sensitivity differential scanning calorimeter from MicroCal (Northampton, MA, USA).

The thermograms were recorded from 25ºC to 100ºC at scan rate of 60 ºC h^{-1}. The albumin and albumin complex concentrations were 0.5 mg ml^{-1} for HSA and 1 mg ml^{-1} for BSA. The data were analyzed with the Origin software provided with the equipment; thus the denaturation enthalpy (ΔH_m) and denaturation temperature (T_m) were obtained.

Isothermal Titration Calorimetry (ITC). The binding between albumin and bilirubin and ibuprofen was monitored by ITC (VP-ITC Titration Calorimeter from MicroCal (Northampton, MA, USA). The reference cell was filled with water while the sample cell was filled with 0.5 mg ml^{-1} albumin (1.442 ml). The syringe was filled with a solution of bilirubin (0.12 mg ml^{-1}) or ibuprofen (0.05 mg ml^{-1}). 29 injections of 10 μl were carried out (except the first injection that it was of 2 μl) and the stabilizing time between injections was 180 seconds. The calorimeter cell was constantly stirred at an angular speed of 307 rpm. The molecules were dissolved in 10 mM Na_2HPO_4/NaH_2PO_4 at pH 7.4 except the bilirubin which was in NaOH.

In bilirubin-albumin experiments the protein and the ligand were in different buffers that affected the reaction heat. Therefore, several controls were carried out in order to evaluate the influence of the buffer dilution. The experiment was divided in four steps as it is explain in [26] (see scheme 6.1)
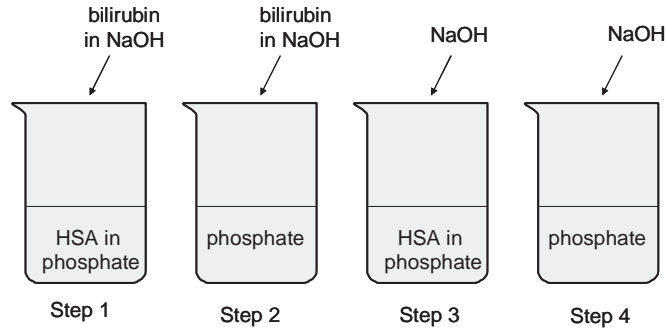
Scheme 6.1. The four steps of HSA-bilirubin ITC experiment

Step 1: *bilirubin in NaOH pH 9 is added to HSA in phosphate buffer pH 7.4*

$$\Delta H_1 = \Delta H_{\text{HSA-bilr}} + \Delta H_{\text{HSA-NaOH}} + \Delta H_{\text{Dilution-HSA}} + \Delta H_{\text{Dilution-bilr}} + \Delta H_{\text{Dilution-NaOH}}$$

Step 2: *bilirubin in NaOH pH 9 is added to phosphate buffer pH 7.4*

$$\Delta H_2 = \Delta H_{\text{Dilution-bilr}} + \Delta H_{\text{Dilution-NaOH}}$$

Step 3: *NaOH pH 9 is added to HSA in phosphate buffer pH 7.4*

$$\Delta H_3 = \Delta H_{\text{HSA-NaOH}} + \Delta H_{\text{Dilution-HSA}} + \Delta H_{\text{Dilution-NaOH}}$$

Step 4: *NaOH pH 9 is added to phosphate buffer pH 7.*

$$\Delta H_4 = \Delta H_{\text{Dilution-NaOH}}$$

Then HSA-bilirubin interaction enthalpy is calculated in the following way:

$$\Delta H_{\text{HSA-bilr}} = \Delta H_1 - \{\Delta H_2 + (\Delta H_3 - \Delta H_4)\}$$

The results showed that the enthalpy of step 3 (ΔH_3) and step 4 (ΔH_4) are similar and they annulated each other (see the formula above). Therefore, as a first approach it was assumed (see appendix 6.2 for more details):

$$\Delta H_{\text{ HSA-bilr}} = \Delta H_1 - \Delta H_2$$

All the data were processed using the Origin software provided with the equipment.

Quartz Crystal Microbalance with Dissipation monitoring. The adsorption of polyelectrolytes, albumin and albumin complexes were followed at real time with QCM-D (QE401 (electronic unit)/QFM401 (flow module) instrument from Q-sense AB (Gothenburg, Sweden). The presented results correspond to the 5th overtone. The QCM-D data were analyzed with Q-Tools (software provided by Q-Sense). The Sauerbrey equation was used to calculate the mass density from the frequency change [27].

ζ-potential. Albumin and albumin complexes ζ-potential were measured by a Nano ZS ZEN 3600 Zetasizer from Malvern Instruments using the Huckel approximation. The measurements were carried out in diluted buffer solutions (2 mM tris-buffer to pH 9. 2 mM Na_2HPO_4/NaH_2PO_4 for pH 7.4 and 1mM sodium citrate/2mM Na_2HPO_4 used at pHs down to 6). The conductivity of all solutions was controlled with a conductimeter (CyberScan CON 1500 from Eutech Instruments) and adjusted to 0.8-0.9 mS cm^{-1}.

Dynamic light scattering (DLS) Nano ZS ZEN 3600 Zetasizer from Malvern Instruments was used to determine the size of albumin and albumin complexes.

Circular Dichroism (CD) (J-800 spectropolarimeter from Jasco) was used to characterize the secondary structure of HSA free albumin, HSA-bilirubin and HSA-ibuprofen complexes. These experiments were carried out with 10 mM phosphate buffer at 0.05 mg ml^{-1} protein concentration.

6.3 Results and discussion

6.3.1 Effect of bilirubin and ibuprofen binding on the thermal denaturation of albumin: Differential Scanning Calorimetry.

The DSC thermograms of albumin and albumin complexes are shown in figure 6.2. In these experiments the temperature was increased from 25ºC to 100ºC.
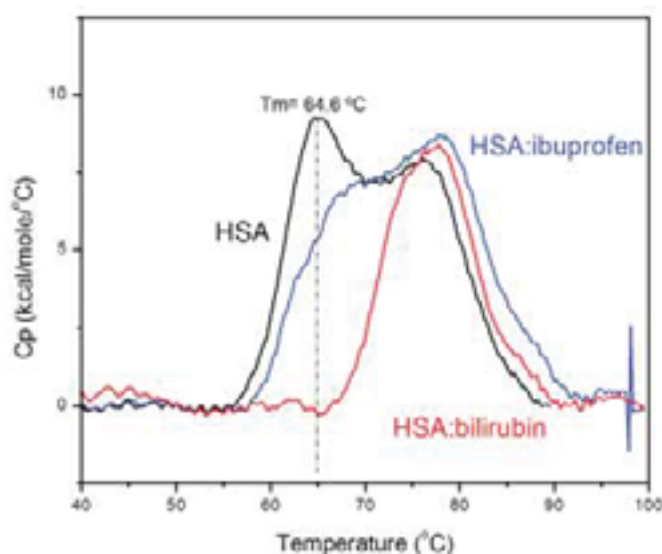
Figure 6.2. DSC thermograms of free HSA (black), HSA-ibuprofen (blue) and HSA-bilirubin (red) thermal denaturation.

All the curves show endothermic induced unfolding. A careful look of the data indicates that pure albumin presents a denaturation peak (T_m) at 64.6ºC; the smaller second peak, obtained at higher temperatures (75-80ºC) might be due to the presence of albumin precipitates. In the case of HSA-ibuprofen the main peak is obtained near 80ºC while around 67ºC a shoulder can be observed. For HSA-bilirubin system a single peak is obtained also at 80ºC.

At this point it was not trivial to distinguish if this temperature corresponded either to single HSA-drug complex or HSA-drug aggregates. Due to this difficulty, we repeated the same experiments with Bovine Serum Albumin (BSA) which is commonly used as a model protein of the albumin family [28]. Figure 6.3 shows the DSC thermograms of BSA, BSA-ibuprofen and BSA-bilirubin. It can be observed that the T_m of BSA is clearly defined at 63.9ºC. In this case a shoulder, which is smaller than the

one reported for HSA, can be detected at around 80ºC. These measurements clarify the main denaturation temperature of albumin complexes. In this case, the T_m for BSA-ibuprofen and BSA-bilirubin seems to be between 67-68ºC. Both complexes show a shoulder at higher temperatures which are caused by aggregates. Therefore, a direct comparison between HSA and BSA leads to the conclusion that the peaks at 80ºC for HSA-ibuprofen and HSA-bilirubin might correspond to aggregates in solution.
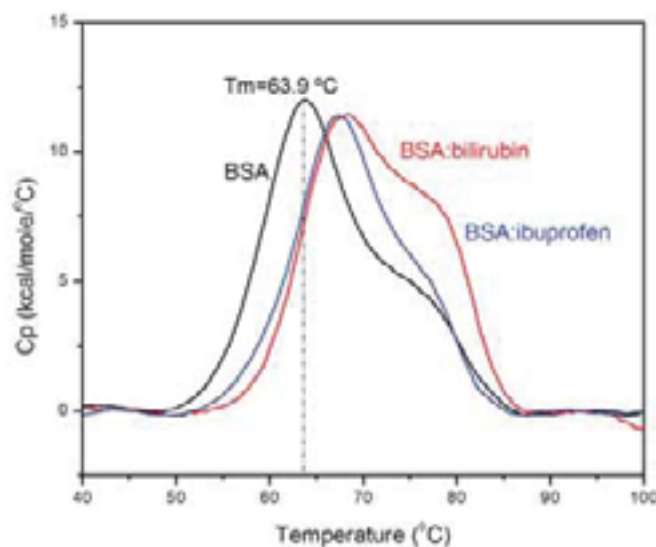
Figure 6.3. DSC thermograms of free BSA (black), BSA-ibuprofen (blue) and BSA-bilirubin (red) denaturation.

Furthermore, we can conclude that albumin complexes present a higher denaturation temperature than single albumin. Thus, the albumin complexes with ibuprofen and bilirubin are thermodynamically more stable.

Additionally, one can obtain the denaturation enthalpy (ΔH) from these experiments. The enthalpy of the denaturation process of albumin and albumin complexes has been determined integrating the area under the peak. Thus, the total enthalpy (ΔH_{tot}) calculated by integrating the whole thermogram (see table 6.1) corresponds to single protein and protein aggregates. The enthalpy of albumin and its complexes was estimated fitting only their peaks by a single Gaussian. The results are shown in table 6.1.

It can be seen that HSA enthalpy is somewhat lower than HSA-ibuprofen enthalpy. In the case of BSA, its enthalpy value is similar to BSA-ibuprofen while a

higher enthalpy value is obtained for BSA-bilirubin complex. The thermodynamic values calculated for HSA and BSA have been compared with values found in the literature, where it is reported that the enthalpy data differ depending on the experimental conditions. In addition, albumin results also have been compared with other proteins as haemoglobin (Hb), which presents similar molecular weight as albumin, and immunoglobulin (IgG), that is larger than albumin. It can be observed that the thermal denaturation enthalpy for Hb and IgG is larger than the one for albumin.

Protein/complex	T_m (ºC)	ΔH_{tot} (Kcal/mol)	ΔH_{mon} (Kcal/mol)	references
HSA	64.6 ± 0.3	168.1 ± 9.8	81.4 ± 0.7	this work
HSA-ibup	68.4 ± 0.4	171.8 ± 10.3	89.3 ± 2.3	this work
HSA-bilr	77.3 ± 0.3	105.1 ± 11.9	99.4 ± 6.1	this work
HSA	59.65±0.05	----	166.3 ± 4.5	Kosa et al.[29]
HSA	63.2 ± 0.4	----	89.9 ± 4.5	Picó et al.[30]
BSA	63.9 ± 0.4	154.9 ± 8.4	121.7 ± 0.7	this work
BSA-ibup	67.4 ± 0.1	135.2 ± 6.2	119.2 ± 0.7	this work
BSA-bilr	68.4 ± 0.4	212.8 ± 12.2	129.7 ± 1.3	this work
BSA	64.2±0.2	----	224	Giancola et al.[31]
BSA	63	----	177	Barone et al.[32]
Hb	65.7	----	214 / 489	Müller et al.[33]
IgG	61.5/71.8	----	437 / 176	Vermeer et al.[34]

Table 6.1. The denaturation temperature (T_m), total enthalpy (ΔH_{tot}), monomer enthalpy (ΔH_{mon}) of HSA, BSA and their respective complexes. In addition, haemoglobin (Hb) and immunoglobulin (IgG) values are included for comparison. The fittings are shown in appendix 6.3.

6.3.2 Binding of bilirubin and ibuprofen to HSA: ITC experiments

Figure 6.4 and figure 6.5 show the ITC experiments concerning the binding between HSA/bilirubin and HSA/ibuprofen respectively. From these figures the following information is obtained: figure 6.4a and figure 6.5a show the heat release or adsorbed upon each injection as a function of time while figure 6.4b and figure 6.5b represent the heat as a function of protein/ligand ratio. The results of figure 6.4a show that upon the addition of ibuprofen into a HSA solution, heat is released indicating an exothermic interaction between HSA and the ibuprofen. The released heat is proportional to the amount of interacting molecules. It can be seen that the peak height (µcal sec) tends to zero with time. This decrease is due to the saturation of albumin binding sites. The same behaviour is observed in figure 6.5a. The quantification of

figure 6.4a and 6.5a is shown in figure 6.4b and 6.5b, respectively. The amount of heat per mol of injectant is obtained by integrating the peaks of figure 6.4a and 6.5a. Afterwards these values are plotted as a function of protein/ligand molar ratio. These measurements permit the calculation of the thermodynamic magnitudes that describe the interaction of albumin and its ligands. In order to do this, we proceed to the fitting of the data to obtain the binding stoichiometry (n), the binding constant (K), the enthalpy (ΔH) and the entropy (ΔS). This information was used to calculate the Gibbs free energy (ΔG), using the equation ΔG= ΔH-T ΔS (table 6.2). The data for HSA-ibuprofen were best fitted with *one class of binding site*, while the data for HSA-bilirubin were best fitted with *two class of binding sites*. The information concerning the fitting models is shown in appendix 6.4.

complexes	n	K (M^{-1})	ΔH (Kcal/mol)	ΔS (Kcal/mol ºC)	ΔG (Kcal/mol)
HSA-ibuprofen	0.94 ± 0.05	$3.81 \times 10^5 \pm 4.5 \times 10^4$	-10100 ± 662	-8.34	-7615
HSA-bilirubin	1.21 ± 0.02	$5.21 \times 10^7 \pm 8.1 \times 10^6$	-9267 ± 151	4.24	-10530
	0.92 ± 0.02	$4.61 \times 10^6 \pm 2.77 \times 10^5$	-1179 ± 320	26.5	-9072

Table 6.2. HSA-ibuprofen and HSA-bilirubin complexes binding sites (n), enthalpy (ΔH), entropy (ΔS) and Gibbs free energy (ΔG). The experiments were carried out at 23ºC.

The stoichiometry of HSA-ibuprofen binding, at this experimental conditions, is 1:1 (see table 6.2), which means that each ibuprofen molecule binds to one HSA protein. The calculated binding constant is in the order of K=10^5 M^{-1} that is in agreement with the values reported in the literature. However, *Aki et al.* reported that ibuprofen has two binding sites at other experimental conditions (e.g. 37ºC); with different binding constants being the first one (K=1.10 x 10^5 M^{-1}) stronger than the second (K=5.617 x 10^3 M^{-1}) binding site [35]. Moreover, the HSA-bilirubin binding stoichiometry (1:2) indicates that two bilirubin molecules bind to one HSA (see table 6.2). From the fitting procedure we have found that the first binding constant is in the order of 10^7 while the second is weaker (in the order of 10^6). However, in the literature it is already reported that 3 bilirubin molecules might bind to each albumin being the first dissociation constant 1.28 x 10^{-6} M and the second and the third 4.80 x 10^{-4} M [26].

This discrepancy with our results might depend on the experimental conditions as *Breaven et al.* already reported [36].
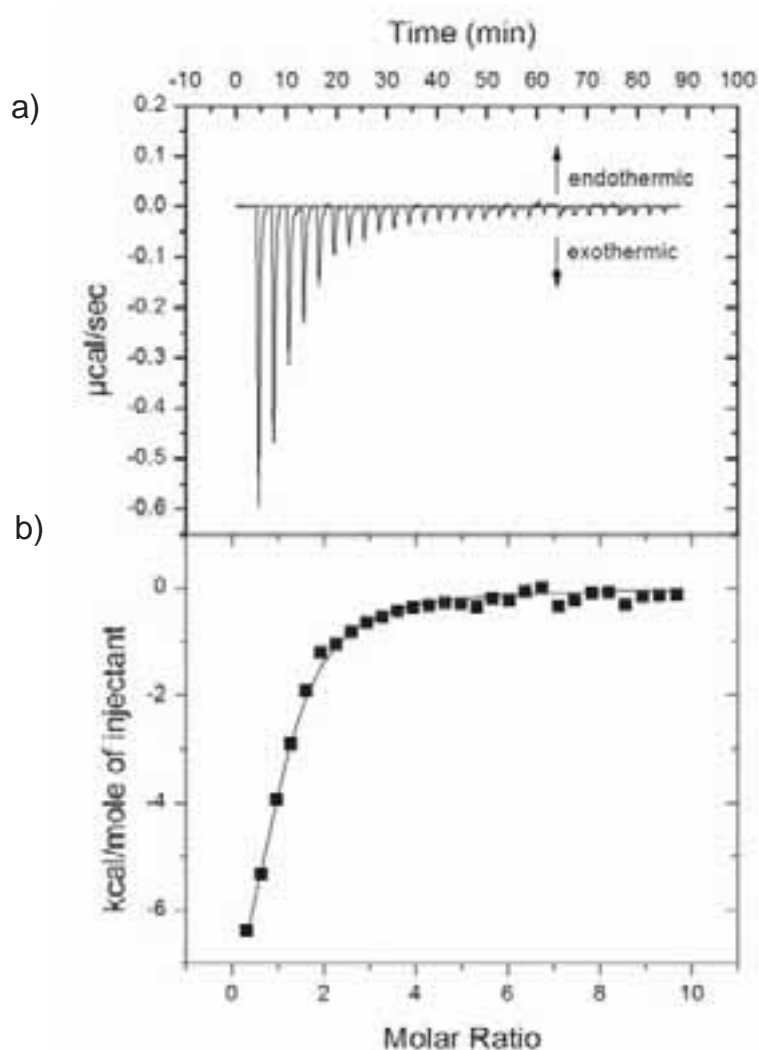
Figure 6.4. ITC measurement of the binding between ibuprofen and HSA; a) raw data of the heat flow (μcal sec) as a function of time obtained after injection of ibuprofen to HSA solution at 25ºC, b) heat of injection per mole of injected ibuprofen as a function of the molar ratio of ibuprofen:HSA. The solid lines are the theoretical fits.
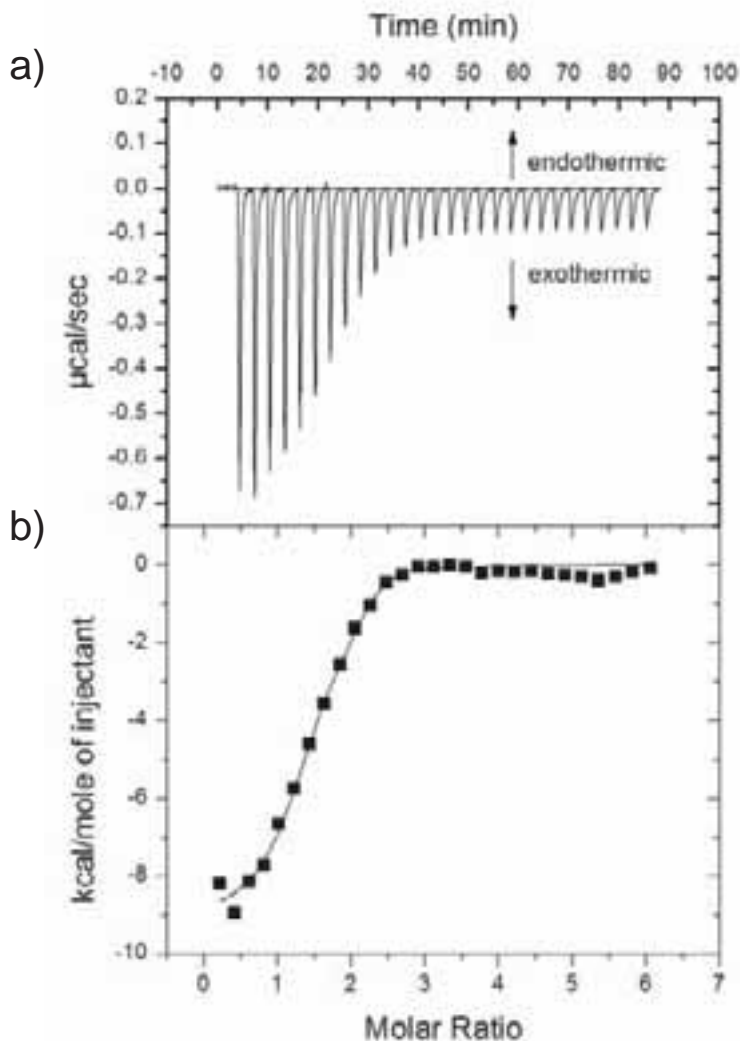
Figure 6.5. ITC measurement of the binding between bilirubin and HSA; a) raw data of the heat flow (µcal sec) as a function of time obtained after injection of ibuprofen to HSA solution at 25 ºC, b) heat of injection per mole of injected bilirubin as a function of the molar ratio of bilirubin:HSA. The solid lines are the theoretical fits.

Human Serum Albumin (HSA) is formed by three continuous domains, I, II, and III, each containing two subdomains, A and B. The HSA binding sites are located in the hydrophobic subdomains IIA and IIIA [7, 37]. The HSA-drug attachment occurs mostly through hydrophobic, van der Waals interactions and hydrogen bonding. The binding will be favoured under standard conditions only when the Gibbs free energy (ΔG) is negative. Thus, negative values of enthalpy and positive of entropy favoured the HSA-drug complex formation. On one hand, the favourable enthalpy changes are related with hydrogen bonding indicating stable drug-albumin complex, while the unfavourable enthalpy change is related with desolvation. On the other hand, favourable entropy

change is associated with the release of water molecules from the binding interface which leads mostly to hydrophobic binding [38].

The negative enthalpy and entropy for HSA-ibuprofen complex formation indicates that the process is governed by H-bonding. However, the unfavourable entropy indicates the loss of degrees of freedom or conformational restrictions. This is in agreement with the results reported by *Aki et al.* for the main ibuprofen binding site [35]. In the case of HSA-bilirubin complex, both enthalpy and entropy favoured the binding between the protein and the drug. It can be observed in table 6.2 that ΔH_1 is larger than the ΔH_2 meaning that the binding of the first bilirubin is driven preferentially by H-bonding. In contrast, ΔS_2 is greater than ΔS_1 indicating that hydrophobic interactions also play a role in the binding of bilirubin in the second binding site. The thermodynamic data reported by *Jacobsen et al.* [39] also showed that the strongest bilirubin interaction is an enthalpy driven process rather than hydrophobic. In contrast, more recent studies performed by *Movahedi et al.* [26] demonstrated that the first bilirubin-HSA binding is governed by entropic forces.

Finally, the negative values of the Gibbs free energy clearly demonstrate that both complexes, HSA-ibuprofen and HSA-bilirubin, are more stable than HSA, being the most stable complex HSA-bilirubin.

6.3.3 Adsorption of HSA on silicon oxide, PEM and glutaraldehyde

After the study of albumin thermal stability and albumin binding properties of albumin- ibuprofen and albumin-bilirubin complexes in solution, the immobilization of these molecules was carried out on three different solid supports. Figure 6.6 displays the time-resolved frequency and dissipation change of HSA adsorption on silicon oxide at pH 3.7, pH 4.9 and pH 7.4. When the albumin solution is injected, an instantaneous decrease in frequency and an increase in dissipation take place indicating adsorption of albumin. The steady state is reached in less than one hour after the injection. The results show that at pH 4.9 and pH 3.7 the initial frequency change is four times greater than pH 7.4. Furthermore, the immobilization at pH 3.7 is faster than at pH 4.9 (value near to the isoelectric point of the protein). This can be observed from the different curvatures of the frequency vs. time curves, which present different decays for the first 15 minutes (see figure 6.6). Finally, the systems were rinsed with their respective buffers and water.

It can be observed that no albumin immobilization takes place at pH 7.4 (the final value of the change in frequency in water is close to zero). The final values for the mass uptake (calculated with Sauerbrey equation) are 704 ng cm^{-2} for pH 4.9 and 502 ng cm^{-2} for pH 3.7 respectively(see table 6.3).
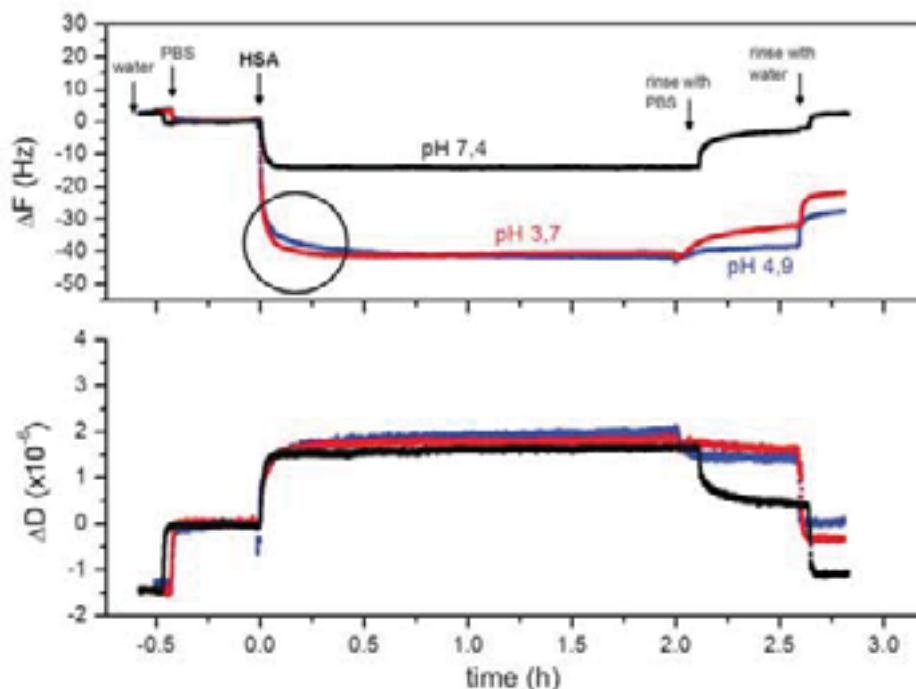
Figure 6.6. QCM-D real time experiments of HSA adsorption on silicon oxide at pH 7.4 (black), pH 4.9 (blue) and pH 3.7 (red). The decrease in frequency is related with the adsorbed mass while the change in dissipation response gives information about the rigidity of the protein layer.

Protein adsorption depends on several factors such as surface properties and the type of protein. In our case the HSA isoelectric point is found at pH 4.9, hence, at physiological conditions (pH 7.4) the protein net charge is negative. The isoelectrical point of silicon oxide particles have been found to be at pH 3.3. Hence, silicon oxide surface is negatively charged in the pH range used in this work [40]. Therefore, the low frequency change is attributed to substrate-protein repulsion interactions that do not allow the albumin attachment to the surface. Decreasing the pH, the albumin net charge turns to neutral at pH 4.9 and positive at pH 3.7, which allows albumin adsorption on silicon oxide.

Theoretically the adsorption and immobilization of HSA can take place in three ways; horizontally, vertically and a mixture of them. For horizontal adsorption (with the long axis parallel to the surface) a theoretical estimation predicts that the mass uptake

should be 173 ng cm^{-2} causing approximately a frequency change of -9.7 Hz. On the other hand, for vertical adsorption (with the long axis perpendicular to the surface) the calculation delivers a mass density increase of 461 ng cm^{-2} (corresponding to -25.9 Hz) (see appendix 6.5)[41-43]. Table 6.3 summarizes the adsorption of albumin on three different substrates and different pHs as well as the albumin orientation on the surface.

According to the frequency values of table 6.3, the fact that the adsorption values are high at pH 4.9 and pH 3.7 might indicate that albumin is adsorbed vertically. The difference between the mass uptakes might be related with differences in the HSA monolayer packing. That is, at pH 4.9 the albumin is neutral and it is expected to form very well packed monolayers, while at pH 3.7 HSA is positively charged and lateral electrostatic repulsion between the neighbouring molecules might diminish the packing density. Additional information about the monolayer packing can be obtained from the dissipation vs. time curves of figure 6.6. It can be observed that the dissipation increases after injection of the protein in the first 15 minutes, achieving afterwards a plateau. After rinsing with buffer and water, the final dissipation decreases to very low values (see table 6.3). The dissipation is similar for pH 3.7 and pH 4.9 systems while the dissipation is close to zero for the system studied at pH 7.4 (note that at these support there is not protein adsorption).

The results demonstrate that on silicon oxide is not possible to have protein adsorption at physiological conditions. Therefore, other alternative supports must be used in order to immobilize albumin.

Substrate	pH	ΔF(Hz) PBS	ΔF(Hz) water	Δm (ng cm^{-2}) PBS	Δm (ng cm^{-2}) water	ΔD(x10^{-6}) PBS	ΔD(x10^{-6}) water	orientation
SiO$_2$	7.4	-1.57	-0.26	28	7	0.38	0.35	no adsorption
	4.9	-39.80	-31.37	704	555	1.50	1.17	vertical
	3.7	-32.24	-25.55	571	452	1.66	1.10	vertical
PDADMAC	7.4	-13.50	-10.7	247	189	0.42	0.31	horizontal
Glutaraldehyde	7.4	-17.97	-14.43	318	255	0.48	0.34	combined
	4.9	-29.43	-27.29	521	483	0.90	0.54	Possibly vertical
	3.7	-23.25	-22.89	411	405	0.28	0.15	combined

Table 6.3. Frequency (ΔF), mass density (Δm) and dissipation (ΔD) change and adsorption orientation characteristic of HSA adsorption on SiO$_2$, PEM and glutaraldehyde at different pHs. Δm is calculated from ΔF applying Sauerbrey equation.

Silicon oxide surfaces can be easily modified with polymer coatings using the layer by layer technique[19] (see scheme 6.2). Since HSA is negatively charged at physiological conditions, we were interested in creating a positive polymer support. This was achieved by using polycationic PDADMAC. New QCM-D experiments were performed to investigate the adsorption of HSA on PDADMAC (see appendix 6.6). As it can be observed albumin is successfully adsorbed being the final mass uptake of 250 ng cm^{-2}. This fact indicates that albumin adsorbs horizontally.
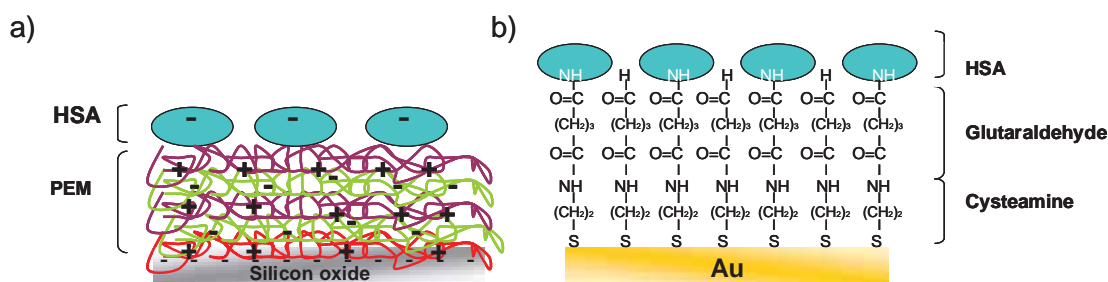
Scheme 6.2. HSA immobilization strategies: a) silicon oxide surfaces coated with PEI(PSS/PDADMAC)$_2$ for electrostatic immobilization of HSA, b) gold surfaces functionalized first with cysteamine hydrochloride followed by glutaraldehyde for HSA immobilization thought protein amine groups.

Another strategy to immobilize albumin on solid supports consisted of modify gold surfaces with glutaraldehyde. The adsorption of albumin on PDADMAC was mainly driven by electrostatic interactions. The idea behind modifying surfaces with glutaraldehyde is to bind HSA covalently through amine groups (see scheme 6.2). The mass uptake of cross-liked albumin at physiological conditions was obtained from QCM-D experiments (see appendix 6.7) as it is summarized in table 6.3. The results show that the mass uptake of HSA through cross-linking to the surface is larger than the results obtained on PDADMAC substrates. As it can be observed chemical immobilization is larger than electrostatic adsorption on PDADMAC. In addition, the dissipation values for albumin layer on glutaraldehyde and PDADMAC are similar, indicating rigid albumin layer formation (see table 6.3).

It has been observed that pH variation influences albumin immobilization on glutaraldehyde. The values in table 6.3 show that albumin adsorption has a maximum (521 ng cm^{-2}) at the isoelectric point of the proteins, probably acquiring vertical conformation. This fact is also observed when albumin is adsorbed on silicon oxide

surfaces. A question to be discussed is if aggregates of HSA were adsorbed on the surface. Electrophoretic mobility measurements (see appendix 6.8) indicate that albumin does not aggregate near the isoelectric point at the working experimental time scale. Figure 6.7 shows the variation of the mass density as a function of protein concentration. It can be observed that the mass uptake rises with concentration from 0.2 mg ml^{-1} to 0.6 mg ml^{-1} indicating a diffusion controlled adsorption. The results also show that for concentrations larger than 0.6 mg ml^{-1} the adsorbed mass is constant (330 ng cm^{-2}).
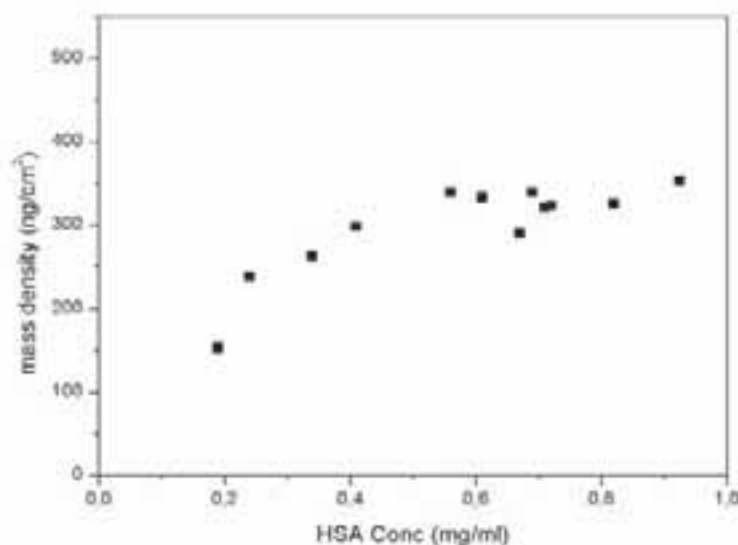
Figure 6.7. HSA adsorption mass density as a function of albumin concentration on glutaraldehyde functionalized surfaces. The data were acquired by QCM-D and the experiments were carried out in PBS at pH 7.4.

Once the best experimental conditions of protein immobilization were established we proceed to test the functionality of the adsorbed albumin monolayer. Immobilized HSA was exposed in static condition to bilirubin and ibuprofen in two different experiments. The corresponding QCM-D data (see appendix 6.9) did not clarify if the binding of bilirubin and ibuprofen was successful. However, albumin and its complexes are normally under flow at physiological conditions. Therefore we designed another strategy to study the interaction of albumin and albumin complexes with surfaces under flow conditions. Figure 6.8 shows the variation of frequency and dissipation as a function of time for the adsorption of HSA and HSA complexes on PDADMAC (figure 6.8a) and glutaraldehyde (figure 6.8b) supports. In these

experiments, the albumin flow was constant (50 μl min^{-1}). Figure 6.8a shows two different adsorption trends. On one hand, the change in frequency as a function of time shows that the complex HSA-bilirubin is eight times lower than the adsorption HSA and HSA-ibuprofen (table 6.4 shows these values in detail). On the other hand, the adsorption of HSA and HSA-ibuprofen is similar but three times larger than the adsorption of HSA in static conditions (which indicate protein multilayer formation).

a)

b)
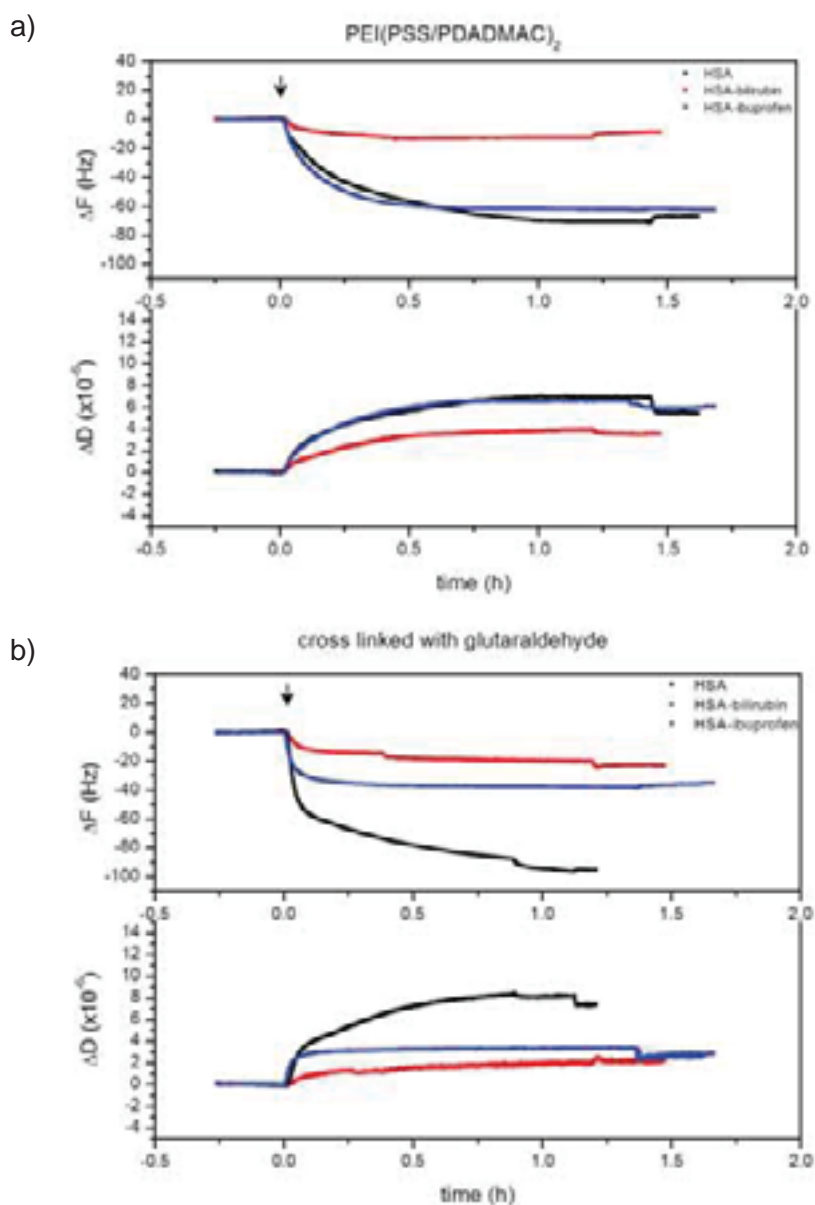
Figure 6.8. Frequency and dissipation change as a function of time of HSA (black), HSA-bilirubin (red) and HSA-ibuprofen (blue) at continuous flow (50 μl min^{-1}) on a) PDADMAC and b) cross-linked with glutaraldehyde.

The variation in dissipation also follows two different behaviours being larger for HSA-ibuprofen complex than for HSA-bilirubin complex. In particular, the value

obtained for HSA under flow conditions is higher than the value obtained under static conditions, indicating that the protein layer is less rigid. Figure 6.8b shows that chemical modification of the surface, changes the main adsorption behaviour with respect to the former case. In this case, the complex HSA-bilirubin again presents the lowest adsorption, while the adsorption efficiency of HSA-ibuprofen complex is reduced in a 50% with respect to PDADMAC system (see table 6.4). In addition, HSA adsorption on glutaraldehyde is even larger than on PDADMAC.

According to the dissipation curves HSA-bilirubin and HSA-ibuprofen complexes layers might have similar viscoelastic properties while the value obtained for pure HSA reveals very lousy and dissipative layer.

Substrate	Protein/ complex	$\Delta F(Hz)$	Δm (ng cm^{-2})	$\Delta D(\times 10^{-6})$
PDADMAC	HSA	-67.3	1186	5.4
	HSA-bilr	-8.6	152	3.5
	HSA-ibup	-62.8	1111	5.3
glutaraldehyde	HSA	-95.4	1681	7.4
	HSA-bilr	-22.6	400	2.2
	HSA-ibup	-40.0	708	2.4

Table 6.4. Frequency shift (ΔF), adsorption mass density (Δm) and dissipation (ΔD) values obtained from QCM-D experiments at continuous flow (50 µl min^{-1}) of HSA, HSA-bilirubin (HSA-bilr) and HSA-ibuprofen (HSA-ibup) adsorption on positively charged PDADMAC and glutaraldehyde carried out at physiological conditions.

In a more specific way, the HSA mass uptake reaches values of 1186 ng cm^{-2} on PDADMAC and 1681 ng cm^{-2} on glutaraldehyde. If a mass uptake of 250-310 ng cm^{-2} was described as a protein monolayer a value larger than 1000 ng cm^{-2} might mean protein multilayer formation. This might be the reason for the high dissipation values. We should also point out that the mass per unit area obtained for albumin complexes at continuous flow differs from the values obtained for HSA. The mass density of HSA-ibuprofen complex on PDADMAC is 1111 ng cm^{-2}, similar to the value of HSA while on glutaraldehyde HSA-ibuprofen reaches only 708 ng cm^{-2}. On the other hand the mass per unit area values measured for HSA-bilirubin are 152 ng cm^{-2} and 400 ng cm^{-2} for PDADMAC and glutaraldehyde respectively.
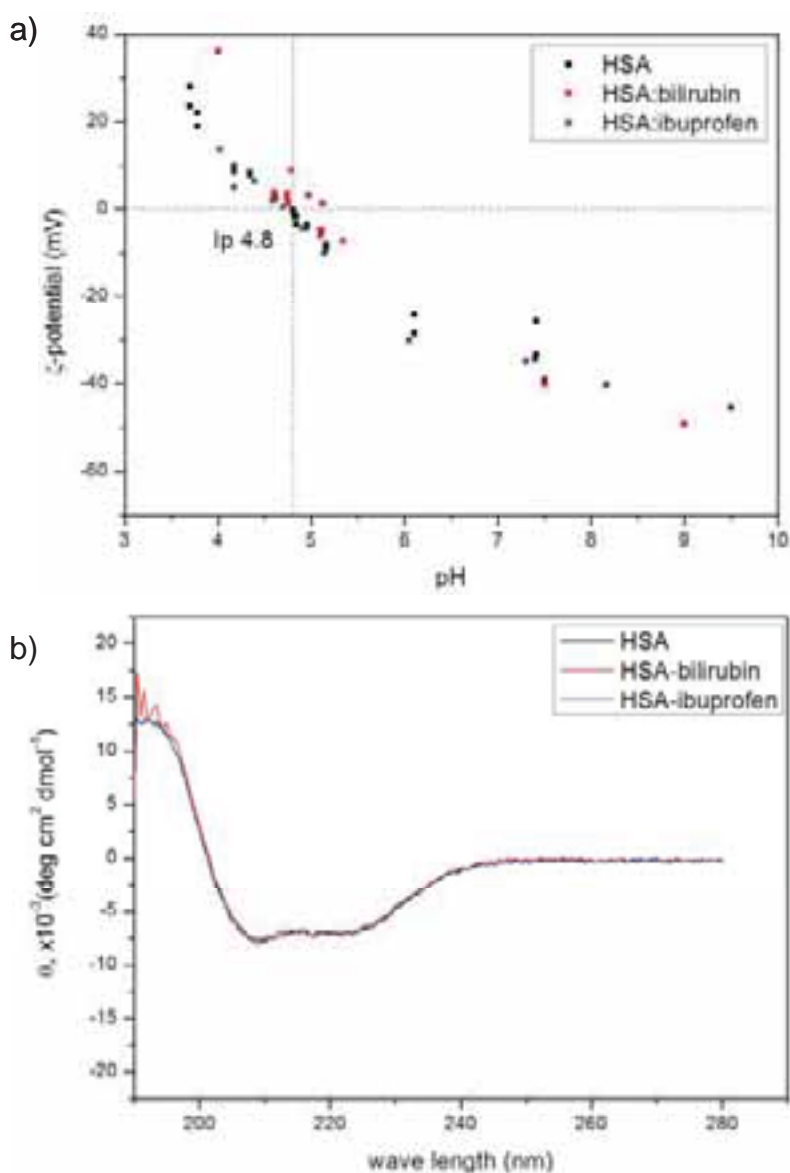
Figure 6.9. Free HSA (black), HSA-bilirubin (red) and HSA-ibuprofen (blue) complexes, a) Zeta potential (ζ) and b) circular dichroism.

As a complementary measurement, the ζ-potential of HSA, HSA-bilirubin and HSA-ibuprofen was determined between pH 4 and pH 9 (figure 6.9a) in solution[p]. The isoelectric point of HSA is pH 4.8 and it does not change when HSA is binding neither ibuprofen nor bilirubin. Furthermore, circular dichroism experiments (see figure 6.9b) also show that when albumin binds to the drugs it does not change its secondary structure.

---

[p] These experiments were compared with free BSA and complexes formed with BSA

In aqueous solution most of protein hydrophobic residues are hidden inside the protein while the surface tent to be more hydrophilic. Upon adsorption, proteins modify their structure and rearrange hydrophobic and hydrophilic residues. In this process they lose their original secondary structure.

The albumin multilayer formation can be explained by the adsorption of albumin on previous denatured protein layer. This will be supported by the fact that albumin does not form aggregates in solution and that after one hour no more protein is adsorbed although fresh albumin is injected continuously in the measuring chamber. HSA-bilirubin complex shows a different behaviour, which seems to form a monolayer on PDADMAC and glutaraldehyde. In this case, even though the complex solution is continuously changed no more adsorption takes place after 30 minutes. It might be reasonable to think that the binding of HSA with bilirubin may stabilize the protein in a way that the restructuration upon adsorption is minimal. However, this is not observed in the case of HSA-ibuprofen complex. The adsorption curve on PDADMAC is similar to the one obtained for free HSA whereas after cross-linked with glutaraldehyde the adsorbed mass is reduced. This fact may indicate that the adsorption of the HSA-ibuprofen complex on glutaraldehyde suffers less structural modifications than on cationic PDADMAC.

6.4 Conclusions

In this chapter we have study the binding properties and the thermodynamic stability of single albumin, albumin-ibuprofen complexes and albumin-bilirubin complexes. We have also investigated the experimental conditions for the immobilization of albumin and albumin complexes on solid surfaces under static and flow conditions.

DSC experiments show that the denaturation temperature (T_m) for albumin is about 64.6ºC while for the albumin complexes is around 67ºC. Thus, the complexes are more stable against temperature variations.

The Gibbs free energy and the affinity constant of the complex formation were determined from ITC experiments. In the case of HSA ibuprofen the binding stechiometry was 1:1 while in the case of HSA:bilirubin was 1:2. The binding constants

indicate that the interaction between bilirubin and HSA is stronger than the interaction between ibuprofen and HSA.

Albumin was immobilized on three main surfaces; hydrophilic silicon oxide, cationic PDADMAC and glutaraldehyde. The experiments carried out at different pHs on silicon oxide and glutaraldehyde indicate that the highest adsorption of albumin takes place at pH 4.9 (near its isoelectric point). However, at physiological conditions (pH 7.4) the best supports for albumin immobilization were PDADMAC and glutaraldehyde achieving a superficial mass density of 247 ng cm^{-2} and 353 ng cm^{-2} respectively.

Experiments carried out under flow conditions show that the immobilization of HSA and HSA-ibuprofen and HSA-bilirubin is different on PDADMAC and glutaraldehyde at physiological conditions. Although albumin adsorption is very high (upper 1000 ng cm^{-2}) leading to protein multilayer formation, more interesting is the different behaviour observed of the albumin complexes on PDADMAC and glutaraldehyde. The complex HSA-bilirubin adsorbs as a monolayer on both substrates while the complex formed by HSA-ibuprofen has more affinity to PDADMAC. The adsorption of the albumin complexes seems to depend on the type of molecule that binds to albumin and the corresponding binding stechiometry.

6.5 References

[1]   W.M. He, D.C. Carter, *Nature* 358 (1992) 209-215.

[2]   D.C. Carter, J.X. Ho, *Adv. Protein Chem.* 45 (1994) 153-203

[3]   Y.-Q. Wang, H.-M. Zhang, G.-C. Zhang, W.-H. Tao, S.-H. Tang, *J. Mol. Struct.* 830 (2007) 40-45.

[4]   B. Stopa, J. Rybarska, A. Drozd, L. Konieczny, M. Król, M. Lisowski, B. Piekarska, I. Roterman, P. Spólnik, G. Zemanek, *Int. J. Biol. Macromol.* 40 (2006) 1-8.

[5]   Y.-J. Hu, Y. Ou-Yang, C.-M. Dai, Y. Liu, X.-H. Xiao, *Biomacromolecules* (2009).

[6]   E.L. Gelamo, M. Tabak, *Spectrochim. Acta A* 56 (2000) 2255-2271.

[7]   J. T. Peters, *All about Albumin, biochemistry, genetics and medical applications*, Academic Press, San Diego, 1996.

[8]   C.E. Petersen, C.-E. Ha, K. Harohalli, J.B. Feix, N.V. Bhagavan, *J. Biol. Chem.* 275 (2000) 20985-20995.

[9]   H. Athar, N. Ahmad, S. Tayyab, M.A. Qasim, *Int. J. Biol. Macromol.* 25 (1999) 353-358.

[10]   Z. Moosavi-Movahedi, H. Bahrami, M. Zahedi, K. Mahnam, J. Chamani, S. Safarian, A.A. Saboury, A.A. Moosavi-Movahedi, *Biophys. Chem.* 125 (2007) 375-387.

[11]   E. Magosso, M. Ursino, L. Colì, O. Baraldi, L. Bolondi, S. Stefoni, *Artif. Organs* 30 (2006) 285-300.

[12]   M.A. Cheema, P. Taboada, S. Barbosa, J. Juárez, M. Gutiérrez-Pichel, M. Siddiq, V. Mosquera, *J. Chem. Thermodyn.* 41 (2009) 439-447.

[13]   J. Everse, N. Hsia, *Free Rad. Biol. Med.* 22 (1997) 1075-1099.

[14]   M.A. Brito, R.F.M. Silva, D. Brites, *Clin. Chim. Acta* 374 (2006) 46-56.

[15]   A.-H. Wu, M.-J. Syu, *Biosens. Bioelectron.* 21 (2006) 2345-2353.

[16]   G.R. Gourley, *Adv. Pediatr.* 44 (1997) 173-229.

[17]   J.L. Oncley, *Biophys. Chem.* 100 (2003) 151-158.

[18]   M. Tencer, R. Charbonneau, N. Lahoud, P. Berini, , *Appl. Surf. Sci.* 253 (2007) 9209-9214.

[19]   G. Decher, *Science* 277 (1997) 1232-1237.

[20]   H.-W. Fang, M.-C. Hsieh, H.-T. Huang, C.-Y. Tsai, M.-H. Chang, *Colloid Surface B* 68 (2009) 171-177.

[21]   Q. Zhang, Y. Huan, R. Zhao, G. Liu, Y. Chen, *Biosens. Bioelectron.* 24 (2008) 48-54.

[22]   Y. Liu, Y. Li, S. Liu, J. Li, S. Yao, *Biomaterials* 25 (2004) 5725-5733.

[23]   R.M.C. Dawson, D.C. Elliot, W.H. Elliot, K. Jones, *Data for biochemical research*, Clarendon Press, Oxford, 1986.

[24]   C.E. Ahlfors, *Anal. Biochem.* 110 (1981) 295-307.

[25]   J.P. Folkers, P.E. Laibinis, G.M. Whitesides, *Langmuir* 8 (1992) 1330-1341.

[26]   Z. Moosavi-Movahedi, S. Safarian, M. Zahedi, M. Sadeghi, A.A. Saboury, J. Chamani, H. Bahrami, A. Ashraf-Modarres, A.A. Moosavi-Movahedi, *Protein J.* 25 (2006) 193-201.

[27]   G. Sauerbrey, *Z. Phys.* 155 (1959) 206.

[28]   L.E. Valenti, P.A. Fiorito, C.D. García, C.E. Giacomelli, *J. Colloid Interf. Sci.* 307 (2007) 349-356.

[29]   T. Kosa, T. Maruyama, M. Otagiri, *Pharm. Res.* 15 (1998) 449-454.

[30]   G. Picó, *Int. J. Biol. Macromol.* 20 (1997) 63-73.

[31]   C. Giancola, C.D. Sena, D. Fessas, G. Graziano, G. Barone, *Int. J. Biol. Macromol.* 20 (1997) 193-204.

[32]   G. Barone, C. Giancola, A. Verdoliva, *Thermochim. Acta* 199 (1992) 197-205.

[33]   R.G. Müller, K. Schmid, *Thermochim. Acta* 15 (1983) 115-125.

[34]   A.W.P. Vermeer, W. Norde, *Biophys. J.* 78 (2000) 394-404.

[35]   H. Aki, M. Goto, M. Yamamoto, *Thermochim. Acta* 251 (1995) 379-388.

[36]   G.H. Breaven, A. D'Albis, W.B. Gratzer, *Eur. J. Biochem.* 33 (1973) 500-509

[37]   V.T.G. Chuang, M. Otagiri, *Chirality* 18 (2006) 159-166.

[38]   G.A. Holdgate, W.H.J. Ward, *Drug Discov. Today* 10 (2005) 1543-1550.

[39]   J. Jacobsen, *Int. J. Pept. Prot. Res.* 9 (1977) 235-239

[40]   B. Kainz, K. Steiner, U.B. Sleytr, D. Pum, J.L. Toca-Herrera, *Soft Matter* 6 (2010) 3809-3814.

[41]   T.J. Su, J.R. Lu, R.K. Thomas, Z.F. Cui, J. Penfold, *J. Phys. Chem. B* 102 (1998) 8100-8108.

[42]   T.J. Su, J.R. Lu, R.K. Thomas, Z.F. Cui, , *J. Phys. Chem. B* 103 (1999) 3727-3736.

[43]   S. Demanèche, J.-P. Chapel, L.J. Monrozier, H. Quiquampoix, *Colloid Surface B* 70 (2009) 226-231.

Chapter 7

Single molecular interaction between HSA and ibuprofen

In the previous chapter the binding of albumin with ibuprofen and bilirubin was monitored in solution with calorimetric experiments. Although albumin was successfully immobilized on cationic PDADMAC and glutaraldehyde surfaces, it was not shown if the adsorbed protein was able to bind to ibuprofen or bilirubin. In this chapter, we have explored a new strategy to investigate the functionality of the adsorbed albumin monolayer; the forces between the adsorbed albumin and ibuprofen have been measured by atomic force spectroscopy.

7.1 Introduction

Molecular recognition is involved in many biological events such as antigen and antibody recognition, molecular transport, lectin and carbohydrate interactions, ligands and cellular receptors, cell adhesion etc. Such interactions are non-covalent, of short range and depending on the recognition site geometry and orientation [1-4]

The binding between proteins with specific ligands is among other things, protein structure dependant. So, any structural rearrangement in proteins might affect the binding with the ligand. Adsorption is one of those events where the protein undergoes structural rearrangements and might cause the lost of its bioactivity [5-7] Therefore, the quantification of the biological surface activity is very important to

develop bioanalytical techniques and bioimmunosensor surfaces which are of medical and pharmacological interest [8].

Atomic Force Microscopy (AFM) is not only a suitable technique to obtain high resolution images of the morphology of biological surfaces under physiological conditions [9, 10]; by means of single molecular force spectroscopy studies it possible to measure molecular forces down to few piconewton as well as to characterize the elastic behaviour of biomaterials at the nanoscale [2, 11-15]. In particular, force spectroscopy has been used successfully to measure forces between individual molecules (e.g. ligand-receptor complexes). This type of experiments allows to understand the energetic landscape of the interaction by quantifying the distance to the transition state and the dissociation rate constant (K_{off}), which is well explained in the work by *Bell et al.* and *Evans and Richtie* [16, 17].

In these experiments the proteins (receptors) are usually immobilized on a substrate while the AFM tip is functionalized with the ligand. The next step is to approach the tip to the surface with the receptor. This can be done at different approaching rate (speed) and at different loads (force exerted on the surface). Once the tip approaches the surface the ligand and receptor complex can be formed. These experiments also permit to vary the ligand-receptor residence time. Then, by pulling the tip away from the unbinding forces of the complex can be measured. An important point to take into account is the binding strength of the receptor and ligand to the substrate and AFM-tip respectively, which must be stronger than the intermolecular forces between both molecules. This is normally achieve by using SAMs or cross linking agents [1].

The importance of this kind of studies has grown in the last 15 years; many biological systems have been investigated by single force spectroscopy, among them we can cite, the interactions of avidin-biotin or biotin-streptavidin, digoxigenin–antibody complex or $\alpha_5\beta_1$ integrin-fibronectin [18-23].

HSA (66.7 kDa), the most prominent plasma protein, is a globular heart-shaped molecule with size of 8 x 8 x 3 nm^3. Its structure presents three main domains named I, II and III, with different grooves and pockets where a wide variety of endogenous and exogenous compounds (eg. bile pigments, fatty acids, drugs, etc.) can be bound to be transported through the blood [24]. The ligands can bind in different binding sites with

different binding affinities but often they also might compete for the same binding pockets which might influence in the effectivity of the drug distribution. The control of such events is especially important in pharmaceutical industry and medicine because albumin is responsible to carry a variety of drugs. Among them ibuprofen is one of the most widely used drug due to its antipyretic, analgesic, and antibacterial activity binding to albumin in the subdomains IIA and IIIA [25].

In this chapter, force spectroscopy is used as a tool to study HSA adlayer bioactivity by means of measuring the force between ibuprofen and immobilized HSA on glutaraldehyde. We also show a procedure to immobilize ibuprofen on gold coated tips. The funcionalization of gold surface with Ibuprofen-$N(EG)_6C_{11}SH$ has also been investigated with QCM-D measurements, contact angle and ellipsometry.

7.2 Materials and methods

Materials

Ibuprofen sodium salt (Mw. 228 g mol^{-1}) and human serum albumin (HSA), 66.4 kDa, were purchased from Sigma. $N_3(EG)_6C_{11}Ac$ (Mw. 535 g mol^{-1}) and $OH(EG)_3C_{11}SH$ (Mw. 336 g mol^{-1}) were supplied by prochimia [q]. N-(3-dimethylaminopropyl)-N'-ethylcarbodiimide hydrochloride (EDCI) and N-hydrosuccinimide (NHS) were supplied by Sigam. Sodium methoxide (MeONa) used in desacetilation was purchased from Sigma**.** Trimethilphosphine (PMe$_3$) and 4-dimethylaminopyridine (dmap) used as a basic catalyzer in the peptidic coupling was provided from Sigma. Amberlite H and sodium sulfate (Na$_2$SO$_4$) were purchased from Sigma.

Methanol (MeOH), tetrahydrofuran (THF), dimethylformamide (DMF), ethyl acetate, ethanol (Scharlau), acetone (Sigma-aldrich) ether were used as solvents. Cysteamine hydrochloride and glutaraldehyde (25%) for gold functionalization were provided by Sigma.

---

[q] EG (ethylene glycol)= $(CH_2CH_2O)_n$, C (methylene)= $(CH_2)_n$, SAc (thioacetate)=$SCOCH_3$

The buffers were prepared with sodium hydroxide (NaOH) Sigma, sodium dihydrogen phosphate anhydrous (NaH_2PO_4) and sodium phosphate dibasic anhydrous (Na_2HPO_4) from Fluka. Finally, mica supports were provided by SPI.

Surface preparation

Gold film deposition on mica. Gold films were deposited on mica (1 x 1 cm^2) using the magnetron sputtering technique (ATC 1800, AJA). A 100 nm gold layer was deposited at 150 W, in argon atmosphere at a pressure of 3 mTorr and during the deposition the substrates rotates at 50 rpm for better uniformity. The deposition time was 4 minutes. The samples were not previously heated. The main of the main vacuum chamber was at $1x10^{-8}$ Torr.

Substrates cleaning procedure. Gold substrates were cleaned alternating ethanol and acetone solutions. The substrates were left in each solvent for 30 minutes. Then, the substrates were treated with ultraviolet radiation (UV-ozone, Bioforce nanoscience) for 30 minutes.

HSA immobilization. Gold substrates were immersed in cysteamine hydrochloride water (20 mM) solution overnight which was covered with aluminum foil. The substrates were rinsed with water to remove excess of cysteamine hydrochloride. Afterwards, the sensor was immersed in 1% glutaraldehyde aqueous for 1 hour. Then, the sensors were rinsed gently with water before use for albumin immobilization. Finally, the functionalized gold supports were immersed in a solution of 1 mg ml^{-1} HSA and left incubating for one hour. The sensors were rinsed with water and used immediately after biofunctionalization. All the steps were carried out at room temperature [26, 27].

Synthesis of Ibuprofen-N(EG)$_6$C$_{11}$SH

Ibuprofen-N(EG)$_6$C$_{11}$SH was synthesized using ibuprofen sodium salt and N$_3$(EG)$_6$C$_{11}$SAc as initial compounds.

For the N$_3$(EG)$_6$C$_{11}$-SAc thioacetate selective deprotection 50 mg (0.093 mmol) of N$_3$(EG)$_6$C$_{11}$SAc were dissolved in 1 ml of MeOH. Then, 155 µl of 0.25 M MeONa were added at 0ºC and left reacting in argon atmosphere at room temperature overnight. When the reaction was finished acid amberlite-H was added and left for 30 minutes to

neutralize the solution. The product was filtrated and evaporated. 40 mg of $N_3(EG)_6C_{11}SH$ (Mw. 493 g mol^{-1}) were obtained (see figure 7.1a). Yield: 85%; ^1H NMR (500 MHz, CDCl$_3$): d=3.65 (m, 18 H), 3.57 (m 2H), 3.43 (t, J=6.8 Hz, 2H), 3.38 (t, J=5.1 Hz, 2H), 2.67 (t, J=7.4 Hz, 0.65 H, (2 H, S$_2$ %)), 2.51 (q, J=7.4 Hz, 1.35 H, (2 H, SH %)), 1.61 (m, 4 H, CH$_2$), 1.37-1.26 (m, 16 H, CH$_2$) ppm (see appendix 7.1a).

Then, the reduction of the azide was carried out following *Staudinger reaction* [28]. 40 mg (0.081 mmol) of $N_3(EG)_6C_{11}$-SH were dissolved in 2 ml of dry THF and 24.4 µl (0.25 mmol) of PMe$_3$ were added with a Hamilton syringe. Iminophosphorane intermediate compound was formed through nucleophilic addition of the PMe$_3$ at the terminal nitrogen atom of the azide and nitrogen was expulsed. Subsequently, water was added to hydrolyze the intermediate to amine and trimethylphosphine oxide. The reaction was left in a close system (without argon) at room temperature overnight. To separate organic and inorganic components 1M NaOH and ethyl acetate were added and stirred while the PMe$_3$ remains were removed by vacuum. The balloon was immersed in ice water to avoid too fast evaporation. 30 mg (0.064 mmol) $NH_2(EG)_6C_{11}SH$ (M$_w$. 467 g mol^{-1}) were achieved (see figure 1a). Yield: 80 %; ^1H NMR (500 MHz, CDCl$_3$): d=3.54 (m, 24 H, CH$_2$O, CH$_2$N), 2.91 (m, 2 H, CH$_2$-SH), 2.67 (t, J=7.4 Hz, 2 H, CH$_2$-S-S), 1.95 (m, 2 H, NH$_2$), 1.62 (m, 4 H, CH$_2$), 1.31 (m, 16 H, CH$_2$) ppm (see appendix 7.1b). The results show that there is a mixture of $NH_2(EG)_6C_{11}SH$ and its disulfide.
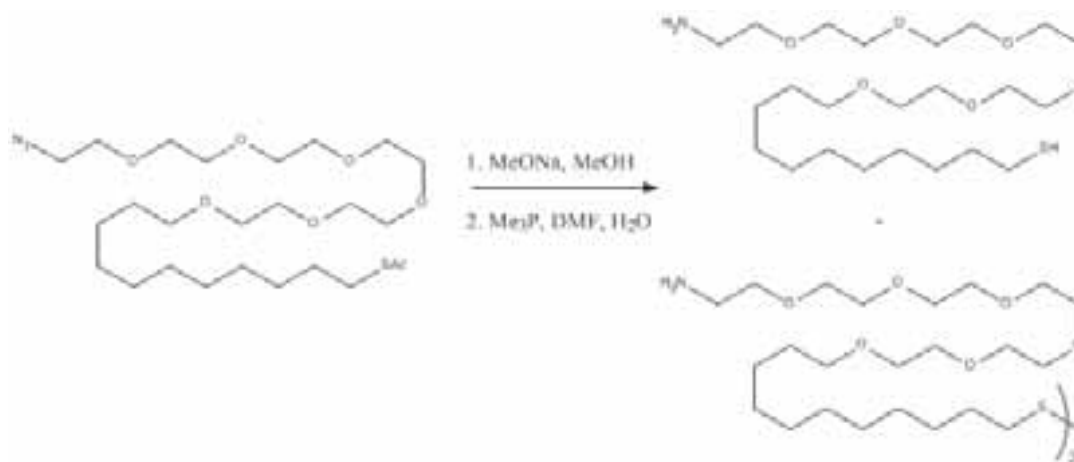
Figure 7.1. $N_3(EG)_6C_{11}$-SAc thioacetate deprotection reaction (1) and the reduction of the azide by Staudinger reaction (2) to obtain $NH_2(EG)_6C_{11}SH$. The product ($NH_2(EG)_6C_{11}SH$) is partially oxidized as a disulfide.

On the other hand, ibuprofen sodium salt activation was carried out by NHS/EDCI where NHS is used as an activator to mediate EDCI reaction on carboxyl to amine containing molecule. 144 mg (0.63 mmol) of ibuprofen sodium salt (M_w. 228 g mol^{-1}), 356 mg (1.85 mmol) of EDCI and 143 mg (1.24 mmol) of NHS were dissolved in 1 ml of water and 3 ml of DMF and left reacting overnight. The active ibuprofen was extracted with a mixture of ether and water. Finally, the excess of water was removed adding NaS_2O_4 and the solution was filtrated and evaporated in vacuum to remove the DMF. 146 mg (0.48 mmol) of activated ibuprofen were obtained (see figure 7.2). Yield: 78 %; ^{1}H NMR (500 MHz, $CDCl_3$): d=7.18 (d, J=8.1 Hz, 2 H, C_6H_4), 7.06 (d, J=8.1 Hz, 2 H, C_6H_4), 3.95 (q, J=7.2 Hz, 1 H, CH-CO), 2.69 (m, J=7.2 Hz, 4 H, C_2CO), 2.38 (d, J=7.2 Hz, 2 H, CH_2), 1.78 (m, 1 H, CH), 1.55 (d, J=7.2 Hz, 3 H, CH_3), 0.83 (d, J=6.7 Hz, 6 H, CH_3) ppm (see appendix 7.1c).
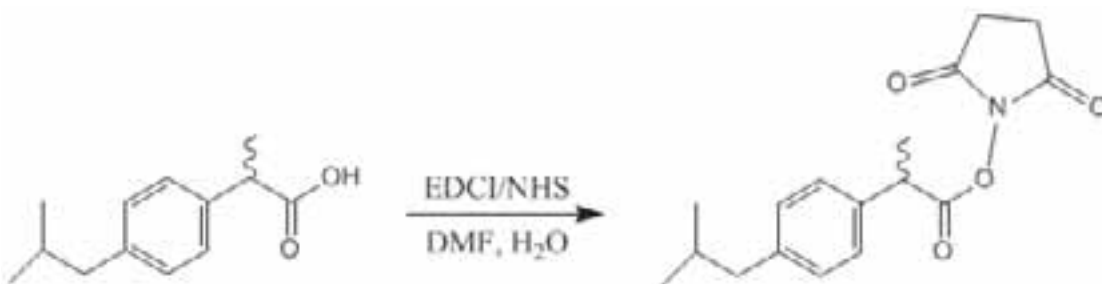
Figure 7.2. Activation reaction of ibuprofen by EDCI/NHS.

Finally, the peptidic coupling was carried out between 7.7 mg (0.025 mmol) of activated ibuprofen (M_w. 304 g mol^{-1}) and 10 mg (0.021 mmol) $NH_2(EG)_6C_{11}SH$ (M_w. 467 g mol^{-1}) mixed in 1.35 ml of DMF with 2 mg (0.0164 mmol) of Dmap at room temperature. The reaction was left stirring overnight. The organic compound was extracted with ether/water solution. The excess of water was removed by Na_2SO_4 and the final compound was filtrated and evaporated. The synthesis was monitorized until all $NH_2(EG)_6C_{11}SH$ reacted with the activated ibuprofen (figure 7.3). 11 mg of a mixture of ibuprofen-$N(EG)_6C_{11}SH$ (M_w. 655 g mol^{-1}) and activated ibuprofen was obtained (see figure 7.3) in 1:1 ratio as the ^{1}H RMN spectrum showed. In addition, ibuprofen-$N(EG)_6C_{11}SH$ is partially found as a disulfide. The compound was used to functionalize gold surfaces without further purification. The gold substrate will act as a filter leading only the adsorption of ibuprofen-$N(EG)_6C_{11}SH$.
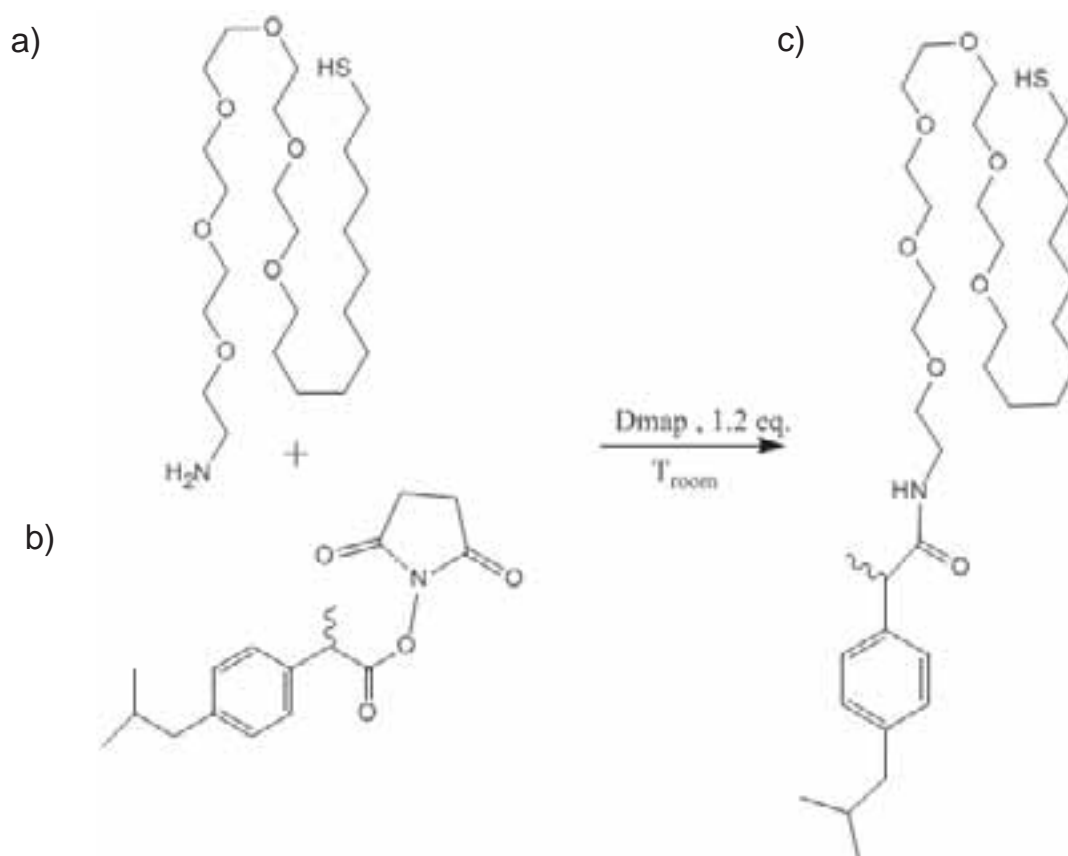
Figure 7.3. Peptidic coupling between a) $NH_2(EG)_6C_{11}SH$ and b) active ibuprofen to obtain c) Ibuprofen-$N(EG)_6C_{11}SH$. The thiol compounds ($NH_2(EG)_6C_{11}SH$ and ibuprofen-$N(EG)_6C_{11}SH$) are partially oxidize as a disulfide.

Methods

Atomic Force Microscopy (AFM). AFM topographic images were recorded in 100 mM NaCl aqueous solution in tapping mode (at 1 Hz) at room temperature using a Multimode AFM with a Nanoscope V controller (Veeco, Santa Barbara, USA). Silicon nitride (Si_3N_4) cantilevers of 0.32 N m^{-1} spring constant with sharpened tips (DNP-S, Veeco) were used and cleaned in ethanol and acetone before use.

For single molecular force spectroscopy two sides gold coated silicon nitride cantilevers (NP-S, Veeco) of 0.22 N m^{-1} spring constant were used. The gold coated tips were functionalized immersing the sensors in a 1 mM thiol mixture formed by Ibuprofen-$N(EG)_6C_{11}SH$ and $OHC_{11}SH$ (1:3) in ethanol and left incubating overnight.

Force-volume measurements were carried out on a to 250 x 250 nm^2 surface area. The pulling speeds were varied from 0.05 μm s^{-1} to 5 μm s^{-1} maintaining the load on the

surface approximately constant at 1.5 nN. All the data were processed with the v720 (Veeco) software. Force histograms were fitted with a Gaussian equation in order to obtain the most probable unbinding force (the software used was origin 7.0).

Quartz Crystal Microbalance with Dissipation Monitoring (QCM-D).
A QCM-D (QE401 (electronic unit)/QFM401 (flow module) instrument from Q-sense AB (Gothenburg, Sweden) was used to characterize the adsorption of Ibuprofen-$N(EG)_6C_{11}SH$ and $NH_2(EG)_6C_{11}SH$ on gold surfaces overnight. The thiol solutions 1.5 mM were prepared in ethanol. The presented results correspond to the 5 overtone. The QCM-D data were analyzed with Q-Tools (software provided by Q-Sense). The Sauerbrey equation was used to calculate mass density from the frequency change [29].

Contact angle. The wettability of Ibuprofen-$N(EG)_6C_{11}SH$ and $NH_2(EG)_6C_{11}SH$ functionalized gold substrates were determined by sessile-drop experiments performed with a contact-angle measurement device (KRUSS D100, Hamburg, Germany). Millipore water (specific resistance 18.2 MΩ cm^{-1}) was used as liquid phase. Three drops of water (2 μl) were deposited on each substrate.

Ellipsometry. The thickness of organic Ibuprofen-$N(EG)_6C_{11}SH$ and $NH_2(EG)_6C_{11}SH$ layers was measured with a commercial spectroscopic ellipsometer (M2000V J. A. Woollam Co. Inc., USA) in air. The changes in the ellipsometric angles, delta (Δ) and psi (Ψ), of elliptically polarized light upon reflection by a planar surface were obtained at different wavelengths and incident angles. Both the refractive index and film thickness could be calculated. Ellipsometric data, Δ and ψ, were acquired over a wavelength range from λ=380 to 1000 nm, at different incident angles varied between 45º-80º at room temperature. The thickness was obtained using the Cauchy dispersion equation assuming a refractive index of 1.45 for the SAM (see appendix 7.2) [30].

Nuclear Magnetic Resonance (NMR) studies were performed with a Bruker Avance 500MHz spectrometer equipped with a 5 mm double resonance inverse probe. One pulse experiments were recorded with 15 seconds of recycled delay and 64 transients. The proton spectral width of 8000 Hz and a total of 64k points were used with 90 degree pulse of 7.5 μs. The data was zero-filled to 128k points and then it was Fourier transformed. All the spectra were processed with Bruker TOPSPIN software.

7.3 Results and discussion

7.3.1 Ibuprofen-N(EG)$_6$C$_{11}$SH self assembly monolayer characterization on gold substrates.

Figure 7.4 shows frequency and dissipation curves of NH$_2$(EG)$_6$C$_{11}$SH and Ibuprofen-N(EG)$_6$C$_{11}$SH complex deposition on gold QCM-D sensors. The fast frequency decrease indicates that both, NH$_2$(EG)$_6$C$_{11}$SH and Ibuprofen-N(EG)$_6$C$_{11}$SH are attached to the gold substrate. The functionalized substrates were rinsed with ethanol after 22 hours of incubation.
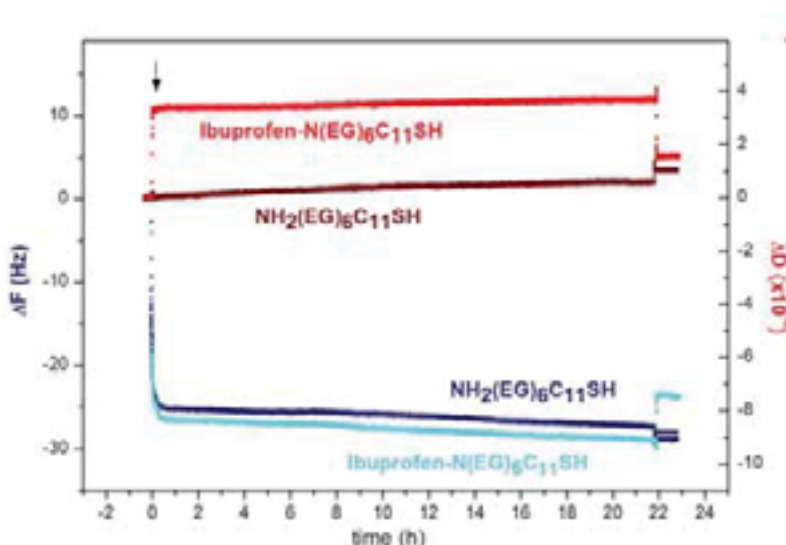
Figure 7.4. QCM-D frequency curves of NH$_2$(EG)$_6$C$_{11}$SH (dark blue) and ibuprofen-N(EG)$_6$C$_{11}$SH (cyan) and dissipation curves of NH$_2$(EG)$_6$C$_{11}$SH (brown) and ibuprofen-N(EG)$_6$C$_{11}$SH (red) on gold substrates. The black arrow at t=0 indicates the injection of the thiol compounds.

In the case of NH$_2$(EG)$_6$C$_{11}$SH (dark blue curve) the final frequency value is -27.9 ± 0.5 Hz which corresponds to a mass per unit area of 494 ng cm^{-2}. A look at the variation of the dissipation with time for NH$_2$(EG)$_6$C$_{11}$SH (brown curve) shows that the adsorbed SAM is well packed (rigid layer) reaching a values of about 0.8 x 10^{-6} ± 0.1 x 10^{-6}. A different behavior can be observed when Ibuprofen-N(EG)$_6$C$_{11}$SH is adsorbed. On one hand the variation of the frequency with time (cyan curve) reaches a value of -23.6 ± 0.1 Hz (418 ng cm^{-2}) after rinsing with ethanol. This value is lower than the obtained for NH$_2$(EG)$_6$C$_{11}$SH which means that the gold surface is less covered by the complex than

by $NH_2(EG)_6C_{11}SH$ molecules. On the other hand, the final value of dissipation is $(1.3 \pm 0.3) \times 10^{-6}$ which is larger than the value obtain for the reference molecule $NH_2(EG)_6C_{11}SH$. Therefore, since the size of the ibuprofen is larger than the amine group, it might happen that the steric interactions among ibuprofen molecules influences SAM package which implies less dense and more dissipative.

Although QCM-D results show the building up of the SAMs, these measurements did not deliver information about the hydrophobic behaviour of the created interface. At that point contact angle measurements are quick and effective method to distinguish the hydrophobic behaviour of the created functionalized layers that might be influence by different surface chemistry. The contact angle results are shown in figure 7.5. A contact angle of 61º was obtained for the gold substrate functionalized with $NH_2(EG)_6C_{11}$ SAM while a value of 90º was obtained when the gold surfaces was funtionalized with the complex Ibuprofen-$N(EG)_6C_{11}SH$. These results indicate that after SAM formation ibuprofen might be located at the interface, exposed to the aqueous phase. A film thickness of 3.2 nm was measured for both SAMs with ellipsometry (appendix 7.2) [31].
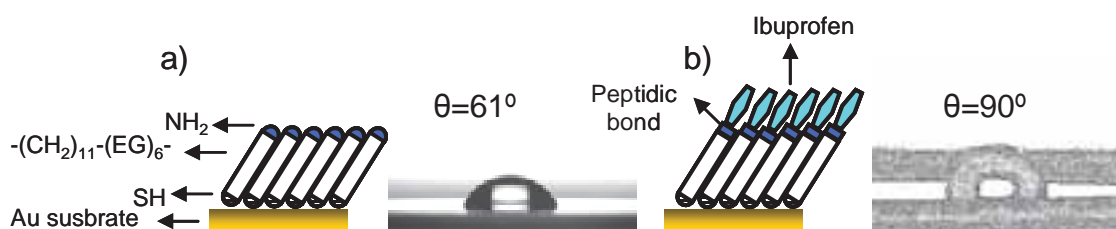
Figure 7.5. A diagram of a) $NH_2(EG)_6C_{11}SH$ and b) ibuprofen-$N(EG)_6C_{11}SH$ SAMs on gold substrates and their respective contact angle measurements. For contact angle measurements 2 µl (millipore) water drops were deposited on SAM coated substrates.

7.3.2 HSA adlayer morphology

Figure 7.6a is an AFM height image (250×250 nm^2) showing the topography of a gold surface functionalized with glutaraldehyde. The image vertical scale is 10 nm and the scale bar is 50 nm. The overall gold substrate roughness was 0.8 nm. However, the roughness of different gold grains (average area of 50×50 nm^2) was 0.3 nm. Figure

7.6b represents the height profile of the gold surface functionalized with glutaraldehyde along the white line shown in figure 7.6a.
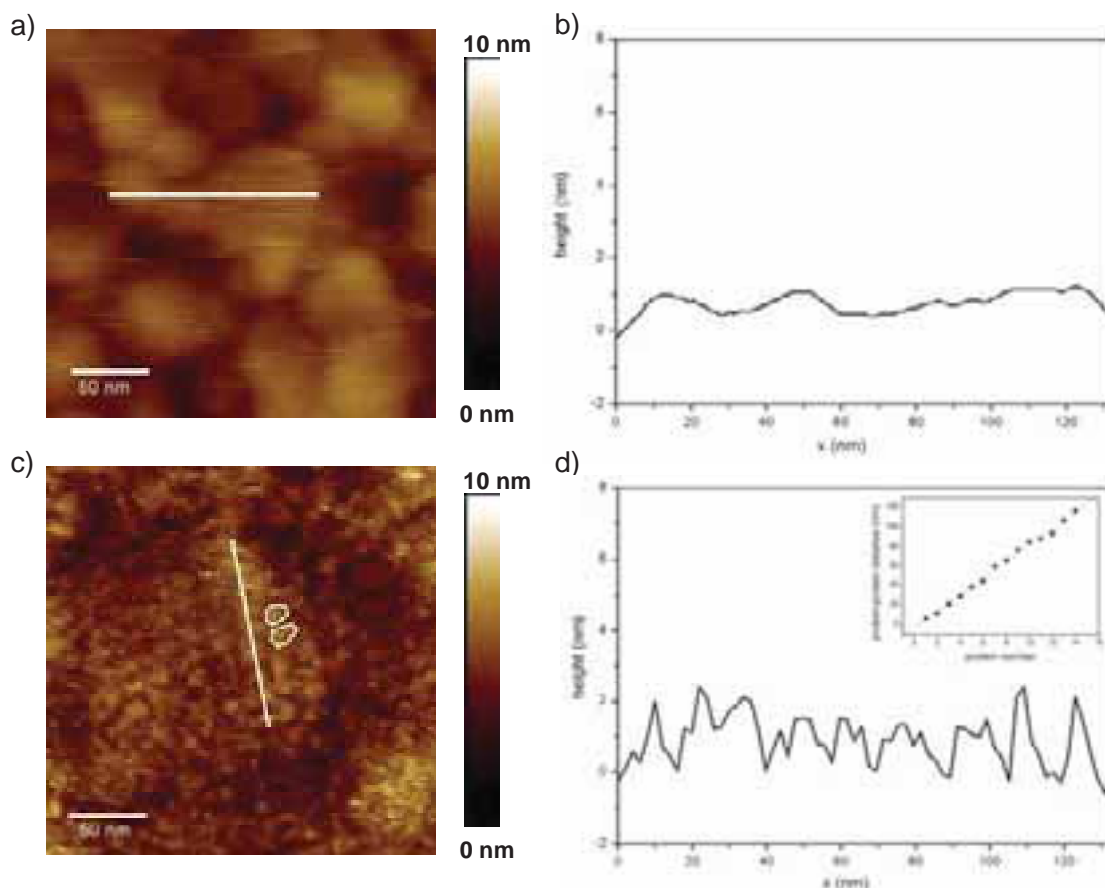
Figure 7.6. a) AFM height image (250 x 250 nm^2) of glutaraldehyde functionalized gold substrate. The white cross section shows the profile of gold/glutaraldehyde surface that is plotted in figure b), c) AFM height image (250 x 250 nm^2) of immobilized HSA with glutaraldehyde. The white circles indicate single HSA proteins and the white cross sections show the albumin profile which is plotted in d). The profile analysis carried out at different points of the surface show that the average height of HSA molecules is 1.8 nm. The inset in figure d) shows the protein-protein distance as a function of protein number. The data were fitted with a linear equation. The slope gives information about HSA width. (These analyses were carried out at 50 different points).

Figure 7.6c shows an AFM height micrograph of HSA immobilized on glutaraldehyde being the vertical scale 10 nm and the scale bar 50 nm. The figure shows that the surface is completely coated with albumin. The white circles in figure 7.6c depict single albumin molecules. In this case protein adsorption leads to an increase in roughness from 0.3 nm (gold surface) to 0.7 nm. Figure 7.6d shows a profile analysis of HSA immobilized on glutaraldehyde along the white line shown in figure 7.6d.

The calculated average height of albumin molecules is 1.8 ± 0.1 nm, while the average protein-protein distance is 8.1 ± 0.4 nm (see inset in figure 7.3d). From these values we can conclude that the thickness of the adsorbed protein seems to be smaller than the thickness measure in solution, while the lateral dimensions did not differ much[r]. This is in agreement with other reported investigations, in which the thickness of albumin adlayers varies depending on the substrate. For example, HSA thickness is 1.6 nm when adsorbed on titania, taking a value of 0.8 nm on gold surfaces [32].

7.3.3   Dynamic force spectroscopy between HSA and ibuprofen.

In section 7.3.1 we establish the conditions to functionalize gold surfaces with Ibuprofen-$N(EG)_6(CH_2)_{11}SH$. This know-how was useful to modify AFM gold tips. Figure 7.7a shows an illustration of the set up to carry out dynamic force spectroscopy experiments.   In this cartoon, it can be distinguish on one hand the gold tip functionalized with Ibuprofen-$N(EG)_6(CH_2)_{11}SH$, and on the other hand the gold substrate with adsorbed HSA.
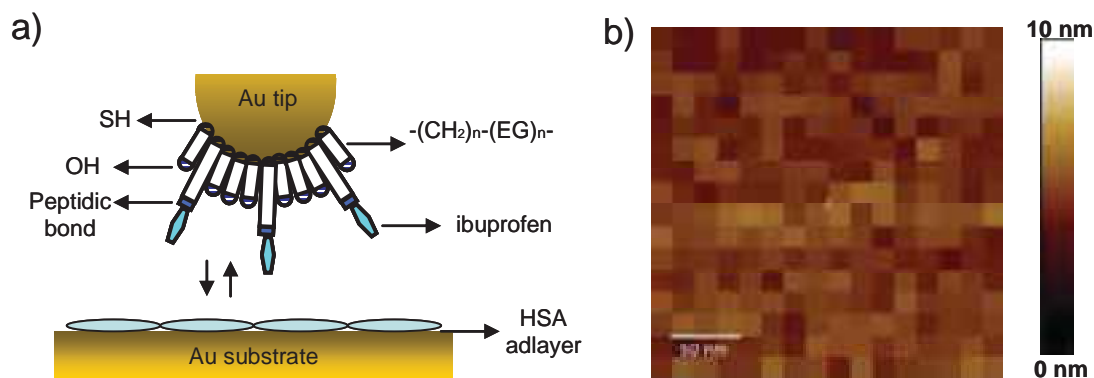
Figure 7.7. a) Schematic representation of force-distance curves experiments set up. The tip is functionalized with a mixture of Ibuprofen-$N(EG)_6(CH_2)_{11}SH$/$OH(EG)_3(CH_2)_{11}SH$ at 1:3 ratio. $OH(EG)_3(CH_2)_{11}SH$ is used as a diluter in order to promote separation between ibuprofen molecules. Since $OH(EG)_3(CH_2)_{11}SH$ is shorter the ibuprofen is found as a protruding groups. On the other hand, HSA is cross linked with glutaraldehyde on gold substrate. The tip will be approached and retracted in order to bind ibuprofen with albumin, b) Force-Volume image where an area of 250 x 250 nm^2 has been divided in 256 squares of 243 nm^2. A force curve was obtained from each section.

---

[r] In this type of measurements the resolution is influenced by the curvature of the tip and can induce little deviations from the real value (convolution effect).

The idea of dynamic force spectroscopy experiments is to approach and retract the ibuprofen functionalized tip to the HSA surface at different speeds (at constant residence time). The unbinding force of the ibuprofen-albumin complex is measured after tip retraction from the surface. Figure 7.6c showed the coverage of the gold/glutaraldehyde surface with albumin molecules. The ibuprofen albumin interaction was measured using force volume approach. In this approach, the gold surface covered with albumin was divided equally in 256 squares of 243 nm^2, as it is described in scheme figure 7.7b. One force curve was obtained from each square.

a)

b)
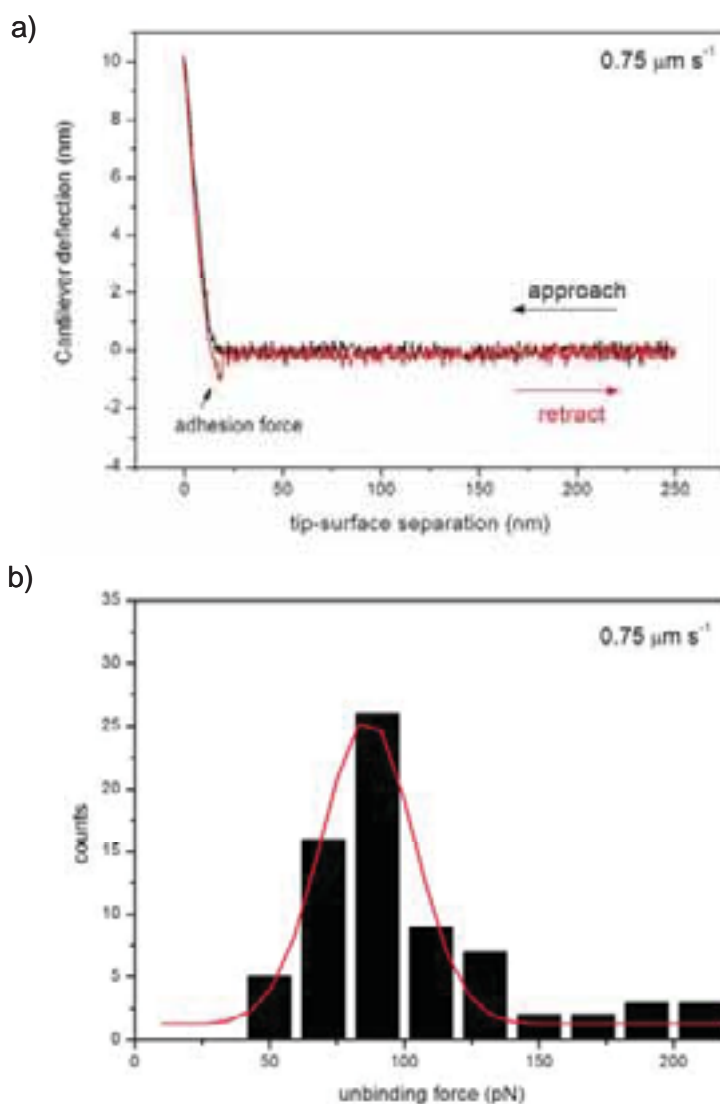
Figure 7.8. a) Force-distance curves obtained in 10 mM phosphate buffer at pH 7.4 at 0.751 μm s^{-1} of HSA modified surface and ibuprofen modified tip. b) Histogram of the unbinding force. The bin size has been taken between 20-30 pN (see appendix 7.3). The histograms were fitted using a Gaussian equation.

A typical force-distance curve for ibuprofen-HSA unbinding experiment is shown in figure 7.8a. The black curve refers to the approaching tip while the red curve indicates the separation of the tip from the surface. When the tip is retracted from the surface a unique adhesion peak at short distances can be observed. Force-Volume experiments show that adhesion peaks only takes place for 30 % of the albumin coated area[s]. The nature of this kind of measurements is probabilistic. Figure 7.8b is a representative histogram of the unbinding of ibuprofen albumin force at 0.75 μm s^{-1}. Normally these histograms are fitted with a Gaussian curve, being the maximum of the curve the most probable adhesion force. The unbinding or adhesive forces obtained for a specific approaching rate is just one point of the whole force spectrum. Thus, the unbinding forces were calculated changing the pulling speed between 0.05 μm s^{-1} and 4.88 μm s^{-1} (see appendix 7.4).

Figure 7.9 illustrates the unbinding forces of the ibuprofen-HSA system as a function of the natural logarithm of the pulling speed. The results show in figure 7.9 that the unbinding forces vary between 68-105 pN.
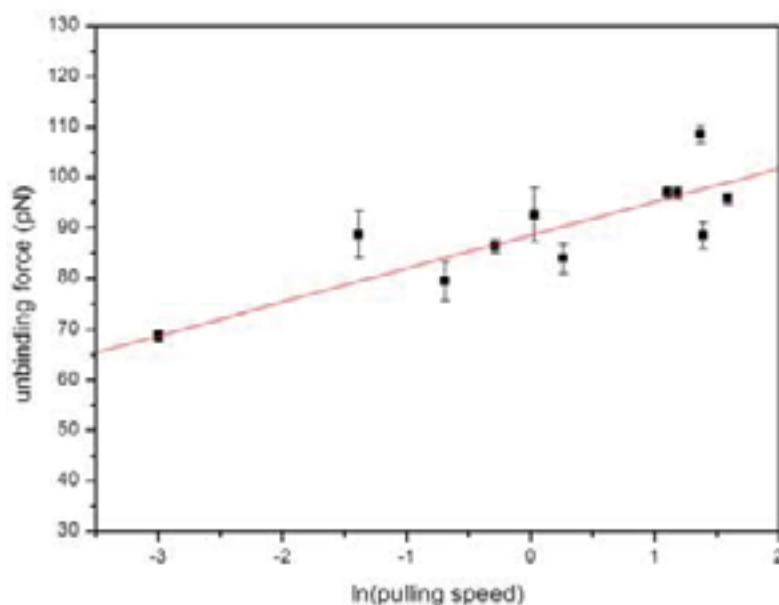
Figure 7.9. Dynamic force spectroscopy measurements of the single albumin-ibuprofen interaction carried out at pulling speeds between 0.05 μm s^{-1} and 0.5 μm s^{-1} in phosphate buffer at pH 7.4. Each unbinding force value is calculated from their respective histogram (see appendix 7.4).

---

[s] This percentage is reduced to 8% for non functionalized gold tips (see appendix 7.4).

In previous works it has been proved that unbinding forces and polymer unfolding depend on loading rate (pulling speed) [15]. Theoretically, this is based on the idea that the applied force distorts the energy landscape of any given ligand-receptor system, in this case HSA-ibuprofen, lowering the activation barrier energy and increasing the dissociation rate constant [16, 17, 33]. The unbinding rate follows a general equation given by.

$$F = \left(\frac{k_b T}{x_u}\right)\ln\left(\frac{x_u k_e v}{k_b T v_0}\right) + \frac{\Delta G}{x_u} \qquad (1)$$

Where F is the mechanical force, k_b is the Boltzmann's constant, T is the temperature, K_e is the effective spring constant, x_u is the width of the potential in the bound state (distance of the transition state), v the pulling speed and v_0 is the vibrational frequency of the bond.

Since the dissociation rate constant (K_{off}) is $K_{off} = v_0 e^{(-\Delta G / K_b T)}$, equation (1) can be expressed as;

$$F = \left(\frac{k_b T}{x_u}\right)\ln\left(\frac{x_u k_e v}{k_b T K_{off}}\right) \qquad (2)$$

The rupture force *(F)* distribution can be expressed as a linear function of the natural logarithm of the pulling speed *(v)*.

$$F = \left(\frac{k_b T}{x_u}\right)\ln\left(\frac{x_u k_e}{k_b T K_{off}}\right) + \left(\frac{k_b T}{x_u}\right)\ln v \qquad (3)$$

Thus, we might be able to calculate the dissociation rate constant at zero force (K_{off}) (see appendix 7.5) [20, 22, 34, 35].

The experimental results of the HSA-ibuprofen unbinding forces as a function of pulling speed were fitted with a linear equation[t]. The slope of the fit is related to the distance of the transition state (x_u) through the thermal energy k_bT (see equation 3). Taking into account that the experimental temperature was 296 K the calculated transition state distance is 0.6 nm. This confirms that ibuprofen-HSA unbinding process is a two state transition process. However, other systems such us $\alpha_5\beta_1$-integrin/fibronecting can present more than one transition state, 0.4 nm for the first transition state and 0.08 nm for the second one [20]. Other studies concerning the mechanical unfolding of proteins have reported values of 0.8 nm for extracellular tenacin and 0.3 nm for the muscle protein titin (see appendix 7.6).

An important kinetic parameter that can be obtained from the dependence of the unbinding force on the pulling speed is the dissociation rate constant (K_{off}) (see appendix 7.6), which is 0.055 s^{-1} for the HSA-ibuprofen system. This value is larger than other typical values for protein-ligand interactions such as biotin-streptavidin and biotin-avidin where the K_{off} is 2.4 x 10^{-6} and 7.5x 10^{-8} respectively [33]. The large dissociation rate (and the low unbinding forces) might indicate that such specific forces between ibuprofen and albumin do not occur, probably due to albumin structural changes suffered after adsorption.

7.4 Conclusion

Dynamic force spectroscopy has been used to measure the forces between gold tips functionalized with ibuprofen on albumin adsorbed monolayers.

Concerning surface functionalization, QCM-D, contact angle and ellipsometry results show that Ibuprofen-(EG)$_6$C$_{11}$-SH molecule can form well packed SAMs on gold surfaces. Moreover, AFM show that glutaraldehyde functionalized gold surface is completely covered with HSA molecules. However, the height of albumin proteins decreases from 3 nm (value in solution) to 1.8 nm (value on glutaldehyde functionalized gold substrate) meaning that upon adsorption HSA undergoes structural changes.

Finally, from dynamic force spectroscopy it is shown that the dependence of the unbinding force as a function of the pulling speed leads to a value of 0.6 nm for the distance of the transition state and a value of 0.055 s^{-1} for the dissociation rate. These

---

[t] *y=1.8 x10^{-10} + 6.6 x10^{-12}x (in international system units, IS)*

results indicate that albumin not only change its structure when it is adsorbed on glutaraldehyde but it also might loses its functionality.

7.5 References

[1]   P. Hinterdorfer, Y.F. Dufrêne, *Nat. methods* 3 (2006) 347-355.

[2]   G.U. Lee, D.A. Kidwell, R.J. Colton, *Langmuir* 10 (1994) 354-357.

[3]   S. Lin, J.-L. Chen, L.-S. Huang, H.-W. Lin, *Current proteom.* 2 (2005) 55-81.

[4]   A. Touhami, B. Hoffmann, A. Vasella, F.A. Denis, Y.F. Dufrêne, *Langmuir* 19 (2003) 1745-1751.

[5]   C.A. Haynes, W. Norde, *J. Colloid Interf. Sci.* 169 (1995).

[6]   J.F. Mooney, A.J. Hunt, J.R. Mcintosh, C.A. Liberko, D.M. Walba, C.T. Rogers, *P. Natl. Acad. Sci.* 93 (1996) 12287-12291.

[7]   T. Vermonden, C.E. Giacomelli, W. Norde, *Langmuir* 17 (2001) 3734-3740.

[8]   F. Cecchet, A.-S. Duwez, S. Gabriel, C. Jérôme, R. Jérôme, K. Glinel, S. Demoustier-Champagne, A.M. Jonas, B. Nysten, *Anal. Chem.* 79 (2007) 6488-6495.

[9]   Y.L. Lyubchenko, *Micron* 42 (2011) 196-206.

[10]   A.S. Paulo, R. García, *Biophys. J.* 78 (2000) 1599-1605.

[11]   G. Binning, D.P.E. Smith, *Rev. Sci. Instrum.* 57 (1986) 1688.

[12]   U. Dammer, M. Hegner, D. Anselmetti, P. Wagner, M. Dreier, W. Huber, H.-J. Güntherodt, G.N. Misevic, *Biophys. J.* 70 (1996) 2437-2441.

[13]   C.H. Chen, S.M. Vesecky, A.A. Gewirth, *J. Am. Chem. Soc.* 114 (1992) 451-459.

[14]   M. Pierce, J. Stuart, A. Pungor, P. Dryden, V. Hlady, *Langmuir* 10 (1994) 3217-3238.

[15]   R.B. Best, D.J. Brockwell, J.L. Toca-Herrera, A.W. Blake, A. Smith, S.E. Radford, J. Clarke, *Anal. Chim. Acta* 479 (2003) 87-105

[16]   G.I. Bell, *Science* 200 (1978) 618-627.

[17]   E. Evans, K. Ritchie, *Biophys. J.* 72 (1997) 1541-1555.

[18]   E.-L. Florin, V.T. Moi, H.E. Gaub, *Science* 264 (1994) 415-417.

[19]   C. Stroh, H. Wang, R. Bash, B. Ashcroft, J. Nelson, H. Gruber, D. Lohr, S.M. Lindsay, P. Hinterdorfer, *P. Natl. Acad. Sci.* 101 (2004) 12503-12507.

[20]   F. Li, S.D. Redick, H.P. Erickson, V.T. Moy, *Biophys. J.* 84 (2003) 1252-1262

[21]   P.P. Lehenkari, M.A. Horton., *Biochem. Bioph. Res. Co.* 259 (1999) 645-650.

[22]   R. Merkel, P. Nassoy, A. Leung, K. Ritchie, E. Evans, *Nature* 397 (1999) 50-53.

[23]   G. Neuert, C. Albrecht, E. Pamir, H.E. Gaub, *FEBS Lett.* 580 (2008) 505-509.

[24]   J. T. Peters, *All about Albumin, biochemistry, genetics and medical applications*, Academic Press, San Diego. 1996.

[25]   G. Fanali, P. Ascenzi, M. Fasano, *Biophys. Chem.* 129 (2007) 29–35.

[26]   Q. Zhang, Y. Huan, R. Zhao, G. Liu, Y. Chen, *Biosens. Bioelectron.* 24 (2008) 48–54

[27]   Y. Liu, Y. Li, S. Liu, J. Li, S. Yao, *Biomaterials* 25 (2004) 5725-5733.

[28]   Y.G. Gololobov, I.N. Zhmurova, L.F. Kasukhin, *Tetrahedron* 37 (1981) 437-472.

[29]   G. Sauerbrey, *Z. Phys* 155 (1959) 206-222.

[30]   J.P. Folkers, P.E. Laibinis, G.M. Whitesides, *Langmuir* 8 (1992) 1330-1341.

[31]   C.D. Bain, J. Evall, G.M. Whitesides, *J. Am. Chem. Soc.* 111 (1989) 7155-7164.

[32]   I.V.D. Keere, R. Willaert, E. Tourwé, A. Hubin, J. Vereecken, *Surf. Interface Anal.* 40 (2008) 157-161.

[33]   U. Piran, W.J. Riordan, *J. Immunol. methods* 133 (1990) 141-143.

[34]   T. Strunz, K. Oroszlan, I. Schumakovitch, H.-J. Güntherodt, M. Hegner, *Biophys. J.* 79 (2000) 1206-1212.

[35]   G. Neuert, C. Albrecht, E. Pamir, H.E. Gaub, *FEBS Lett.* 580 (2006) 505-509.

Chapter 8

Conclusions and future work

The adsorption, self-assembly, structure and function of S-protein (SbpA) and Human Serum Albumin (HSA) have been investigated using controlled surface modification strategies.

On one hand, Self Assembly Monolayers (SAMs) of different well-defined chemistry were used to induce new S-protein recrystallization pathways. The monitoring at real time of S-protein self-assembly demonstrated that S-protein recrystallization takes place in three steps: adsorption, recrystallization (self-assembly) and crystalline domain reorganization.

The S-protein adsorbed and recrystallized independently of surface chemistry, with the only exception of OH terminated thiols. The protein thickness layer, the final protein adsorbed mass and lattice parameters were not affected by surface chemistry.

However, the protein-substrate affinity (adsorption rate) influences the S-layer domain size. Hydrophobic (CH_3, NH_2) and charged (COOH) SAMs induce faster adsorption than hydrophilic silicon oxide. Quantitatively, protein domain size is large and unidirectional on silicon oxide surface (32 μm^2), while on hydrophobic and $COOHC_{10}S$ surfaces the domains are small and differ in lattice direction (0.02-0.008 μm^2). Partial S-layer recrystallization occurs on hydrophilic $ManC_5S$ SAMs.

S-layer formation also depends on S-protein concentration. Protein adsorption is a diffusion dependant process, being the threshold concentrations 0.5 mg ml^{-1} on hydrophobic and COOHC$_{10}$S substrates and 0.7 mg ml^{-1} on silicon oxide. Furthermore, the crystalline domain size decreases with concentration except for COOHC$_{10}$S SAMs. Amorphous and crystalline biopolymers based on polylactide derivatives have been proved to be suitable surfaces for S-layer recrystallization. S-protein adsorption and recrystallization pathway is also influenced by pH variation. Nevertheless, the shear modulus and the viscosity of the recrystallized S-layer on COOHC$_{10}$S substrate do not vary significantly with pH.

The thermal stability of albumin, albumin-ibuprofen and albumin-bilirubin have been determined. Albumin complexes are more stable than single albumin molecules. Furthermore, negative Gibbs free energy of HSA-ibuprofen (ratio 1:1) and HSA-bilirubin (ratio 1:2) confirms that HSA-bilirubin complex is the most stable.

Surface chemistry strategies have been used to adsorb albumin on silicon oxide, positively charged PDADMAC and glutaraldehyde.

Adsorption of HSA on silicon oxide was successful at pH 3.7 and 4.9, leading to a protein monolayer, but was not possible at physiological pH.

Glutaraldehyde modified surfaces were suitable for HSA adsorption at physiological conditions, increasing with protein concentration (diffusion controlled) until reaching a threshold of 0.5 mg ml^{-1}. AFM images height analysis show that after adsorption on glutaraldehyde albumin thickness decreases, indicating albumin structural modifications.

The adsorption of the albumin complexes on PDADMAC and glutaraldehyde depends on the type of molecule that binds to albumin and the corresponding binding stechiometry.

Dynamic force spectroscopy experiments between functionalized AFM tip with ibuprofen and adsorbed albumin on glutaraldehyde, permitted the calculation of the the distance to the transition state (0.6 nm) and the dissociation rate constant, K$_{off}$, (0.055 s^{-1}). The high dissociation constant value indicates the loose of HSA functionality after adsorbed on glutaraldehyde.

Some open questions remain to investigate in the near future. In the case of S-protein adsorption, new chemistry will be needed to control of protein domain size and the influence of the surface roughness in the S-layer formation. Techniques high resolution AFM images at real time can be combined with molecular simulations to explain and predict protein crystallization and domain growth. This will be especially useful to be able to recrystallize S-layer fusion proteins at different interfaces creating ordered functionalities on a bacterial based nanostructure scaffold.

The immobilization of proteins in general will need the development of new surface strategies linked to synthetic biology if we want to keep protein functionality in order to create smart biomimetic materials.

Dynamic force spectroscopy has still a long way in proving and testing the functionality of proteins at interfaces. AFM tip modification with clean organic chemistry as well as new scanner development making possible to carry out experiments at very low speeds will deliver new valuable information about the energetic landscape of the interaction between molecules.

Appendix I-chapter 3

Appendix 3.1
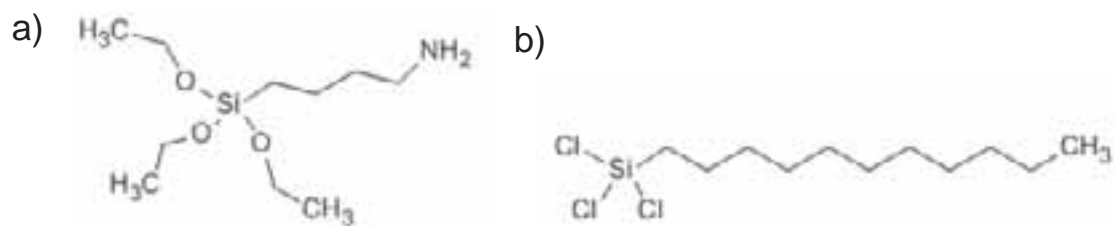
Molecular structures of a) 3-aminopropyltriethoxysilane (APTS) and
b) n-ocatecyltrichlorosilane (OTS)

c) Contact angle images of a water droplet on SiO_2, and on silicon dioxide coated with
APTS and OTS.

Appendix 3.2
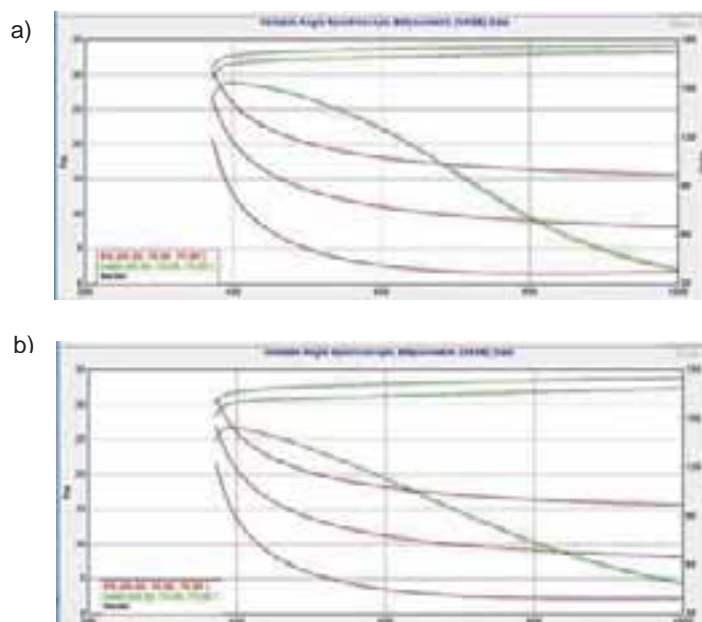
Ellipsometry Ψ (red) and Δ (green) data of silicon dioxide functionalized with a) APTS
and b) OTS. Ψ and Δ data were fitted with the Cauchy model.

Appendix 3.3
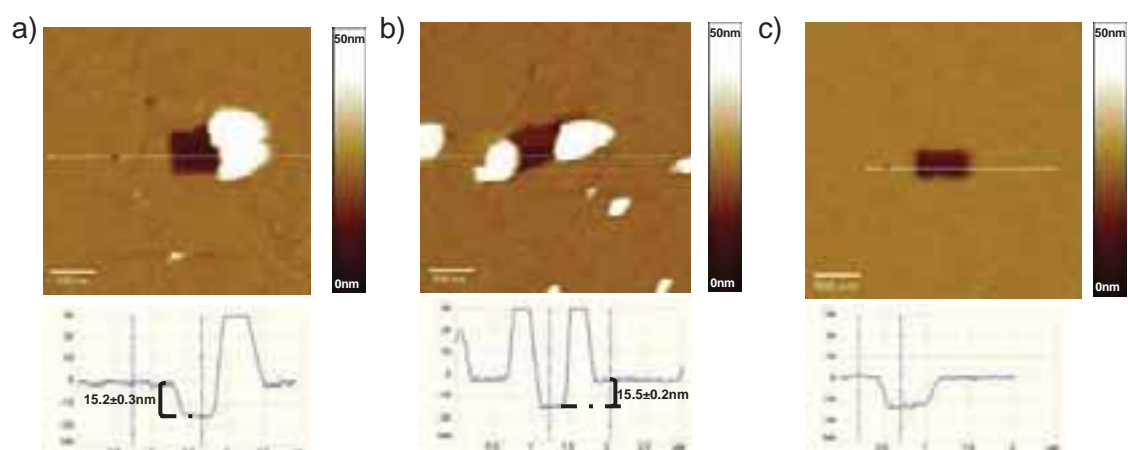
a) AFM-scratching on SbpA protein layer on SiO$_2$. Note that the thickness of the protein layer is ca. 15.2 nm, b) AFM scratching on SbpA protein layer on OTS. Note that the thickness of the protein layer is ca. 15.5 nm, c) AFM scratching on SbpA protein layer on APTS. Note that the thickness of the protein layer is ca. 15.5 nm. In these three cases the minimum shear force is 10 nN.

Appendix 3.4
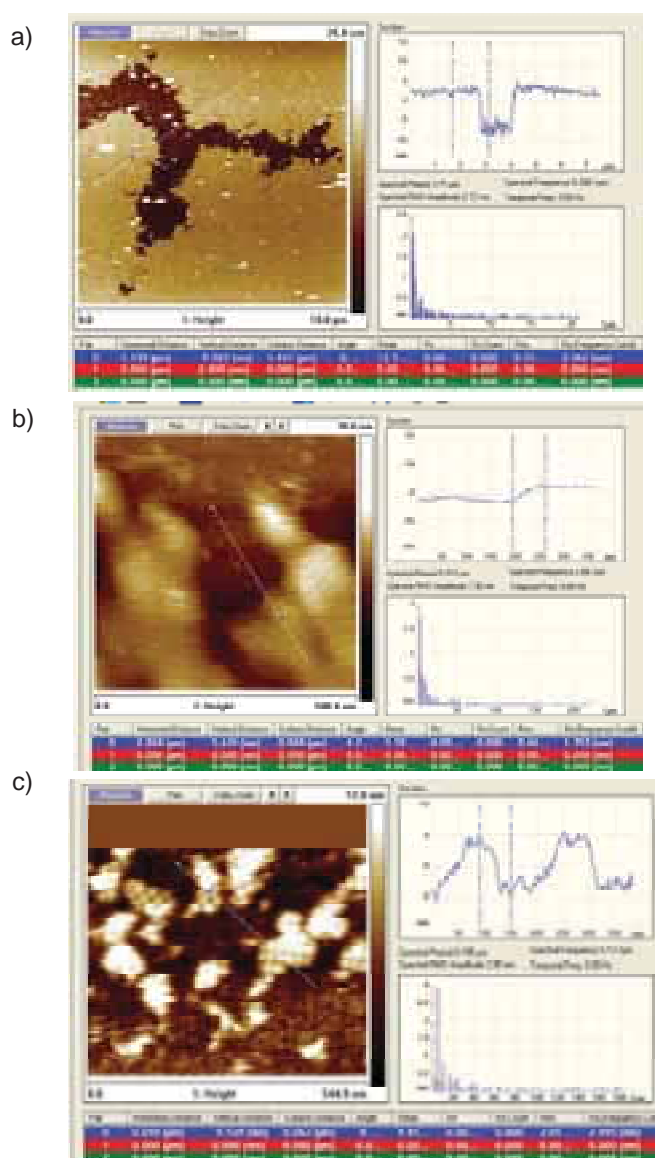
a) AFM profile of SbpA protein layer on SiO_2. The profile analysis along the white line shows that the difference in thickness between the protein front (bright area) and the substrate (dark area) is 9.5 nm. This value is closer to the thickness of a protein monomer.

b) AFM profile of SbpA recrystallized on OTS. The profile analysis along the white line shows that the difference in thickness between the crystalline protein layer (bright area) and the "substrate" (dark area) is ca. 6 nm, which does not correspond to a protein dimer.

c) AFM profile of SbpA recrystallized on APTS. The profile analysis along the white line shows that the difference in thickness between the crystalline protein layer (bright area) and the "substrate" (dark area) is approximately 9 nm, which corresponds to the thickness of a protein.

Appendix II-Chapter 4

Appendix 4.1
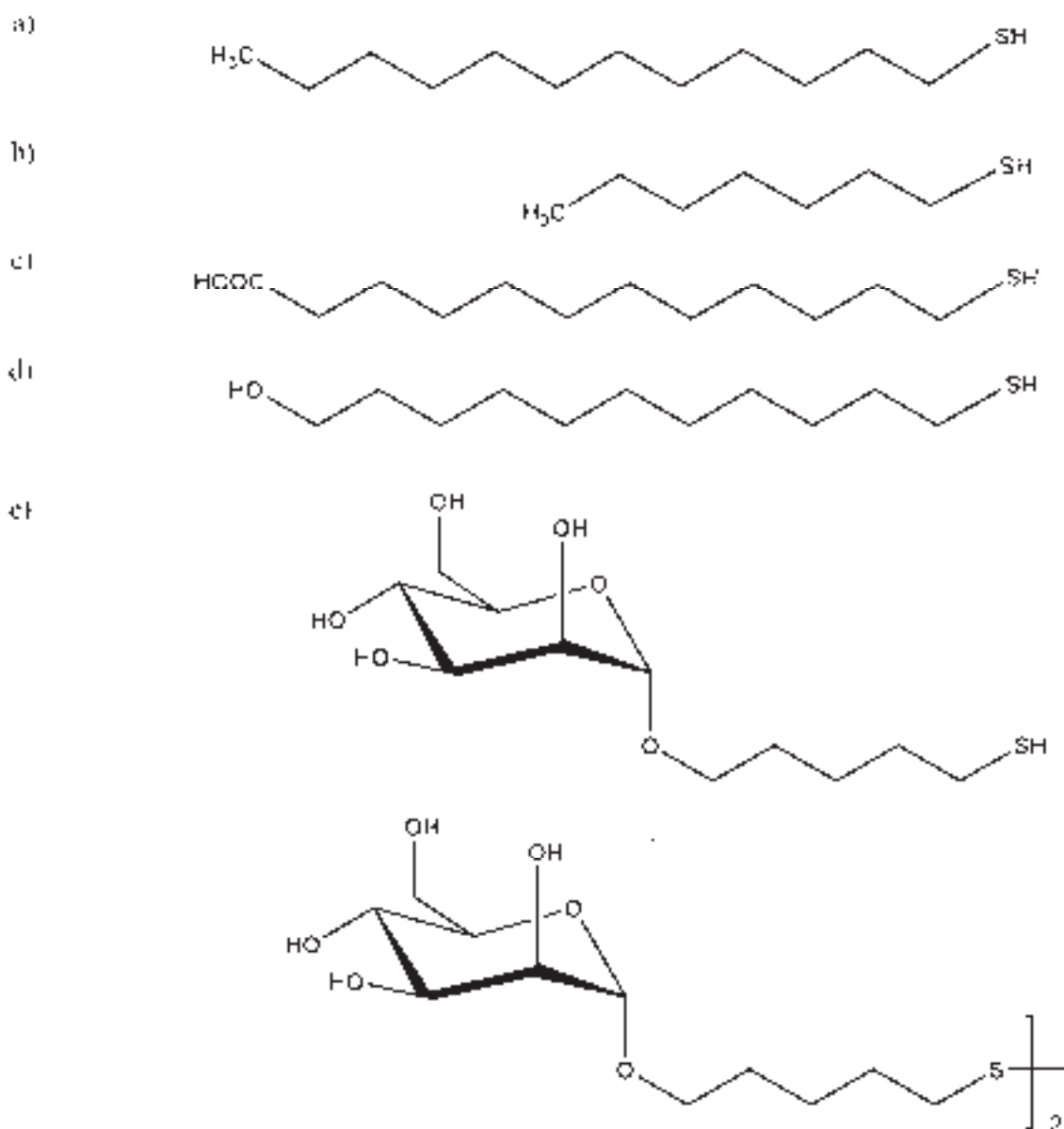
Molecular structure of: a) 1-dodecanethiol ($CH_3C_{11}S$), b) 1-hexanethiol (CH_3C_5S), c) 11-mercapto undecanoic acid ($COOHC_{10}S$), d) 11-mercapto-1-undecanol ($OHC_{11}S$) and e) mannose glycoconjugate, 5,5'-Dithio bis (penthyl-α-D-mannopyranoside) mixture with the corresponding thiol ($ManC_5S$)

Appendix 4.2
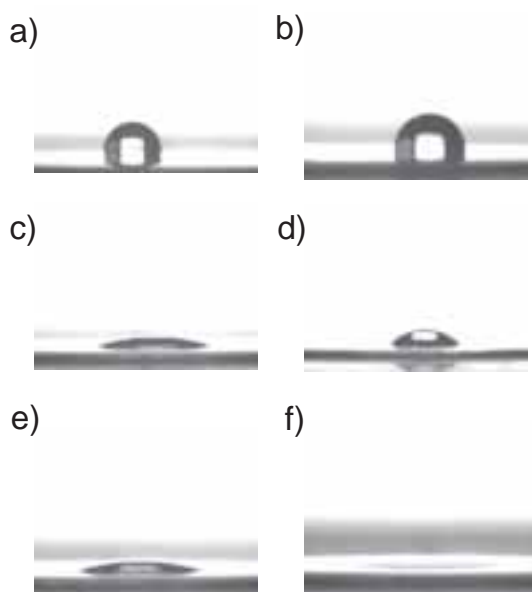
Contact angle measurement: a water droplet on a) $CH_3C_{11}S$, b) CH_3C_5S, c) $COOHC_{10}S$ immediately after to take the sample out of the thiol solution, b) $COOHC_{10}S$ one minute after taking the sample out, e) $OHC_{11}S$ an f) $ManC_5S$ self assembly monolayers.

Appendix 4.3
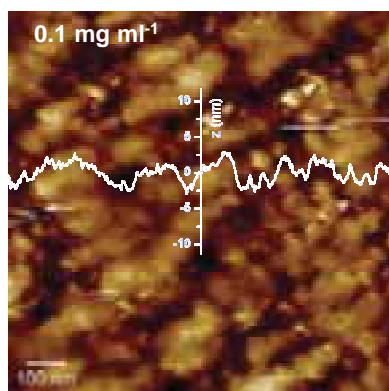
AFM height image of SbpA (0.1 mg ml^{-1}) on CH_3C_5S self assembly monolayer. The white line is the profile.

Appendix 4.4

SbpA on COOHC$_{10}$S	buffer	Initial adsorption rate (ng cm^{-2} min^{-1})
pH 9	Ca^{2+}	6664
pH 5		3374
pH 9	No Ca^{2+}	850
pH 5		2238

a) A table with the initial adsorption rates for SbpA adsorption on COOHC$_{10}$S at pH 9 and pH 5 in a buffer with and without calcium.
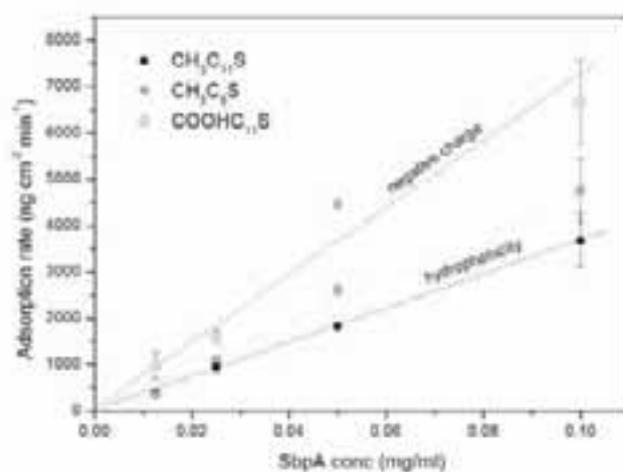
b) SbpA inicial Adsorption rate calculated from QCM-D frequency curves for CH$_3$C$_{11}$S, CH$_3$C$_5$S and COOHC$_{10}$S SAM at 0.1 mg ml^{-1}, 0.05 mg ml^{-1}, 0.025 mg ml^{-1}, 0.0125 mg ml^{-1}.

172

Appendix 4.5

a)

b)

c)
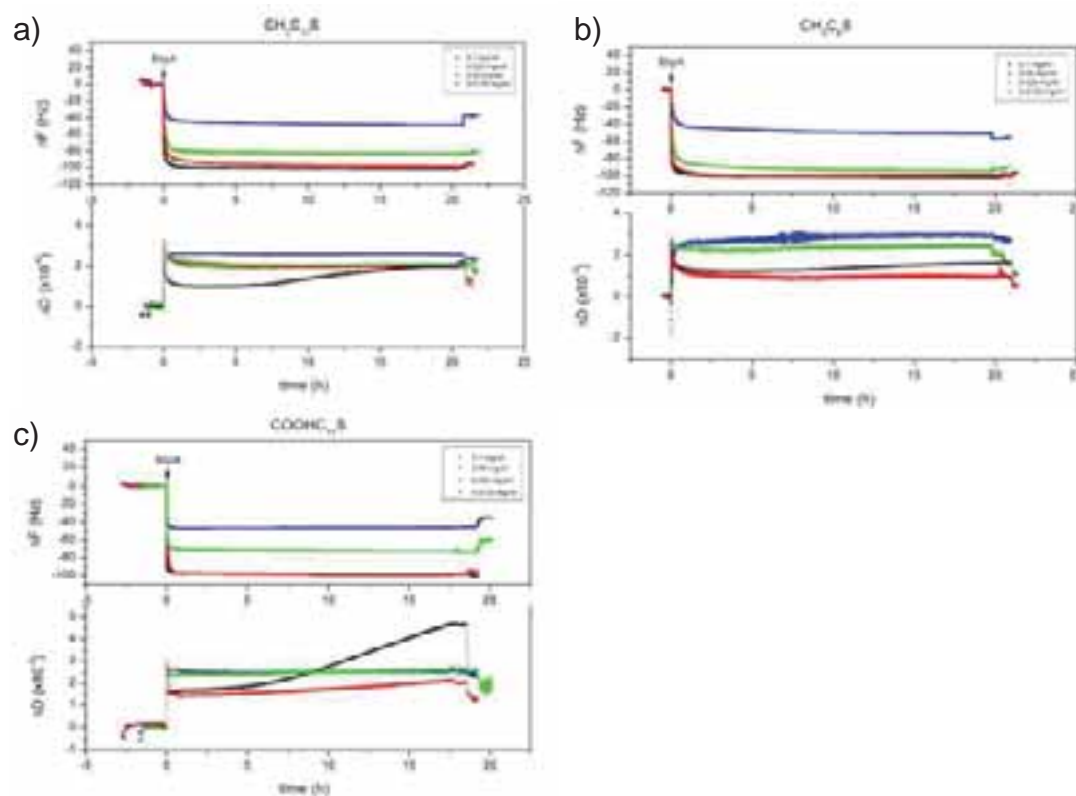
QCM-D curves (frequency and dissipation) of SbpA adsorption on a) $CH_3C_{11}S$, b) CH_3C_5S and c) $COOHC_{10}S$ SAM at four different concentrations; 0.1 mg ml^{-1}, 0.05 mg ml^{-1}, 0.025 mg ml^{-1}, 0.0125 mg ml^{-1}.

Appendix 4.6

a)

b)
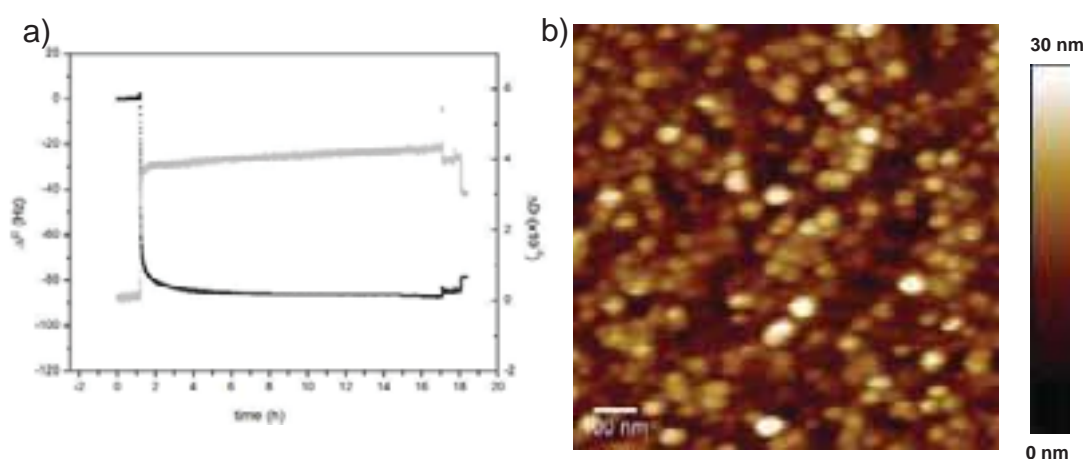
a) QCM-D and b) AFM height images of SbpA adsorption on $COOHC_{10}S$ at pH 5 with a buffer without calcium.

Appendix 4.7
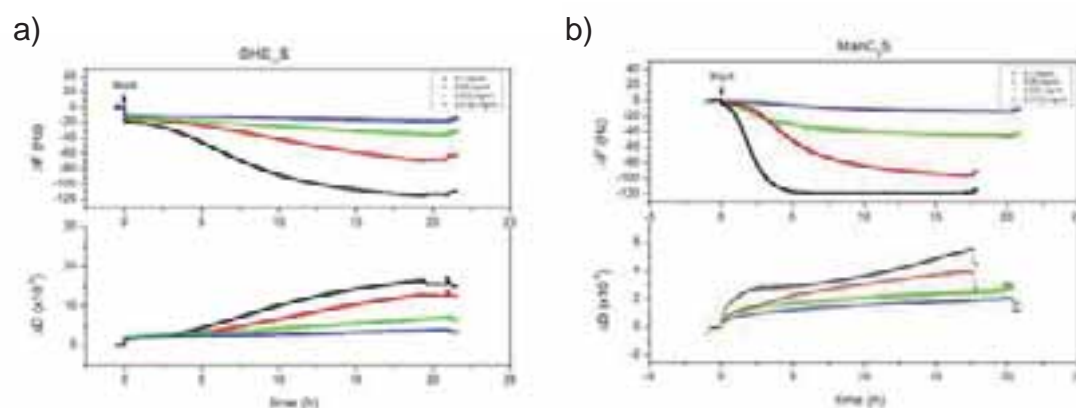
QCM-D curves (frequency and dissipation) of SbpA adsorption on a) $OHC_{11}S$ and b) $ManC_5S$ at 0.1 mg ml^{-1}, 0.05 mg ml^{-1}, 0.025 mg ml^{-1}, 0.0125 mg ml^{-1}.
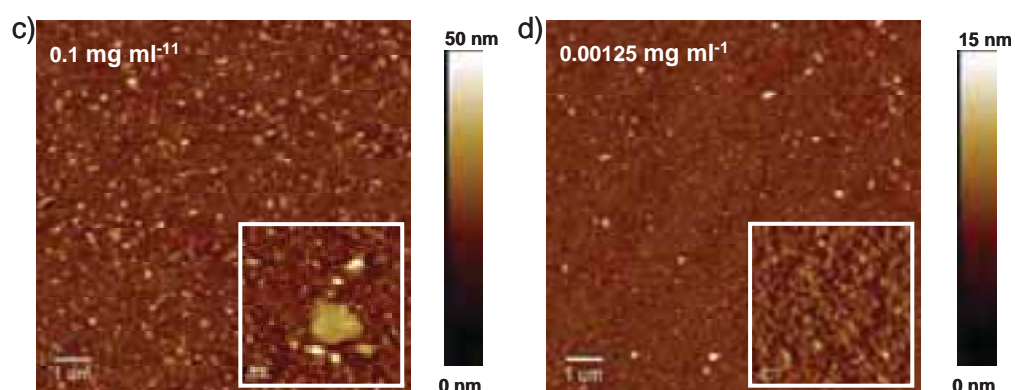
AFM height images of SbpA on $OHC_{11}S$ SAM at c) 0.1 mg ml^{-1} and d) 0.0125 mg ml^{-1}
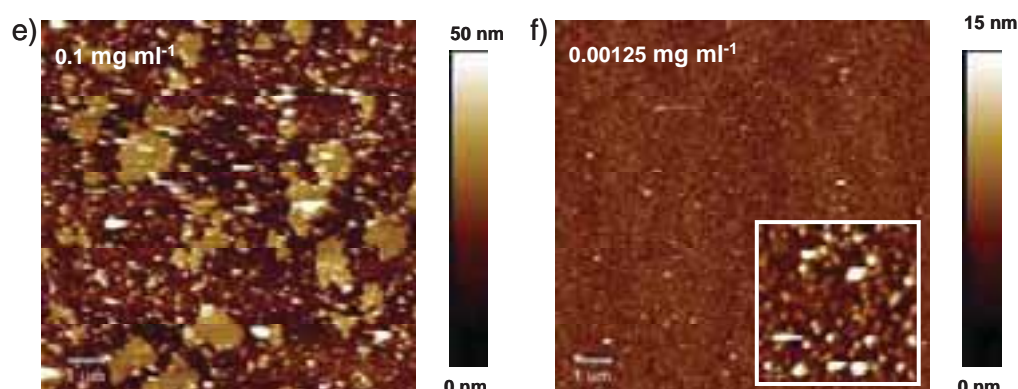
AFM height images of SbpA on $ManC_5S$ SAM at e) 0.1 mg ml^{-1} and f) 0.0125 mg ml^{-1}

Both on $OHC_{11}S$ and $ManC_5S$ at 0.1 mg ml^{-1} concentration small protein patches are observed while at 0.0125 mg ml^{-1} concentration nothing is attached to the surface.

Appendix 4.8
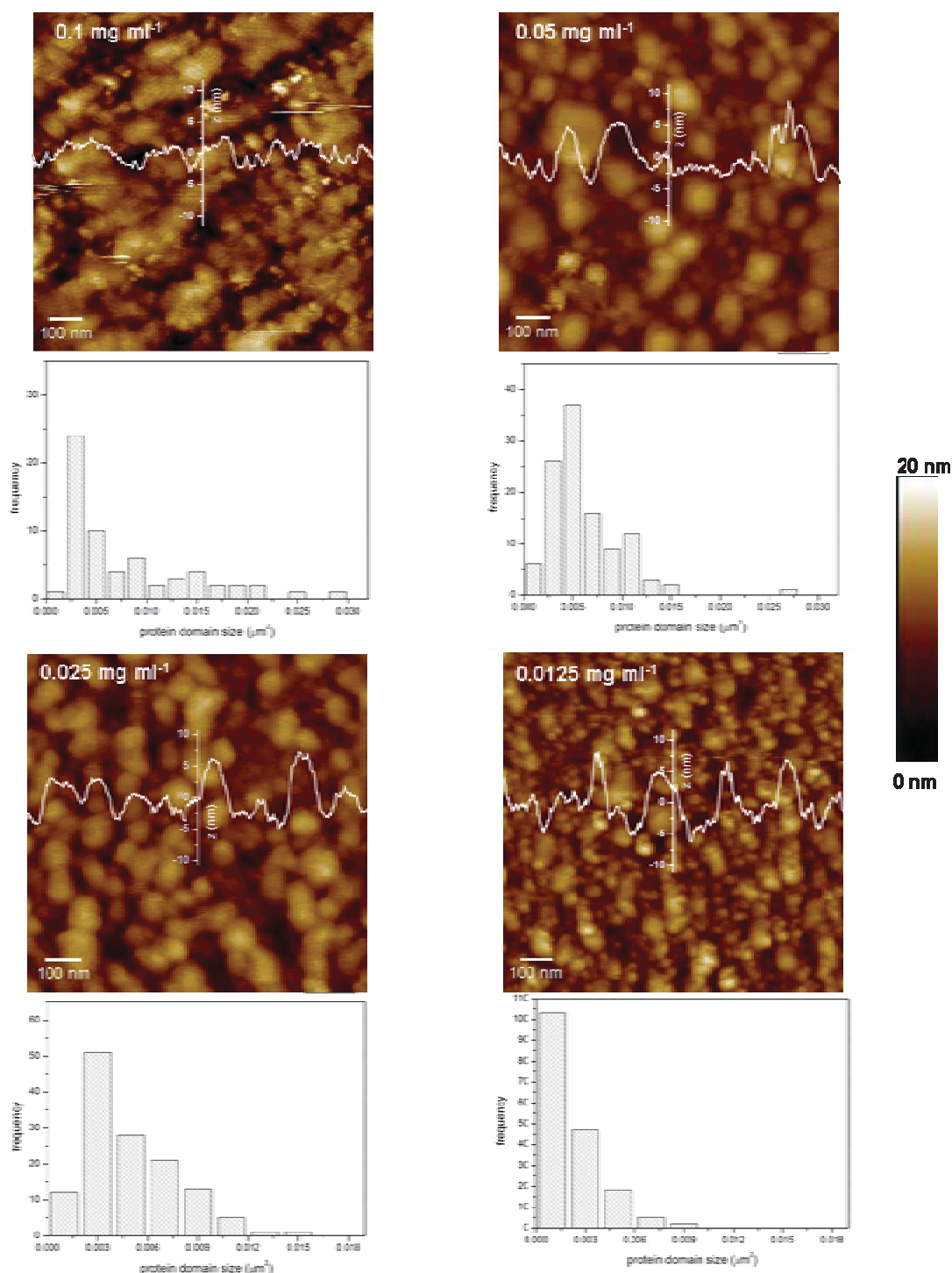
a) AFM height images of S-layer on CH_3C_5S different concentrations: 0.1 mg ml^{-1}, 0.05 mg ml^{-1}, 0.025 mg ml^{-1}, 0.0125 mg ml^{-1} with their respective profile and histogram of protein domain size
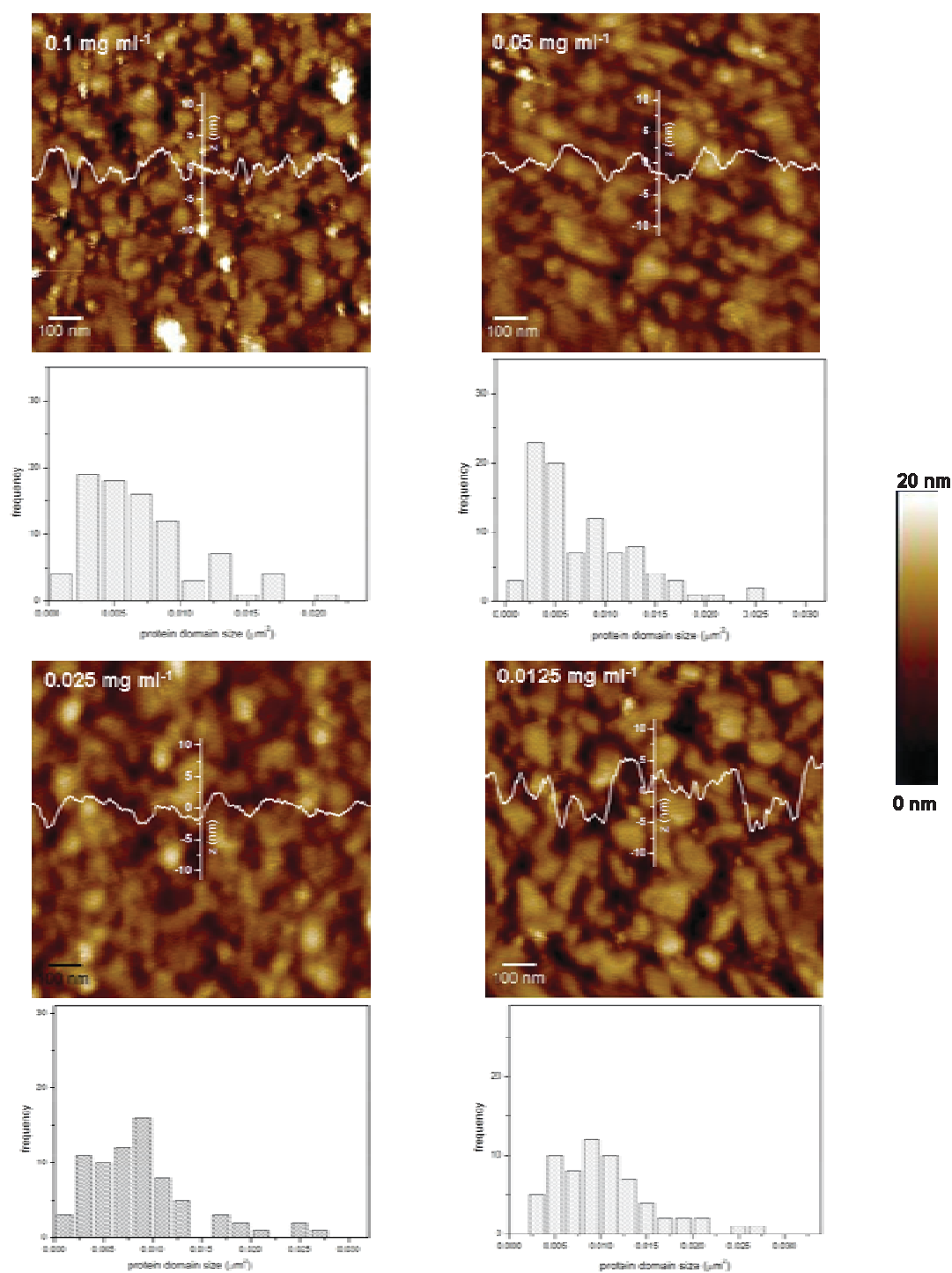
b) AFM height images of S-layer on COOHC$_{10}$S different concentrations: 0.1 mg ml^{-1}, 0.05 mg ml^{-1}, 0.025 mg ml^{-1}, 0.0125 mg ml^{-1} with their respective profile and histogram of protein domain size.

Appendix 4.9
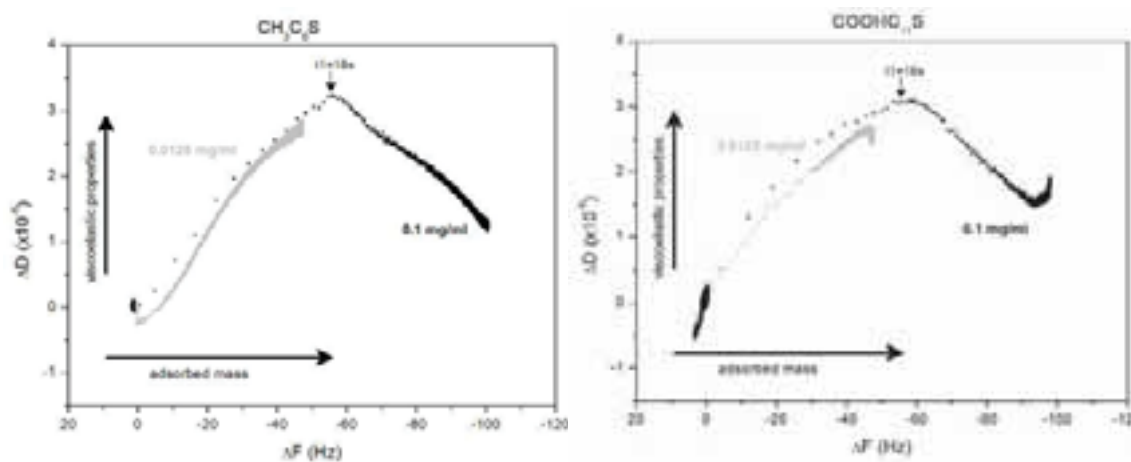
Frequency-dissipation curves (F/D) of SbpA on CH_3C_5S and $COOHC_{10}S$ for 0.1 mg ml^{-1} and 0.0125 mg ml^{-1}.

Appendix 4.10
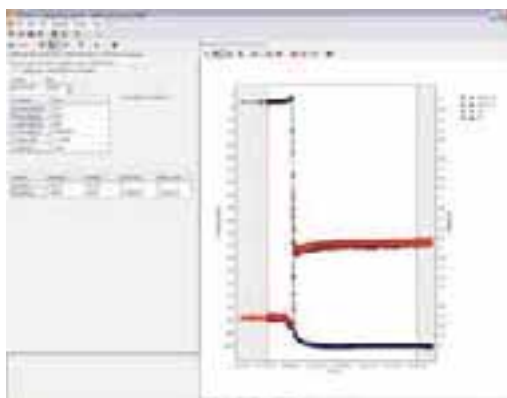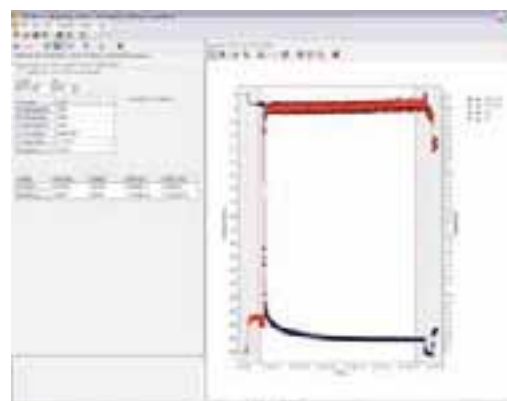
QCM-D curves fitting of frequency and dissipation curves by Kelvin-Voigt model of SbpA adsorption on $COOHC_{10}S$ at a) pH 9 and b) pH 5. The fittings are carried out considering only the first five hours of the protein adsorption.

Appendix III-Chapter 6

Appendix 6.1
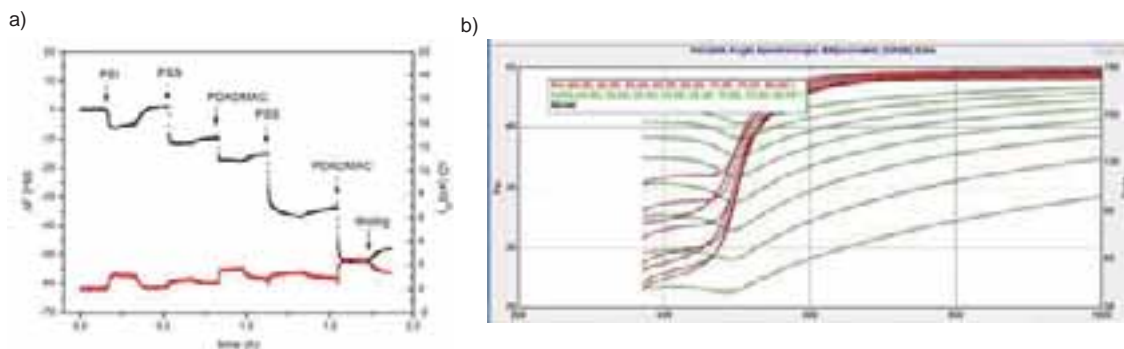
a) Frequency (black) and dissipation (red) curves as a function of time of polyelectrolyte multilayer building up monitored by QCM-D. The PEM has five layers formed by the combination of PEI, PSS and PDADMAC. The arrows indicate the injection of each polymer and the final rinsing. The last layer is the positively charged PDADMAC.

b) Ellipsometry Ψ (red) and Δ (green) data of gold substrate functionalized with cysteamine and glutaraldehyde. Ψ and Δ data were fitted with the Cauchy model obtaining thickness value of 1.1 ± 0.1 nm

Appendix 6.2
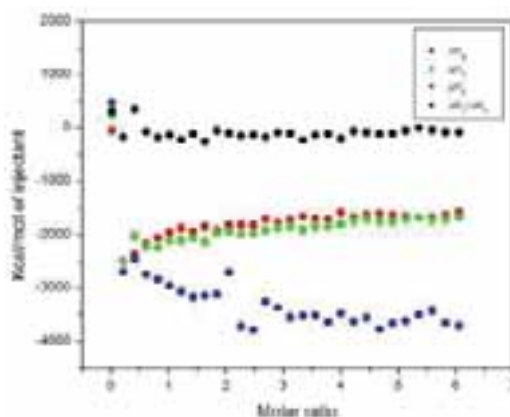
The effect of the heat in ITC HSA-bilirubin experiment for step 2 (blue), step 3 (green) and step 4 (red) as a function of the molar ratio. The black curve is the rest of the enthalpies obtained in step 3 and step 4.

Appendix 6.3
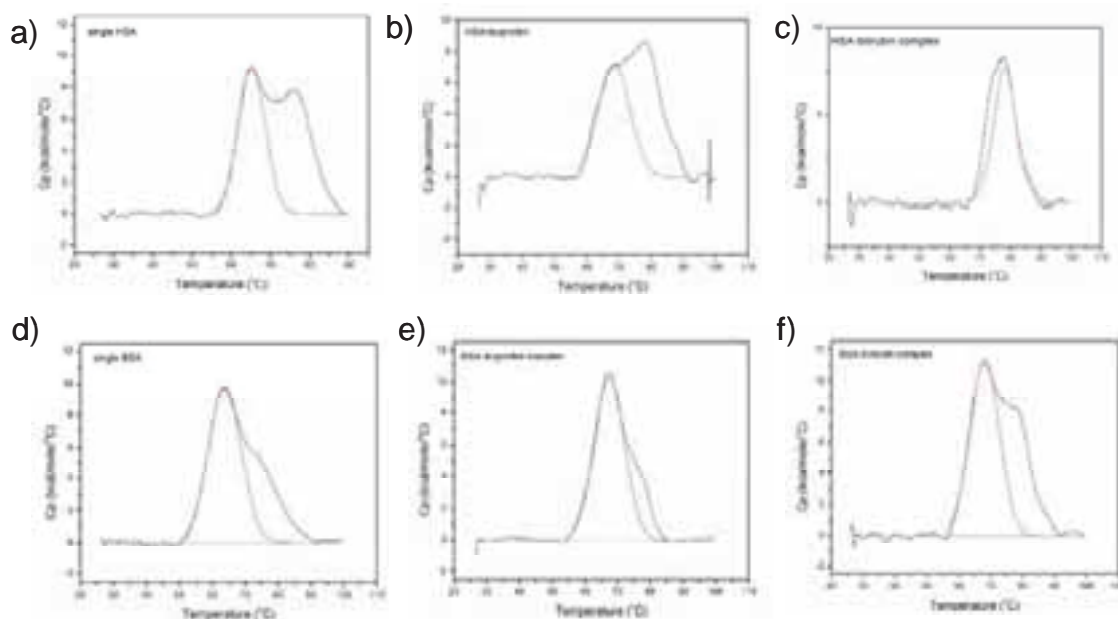
DSC thermogram fittings using a single Gaussian for a) HSA, b) HSA-ibuprofen, c) HSA-bilirubin, d) BSA, e) BSA-ibuprofen and f) BSA-bilirubin.

Appendix 6.4[u]

i) General Considerations

It will be assumed throughout that the macromolecule M is in the cell at an initial bulk concentration M_t^0 (moles/liter) before the first injection, and the ligand X to be injected is initially at zero concentration in the cell. The *working volume* (cross-hatched area below) of the lollipop-shaped cell is V_o, the size of the ith injection is ΔV_i and the total liquid which has been injected at any point during the experiment, ΔV, is simply the sum of the individual ΔV_i for all injections.

---
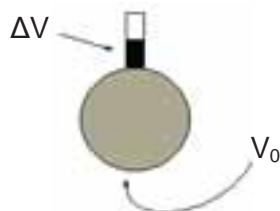
[u] Adapted from *ITC Data Analysis in Origin® Tutorial Guide.*

At the beginning of an experiment, both the cell and the long communication tube are filled with macromolecule solution, but it is only that contained within V_o that is sensed calorimetrically, Because of the total-fill nature of the cell each injection acts to drive liquid out of the working volume and up into the inactive tube as shown by the darkened portion representing ΔV. Thus, the concentration of macromolecule in V changes a small amount with each injection since the total number of moles of macromolecule initially in V (i.e. M_t^0 times V_o) at the beginning of the experiment is later distributed in a larger volume, $V_o + \Delta V$. Since the average bulk concentration of macromolecule in ΔV is the mean of the beginning concentration M_t^0 and the present concentration M_t in the active volume, then conservation of mass requires that

$$M_t^0 V_0 = M_t V_0 + \frac{1}{2}(M_t + M_t^0)\Delta V \qquad (1)$$

So that,

$$M_t = M_t^0 \left(\frac{1 - \dfrac{\Delta V}{2\Delta V_0}}{1 + \dfrac{\Delta V}{2\Delta V_0}} \right) \qquad (2)$$

Using similar reasoning, it is easily shown that the actual bulk concentration of ligand in V_o, X_t, is related to the *hypothetical* bulk concentration X_t^0 (assuming that all of the injected ligand remained in V_o) as follows:

$$X_t^0 V_0 = X_t V_0 + \frac{1}{2} X_t \Delta V \qquad (3)$$

$$X_t = X_t^0 \left(1 - \frac{\Delta V}{2V_0} \right) \qquad (4)$$

The above expressions for M_t and X_t are used by Origin to correct for displaced volume effects which occur with each injection.

ii) Single set of identical sites

In the following equations,
$\qquad K$ = Binding constant;
$\qquad n$ = # of sites;
$\qquad V_o$ = active cell volume;
$\qquad M_t$ and *[M]* are bulk and free concentration of macromolecule in V_o;
$\qquad X_t$ and *[X]* are bulk and free concentration of ligand, and

Θ = fraction of sites occupied by ligand X.

$$K = \frac{\Theta}{(1-\Theta)[X]} \qquad (5)$$

$$X_t = [X] + n\Theta M_t \qquad (6)$$

Combining equations (5) and (6) above gives

$$\Theta^2 - \Theta\left[1 + \frac{X_t}{nM_t} + \frac{1}{nKM_t}\right] + \frac{X_t}{nM_t} = 0 \qquad (7)$$

The total heat content Q of the solution contained in V_o (determined relative to zero for the unliganded species) at fractional saturation Θ is

$$Q = n\Theta M_t \Delta H V_0 \qquad (8)$$

where ΔH is the molar heat of ligand binding. Solving the quadratic equation (7) for Θ and then substituting this into eq. (8) gives

$$Q = \frac{nM_t \Delta H V_0}{2}\left[1 + \frac{X_t}{nM_t} + \frac{1}{nKM_t} - \sqrt{\left(1 + \frac{X_t}{nM_t} + \frac{1}{nKM_t}\right)^2 - \frac{4X_t}{nM_t}}\right] \qquad (9)$$

The value of Q above can be calculated (for any designated values of n, K, and ΔH) at the end of the ith injection and designated $Q(i)$. The parameter of interest for comparison with experiment, however, is the *change* in heat content from the completion of the *i-1* injection to completion of the *i* injection. The expression for Q in eq. (9) only applies to the liquid contained in volume V_o. Therefore, after completing an injection, it is obvious that a correction must be made for displaced volume (i.e., ΔV_i = injection volume) since some of the liquid in Vo after the *i-1* injection will no longer be in V_o after the ith injection, even though it will contribute to the heat effect (assuming the kinetics of reaction and mixing are fast) *before* it passes out of the working volume V_o. The liquid in the displaced volume contributes about 50% as much heat effect as an equivalent volume remaining in V_o[v] The correct expression then for heat released, $\Delta Q(i)$, from the ith injection is

$$\Delta Q(i) = Q(i) + \frac{dV_i}{V_0}\left[\frac{Q(i) + Q(i-1)}{2}\right] - Q(i-1) \qquad (10)$$

---

[v] The first infinitesimal volume element in the *i* injection contributes no heat effect since it has already equilibrated at existing concentrations after the *i-1* injection. The last volume element of an injection contributes heat effects equal to the liquid remaining in *Vo* since its concentrations are equivalent to those in V_o after the *i* injection. Assuming linearity over the small ΔV_i volume increment, then the liquid in the displaced volume is only half as effective in producing heat relative to the liquid in V_o.

The process of fitting experimental data then involves 1) initial guesses (which most often can be made accurately enough by Origin) of *n, K,* and *ΔH*; 2) calculation of *ΔQ(i)* for each injection and comparison of these values with the measured heat for the corresponding experimental injection; 3) improvement in the initial values of n, K, and *ΔH* by standard Marquardt methods; and 4) iteration of the above procedure until no further significant improvement in fit occurs with continued iteration.

iii) Two sets of independent sites

Using the same definition symbols as above for set 1 and set 2, we have

$$K_1 = \frac{\Theta_1}{(1-\Theta_1)[X]} \qquad\qquad K_2 = \frac{\Theta_2}{(1-\Theta_2)[X]} \qquad (11)$$

$$X_t = [X] + M_t(n_1\Theta_1 + n_2\Theta_2) \qquad (12)$$

Solving equation (11) for Θ_1 and Θ_2 and then substituting into equation (12) gives

$$X_t = [X] + \frac{n_1 M_t[X]K_1}{1+[X]K_1} + \frac{n_2 M_t[X]K_2}{1+[X]K_2} \qquad (13)$$

Clearing equation (13) of fractions and collecting like terms leads to a cubic equation of the form

$$[X]^3 + p[X]^2 + q[X] + r = 0 \qquad (14)$$

$$p = \frac{1}{K_1} + \frac{1}{K_2} + (n_1 + n_2)M_t - X_t$$

$$q = \left(\frac{n_1}{K_2} + \frac{n_2}{K_1}\right)M_t - \left(\frac{1}{K_1} + \frac{1}{K_2}\right)X_t + \frac{1}{K_1K_2}$$

$$r = \frac{-X_t}{K_1K_2} \qquad (15)$$

Equations 14 and 15 can be solved for *[X]* either in closed form or (as done in Origin) numerically by using Newton's Method if parameters n_1, n_2, K_1, and K_2 are assigned. Both Θ_1 and Θ_2 may then be obtained from equation 11 above. As discussed earlier in section II, the heat content after any injection *i* is equal to

$$Q = M_t V_0 \left(n_1 \Theta_1 \Delta H_1 + n_2 \Theta_2 \Delta H_2 \right) \qquad (16)$$

After a similar correction for displaced volume, the pertinent calculated heat effect for the i injection is

$$\Delta Q(i) = Q(i) + \frac{dV_i}{V_0} \left[\frac{Q(i) + Q(i-1)}{2} \right] - Q(i-1) \qquad (17)$$

which may be used in the Marquardt algorithm to obtain best values for the six fitting parameters

Appendix 6.5

Theoretical estimation of the adsorbed HSA mass per unit area on QCM-D sensors;

i) Human Serum Albumin dimensions

HSA size = 3 x 8 x 8 nm^3

Horizontal adsorption	$A_{HSA(h)} = 8 \times 8 \text{ nm}^2 = 64 \text{ nm}^2$
Vertical adsorption	$A_{HSA(v)} = 3 \times 8 \text{ nm}^2 = 24 \text{ nm}^2$

ii) QCM-D crystal area (A_{QCM})

Crystal diameter = 14 mm = 14×10^6 nm
Crystal radio (r) = 7×10^6 nm

$$A_{QCM} = \pi r^2 = \pi (7 \times 10^6)^2 \text{ nm} = 1.539 \times 10^{14} \text{ nm}^2 = 1.539 \text{ cm}^2$$

1. Horizontal adsorption

HSA molecules on a monolayer

$A_{QCM}/A_{HSA(h)} = 1.539 \times 10^{14} \text{ nm}^2 / 64 \text{ nm}^2 = 2.404 \times 10^{12}$ HSA molecules per layer

Avogadro number: $N_A = 6.022 \times 10^{23}$ molecules mol^{-1}

HSA molecular weight: M_w(HSA)= 66700 g mol^{-1}

HSA mol per layer: 2.404×10^{12} / 6.022×10^{23}= 3.994×10^{-12} HSA mol per layer

HSA gram per layer: 3.994×10^{-12} * 66700 = 2.664×10^{-7} HSA g per layer

= **266.4 HSA ng per layer**

HSA monolayer mass density if the adsorption is horizontal
Mass(HSA)/A_{QCM}= 266.40 ng / 1.54 cm^2 = **172.99 ng / cm^2**

2. Vertical adsorption

HSA molecules on a monolayer

A_{QCM}/$A_{HSA(v)}$=1.539×10^{14} nm^2 / 24 nm^2 = **6.413×10^{12} HSA molecules per layer**

Avogadro number: N_A = 6.022×10^{23} molecules mol^{-1}

HSA molecular weight: M_w(HSA)= 66700 g mol^{-1}

HSA mol per layer: 6.413×10^{12} / 6.022×10^{23}= 1.065×10^{-11} HSA mol per layer

HSA gram per layer: 1.065×10^{-11} * 66700 = 7.104×10^{-7} HSA g per layer

= **710.4 HSA ng per layer**

HSA monolayer mass density if the adsorption is vertical
Mass(HSA)/A_{QCM}= 710.40 ng / 1.54 cm^2 = **461.30 ng / cm^2**

Appendix 6.6
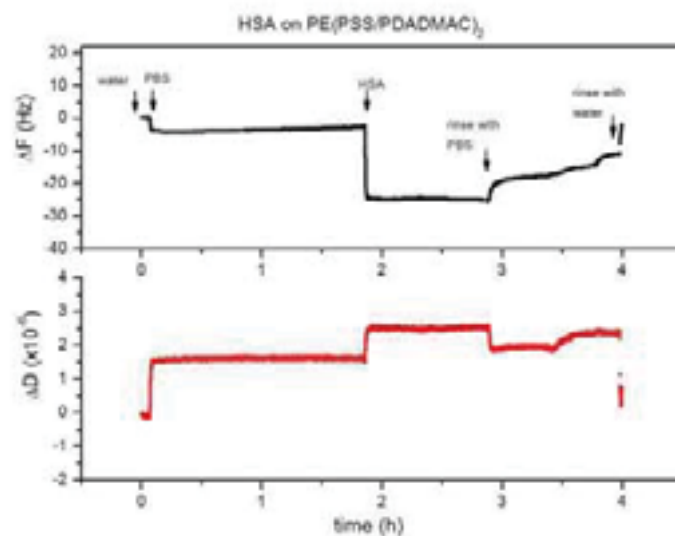
QCM-D frequency and dissipation curves for HSA (1 mg ml^{-1}) adsorption on PDADMAC

Appendix 6.7
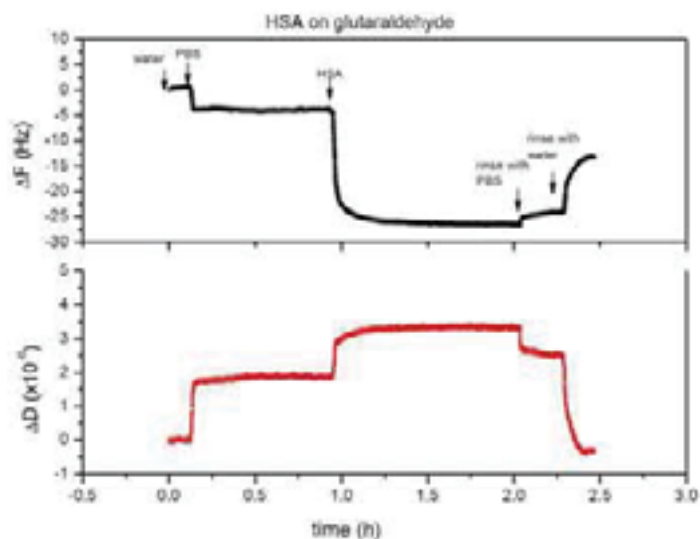
QCM-D frequency and dissipation curves for HSA (1 mg ml^{-1}) adsorption on glutaraldehyde.

Appendix 6.8
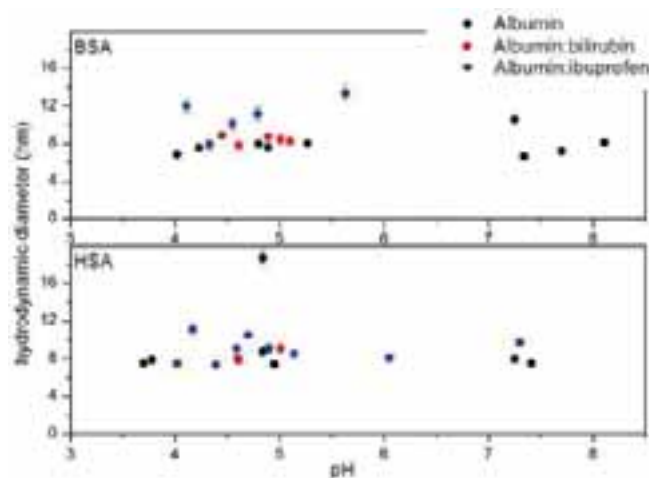
The hydrodynamic diameter of HSA, BSA and the complexes formed with ibuprofen and bilirubin. HSA-bilirubin presented high amount of aggregates. This data are not included.
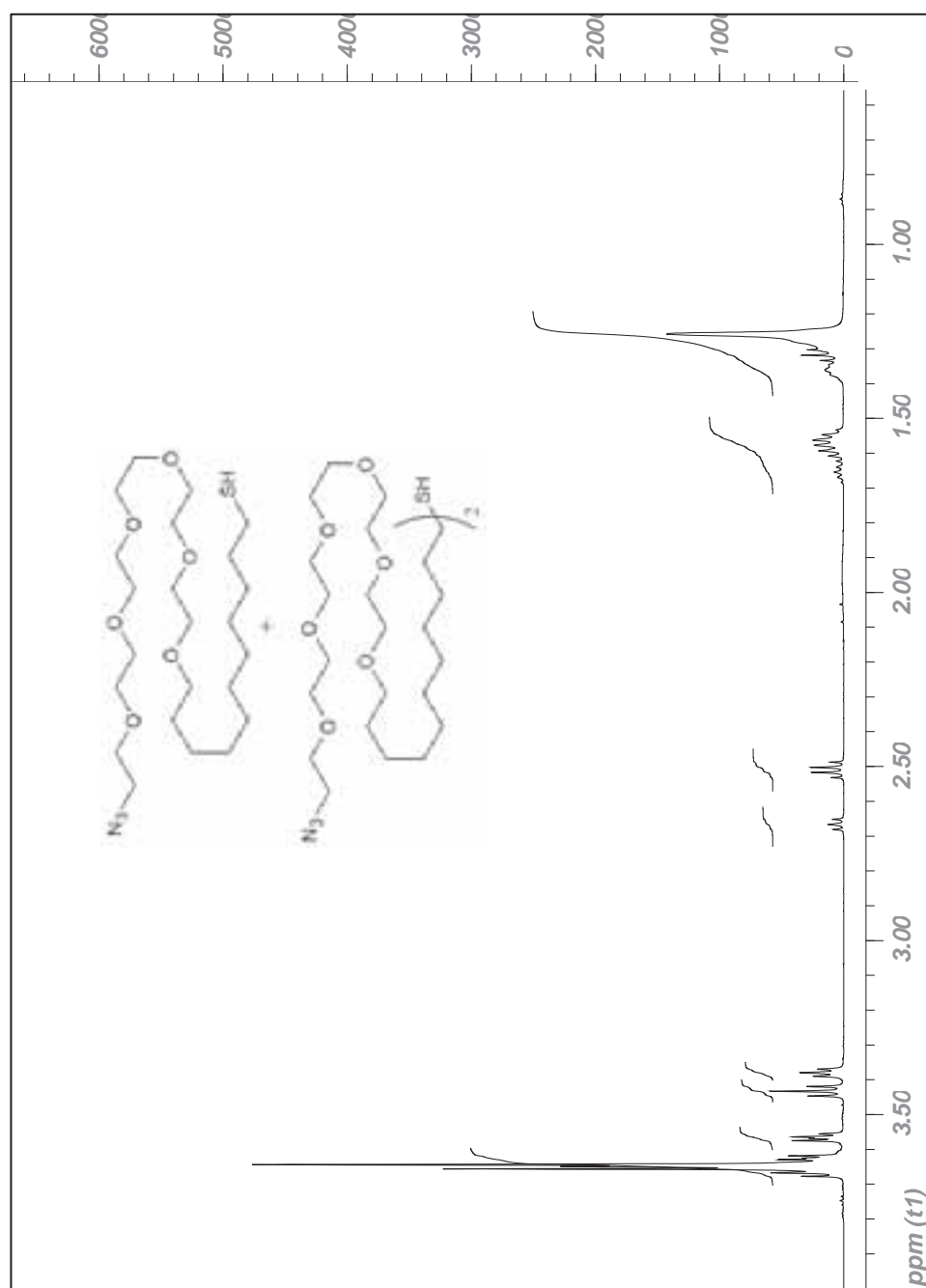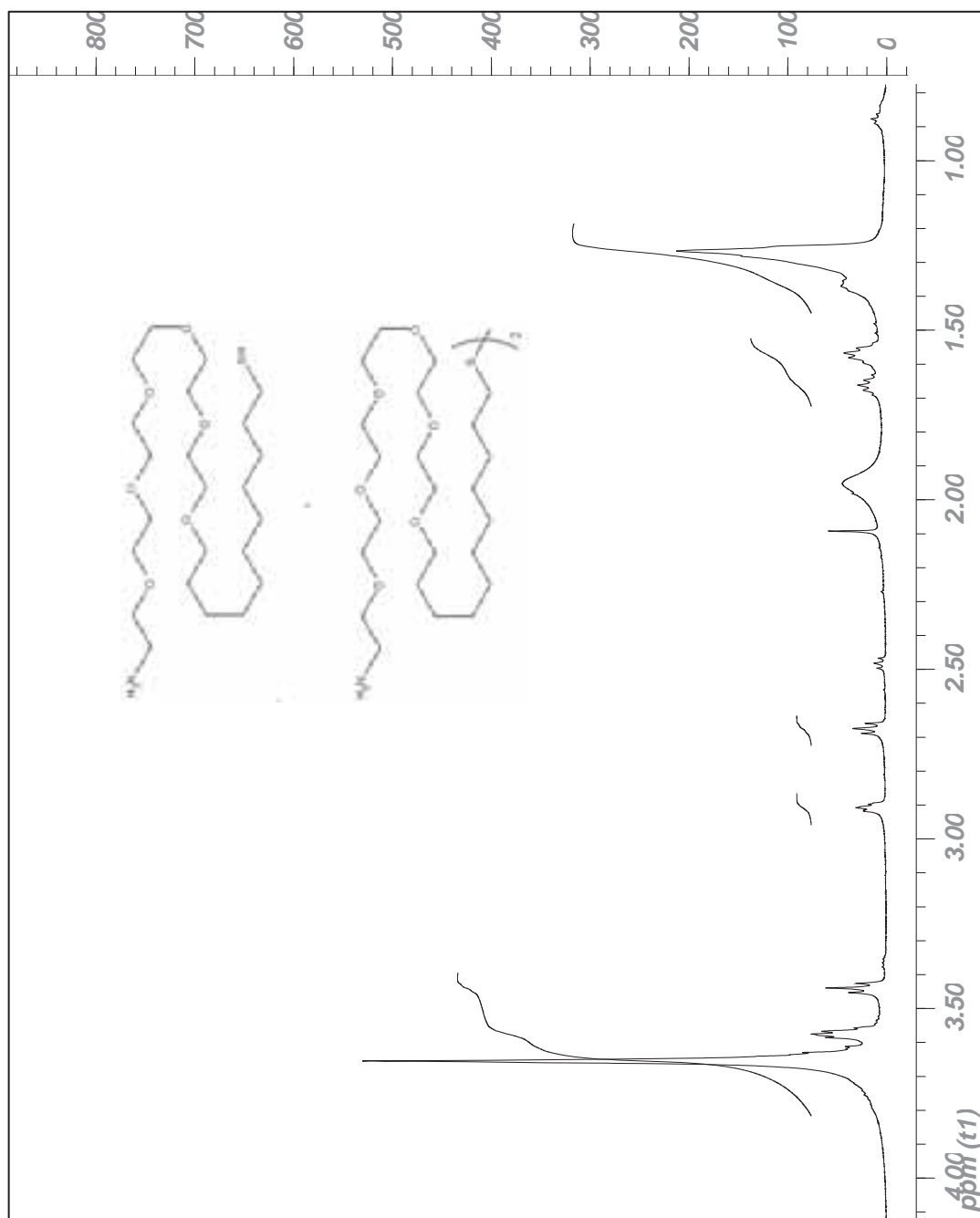
Appendix 6.9
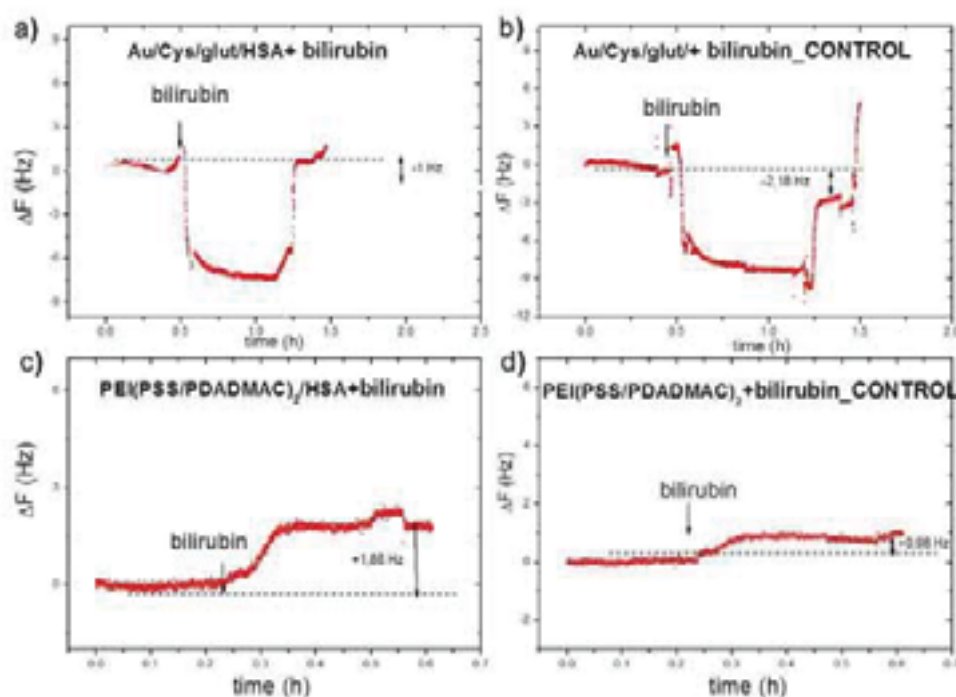
Bilirubin 0.1 mg ml^{-1} adsorption on HSA immobilized sensors on a) glutaraldehyde, c) PDADMAC substrates. The control experiments were carried out injecting bilirubin to b) glutaraldehyde and d) PDADMAC.

Appendix IV-Chapter 7

Appendix 7.1

a) NMR spectrum of $N_3(EG)_6C_{11}SH$ and its disulfide after thioacetate deprotection.

b) NMR spectrum of $NH_2(EG)_6C_{11}SH$ and its disulfide after Staudinger reaction
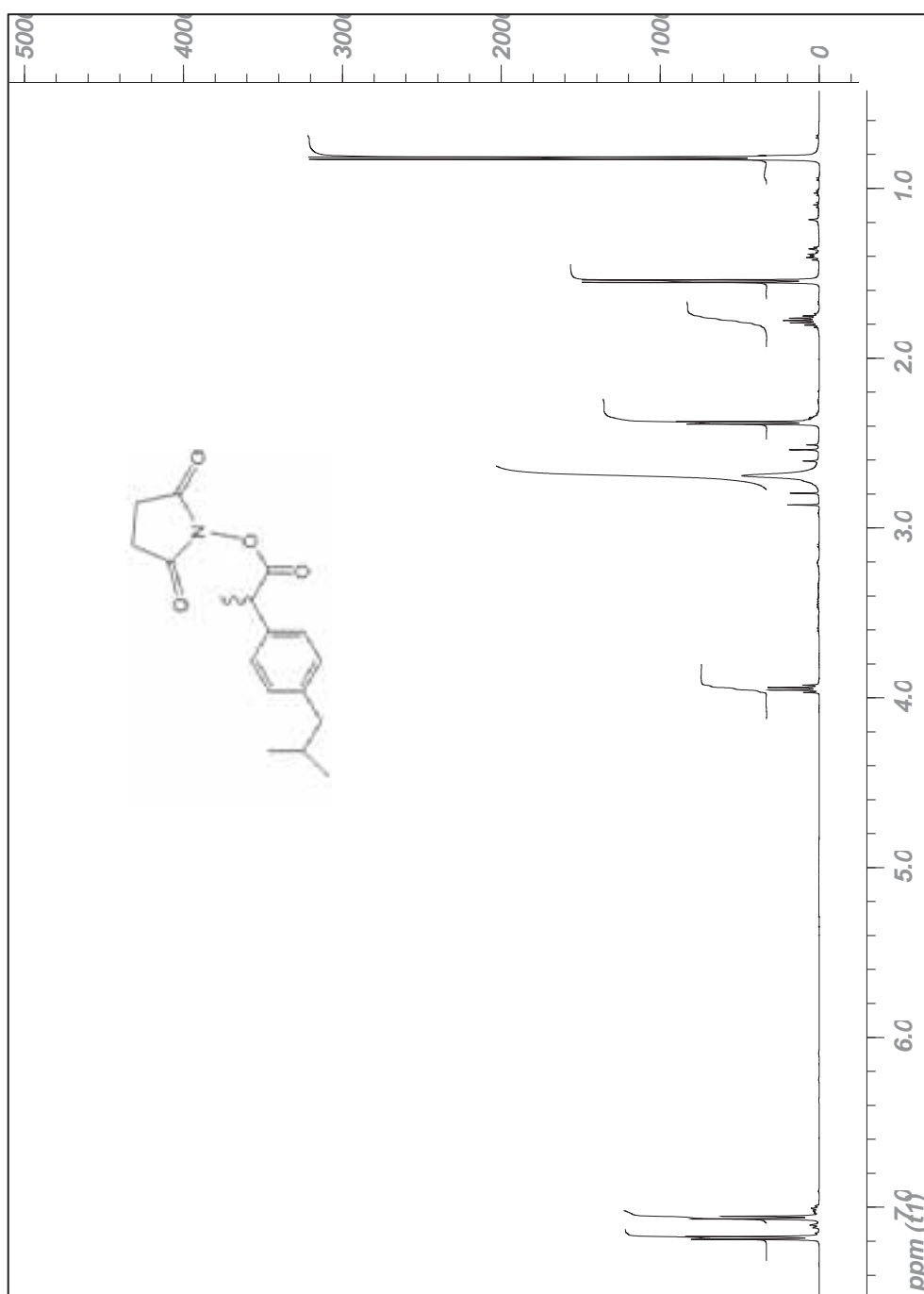
c) NMR spectrum of activated ibuprofen with NHS.

Appendix 7.2
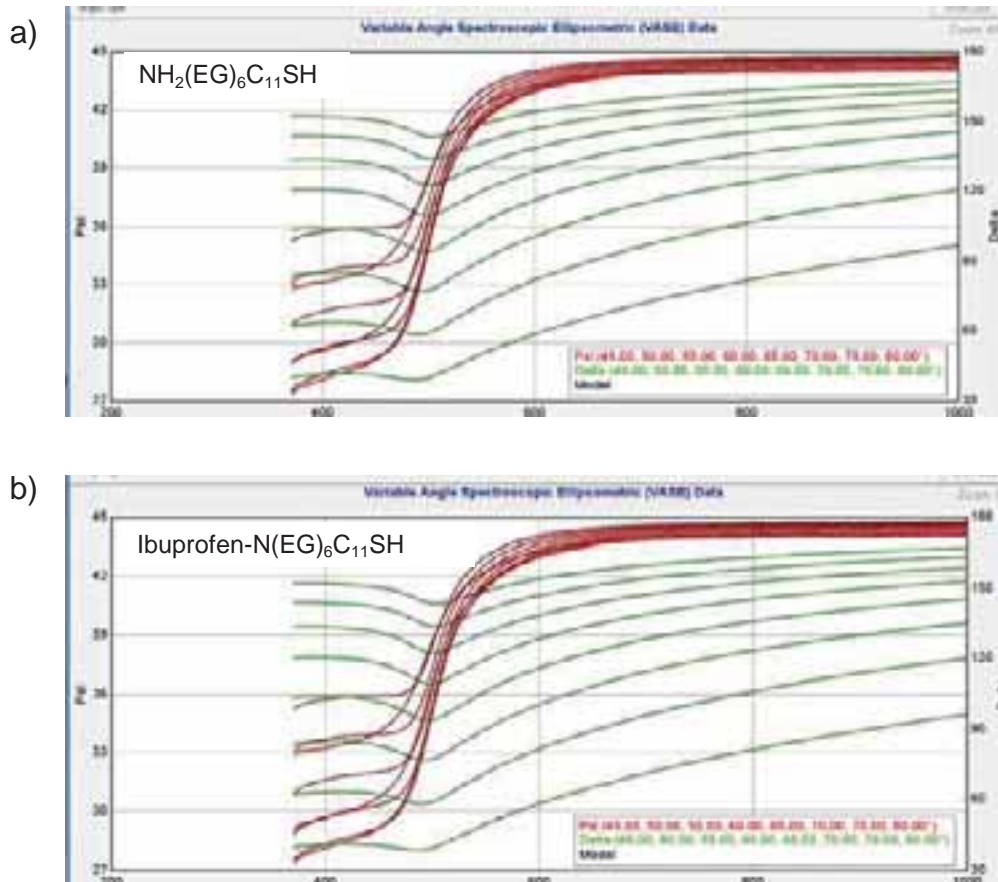
Ellipsometry data, ψ and Δ, of a) $NH_2(EG)_6C_{11}SH$ and b) Ibuprofen-$N(EG)_6C_{11}SH$ self assembly monolayer on gold substrate. The thickness calculated by fitting the curves with Cauchy model. Similar thickness values were obtained for both cases; 3.18 ± 0.1 nm for $NH_2(EG)_6C_{11}SH$ and 3.22 ± 0.1 for Ibuprofen-$N(EG)_6C_{11}SH$.

Appendix 7.3

The AFM cantilever oscillates due to thermal movement. Thus, the cantilever oscillation amplitude can be calculated to estimate which might be the experimental noise in AFM experiments.

- *Thermal energy (E_T) in z direction* → $E_T = 0.5\, k_b\, T$

    T: Temperature (K) = 296K
    k_b: Boltzman constant = 1.38×10^{-23} J/K   (1 J = 1 N/m)

- *Mechanical energy (E_M) in z direction* → $E_M = 0.5\, K_e\, z^2$

Ke: cantilever spring constant
z: oscillation amplitude

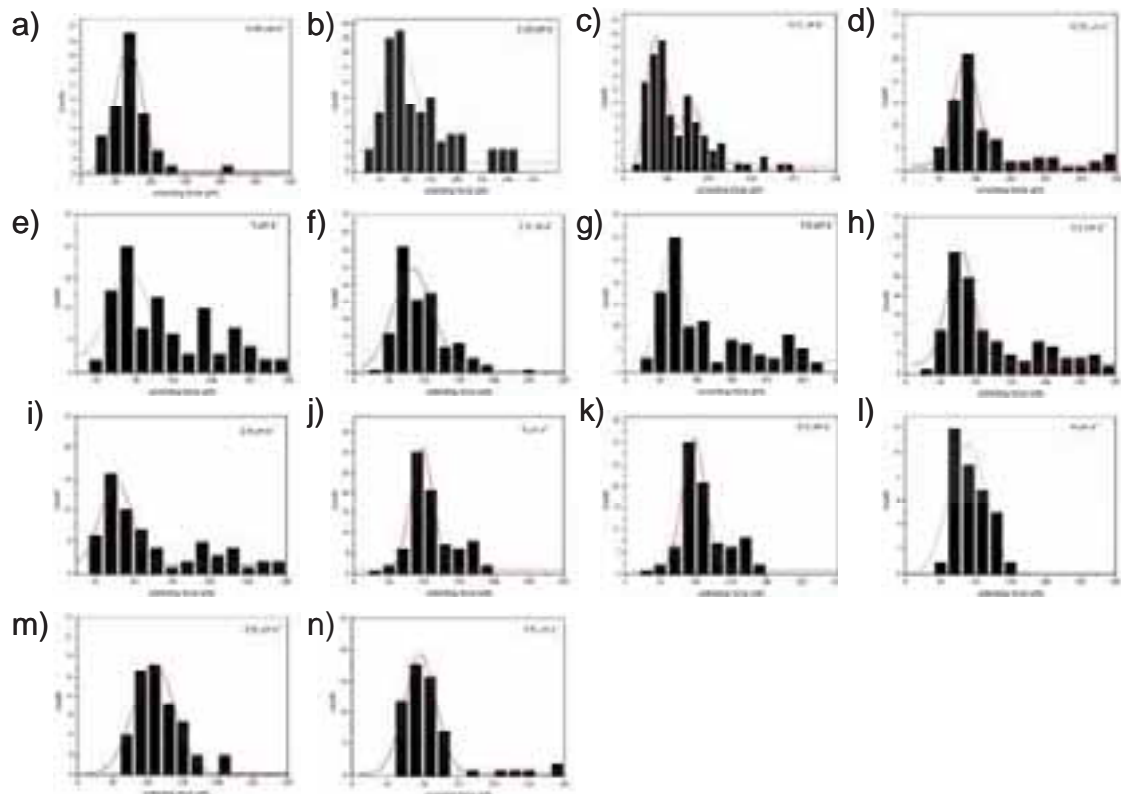If we equalize the thermal energy and mechanical energy we are able to calculate the oscillation amplitude.

$$E_T = E_M$$

$$0.5\ k_b\ T = 0.5\ K_e\ z^2 \rightarrow z = \left[\frac{k_b T}{K_e}\right]^{1/2} = \left[\frac{4.08 x 10^{-21}}{0.22}\right]^{1/2} = 1.36 x 10^{-10}\ m$$

$K_e = 0.22 \rightarrow K_e\ z = 0.22 \times 1.36 \times 10^{-10} = 29\ pN$

$K_e = 0.12 \rightarrow K_e\ z = 0.12 \times 1.36 \times 10^{-10} = 22\ pN$

Appendix 7.4.

Histograms of the unbinding force between HSA and ibuprofen functionalized tip at different approaching speeds fitted with Gaussian equation; a) 0.05 μm s^{-1} (68.7±1.1 pN), b) 0.25 μm s^{-1} (88.7±4.6 pN), c) 0.5 μm s^{-1} (79.4±3.9 pN), d) 0.75 μm s^{-1} (86.3 ±1.4 pN), e) 1 μm s^{-1} (118.1±12.2 pN), f) 1.3 μm s^{-1} (83.9±2.9 pN), g) 1.5 μm s^{-1} (66.7±2.1 pN), h) 2.2 μm s^{-1} (78.3±1.9 pN), i) 2.8 μm s^{-1} (76.9±2.8 pN), j) 3 μm s^{-1} (96.8±1.9 pN),

k) 3.3 μm s^{-1} (96.9±1.3 pN), l) 4 μm s^{-1} (108.6±1.7 pN), m) 3.9 μm s^{-1} (88.5±2.6 pN), n) 4.9 μm s^{-1} (95.8±1.2 pN). The values in brakets indicate the maximum of the Gaussian curves which is related with the most probable unbinding force.
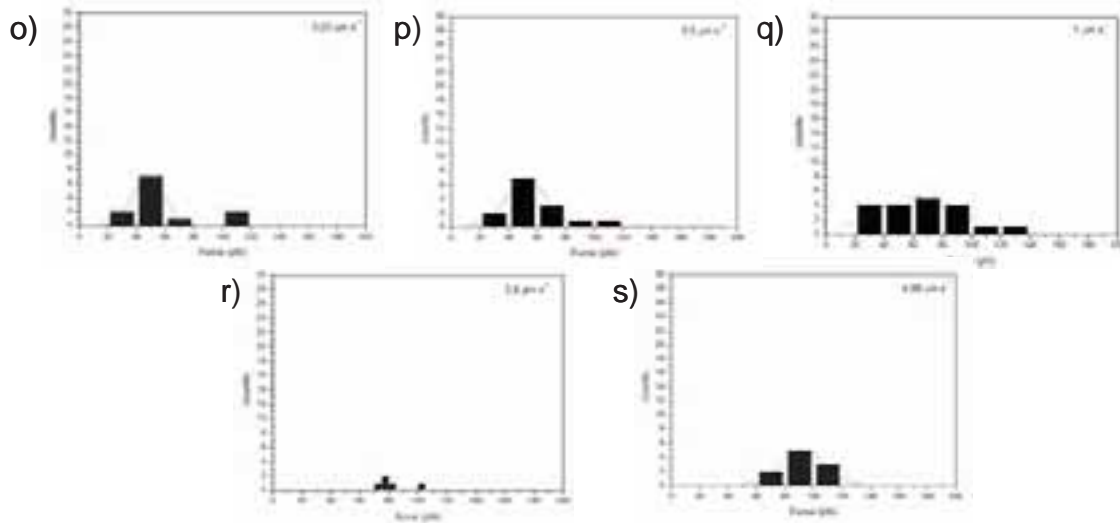
Histograms of the unbinding force between HSA and gold tip (No functionalized with ibuprofen) at different approaching speeds fitted with Gaussian equation; o) 0.25 μm s^{-1} (47.6±2.7 pN), p) 0.5 μm s^{-1} (52.1±1.3 pN), q) 1 μm s^{-1} (63.8±4.1 pN), r) 2.6 μm s^{-1} (77.5±1.2 pN), s) 4.9 μm s^{-1} (92.6±0.6 pN). The values in brakets indicate the maximum of the Gaussian curves which is related with the most probable force.

Appendix 7.5

Calculation of the distance to the transition state (x_u) and dissociation rate constant (K_{Off}).

$$F = \left(\frac{k_b T}{x_u}\right) \ln\left(\frac{x_u k_e}{k_b T K_{off}}\right) + \left(\frac{k_b T}{x_u}\right) \ln v \rightarrow \text{After fitting figure 7.9} \rightarrow y=1.8*10^{-10} + 6.6*10^{-12}x$$

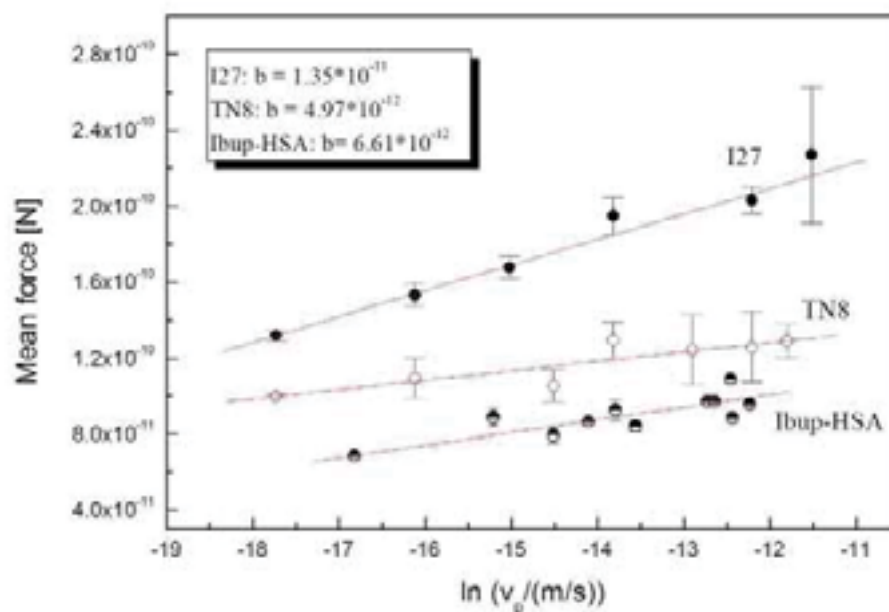$k_b T$ (23°C)= 4.08*10^{-21} N/m
K_e= 0.22 N/m

$$b = \frac{k_b T}{x_u} = 6.6*10^{-12} \rightarrow x_u= 6.2*10^{-10} \text{ m} = 0.62 \text{ nm}$$

$$a = \left(\frac{k_b T}{x_u}\right) \ln\left(\frac{x_u k_e}{k_b T K_{off}}\right) = 1.8*10^{-10} \rightarrow K_{off} = 0.055 \text{ s}^{-1}$$

Appendix 7.6

Comparison between the unfolding of poly-proteins TN8 (white circles) and I27 (black circles) with HSA-ibup (white&black circles) interactions. The x_u for Tenascin is 0.82 (±0.13) nm, for titin 0.304 nm and for Ibup-HSA 0.6 nm. The unfolding rate of tenascin is 0.001 s^{-1}, for titin 0.0001 s^{-1} and for Ibup-HSA 0.055 s^{-1}. (b is the slope of the linear fitting). Data of TN8 and I27 adapted from *Best et al.* (*Anal. Chim. Acta 2003*).